

FINAL TECHNICAL REPORT

Hawaii Energy and Environmental Technologies Initiative

Office of Naval Research

Grant Award Number N00014-10-1-0310

For the period December 1, 2009 to September 30, 2015



May 2016

Table of Contents

| | |
|---|-----|
| EXECUTIVE SUMMARY | 4 |
| TASK 1. FUEL CELL SYSTEMS | 11 |
| 1.1 Fuel Cell Testing and Evaluation | 11 |
| 1.2 Bioactive Fuel Cells | 52 |
| TASK 2. TECHNOLOGY FOR SYNTHETIC FUELS PRODUCTION | 63 |
| 2.1 Biofuel Characterization Planning | 64 |
| 2.2 Plasma Arc Processing | 66 |
| 2.3 Thermocatalytic Conversion of Synthesis Gas into Liquid Fuels | 84 |
| 2.4 Novel Solvent Based Extraction of Bio-oils and Protein from Biomass | 85 |
| 2.5 Biochemical Conversion of Synthesis Gas into Liquid Fuels | 88 |
| 2.6 Biocontamination of Fuels | 92 |
| 2.7 Biofuel Corrosion | 96 |
| 2.8 Waste Management Using the Flash-Carbonization™ Process | 111 |
| TASK 3. METHANE HYDRATES | 112 |
| 3.1 Hydrate Energy | 114 |
| 3.2 Environmental Impacts of Methane Release from Seafloor Hydrates | 136 |
| 3.3 Hydrate Engineering Applications | 140 |
| 3.4 International Collaborative Research and Development | 146 |
| TASK 4. ALTERNATIVE ENERGY SYSTEMS | 150 |
| 4.1 OTEC Heat Exchanger | 150 |
| 4.2 Grid Storage | 152 |
| 4.3 PV Deployment and Testing | 168 |
| 4.4 Power Park Support | 180 |
| 4.5 Energy Test Platforms | 191 |
| 4.6 Variable Power Ice maker | 222 |
| 4.7 Alternative Biofuels Development | 240 |
| 4.8 Algal Production Studies | 240 |

Final Technical Report
Hawaii Energy and Environmental Technologies Initiative
Grant Award Number N00014-10-1-0310
December 1, 2009 to September 30, 2015

EXECUTIVE SUMMARY

This report summarizes work conducted under Grant Award Number N00014-19-1-0310, the Hawaii Energy and Environmental Technologies Initiative 2009 (HEET09), funded by the Office of Naval Research (ONR) to the Hawaii Natural Energy Institute (HNEI) of the University of Hawaii at Manoa (UH). This continued efforts initiated under previous HEET awards on critical technology needs associated with the development of advanced fuel cells and fuel cell systems, an expanded effort on fuel processing and purification, the extraction and stability of seabed methane hydrates, and testing and evaluation of alternative energy systems for the Pacific Region. Testing and evaluation of alternative energy systems includes heat exchangers for Ocean Thermal Energy Conversion (OTEC), grid-scale battery energy storage, photovoltaic (PV) systems, a fast-fill hydrogen fueling station, energy efficiency test platforms, and alternative biofuels development.

Under HEET09 fuel cell testing and evaluation continued with upgrades to the test stand along with further evaluation of fuel and airborne contaminant impact testing on fuel cell performance. The impact of fuel and airborne contaminant mixtures on fuel cell performance was continued. In support of the fuel cell bus demonstration program in Hawaii Volcanoes National Park (HAVO), another ONR activity, the effect of relevant contaminants and their mixtures were characterized to set air filter specifications. The potential synergy between different classes of airborne contaminants was also explored using a wetting agent that can affect product liquid water management in a fuel cell and promote the transport of ions towards and into the membrane, ultimately lowering fuel cell efficiency. Fuel cell hardware-in-loop and system simulation activities were focused on the benefits of novel fuel cell/battery hybrid system architecture for UAV applications. These were determined by testing the hardware controller and assessing its impact on UAV flight duration for a given propulsion and ancillary load profile. In support of the Naval Research Laboratory, HNEI conducted testing of NRL's variable current battery discharge method intended to improve the specific energy of a lithium-ion battery pack.

In support of the development of bioactive fuel cells, quantitative characterization of the electrode properties and cell performance were performed in order to enhance fundamental understanding of the underlying mechanism in electrobiocatalysis. This work was conducted in two parts, first to develop and characterize chitosan co-block polymers to immobilize multiple enzymes that can more fully oxidize complex energy fuels, and secondly to develop integrated *in situ* characterization methodologies, to better understand the charge transfer process involved by more direct measurement and correlation. Polar sensitive fluorophores in combination with fluorescent spectroscopy and microscopy techniques were used to probe the chemical microenvironments of native and hydrophobically modified chitosan polymer matrices used to immobilize enzymes. Results indicate that electrostatic forces dominate the interaction between fluorophores and polymer when both are freely suspended in solution. Secondly, unique

capabilities were demonstrated using spectroscopic imaging ellipsometry and electrochemical techniques to investigate mediator immobilization on platinum electrodes.

For Navy application, there is particular interest in liquid biofuels that can be introduced into the current fuel supply chain. This task identified operational challenges and analyzed issues related to the introduction of liquid biofuel, focusing on the variability caused by primary feedstock sources, conversion methods, storage methods, and the presence of contaminants.

In subtask 2.1, Biofuel Characterization Planning, high priority, critical testing capabilities were developed and interfaced with the supply chain. These capabilities were identified in the previous phase of HEET and included equipment, personnel, and lab facilities to support the Navy's greater use of alternative fuels blended with petroleum F76 diesel and JP5 jet fuel. Under this award, "fit-for-purpose" properties of the fuels were identified including their compatibility with fuel tank and piping materials, their compatibility with elastomer seals in engines and fuel delivery equipment, and their capacity to maintain levels of microbial and corrosion activity comparable to, or lower than, petroleum. Storage stability testing capabilities for fuel quality were down-selected from the selected list of methods to assess special equipment requirements for fuel quality.

In Subtask 2.2, Plasma Arc Processing, the use of a non-thermal reverse vortex flow (RVF) gliding-arc reformer for liquid fuels was explored. Previous work had focused on non-thermal, RVF stabilized gliding-arc plasma reforming of methane. Under this subtask, the same system was adapted for the reforming of marine diesel (F-76), hydroprocessed renewable diesel (HRD-76) and dodecane; liquid fuels that could be reformed into hydrogen rich gas for shipboard applications. Ultrasonic atomization of the fuel was used to axially inject fuel into the reformer. Injected fuel vaporized due to elevated temperatures in the reactor. Vapor clouds were eliminated by insulating the upper half of the reaction chamber. Parametric and factorial tests resulted in dodecane conversion that remained fairly constant across all of the tests while the selectivity, hydrogen yield, efficiency, and other parameters varied greatly. Decreasing power input, increasing fuel input, and increasing steam input improved system performance.

In Subtask 2.3, Thermocatalytic Conversion of Synthesis Gas into Liquid Fuels, catalyst characterization and activity of Zr or Mn containing Ru/Q10 were investigated for Fischer-Tropsch synthesis in a stirred slurry tank reactor. The addition of Zr or Mn in Ru/Q10 enhanced CO conversion, C5+ selectivity and space time yield under the tested conditions. The catalyst activity was highly stable during the period of reactor operation. Catalyst characterization results suggest that a small amount of Zr or Mn addition can increase the surface atomic concentration of Ru and inhibit the oxidation of Ru species, resulting in enhanced catalyst activity and stability.

The objective of 2.4, Novel Solvent Based Extraction of Bio-oils and Protein from Biomass, was to optimize methods and compositions of co-solvent mixtures for the one-step extraction of bio-oils and protein from biomass, and to further develop unit operations capable of fractionating and purifying both products. Three main tasks were completed: (1) to quantify the degree to which 1-step extraction using a hydrophilic co-solvent system extracts protein from corn and oil seeds; (2) to determine the extent to which proteins denature in the co-solvent system; and (3) to optimize the composition of the co-solvent for protein extraction. In this work, an ionic liquid –

methanol co-solvent was shown for the first time to effectively co-extract phorbol esters and bio-oil from jatropha kernel biomass in a single extraction step. Under optimized conditions for simultaneous extraction of bio-oil and phorbol esters, 30 wt% ionic liquid, [C2mim][MeSO₄] and 70 wt% methanol, nearly all the bio-oil was extracted and auto-partitioned to a separate immiscible phase. Additionally, approximately 98% of the phorbol esters were extracted from the original biomass. The co-solvent did not extract significant amounts of protein which remained with the jatropha biomass even after washing steps. In addition to achieving effective co-extraction of both bio-oil and phorbol esters, the low phorbol esters - high protein content of the de-lipified biomass also possessed high potential as an animal feed.

In Subtask 2.5, Biochemical Conversion of Synthesis Gas into Liquid Fuels, the effect of CO on microbial activity was investigated in a gas tight bioreactor, revealing the toxicity of CO in a typical biomass syngas (CO>10%). A thermal reactor with Cu/ZnO catalyst was developed to convert CO into CO₂ and hydrogen. A dual reactor system was built up for continuous gas circulation between the bioreactor and the catalytic reactor to reach a very high CO conversion (> 90%). Three major conclusions were drawn from the work: the microbial strain cannot work directly on syngas because of the high CO content (>10%) and its toxicity to microbes; the strain can work on residual gas from other processes if CO content is 5% or below, and; a dual reactor system can effectively reduce the CO content of syngas for its direct utilization and conversion into biopolyester by the microbes.

Subtask 2.6 Biocontamination of Fuels, examined the microbial contamination of biofuels and the associated impacts on fuel stability, biofouling, and corrosion of fuel-related components. Development focused on a DNA based rapid molecular detection method and investigation of microbiologically induced corrosion. Results suggest that corrosion also occurs due to the direct metabolism of fuel components. This metabolism can provide basal support for the development of complex microbiological communities that include sulfate reducing bacteria and others that may also play a role in biofouling and corrosion. Detection of this specific metabolic pathway is fundamental to development of an effective control methodology. The research is now focused on finding specific genetic elements that are expressed during fuel metabolism using *Moniliella wahieum* Y12T as a model. Prokaryotic isolates have also been obtained and will be included in subsequent work.

Under Subtask 2.7 Biofuel Corrosion, static immersion tests were conducted in water/biofuel mixtures using unfiltered and filtered fuels in the anaerobic, sterile aerobic, and aerobic conditions. The results indicated that presence of microorganisms in the unfiltered biofuel resulted in the most severe corrosion rate of steel after 6 months in the anaerobic condition. The corrosion products on steel immersed in the biofuel phase were identified as mainly iron formate hydrate and iron oxalate hydrate. The formation of iron formate and iron oxalate suggests the presence of organic acids (i.e., formic acid and oxalic acid) in the biofuel.

Under Subtask 2.8, Waste Management Using the Flash-CarbonizationTM Process, fundamental measurements were conducted of the specific isobaric heat capacity of pure water at elevated pressure to enable design of advance waste treatment systems. The aim of this study was to compare experimental results with values predicted by the IAPWS-95 formulation, in which most of the data are based on measurements of Sirota's group in the former Soviet Union in the

period from 1956 to 1970. The present calorimetric results for the specific heat capacity of pure water were found to be substantially in disagreement with the values obtained using the IAPWS-95 formulation, especially at high temperatures, where the differences were greater than 20%.

Task 3, Methane Hydrates comprised four activities: hydrate energy, environmental impacts of methane release from seafloor hydrates, hydrate engineering applications, and international collaborative R&D.

Work on hydrate energy focused on fundamental laboratory studies of methane hydrate formation and dissociation in porous media, plus determining the effects of transition metal salts on hydrate behavior. Most of the transition metal salts tested inhibited methane hydrate formation at high concentrations, but none to the extent of sodium chloride except for ferric chloride. FeSO_4 and CuSO_4 at concentrations up to 2 mol% were observed to have minimal impact on hydrate stability. At lower concentrations (0.5 mol%), some of the salts appeared to promote hydrate formation, an effect that is also observed with alcohols.

When methane hydrate forms in porous media, the data suggests that a small shift in its phase boundary will occur. The implication of this result is that, over a range of pressures relevant to deep ocean sediments, the generally-employed phase boundary for a simple water-methane binary system tends to over predict hydrate melting temperature. Lower melting temperatures means that natural hydrate deposits in seafloor sediment are more vulnerable to purposeful or inadvertent increases in temperature. While this can be advantageous for certain methane recovery strategies, it raises concerns about outgassing and seafloor stability in a warming climate. Additional experiments appear to be warranted to confirm this phenomenon for a broader range of porous media properties and to more definitively quantify the shift in the phase boundary and to understand the underlying mechanism.

Microbial processes in the sediment and the water column are believed to play a major role in determining methane levels throughout the marine environment. Combined use of molecular analysis, chromatography and microcalorimetry was attempted with Beaufort Sea samples to elucidate the aerobic biological metabolisms by which microbes can regulate methane level in both the water column and near-surface. The development of submodels of microbial methane sources and sinks for integration into an ocean general circulation model also progressed during this period.

A preliminary experimental study of hydrate desalination and biofiltration was completed as part of the goal to explore the use of gas hydrates for various engineering applications. The data suggest that hydrates can be used to substantially decrease the salt content of low salinity water, but may not be able to significantly remove biological contaminants.

To foster international collaborative R&D on methane hydrates, HNEI supported and helped to organize the 8th International Workshop on Methane Hydrate R&D that was held in Sapporo, Japan in June 2012, as well as the 9th workshop held in Hyderabad, India in November 2014.

Task 4, Alternative Energy Systems focused on Ocean Thermal Energy Conversion, grid energy storage, PV systems, hydrogen production and fueling, energy efficient building platforms, variable powered ice maker, and alternative biofuels for Navy applications.

Under 4.1, Makai Ocean Engineering continued work to design, construct and test subscale heat exchangers to validate performance for Ocean Thermal Energy Conversion applications. Under this award, shakedown testing of the heat exchanger test facility was completed, the control system was developed and validated, development and testing of the brazed aluminum evaporator and the shell and tube condenser were completed, and the hollow extrusion corrosion samples were evaluated. The brazed aluminum evaporator uses brazed aluminum fins in the ammonia channels and square extruded passages for the seawater channels. The fins enhance heat transfer and the extruded channels eliminate exposing brazed joints to the corrosive seawater environment. The shell and tube condenser showcases the use of tubular friction stir welding – a new manufacturing technique – to join tubes to the tubesheet. The use of aluminum alloys and friction stir welding combine the desirable corrosion resistance of the alloy and manufacturing method, as well as a lowered cost of manufacturing. Major improvements in instrumentation, data collection, and control software enabled a wide range of testing conditions and relatively short transient time between testing points. The preliminary results of the corrosion testing program indicate localized corrosion will determine the viability of aluminum heat exchangers.

Under Subtask 4.2, Grid Storage, a grid-scale Battery Energy Storage System (BESS) was installed, connected to the grid and commissioned on the Island of Hawaii. It has been operating for three years, cycling over 3 gigawatt-hours in energy throughput. A second BESS, intended for the island of Molokai, was developed through the factory acceptance test phase. In an effort to realize these two BESS installations, HNEI formed and led public-private partnerships between UH, utility owners, hardware manufacturers, algorithm developers, and independent power producers.

On the Island of Hawaii, the 1 MW, 250 kWh BESS installed at a 10.6 MW wind farm can be controlled by either of two real-time algorithms: a primary frequency response algorithm, and a wind power smoothing algorithm. An Altairnano, lithium-ion titanate battery was chosen for an extended cycling lifetime and faster charge/discharge rates compared to the more common carbon anode electrochemistry. The two algorithms, frequency response and wind smoothing, were developed in tandem with the hardware, and were put through a series of acceptance tests. Over 100 switching experiments were conducted targeting a variety of grid conditions (day/night, windy/calm, etc.) and a variety of algorithm parameter settings (gain, limit on maximum power, and a “dead band” in which the algorithm does not respond to small fluctuations). The results show that the BESS reduces the overall frequency variability by 30-50% under typical grid conditions.

A 2 MW, 397 kWh BESS planned for the Molokai grid system is intended to provide the very fast response time needed to balance the intermittency in PV power generation on the low inertia grid system. While still under development, the Molokai BESS has helped identify current technological barriers related to BESS and inverter response times, as well as meter sensing delays. An improvement in this area is likely to have applications in real-world micro-grids

under heavy penetration from intermittent renewable energy resources. HNEI will continue to test both systems under other awards to assess grid benefit and long-term battery health.

Under Subtask 4.3, PV module and inverter technologies were tested to characterize performance and durability under differing environmental conditions. PV test platforms were installed at Hawaii Project Frog classrooms on Oahu and Kauai for side-by-side comparison of grid-connected PV systems. Efforts focused on three areas: instrumentation for data collection and subsequent performance analysis based on two years of collected data; design of larger test platforms for future installation on Maui and at MCBH on Oahu, and; development of a new data acquisition system (DAS) with added capabilities including measurement of open-circuit voltage and short-circuit current.

In August 2013, 2.6kW PV arrays were installed on the rooftops of classrooms at Ilima Intermediate School on south Oahu and at Kawaikini Charter School in Lihue, Kauai. These energy-neutral buildings were being studied as part of the energy efficiency task of this ONR award. At the Ilima site, two PV material technologies, heterojunction with intrinsic thin layer (HIT) and thin film made of copper, indium, gallium and diselenide (CIGS) were compared side-by-side. At Kawaikini three PV technologies were compared, HIT, CIGS, and monocrystalline with two different system architectures, string vs microinverter. Data collection was initiated in November 2013 for two years of operation at both locations.

The larger test platforms were designed for 25kW and 100kW, comprised of a broad range of module manufacturers, system architectures, and module technologies, including mono and polycrystalline, bifacial, HIT, and thin films (Cadmium Telluride (CdTe) and CIGS). The 100kW MCBH test platform is design to be installed on two carport structures to support the hydrogen filling station, another HNEI/ONR project, offsetting the electrical load of the electrolyzer at the station.

The Power Park Support Subtask 4.4 expanded on work begun under a US Department of Energy funded effort to deploy a 350 bar hydrogen production and fueling station at HAVO. Due to operational changes, this system was deployed at the Marine Corps Base Hawaii (MCBH) on Oahu to support the ONR General Motors Equinox fuel cell electric vehicle project. With funding from this award, the system was modified by adding a 700 bar fast fill capability. The new 350/700 bar fast fill station became operational on 19 November 2014. It has successfully completed over 300 fills without any operational downtime.

Under Subtask 4.5 Energy Test Platforms, energy efficient building platforms were deployed and evaluated for potential mass-deployment to the Pacific region. Working with Project Frog, HNEI installed three test platforms at two sites and assessed the structures in terms of manufacturing and installation cost effectiveness as well as logistical efficiency. The components of this systematized kit-of-parts for use in the Pacific islands includes structure, envelope, construction materials, energy generation and management, sensors and controls, and integrated building technologies. The research further evaluated the integration of clean energy generation technology within the test platforms.. The assembly of the test platform at Ilima Intermediate School was completed and ownership transferred from UH to the Department of

Education on September 30, 2011. The two test platforms at Kawaikini were completed and transferred March 15, 2013.

During the process, Frog identified two ways to improve future deployments. Optimizing the packaging and shipping procedures would decrease the costs by 17%-26%; and creating a certified installer network would allow use of 100% locally sourced labor and management.

After the first complete year of data collection in 2014, the three platforms performed as designed. The structure in the hotter Oahu microclimate performed at the “High Estimate” which assumed significant dependence on air conditioning, resulting in an actual electric site EUI of 7.8 kWh/sf-yr (excluding solar). The two predominantly naturally ventilated structures in the more temperate Kauai location produced twice as much energy than was used, realizing an average electric site EUI of about 4.7 kWh/sf-yr, achieving the “Optimal Performance” target. This difference in performance may be attributable to two factors: differences in micro-climates and difference in policies, awareness and user response to the internal environment.

A second objective under this subtask was to install, test and evaluate small wind turbine technologies to determine the relative effectiveness of differing designs, the impact of different climatic conditions. HNEI contracted the Golden Gate National Parks Conservancy to install 1 kW wind turbines adjacent to, and connected with the test platforms located at the Crissy Field Center in the Presidio of San Francisco, a proven wind resource for collection of comparative wind energy data. Vertical axis technology, turbines manufactured by Venco Power, Windspire Energy and Tangarie Alternative Energy Power were selected. A data acquisition system was installed to monitor wind turbine performance as well as building performance of the Center. Simultaneous wind speed and turbine output was recorded for 816 days with minute-level data. Actual performance was compared to expected performance for both wind resource and turbine generation. Both Windspire turbines operated from October 6, 2012 through December 31, 2014, however the Venco turbines had intermittent operating issues and the Tangarie turbine operated for only 268 days, having failed by June 30, 2013.

Under Subtask 4.6, a variable powered ice-maker (VPI) was procured and tested in a subtropical climate, at NELHA. Initial testing using salt water produced high quality sea water ice that was used by local aquaculture companies at the Natural Energy Laboratory of Hawaii Authority to freeze their fish. Over the course of several months, the high heat levels experienced in the system enclosure coupled with the aggressive corrosive environment caused the electronic control equipment to degrade and eventually fail. A major design issue identified was the use of two compressors to turn down the system in the event of a loss of power. While the system was able to meet moderate power variability, when it was tested with an instantaneous loss of power one of the two compressors successfully shut down as it was programmed to do but vapor-locked, and could not be restarted for up to 40 minutes until the vapor lock naturally cleared. A solution is to use one compressor. Given these issues it was not possible to test the system’s ability to desalinate saltwater. If this system is still of interest to ONR, it would need to be redesigned to address the design issues identified during this experiment.

An alternative biofuels assessment was conducted by Green Era LLC. The assessment comprised four areas: a site survey of agricultural lands in Hawaii; a crop assessment; production, harvesting, and handling methodologies, and; feedstock, processing, and waste handling for a number of thermochemical, biochemical and hybrid conversion technologies that could be used to convert the selected feedstocks into usable, sustainable, high-value energy products.

Hawaii BioEnergy reported the results of an assessment of the feasibility of growing microalgae as a biofuel, including the challenges of both an open, mixotrophic algal system, and a heterotrophic system.

TASK 1. FUEL CELL SYSTEMS

Expanding on work initiated in prior HEET awards, both proton exchange membrane fuel cell (PEMFC) systems and bioactive fuel cells were evaluated in this task. The impact of fuel and airborne contaminants was tested on PEMFC performance at the component, cell and stack level. Additionally, air filter specifications were determined, cell/battery hybrid systems were evaluated and the impact of system architecture was tested. Bioactive fuel cell efforts focused on quantitative characterization of the electrode properties and cell performance to advance understanding of the underlying mechanism in electrobiocatalysis. First, chitosan co-block polymers were developed and characterized to immobilize multiple enzymes that can more fully oxidize complex energy fuels. Secondly, more direct measurement and correlations were developed through integrated *in situ* characterization methodologies, to better understand the charge transfer process.

1.1 Fuel Cell Testing and Evaluation

Expanding on efforts under previous ONR awards, this sub-task continued work to improve on the understanding, performance, and durability of fuel cells exposed to harsh environments; and power system issues of relevance to UAV and Unmanned Underwater Vehicle (UUV) applications.

Studies aimed at the performance and durability of fuel cells exposed to contaminants were continued and expanded into operating conditions that are closer to those encountered in the field. Fuel contamination was studied with CO at a relevant and low concentration level of the same order as stated in the International Standardization Organization hydrogen fuel standard (ISO 14687-2). These activities made use of the gas analysis infrastructure installed at the facility (gas chromatography) to identify predominant reactions and clarify the contamination mechanism at a low contaminant concentration of 1 ppm. Air and hydrogen streams are more likely in practice to contain several contaminants. In support of the fuel cell bus demonstration program in HAVO, the impact of relevant contaminants and their mixtures on fuel cell performance was characterized to define air filter specifications. For this work, the major contaminant in volcanic plumes SO₂, as well as NO₂ and benzene, representative of automotive

exhausts, were used. The coupling between different classes of contaminants was also explored. Initial efforts focused on an organic molecule that can alter the wetting properties of electrodes and increase their liquid water content. This in turn promotes the transport of positive ions into the membrane, adversely affecting its transport properties. Isopropanol, a cleanser component and solvent, and Na^+ , a major ion in oceans, were used as model contaminants for this investigation.

Power system tests for this period encompassed both fuel cell systems and battery systems. A hardware controller was built to demonstrate the previously proposed UAV fuel cell/battery conceptual partial hybrid system architecture. Tests made use of HNEI's hardware-in-loop test system to show the benefit of the novel architecture on the UAV flight duration. The hardware-in-loop system as well as the previously developed custom designed multi-channel impedance spectrometry tool was used to investigate the advantage of a variable current battery discharge protocol proposed by NRL on the specific energy of a 4-cell Li ion battery pack.

1.1.1 Component, Cell and Stack Testing

Reactions of Carbon Monoxide within a PEMFC:

In this section we report the results of a study that investigated the reactions that occur from exposing the anode of a PEMFC to one part per million (1ppm) carbon monoxide (CO) in hydrogen (H_2). This concentration is more practically relevant than prior work because it is closer to the published specification for hydrogen fuel of 0.2ppm (ISO 14687-2). Reactions were investigated with gas chromatography and cyclic voltammetry (CV).

This work supports the Navy's efforts to deploy fuel cells because H_2 is most commonly produced from the steam reformation of methane and will contain trace amounts of CO , which is known to significantly decrease fuel cell performance. This work studied the reactions that occur within the fuel cell to gain a greater understanding of which reactions most significantly affect fuel cell performance. The results will be used in future efforts to develop mitigation strategies to recover performance and maintain performance for fuel cells subjected to H_2 fuel with varying concentrations of CO in the gas. Reactions were studied using gas chromatography and cyclic voltammetry at a CO concentration of 1ppm using a single fuel cell with commercially available membrane/electrode assembly operated at temperatures of 10 and 80°C with an anode catalyst loading of 0.1mg Pt cm^{-2} . The temperatures represent extremes of operation and the catalyst loading is near the expected loading in a commercial fuel cell powered vehicle.

CO was found to enhance a carbon corrosion reaction that showed a strong thermal dependence over the temperatures tested. CO readily reacted chemically with oxygen at 80°C while virtually no conversion to CO_2 was observed at 10°C . The water gas shift reaction appeared to have been enhanced via electrochemical promotion since nearly 100% conversion of CO was observed at both temperatures despite being kinetically limited at the temperatures used in this work. Potential oscillations were also observed for the first time for a cell with a Pt/C catalyst.

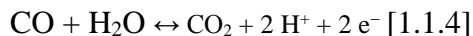
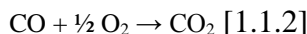
Gas chromatography (GC) was used to measure the inlet and outlet concentrations of CO and CO_2 on the anode before, during, and after exposure to 1ppm CO . The properties of the GC

instrument are given in Table 1.1.1. Concentrations were converted to molar flow rates using the injection concentration and volumetric flow rates.

Table 1.1.1 Properties of the gas chromatograph

| |
|--|
| Manufacturer: Varian |
| Detector: Flame Ionization Detector |
| CO/CO ₂ Detection Limit: 0.05 ppm |
| Separation Columns: Mol Sieve 5A Hayesep dB |

Reactions studied in this work are shown below in Equations 1.1.1 to 1.1.4. Individual reactions with CO were studied by considering the type of gas that was supplied to each electrode, the relative humidity of each electrode's gas feed stream, and the electrical condition of the fuel cell. For example, in some cases the fuel cell was short-circuited (SC) or held at open circuit voltage (OCV) to study the effects of current on the rate of the reaction.



The gas stream species and relative humidity used in each experiment are given with respect to the individual reaction with CO to be studied in Table 1.1.2 below.

Table 1.1.2 Experimental testing matrix with respect to the reaction being studied

| Experimental Set | Reaction Studied | Anode Gas | Anode Relative Humidity [%] | Cathode Gas | Cathode Relative Humidity [%] | Cell Electrical State |
|------------------|--|----------------|-----------------------------|----------------|-------------------------------|-----------------------|
| 1 | $\text{CO} + \text{Pt} \leftrightarrow \text{CO} - \text{Pt}$ | N ₂ | 0 | N ₂ | 0 | OCV |
| 2 | $\text{CO} + \frac{1}{2} \text{O}_2 \rightarrow \text{CO}_2$ | N ₂ | 0 | Air | 0 | OCV |
| 3 | $\text{CO} + \text{H}_2\text{O} \leftrightarrow \text{CO}_2 + \text{H}_2$ | N ₂ | 100 | N ₂ | 100 | OCV & SC |
| 4* | $\text{CO} + \text{H}_2\text{O} \leftrightarrow 2 \text{H}^+ + 2 \text{e}^- + \text{CO}_2$ | N ₂ | 100 | H ₂ | 100 | CV |
| 5 | Multiple Reactions Possible | H ₂ | 100 | Air | 50 | 1 A cm ⁻² |

* Experimental sets 1 to 3 and 5 used GC while experimental set 4 was a cyclic voltammagram (CV) study of CO stripping.

The PEMFC, membrane parameters and operating conditions used in this work are given below in Table 1.1.3.

Table 1.1.3 Fuel cell and membrane parameters and operating conditions

| Operating Parameter | Anode | Cathode |
|---------------------|----------|---------|
| Temperature [°C] | 80 or 10 | |

| | | |
|---|------------------------|----------------------|
| Cell active area [cm ²] | 50 | |
| Membrane/Electrode Assembly | Commercially Available | |
| Gas Diffusion Layer | SGL 25 BC | SGL 25 BC |
| Back-pressure [kPa _g] | 48.3 | 48.3 |
| Gases flow rate [Standard L min ⁻¹] | 0.697 | 1.658 |
| Flow Field Geometry | 2-Channel Serpentine | 3-Channel Serpentine |
| CO concentration [ppm] | 1 | 0 |
| Catalyst Loading [mg Pt cm ⁻²] | 0.1 | 0.4 |

The results shown in Figure 1.1.1 give the molar flow rates of CO and CO₂ at the anode inlet and outlet for a fuel cell operated with an anode gas stream of dry nitrogen (N₂) and a cathode gas stream with dry N₂. The goal of this experiment was to study the retention of CO within the fuel cell. The plot on the left in Figure 1.1.1 shows the results for the 80°C experiment and the plot on the right shows the 10°C results.

The 80°C results show that the molar balance of the carbon species between the inlet and outlet did not close upon injection of CO into the cell. The outlet CO₂ was initially greater than the amount of CO supplied to the cell. This indicated that the injection of CO into the cell promoted a carbon corrosion reaction with an oxygen containing species. Water or molecular oxygen is presumed to be the oxygen containing species. However, the specific type of species and origin is not definitively known although molecular oxygen is suspected to be present in the nitrogen in sub-ppm amounts. The results were unexpected because it was presumed that the CO would be retained within the cell without reaction. The results are still significant though because they show that purging with dry inert gases can still degrade the membrane through a carbon corrosion reaction even if only 1ppm of CO is present in the anode stream.

The 10°C results show that some of the CO is converted to CO₂ after the CO injection is initiated after 10 hours of operation. In this case, the carbon balance initially does not close as CO is retained within the cell because it is presumably adsorbing to the Pt/C catalyst. In contrast to the 80°C results, a definite steady state is attained after approximately 10 hours of CO exposure as indicated by the closure of the carbon balance. At steady state nearly the entire amount of CO that enters the cell exits the cell showing very little reaction to form CO₂. A comparison of the conversion of CO to CO₂ between the 80°C and 10°C results show that the carbon corrosion reaction has a thermal dependence.

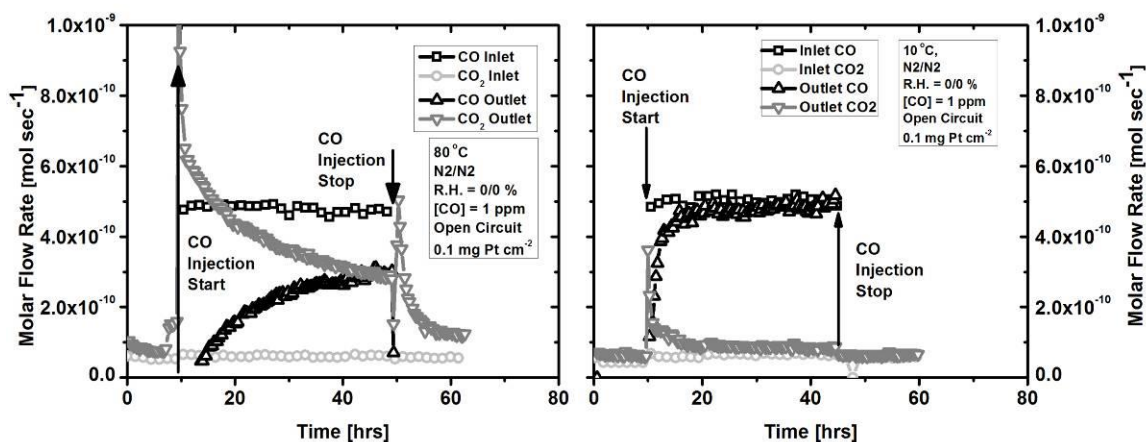


Figure 1.1.1 Molar flow rate of CO and CO₂ into and out of the anode. Experimental conditions are given in the figure and table 1.1.3. Anode/cathode gases and gas stream inlet humidity were selected to study CO retention within the fuel cell at open circuit

The results shown in Figure 1.1.2 give the molar flow rates of CO and CO₂ at the anode inlet and outlet for a fuel cell operated with an anode gas stream of dry N₂ and a cathode gas stream with dry air. The goal of this experiment was to study the reaction of CO with oxygen crossing over from the cathode within the fuel cell. The plot on the left in Figure 1.1.2 shows the results for the 80°C experiment and the plot on the right shows the 10°C results.

The 80°C results in Figure 1.1.2 show that the amount of CO₂ exiting the cell is greater than the amount of CO and CO₂ entering the cell both before and after the injection of CO is initiated. This indicates that the carbon corrosion reaction is likely enhanced due to the crossover of oxygen from the cathode in dry conditions. Upon introducing CO into the cell at hour 20 the entire amount of CO that enters the cell is converted to CO₂. Additionally, the rate of the carbon corrosion reaction appears to increase during CO exposure because the difference between the amount CO₂ exiting the cell during CO exposure to the amount of CO and CO₂ entering the cell is larger during CO exposure than it was prior to exposure. Thus, this provides additional evidence that CO exposure in dry conditions enhances a carbon corrosion reaction with an oxygen containing species.

The 10°C results in Figure 1.1.2 are quite similar to those in Figure 1.1.1. After an initial increase in the conversion of CO to CO₂, nearly 100% of the CO entering the cell was observed to exit the cell. This indicates that the reaction of CO with O₂ is strongly dependent upon temperature in the range of 10 to 80°C in a PEMFC.

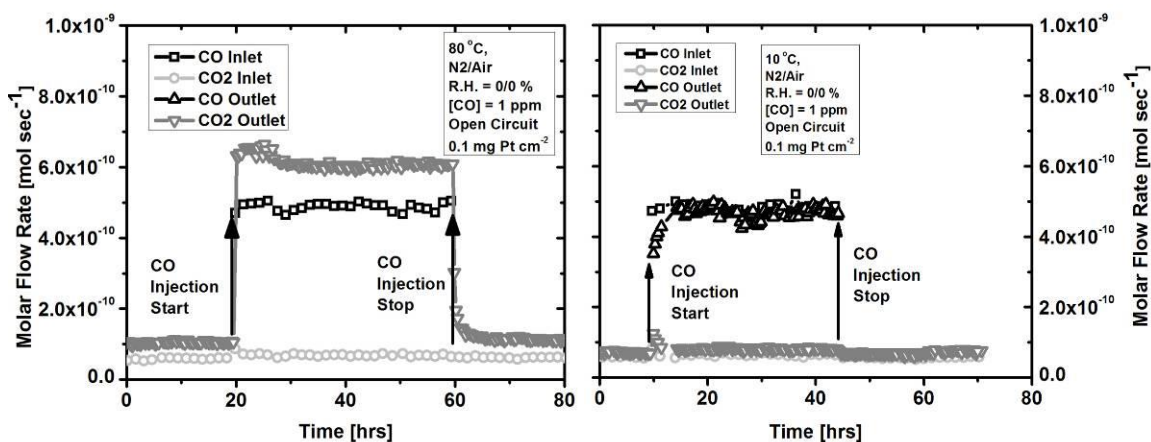


Figure 1.1.2 Molar flow rate of CO and CO₂ into and out of the anode. Experimental conditions are given in the figure and table 1.1.3. Anode/cathode gases and gas stream inlet humidity were selected to study the reaction of CO and O₂ within the fuel cell at open circuit

The results shown in Figure 1.1.3 give the molar flow rates of CO and CO₂ at the anode inlet and outlet for a fuel cell operated with an anode gas stream of N₂ with a relative humidity of 100% and a cathode gas stream with N₂ at 100% relative humidity. The goal of this experiment was to study the catalytic reaction of CO with water vapor or what is commonly referred to as the water gas shift (WGS) reaction. The plot on the left in Figure 1.1.3 shows the results for the 80°C experiment and the plot on the right shows the 10°C results. Also shown in both plots in Figure 1.1.3 is the measured open circuit voltage of the cell versus time.

The 80°C results in Figure 1.1.3 show the voltage of the fuel cell increasing over time, which, as noted above, may be due to the presence of sub-ppm amounts of O₂ in the N₂. The increasing voltage over time may be due to oxygen adsorption to the catalyst and partial pressure differences of O₂ in the anode and cathode due to different pressure drops across each electrode as a result of different flow rates and flow field geometry. In Figure 1.1.3, the cell voltage continues to increase until CO is injected into the cell at approximately hour 15. At this point, the cell voltage begins to decrease and both CO and CO₂ are observed at the outlet of the cell during the first 5 hours of CO exposure. After this time, the cell voltage decreases abruptly by nearly 500mV and a significant increase in the production of CO₂ is observed. This increase in CO₂ production is clearly greater than what would be observed for 100% conversion of CO to CO₂. Thus, a carbon corrosion reaction is clearly occurring in addition to the WGS. The decrease in voltage with the increase in CO conversion to CO₂ suggests a relationship between the cell voltage and the corrosion reaction. Interestingly, subsequent to hour 22 the cell voltage remains low for the remainder of the CO exposure. Additionally, the entire amount of CO entering the cell is converted to CO₂ and carbon corrosion is observed throughout the remainder of the duration of the CO exposure. This suggests a relationship between cell voltage and the rate of the WGS reaction.

The GC results for the 10°C data in Figure 1.1.3 initially show similar behavior to the 10°C data in Figures 1.1.1 and 1.1.2 over about the first 8 hours of CO exposure where there is an initial

increase in CO₂ production followed by a period of CO retention within the cell. Eventually, however, the behavior becomes more similar to that observed for the 80°C in Figure 1.1.3 where the cell voltage decreases rapidly and complete conversion of CO to CO₂ is observed with carbon corrosion. The carbon corrosion reaction appears to cease after hour 22 in Figure 1.1.3 for the 10°C data because the carbon balance closes after this point. This again points to a thermal dependence for the carbon corrosion reaction. The increase in carbon corrosion and decrease in cell voltage suggests that there is a relationship between the carbon corrosion reaction and the cell voltage that is enhanced by the presence of CO as well.

Also of interest for both the 80 and 10°C experiments is that after the cell voltage decreases nearly the entire amount of CO is converted to CO₂. In other words, the conversion of CO to CO₂ via the water gas shift reaction is nearly 100% in both cases. From a thermodynamic standpoint, the water gas shift (WGS) reaction is strongly favored at lower temperatures; however, the reaction kinetics are strongly dependent upon temperature and expected to be quite slow at both 10°C and 80°C. In industrial practice the WGS is typically carried out over different catalysts at significantly higher temperatures than those used in this work. Thus, it is possible that another process is enhancing the rate of the reaction. Electrochemical promotion of the WGS has been reported previously to enhance the rate of the WGS;¹ however, this requires the application of a current and these measurements were performed at open circuit voltage. It may be plausible though that internal currents are being established within the cell that promote the rate of reaction for the WGS. This would be consistent with the drop in cell voltage observed for both temperatures in Figure 1.1.3.

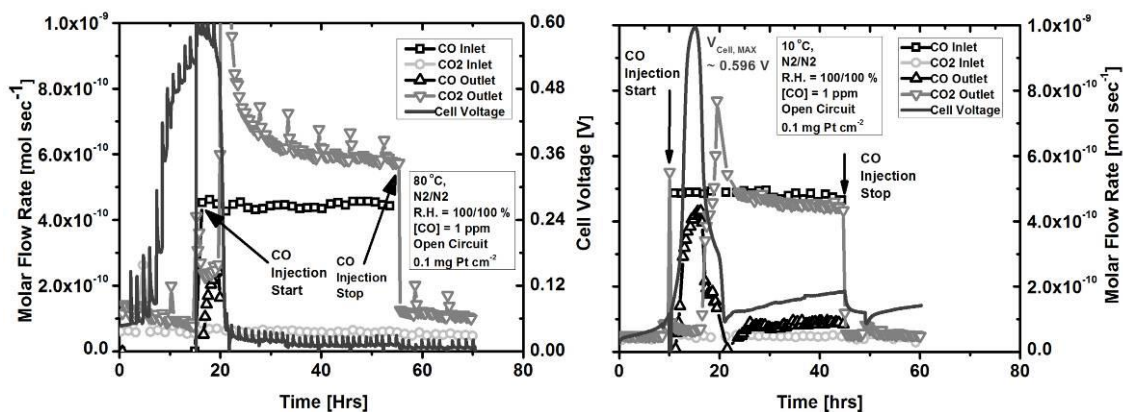


Figure 1.1.3 Molar flow rate of CO and CO₂ into and out of the anode. Experimental conditions are given in the figure and table 1.1.3. Anode/cathode gases and gas stream inlet humidity were selected to study the catalytic reaction of CO and H₂O within the fuel cell at open circuit. The measured cell voltage versus time is also shown and represented by the dark grey line. The scale for the voltage data is the same for both and given on the right axis for the 80°C data and the left axis for the 10°C data

To investigate the effects of an applied current on the WGS reaction an experiment was performed at 80°C at the same conditions as those in Figure 1.1.3 except, in this case, the cell was electrically short circuited. The results are shown below in Figure 1.1.4. From Figure 1.1.4, it is clear that complete conversion of CO to CO₂ is observed with the application of an electrical current. The results in Figure 1.1.4 also indicate that there is no carbon corrosion reaction

observed because the carbon molar balance closes throughout the duration of CO exposure. Because the cell was electrically shorted throughout the experiment this suggests that the cell voltage, or more specifically the anode potential, plays a role in enhancing the carbon corrosion reaction. The complete conversion of the WGS despite not being kinetically favored at 80°C provides further evidence that electrochemical promotion is enhancing the reaction rate.

To study the role that the electrochemical oxidation of CO and water (H₂O) to CO₂, protons (H⁺) and electrons (e⁻) may have in an operating fuel cell, cyclic voltammetry with CO stripping was performed to determine the onset potential for CO electrochemical oxidation at temperatures of 10, 60, and 80°C. The results are shown in Figure 1.1.5 versus a hydrogen reference electrode which was held at the same conditions as the experiments in Figure 1.1.3. From Figure 1.1.5, the onset potential for the electrochemical oxidation of CO increased as the operating temperature was decreased. Onset potentials ranged from 0.75V at 10°C to 0.59 V to at 80°C. However, in order to determine if electrochemical oxidation occurs during normal fuel cell operation information on the change in anode over-potential is needed.

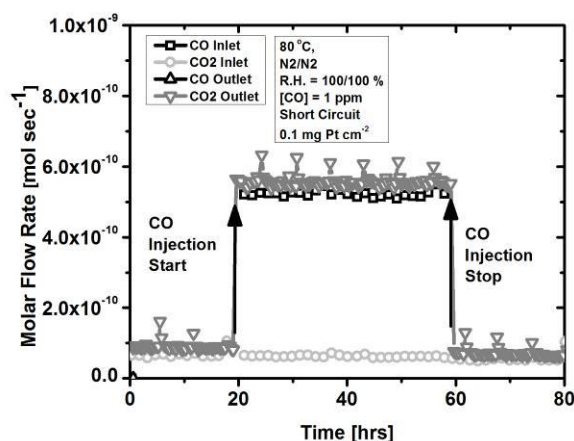


Figure 1.1.4 Molar flow rate of CO and CO₂ into and out of the anode. Experimental conditions are given in the figure and table 1.1.3. Anode/cathode gases and gas stream inlet humidity were selected to study the catalytic reaction of CO and H₂O within the fuel cell in an electrically short circuited fuel cell

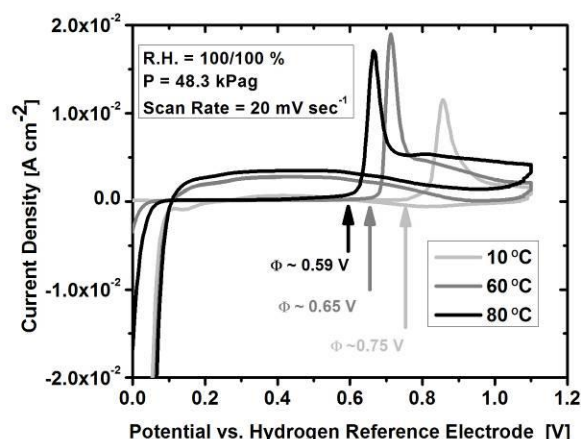


Figure 1.1.5 Cyclic Voltammogram with CO stripping for cell temperatures of 10, 60, and 80°C. Note that potentials are reported with respect to a hydrogen reference electrode at the conditions shown in the figure which are similar to those used to generate the data from the operating fuel cells shown below

Change in anode over-potential data can be determined from the data shown in Figure 1.1.6. Figure 1.1.6 shows the loss in cell voltage resulting from exposure of 1 ppm CO to a fuel cell operating with H₂ and air at 80°C on the left and 10°C on the right. If it is assumed that all voltage loss shown in Figure 1.1.6 can be attributed to the change in anode over-potential from CO, the maximum change in over-potential is observed to be 0.044 and 0.530V for cell temperatures of 80 and 10°C, respectively. A comparison of the maximum change in over-potential for 10 and 80°C data given in Figure 1.1.6 to the onset potential for electrochemical oxidation given in Figure 1.1.5 shows that the increase in anode over-potential due to CO is not large enough to initiate electrochemical oxidation at either operating temperature. Thus, the reactions with CO can likely be attributed to reaction with crossover oxygen from air at the cathode and the WGS reaction.

Also shown in Figure 1.1.6 are the molar flow rates of CO and CO₂ at the anode inlet and outlet for fuel cells operated at 80 and 10°C. From the 80°C data, incomplete conversion of CO to CO₂ is observed, however, the carbon species molar flow balance closes indicating that steady state was attained. For the 10°C data, however, steady state was not attained. This was due to the fact that, as shown in the plot inset in the 10°C data, potential oscillations were observed. This behavior has been reported in the past for PEMFCs utilizing PtRu/C²⁻⁴ and Pt-Pd/C alloys,⁵ but not for Pt/C as the anode catalyst.⁵ For Pt-Pd/C alloys, the potential oscillations were attributed to a variety of related factors such as the CO partial pressure and CO electro-oxidation potential but a definitive mechanism was not postulated.⁵ The potential oscillations observed in the PtRu/C alloys, however, were attributed to the formation of OH adsorbates at lower cell anode overpotentials because of the coupling of the anode electro-oxidation of H₂ and CO which enabled the formation of OH adsorbates at lower anode over-potentials.² As noted above, electrochemical oxidation of CO most likely did not occur for the 10°C data in Figure 1.1.6. The oscillations, in this case, are likely the result of changes in the rate of the WGS with changes in anode potential and CO catalyst coverage. The rate of O₂ crossover from the cathode presumably

plays a role as well. It is difficult to quantitatively study the conversion of CO to CO₂ for the 10°C data with the GC because the rate of change in the cell voltage is occurring much more rapidly during the oscillations than the frequency at which the GC can sample. Regardless, the data show that the reaction of CO within the fuel cell can be significantly different depending on the cell operating conditions and show the importance of continuing to study CO in PEMFCs.

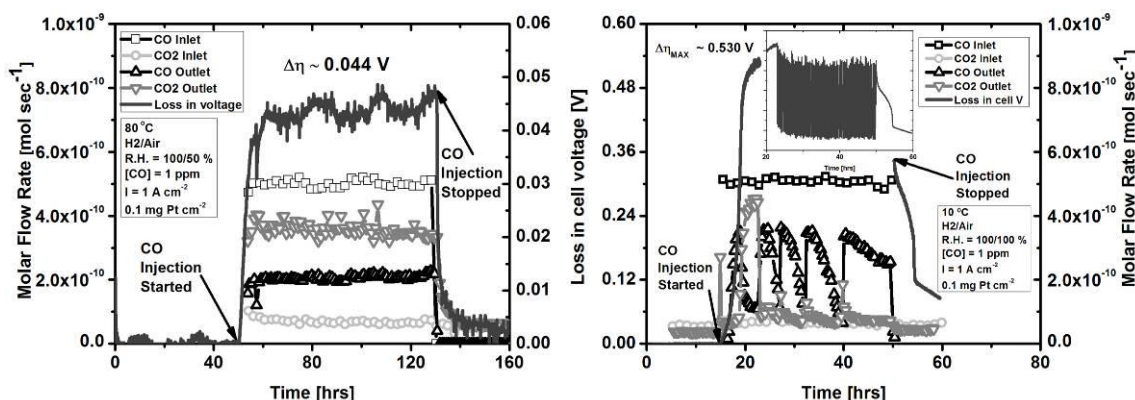


Figure 1.1.6 Molar flow rate of CO and CO₂ into and out of the anode for operational fuel cell. The operating current density was 1A cm⁻². Experimental conditions are given in the figure and table 1.1.3. Note that the loss in cell voltage scale differs by a factor of ten between the left and right plots. Also note that the voltage oscillations for the 10°C experiment are given within the plot inset on the right figure

In this work several reactions involving CO were studied using gas chromatography at operating temperatures of 80 and 10°C in a PEMFC. The CO concentration was 1ppm. The exposure of the PEMFC to CO enhanced a carbon corrosion reaction when oxygen or water was present as the lone reactant with CO. The corrosion reaction was most significant at 80°C and appeared to exhibit a thermal dependency. For the case where water was present as the lone reactant with CO, a relationship between carbon corrosion and cell voltage was observed with higher voltage resulting in greater corrosion. CO was also observed to react readily with oxygen when oxygen was present as the lone reactant. Complete conversion to CO₂ was observed at 80°C when reacting with oxygen while nearly zero conversion to CO₂ was observed at 10°C. This indicated the reaction had a strong dependence on operating temperature. The conversion of CO to CO₂ in the water gas shift reaction appeared to be related to the cell voltage. At high cell voltage the conversion of CO to CO₂ was observed to be significantly less than 100% for both operating temperatures studied. The conversion increased to over 100% when the cell voltage abruptly dropped significantly. This may be indicative of the electrochemical promotion of the water gas shift reaction enhanced by the establishment of internal currents within the fuel cell. Further evidence of the occurrence of electrochemical promotion of the water gas shift reaction was observed when 100% conversion of CO to CO₂ was observed at 80°C when only water was supplied as the reactant with CO and the cell was electrically short circuited. Potential oscillations were observed and reported for the first time in a PEMFC with a Pt/C catalyst. The oscillations were likely related to changes in the rate of the water gas shift reaction as the CO coverage on the catalyst changed. CO electrochemical oxidation most likely did not occur during normal fuel cell operation with H₂ and air at 1A cm⁻².

The Effect of Airborne Contaminants and Mixtures on PEMFC Performance and Durability:

This section discusses the performance and durability effects that the airborne contaminants sulfur dioxide (SO₂), benzene (BZ), and nitrogen dioxide (NO₂) have on proton exchange membrane fuel cell (PEMFC) performance and durability as individual contaminants and in mixtures. The work was performed to support the deployment of fuel cell stacks under real world conditions (air contaminants occur as mixtures rather than single species) with challenging operating environments including battlefield conditions and different regions throughout the world which will have varying air quality.

This research supports another ONR funded effort to deploy fuel cell powered buses in HAVO, which serves as a proving ground for evaluating fuel cell stack performance in harsh conditions. The air quality in the park is affected by exhaust from vehicular traffic (SO₂, BZ, NO₂) and volcanic gas emissions (SO₂). This study is the first phase of the project and will investigate the effects of individual contaminants and mixtures at a total dry gas concentration of two parts per million (2ppm) on the performance of a single cell configuration fuel cell. Testing was performed at a high and low current density (1 and 0.2A cm⁻²) to assess contaminant effects at different power output. Single cells were used to gain insight into the effects that would occur on a full-scale stack. The data presented here will support future development of a stack performance model that accounts for the presence of contaminants in the air stream, determining specifications for air filters used to prevent contaminants from entering the fuel cell, and employing clean air as a method to remove contaminants and restore system performance.

Accomplishments included characterizing the performance loss and durability effects of exposing fuel cells to individual contaminants and mixtures of SO₂, NO₂, and BZ. The irrecoverable performance loss due to contaminant exposure was also quantified. In general, contaminants were shown to significantly decrease fuel cell performance with mixtures affecting performance loss more than individual contaminants. Performance recovery was possible using only clean air for inlet streams consisting of only NO₂ and/or BZ. Complete performance loss was irrecoverable with pure air when SO₂ was in the stream. Contaminant exposure increased electrochemically active area catalyst loss, thus decreasing the lifetime of the fuel cell.

The following 4 tables and figure give details of the fuel cell testing station and set-up, the properties of the fuel cell testing hardware, membrane/electrode assembly (MEA), experimental test plan, and operating conditions for each of the experiments in the test plan.

The fuel cell testing station was custom built based on a United Technologies design. A detailed description of the experimental set-up used to test the fuel cell and inject the contaminants was given by Bender et al.⁶ The properties of the fuel cell hardware are given in Table 1.1.4. All contaminant testing was performed using a single fuel cell. The MEA used was a commercially available reinforced Nafion based membrane with an anode and cathode catalyst of platinum supported on carbon (Pt/C) and loadings of 0.4 and 0.4mg Pt cm⁻².

Table 1.1.4 Properties of single cell hardware

| | Flow field geometry | Active area [cm ²] |
|---------|---------------------|--------------------------------|
| Anode | 2-channel | 50 |
| Cathode | 3-channel | 50 |

The experimental test plan consisted of three phases: (i) beginning of test (BOT), (ii) contaminant exposure at constant current, and (iii) end of test (EOT). The steps of the test plan and their respective purpose are given within Table 1.1.5. The operating conditions for each experiment are given in Table 1.1.6.

Experiments in the beginning of the test (BOT) phase were used to adequately hydrate the membrane through a conditioning sequence and to assess the initial performance of the fuel cell prior to contaminant exposure through air and oxygen polarization (IV) curves. Cyclic voltammetry was also used to measure the electrochemically active surface area (ECSA) of the anode and cathode.

Table 1.1.5 Sequence and details of testing plan

| Experimental tests in sequential order | Purpose |
|--|--|
| Phase I: Beginning of test (BOT) | |
| Conditioning | Ensure adequate membrane hydration |
| Cyclic voltammetry | Quantify electrochemically active surface area and ensure clean electrode surface |
| Air and oxygen polarization curves | Air: measure fuel cell performance prior to contaminant exposure |
| | Oxygen: measure fuel cell performance prior to contaminant exposure without mass transport or concentration losses |
| Phase II: Contaminant exposure at constant current | |
| Constant current testing | Measure fuel cell performance loss due to contaminant exposure and subsequent recovery with pure air at a constant current |
| Phase III: End of test (EOT) | |
| Cyclic voltammetry | Quantify electrochemically active surface area Remove residual contaminant from electrode surface |

Air and oxygen polarization curves

Air: measure fuel cell performance after contaminant exposure and removal using pure air and cyclic voltammetry

Oxygen: measure fuel cell performance after contaminant exposure and removal using pure air and cyclic voltammetry without mass transport or concentration losses

The contaminant exposure experiment was performed at a constant current density of 0.2 or 1A cm^{-2} . Contaminant testing was performed for individual exposures of SO_2 , NO_2 , and BZ as single contaminants and all possible combinations of each contaminant at both current densities. The contaminants and their respective dry gas exposure concentrations are given in Table 1.1.7. In all cases, the total mixture concentration was 2ppm. Contaminants were mixed into the air stream by injection well upstream of the fuel cell inlet to ensure adequate mixing. The purpose of contaminant exposure test was to quantify the magnitude of performance loss and to assess how much of the performance could be recovered using only pure air.

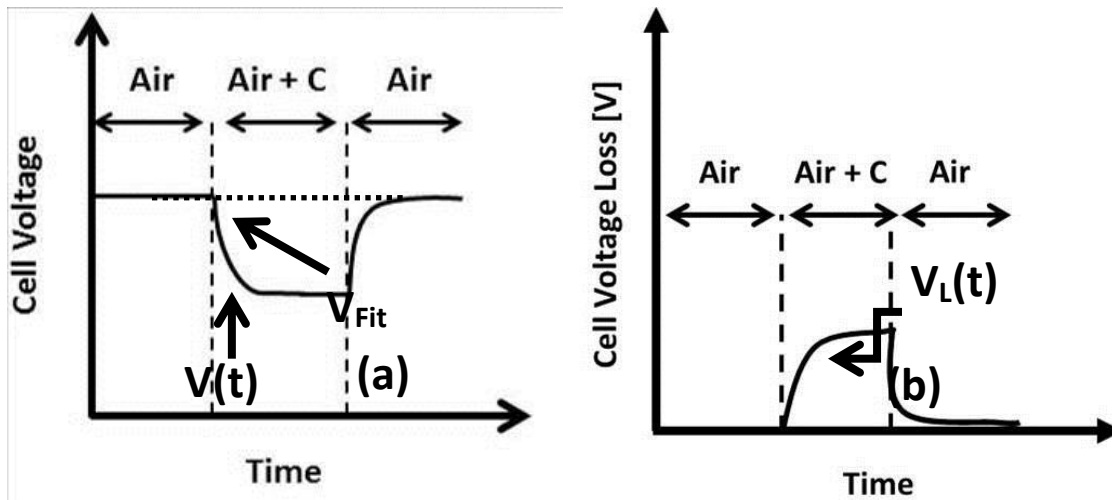


Figure 1.1.7 Illustration of contaminant exposure experiment at constant current density for cell voltage versus time (a) and cell voltage loss versus time (b)

Figure 1.1.7a shows an illustration of how the contaminant exposure experiments were performed. Initially, the fuel cell was operated with pure air. This was followed by a period where the contaminant (C) was supplied to the air stream of the fuel cell for a fixed duration. After this period of time, the flow of contaminant was stopped and clean air was again supplied to the fuel cell. The purpose of supplying clean air was to assess its efficacy as a performance recovery technique.

To calculate the performance loss and recovery of the fuel cell, voltage data from the initial pure air exposure was extrapolated using linear least squares regression over the entire duration of the experiment. The extrapolation is illustrated in Figure 1.1.7a by the dotted line representing V_{Fit} . The cell voltage loss $V_L(t)$ at time t was determined by the difference between the measured

voltage $V(t)$ and the fit voltage $V_{Fit}(t)$ as shown in Equation 1.1.5. Figure 1.1.7b shows how a typical $V_L(t)$ curve looks.

$$V_L(t) = V(t) - V_{Fit}(t) \quad [1.1.5]$$

The third phase of testing was the end of test diagnostics which consisted of cyclic voltammetry to remove any remaining contaminant on the electrode and air and oxygen IV curves. The irrecoverable performance loss was calculated from the difference between the voltages at each current density using the current resistance (IR) corrected data. IR corrections were made from resistance measurements obtained using a high frequency resistance milliohmmeter at 1 kHz.

Table 1.1.6 Operating conditions during experiments

| Experiment | An/Ca Flow Rate or Stoichiometry | An/Ca Gas | Current Density or Scan Rate | Cell Temperature [°C] | An/Ca Relative Humidity [%] | An/Ca Cell Back- Pressure [kPag] |
|-----------------------|---|--|---|-----------------------------|--------------------------------------|---|
| Cyclic Voltammetry | 500/500cm ³ min ⁻¹ | Reference: H ₂ Working: N ₂ | 20mV s ⁻¹ from 0.085 to 1.2V versus HRE for 10 cycles | 35 | 100/100 | 0/0 |
| I-V Curve | 2/2 Stoichiometry | H ₂ /Air or H ₂ /O ₂ | Decreasing current steps from 1.2A cm ⁻² to open circuit voltage in 0.2A cm ⁻² steps with 15min hold at each step. IV curve data were averaged over last 5min at each step | 60 | 100/50 | 48.7/48.7 |
| Constant Current | 2/2 Stoichiometry | H ₂ /Air | 1 or 0.2 A cm ⁻² | 60 | 100/50 | 48.7/48.7 |

Table 1.1.7 Individual contaminants and mixtures and their dry gas concentrations supplied to the fuel cell during constant current testing

| Contaminants and mixtures | Dry gas concentration [ppm] |
|--|-----------------------------|
| NO ₂ | 2 |
| BZ | 2 |
| SO ₂ | 2 |
| BZ + SO ₂ | 1,1 |
| NO ₂ + SO ₂ | 1,1 |
| NO ₂ + BZ | 1,1 |
| BZ + SO ₂ + NO ₂ | 0.67,0.67,0.67 |

The rate and magnitude of performance loss during contaminant exposure is an important consideration for manufacturers designing air filtration media for fuel cells. A thorough understanding of the performance loss resulting from operating a fuel cell using air with multiple contaminants is needed so that adequate performance benchmarks can be developed for the filters. Additionally, filter manufacturers will also need to know which contaminants cannot be easily removed from the fuel cell using simple recovery methods so that they can ensure their systems prevent ingress of these compounds. This section first describes the rate of performance loss observed during contaminant exposure at constant current densities of 1 and 0.2A cm⁻². This is followed by a discussion of the magnitude of performance loss at steady state and finally the ability of the fuel cell to “self-recover” using only pure air.

The results of the contaminant exposure tests at constant current density are given in Figures 1.1.8 and 1.1.9. Figure 1.1.8 shows the loss in cell voltage versus time for a constant current hold of 1 Acm⁻² for individual contaminants (a) and mixtures (b). Figure 1.1.9 shows the loss in cell voltage versus time for a constant current hold of 0.2A cm⁻² for individual contaminants (a) and mixtures (b).

From Figure 1.1.8a, SO₂ and BZ had the highest rates of performance loss as individual contaminants for cells operated at 1A cm⁻². The rate of performance loss was significantly slower during NO₂ exposure. The data in Figure 1.1.9a showed BZ having the greatest rate of performance loss at 0.2A cm⁻² for the individual contaminants followed by SO₂ and NO₂. A comparison of the data from Figures 1.1.8a and 1.1.8b, and, Figures 1.1.9a 1.1.9b shows that steady state was attained more slowly in the contaminant mixtures than for the individual contaminants and, in some cases, performance loss was still occurring after 20 hours for the mixed contaminants. The reason for the increased time to reach steady state with the mixtures may have been due to an increased number of reactions occurring when multiple contaminants were present. This would likely affect the rate limiting steps of the reaction processes that caused the performance loss thereby increasing the time required to reach steady state.

The largest decrease in cell voltage for the individual contaminants at 1A cm⁻², as shown in Figure 1.1.8a, was for SO₂ and the smallest was for NO₂. The trend was reversed for the individual contaminants in Figure 1.1.9a at 0.2A cm⁻² where the loss was largest for NO₂ and SO₂ had the smallest effect. The reasons for the differences in the trends in performance loss between the data sets were not known since the reaction mechanisms for the performance loss in the fuel cell are complex and not thoroughly understood for these contaminants. However, SO₂ poisoning is known to occur via at least two processes which have a potential dependence.⁷ These processes likely affected the magnitude of performance loss differently for the 1 and 0.2A cm⁻² experiments since the cathode potential would be different. Also of particular significance is that when comparing the data from the individual contaminants in Figures 1.1.8a and 1.1.9a to the mixed contaminants at the same current density in Figures 1.1.8b and 1.1.9b, a synergistic effect was observed for the contaminant mixtures. That is, when more than one contaminant was present, the performance loss was greater than what would be expected from the sum of the performance losses that would occur if the contaminants in the mixture were supplied to the cell as individual contaminants. To provide perspective on how much the contaminant mixtures can increase performance loss, after one hour of exposure to 2ppm SO₂, the fuel cell performance decreased by 17.5%. For a one hour exposure of a 1/1ppm mixture of SO₂ and BZ at 1A cm⁻²,

the performance loss increased to 30.6%. Given the substantial increase in performance loss resulting from contaminant mixtures data from individual exposure experiments is not sufficient to estimate fuel cell performance loss for real world conditions where multiple contaminants will be present in the air. Thus, filtration media performance benchmarks will need to consider the effects of contaminant mixtures on fuel cell performance.

Figures 1.1.8a and 1.1.8b, and, Figures 1.1.9a 1.1.9b showed performance could be recovered completely when NO₂ or BZ were the contaminants regardless of the current density and whether NO₂ or BZ were supplied to the cell as single contaminants or as a NO₂/BZ mixture. Complete performance recovery with pure air after NO₂ exposure was in agreement with previously reported research.⁸ If SO₂ was present in the air either as a single contaminant or in a mixture, complete performance recovery was not attainable using pure air. The performance recovery results for the individual SO₂ exposures were similar to those reported by Zhai et al⁷ where at cell voltages greater than 0.63V, such as when the fuel cell was operated at 0.2A cm⁻², SO₂ was strongly bound to the catalyst and virtually no performance recovery was observed with pure air. When the cell voltage dropped below 0.63V, however, such as when the cell was operated at a current density of 1A cm⁻², partial performance recovery was possible with pure air. Thus, if SO₂ has entered the system, other methods will be required to achieve complete performance recovery.

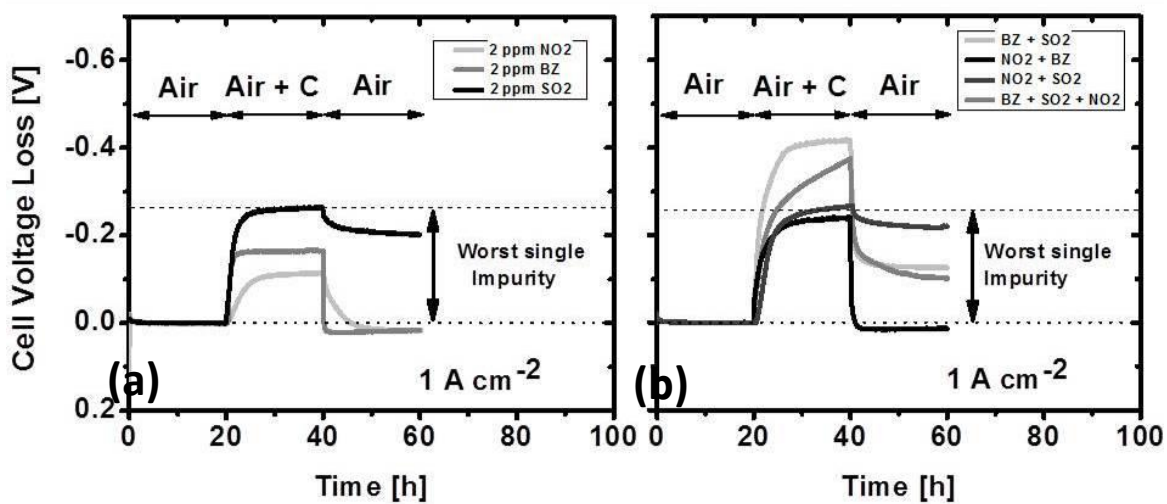


Figure 1.1.8 Loss in cell voltage during 1A cm⁻² constant current hold for individual contaminants (a) and mixed contaminants (b)

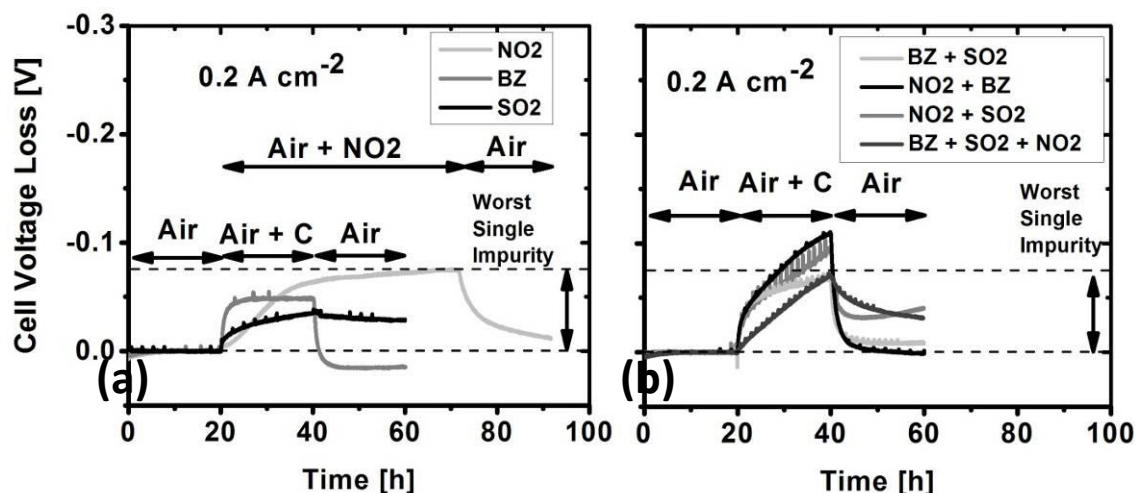


Figure 1.1.9 Loss in cell voltage during 0.2 A cm^{-2} constant current hold for individual contaminants (a) and mixed contaminants (b)

Data from the air and oxygen polarization curves were used to determine the irrecoverable performance loss of the fuel cell due to contaminant exposure. Irrecoverable performance loss was calculated by taking the difference between the IR corrected polarization data from the EOT and IR corrected polarization data from the BOT. The IR free data was used to eliminate changes in the membrane resistivity due to any differences in the hydration state of the MEA between BOT and EOT. However, there was no measurable change in the high frequency resistance data between the BOT and EOT. The EOT data were measured after the pure air and CV performance recovery techniques were used. The irrecoverable performance loss data are given in Figures 1.1.10 to 1.1.13.

Figure 1.1.10 shows the irrecoverable performance losses versus current density for the individual contaminants at 1 A cm^{-2} in air (a) and oxygen (b). In each of the Figures 1.1.10 to 1.1.13, the “a” and “b” figures give the results for the air and oxygen measurements, respectively. Figure 1.1.11 shows the losses from individual contaminants at 0.2 A cm^{-2} . Figure 1.1.12 shows the losses from mixed contaminants at 1 A cm^{-2} and Figure 1.1.13 gives the results from the contaminant mixtures at 0.2 A cm^{-2} .

The results in Figure 1.1.10a showed that exposure to the individual contaminants at 1 A cm^{-2} actually may have improved fuel cell performance for NO₂ and BZ from a few mV at open circuit to approximately 0.011V for NO₂ and 0.020V for BZ at 1.2 A cm^{-2} . The reasons for the improved performance are not known, though improved performance subsequent to contaminant exposure was observed in other experiments with different contaminants.^{9,10} The experiments here should be performed again to assess the repeatability of the results. One potential explanation for improved performance is that NO₂ or BZ exposure affected the gas diffusion layer and/or ionomer in such a way that reactant interaction with the catalyst progressively improved as water production increased at higher current densities. An investigation of potential reaction mechanisms that could improve performance needs to be undertaken.

For SO₂ exposure, Figure 1.1.10a showed performance was irreversibly decreased for all current densities and the magnitude of performance loss progressively increased at current densities $\geq 0.8 \text{ A cm}^{-2}$. The progressively increasing loss in performance with current density at current densities $\geq 0.8 \text{ A cm}^{-2}$ indicated that the mass transport over-potential was increased due to SO₂ exposure. The SO₂ results are in agreement with those recently reported by Zhai et al.¹¹ SO₂ is clearly a contaminant that needs to be kept out of the fuel cell since exposure irreversibly decreased performance loss by approximately 0.010V at each current density with the losses increasing to nearly 0.030V at 1.2 A cm^{-2} .

The results from Figure 1.1.10b showed that when oxygen was used in the polarization measurements, differences in voltage at open circuit for NO₂ and BZ were similar to what was observed for the measurements performed with air. The data in Figure 1.1.10b also showed that for NO₂ and BZ, the performance improved slightly between the BOT and the EOT and the magnitude of improvement did not change with current density. That is, when more water was being produced by the cell at higher current densities, the magnitude of performance loss from BOT to EOT remained relatively constant. The change in performance was quite small though and more experiments should be performed to ascertain if the gain is repeatable. The SO₂ results in Figure 1.1.10b showed a decrease in open circuit voltage that was similar to what was observed in Figure 1.1.10a. However, in contrast to the air polarization measurements, when the cell was operated with oxygen, virtually no difference in performance was observed between the BOT and EOT.

Comparing the oxygen results for SO₂ in Figure 1.1.10b to the air results in Figure 1.1.10a for SO₂, the data indicated that operating the cell with pure oxygen was sufficient to overcome any changes to the MEA/gas diffusion layer (GDL) caused by SO₂ exposure. Comparing the oxygen and air results also suggested that SO₂ exposure affected the GDL and/or MEA in such a way that it decreased the transport of oxygen to the catalyst. Pure oxygen eliminates mass transport effects in the fuel cell. From Figure 1.1.10b, no change in performance between the BOT and the EOT was observed with oxygen while, from Figure 1.1.10a, the performance loss increased with current density when the cell was operated with air at current densities $\geq 0.8 \text{ A cm}^{-2}$. More information on mass transport could be gained by performing impedance spectroscopy during the impurity exposure experiments at constant current to determine if mass transport resistance increased due to SO₂ exposure. Regardless, changes to the MEA and/or GDL from impurity exposure are likely dependent on the performance loss mechanisms associated with a particular contaminant. A greater understanding of the performance loss mechanisms are needed to gain additional insight into the effects of these contaminants on the MEA and GDL so that performance can be maximized and mitigation strategies can be developed.

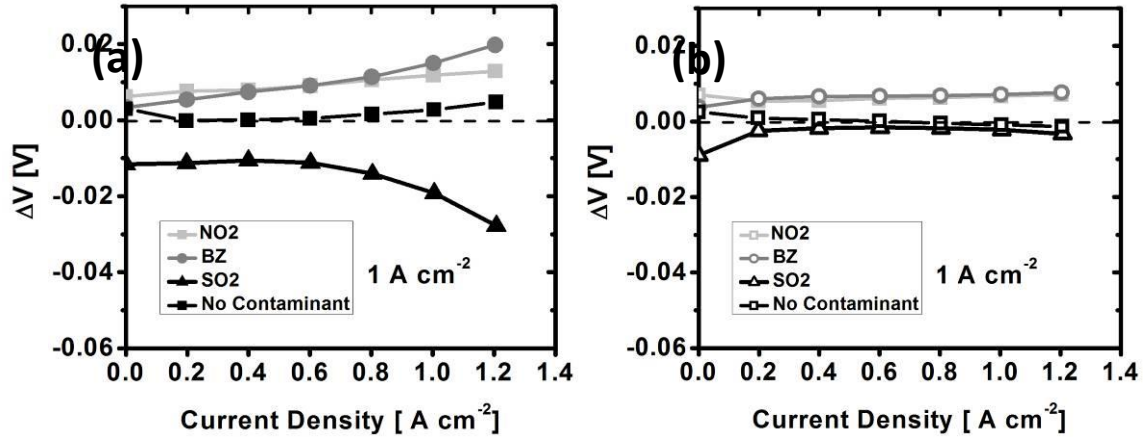


Figure 1.1.10 Change in cell voltage versus current density from beginning of test to end of test for IV curves measured with air (a) and oxygen (b). Data shown are for individual contaminant exposures performed at 1 A cm^{-2}

The results in Figures 1.1.11a and 1.1.11b were similar to those in Figures 1.1.10a and 1.1.10b for BZ. Some differences between the data were observed though for SO_2 and NO_2 . From Figure 1.1.11a, the SO_2 irrecoverable performance loss progressively increased with current density compared to Figure 1.1.10a where the performance loss value remained constant through 0.6 A cm^{-2} before steadily decreasing. In Figure 1.1.11a the NO_2 performance was higher at the EOT for each current density except 1.2 A cm^{-2} . However, the magnitude of the performance improvement steadily decreased at current densities beyond 0.6 A cm^{-2} . The reasons for the differences in the trends between the 1 A cm^{-2} results and the 0.2 A cm^{-2} results are likely related to different performance loss mechanisms occurring at each current density. For example, Zhai et al. showed that SO_2 poisoning is a multistep process that is potential dependent.⁷ Thus, there were likely different poisoning processes occurring during SO_2 experiments in this work since the cathode potential would have differed at 1 A cm^{-2} and 0.2 A cm^{-2} . Overall, the results again emphasize the importance of preventing SO_2 from reaching the fuel cell.

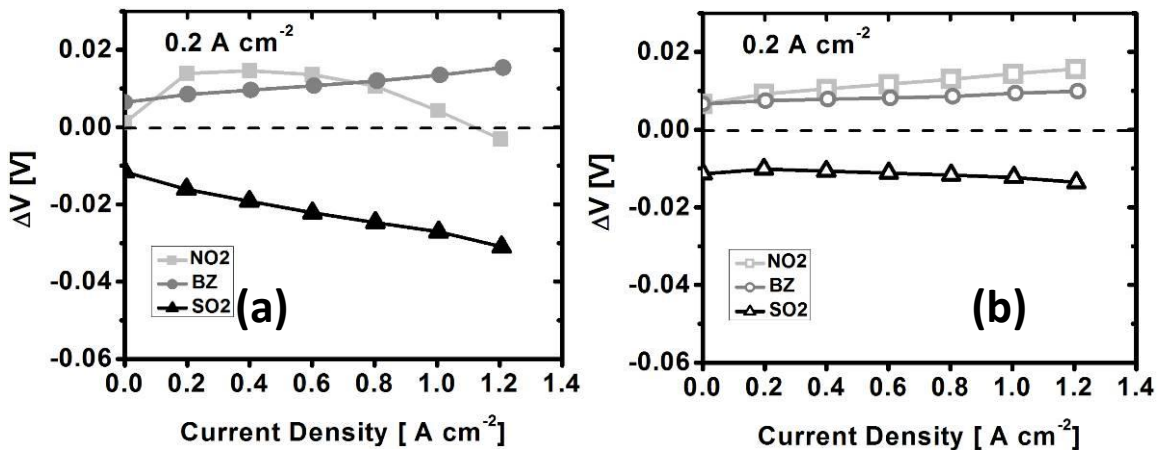


Figure 1.1.11 Change in cell voltage versus current density from beginning of test to end of test for IV curves measured with air (a) and oxygen (b). Data shown are for individual contaminant exposures performed at 0.2 A cm^{-2}

Figures 1.1.12a and 1.1.12b give the results from the mixed contaminant experiments at 1 A cm^{-2} from the air and oxygen polarization curves, respectively. The results were similar to the individual contaminants in Figure 1.1.10a in that the NO_2 and BZ mixture resulted in improved performance between BOT and EOT. From Figure 1.1.12a, mixtures that had SO_2 all decreased performance with the performance loss increasing with current density. The most significant irrecoverable performance loss was observed for a mixture of NO_2 and SO_2 with the voltage losses approaching 0.05 V at 1 A cm^{-2} . This would result in a nearly 8% irrecoverable performance loss for a cell whose operating voltage was 0.65 V at 1 A cm^{-2} . From Figure 1.1.12b, when the polarization measurements were performed with oxygen, the change in performance between the BOT and EOT was much smaller. The oxygen results again provided some evidence that the contaminants are affecting the GDL and/or membrane in such a way that reactant transport to the catalyst is either enhanced (NO_2 and BZ) or diminished (SO_2) when operating with pure air.

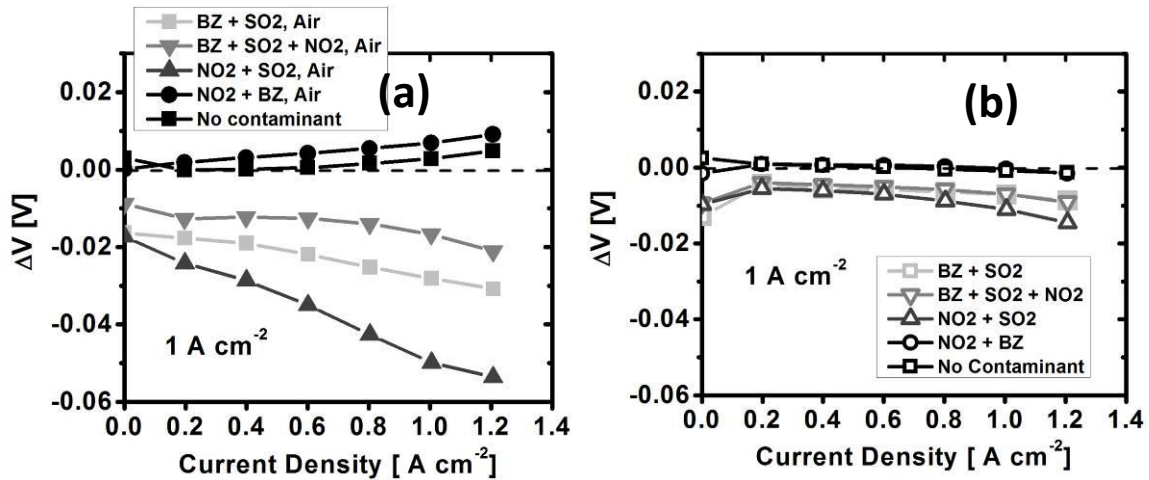


Figure 1.1.12 Change in cell voltage versus current density from beginning of test to end of test for IV curves measured with air (a) and oxygen (b). Data shown are for mixed contaminant exposures performed at 1 A cm^{-2}

Figures 1.1.13a and 1.1.13b give the irrecoverable performance loss data versus current density for cells exposed to contaminant mixtures at 0.2 A cm^{-2} in air and oxygen, respectively. Figure 1.1.13a shows that performance was again enhanced with a mixture of NO_2 and BZ while mixtures of NO_2/SO_2 and BZ/SO_2 irreversibly decreased performance and the magnitude of performance loss increased with higher water production as the current density increased. Interestingly, small improvements in performance were observed for the three contaminant mixture of NO_2 , SO_2 , and BZ. This may have indicated that the NO_2 and BZ were responsible for the majority of the performance loss. The oxygen results in Figure 1.1.13b showed that under increasing water production conditions at higher current densities the performance loss between the BOT and EOT was less than the measurements performed with air. In general the performance loss or gains with oxygen shown in Figure 1.1.13b were more constant compared to the air experiments. This indicated again that the contaminants may have changed the MEA and/or GDL in such a way that at the higher current densities, where the rates of water production were greater, the interaction of the catalyst and oxygen was decreased for SO_2

containing mixtures (with the exception of the three gas mixture) and increased with NO₂ and BZ as long as SO₂ was not present.

Figures 1.1.14 and 1.1.15 give the results of the percentage change in the electrochemically active surface area (ECSA) of the anode and cathode after contaminant exposure testing and recovery in pure air. ECSA was determined from CV. All CV scans were performed from 0.085 to 1.2V versus HRE for 10 scans to ensure full contaminant removal from the catalyst. ECSAs were determined from the hydrogen desorption peaks. The relative change in ECSA from BOT to EOT was used to assess the effects of the contaminants on MEA durability.

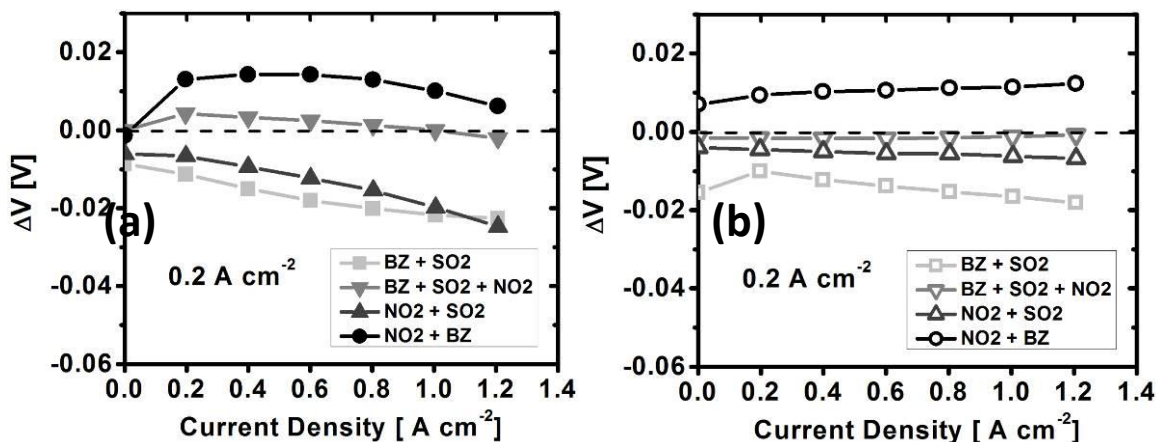


Figure 1.1.13 Change in cell voltage versus current density from beginning of test to end of test for IV curves measured with air (a) and oxygen (b). Data shown are for mixed contaminant exposures performed at 0.2A cm⁻²

The data in Figures 1.1.14a, 1.1.14b, 1.1.15a and 1.1.15b showed that contaminant exposure increased the loss in ECSA on both the anode and cathode when compared to the ECSA losses from experiments where no contaminant was present with two exceptions. The data in Figure 1.1.14b showed that the loss in anode ECSA was lower for the NO₂ and BZ mixture at 1 A cm⁻² than when the cell was operated without contaminants. Similarly, the data in Figure 1.1.15a showed a smaller loss in anode ECSA for NO₂ at 0.2A cm⁻² than when operated with pure gases. The reason that there was less relative loss in anode ECSA for those two cases was not known. However, the difference between the losses for the contaminant exposed MEAs and the MEAs subjected only to pure gas was small enough that the experiments should be repeated to assess if the differences were within variability of the experiments.

For the majority of the data, however, the loss in anode and cathode ECSA was larger for MEAs exposed to contaminants than when the MEAs were exposed only to pure gases. Exposure of MEAs to contaminants is known to induce mechanisms that decrease the electrochemically active area of the electrodes. Some examples of these mechanisms are given in the paragraph below. Contaminant induced electrode degradation mechanisms likely explain the increased loss in cathode ECSA when compared to the MEA operated without contaminants in the stream since the contaminants were supplied directly into the cathode stream. However, the anode electrochemically active area also decreased, beyond what would be expected if it was operated with pure gases, despite not being directly subjected to any contaminants. The increased loss in

ECSA on the anode was likely related to the crossover of the airborne contaminants or their byproducts from the cathode. Interaction of the anode with crossover SO_2 from the cathode has been reported previously.⁷ Cathode contaminants can reach the anode through various transport mechanisms such as diffusion through the polymer electrolyte membrane (PEM). Diffusion of cathode contaminants to the anode was probable because the MEAs used in this work were manufactured with PEMs made of reinforced Nafion, which is semi-permeable to gases and has a thickness of only $18\mu\text{m}$. The potential for cross contamination from different electrodes is especially important for newer generation MEAs because they are much thinner than most types of older MEAs because of the addition of reinforcement materials such as Teflon (PTFE). The thickness of older generation PEMs was greater than $50\mu\text{m}$. The increased potential for cross contamination of electrodes with even low concentrations of gas contaminants further emphasizes the importance of developing filter technology to prevent the contaminants from entering the fuel cell system.

One example of a contaminant induced mechanism that decreases ECSA is Pt dissolution, which is known to be enhanced in the presence of SO_2 .¹² Hydrogen peroxide (H_2O_2) formation is another reaction that occurs in the presence of contaminants which cause the ORR reaction pathway to shift from a four electron process to a two electron process. H_2O_2 formation in PEMFCs leads to the generation of hydroxyl and hydroperoxyl radicals that degrade the catalyst and ionomer.¹³ H_2O_2 formation has been observed in rotating ring disc electrode (RRDE) experiments on Pt/C electrodes when exposed to airborne contaminants that were different than those used in this work^{14–16} and also with SO_2 .^{17–19} H_2O_2 is an electrode degradation mechanism that results in irrecoverable ECSA loss and thus decreased performance. Given the documented cases of contaminants inducing ECSA loss mechanisms and the increased loss in ECSA observed in this work from contaminant exposure it is critical that airborne contaminants, especially SO_2 , NO_2 , and BZ, be prevented from entering the fuel cell to maximize the lifetime of the fuel cell stack and prevent irrecoverable losses in performance. Future work should investigate the specific degradation mechanisms that occur when fuel cells are subjected to mixtures of the common airborne contaminants such as those used in this work.

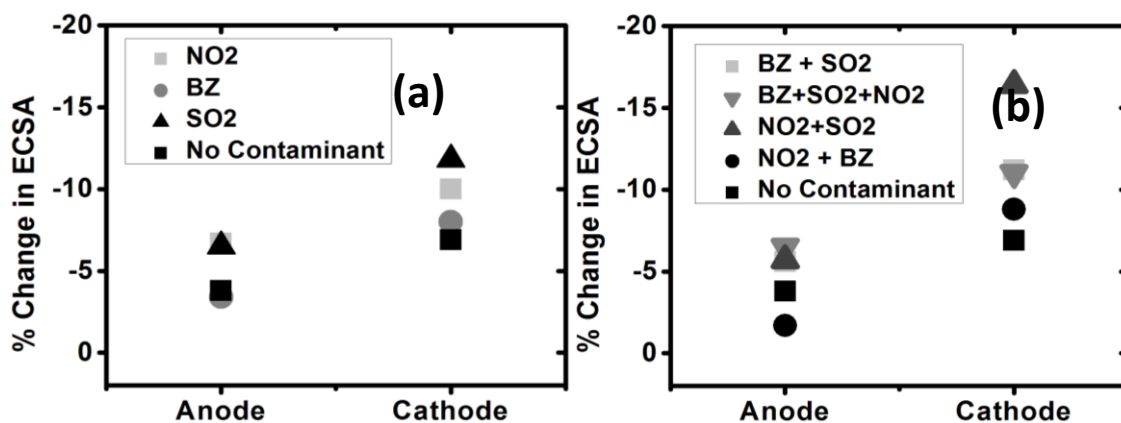


Figure 1.1.14 Change in anode and cathode ECSA for 1A cm^{-2} experiments for individual contaminants (a) and contaminant mixtures (b)

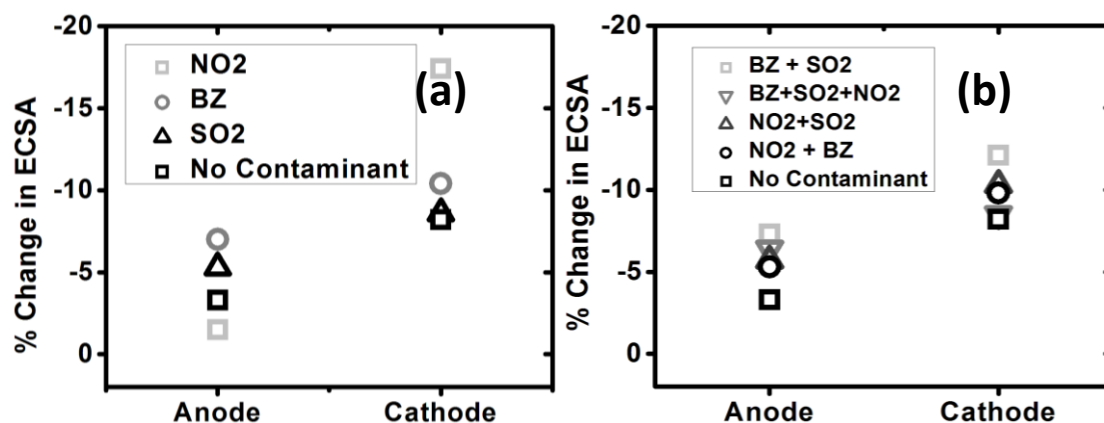


Figure 1.1.15 Change in anode and cathode ECSA for 0.2A cm⁻² experiments for individual contaminants (a) and contaminant mixtures (b)

The performance and durability effects of the common airborne contaminants SO₂, NO₂, and BZ were studied at current densities of 1 and 0.2A cm⁻². All contaminants were found to decrease fuel cell performance significantly and a synergistic effect was observed for contaminant mixtures. Performance loss was completely recoverable using pure air when only NO₂ or BZ was the contaminant. Interestingly, when NO₂ or BZ were the contaminants, the performance of the fuel cell improved slightly above its initial performance after being subjected to pure air and CV recovery techniques. The performance improvement was quite small in comparison to the amount of performance lost when the contaminants were present in the gas stream and additional experiments should be performed to assess repeatability. When SO₂ was the contaminant, either as an individual contaminant or in a mixture, only partial performance recovery was possible using pure air and cyclic voltammetry. Contaminant exposure decreased fuel cell durability because the percent loss in anode and cathode ECSA after contaminant exposure was larger than it was when no contaminants were present. Filtration media benchmarks will need to ensure that the air supplied to the fuel cell removes BZ, NO₂, and SO₂ to levels much lower than 2ppm. Given the substantial irrecoverable performance loss induced by SO₂ this contaminant should be prevented from entering the fuel cell in any measurable concentration. In general exposure to the contaminants BZ, NO₂, and SO₂ should be limited to concentrations much less than 2ppm. Future work should consider the effects of contaminant mixtures at much lower concentrations to attempt to identify acceptable levels of air filter break through that have negligible effects on fuel cell performance. A more fundamental understanding of the performance loss mechanisms for these contaminants is desirable to assist in developing mitigating strategies and maximizing device performance and lifetime to facilitate large-scale entry of fuel cells into the marketplace. Future work should include impedance spectroscopy with individual contaminants during exposure experiments to investigate changes in mass transport.

Cathode Contamination from Foreign Cations and Organic Compounds:

To continue the previous work on cathode contamination using single and mixed gas phase contaminants, an effort was initiated to study the possible synergy between foreign cation species introduced in the liquid phase and an organic compound introduced in the gas phase. Both foreign cations and organic compounds have been the focus of another project underway at HiSERF as part of the Department of Energy's (DOE) Hydrogen and Fuel Cell research and development program studying the effect of airborne contaminants. This research program only

focuses on single contaminant performance impacts. There has been very little work reported on the impact of mixed contaminants, where both deleterious and beneficial effects have been observed.^{20–22} Determining the origins of the synergy between contaminants is difficult not only due to the experimental complexity to separate the effects and compare with single contaminant mechanisms previously documented, but also due to the need to down select from a potentially large number of relevant combinations that may exist from system-borne, air, and fuel impurity sources.²³

With the possibility of seawater incursion in fuel cells for navy applications, either by the natural NaCl content in air or by direct contact with liquid seawater or in deicing operations, sodium was selected as the foreign cation species. Mikkola et al²⁴ first presented work on NaCl contamination in the cathode air stream of PEMFCs and concluded that for the conditions tested, performance losses observed were due to the reduction in proton conductivity due to the displacement of the protons in the membrane by sodium ions. Chloride performance impacts were not observed in the fuel cell experiments, however similar to previous work by Schmidt et al,²⁵ non-fuel cell studies performed using Pt/C in 0.5M H₂SO₄ did show that chloride ions poison the catalyst surface and thus NaCl was not used as the sodium ion source in this study. Also of note is for the experiments presented by Mikkola et al,²⁴ an excessive amount of NaCl was injected into the cell using a 1 ml min⁻¹ injection of a 1M NaCl solution, which is saying enough NaCl was delivered to the cell to replace every available proton in the Nafion® 112 membrane with sodium ions every 15 seconds.

For the experiments presented in this work, a significantly lower Na⁺ concentration was selected using a 0.01M solution of HNO₃/Na₂SO₄. St-Pierre presented models of foreign cation ion exchange with protons in Nafion® where models and validation isotherm data showed that to minimize contamination the amount of foreign cations in the product water in contact with the ionomer must be significantly lower than the amount of protons.^{26,27} Thus for this work, the opposite was utilized, injecting a solution with the ratio of [Na⁺]/([Na⁺]+[H⁺])=0.9, which was achieved by adding nitric acid. This ratio did not consider the diluting effect of the protons that might be present in the product water of the fuel cell. The use of 0.01M solution would also limit the NO₃⁻ and SO₄⁻ concentration below the Donnan exclusion limit of the ionomer, preventing anions from entering and contaminating the ionomer.^{28,29} The possibility of catalyst contamination by NO₃⁻ and SO₄⁻ was also considered not significant for the same reason as the majority of active catalyst sites participating in the fuel cell reactions are covered in ionomer which the anions are prevented from permeating through. Thus, NaCl could have been used as well as Cl⁻ concentrations would also be below the Donnan exclusion limit.

Mitchel et al also observed a delay in the onset of the performance drop of approximately 24h after the start of injection, and continued performance drop for 10h after the injection of the salt solution was halted.²⁵ The authors suggested the slow transport from the gas channel could be due to numerous factors such as water produced or electro-osmotically transported from the anode to the cathode, a mass transfer barrier due to the properties of the gas diffusion layer (GDL), and the effect of the cell potential which pushes protons to the cathode catalyst layer. Li et al did not observe any delay on performance drop during injections of liquid solutions into the cathode stream containing cobalt ions.³⁰ However, the liquid injection rate was such that the inlet water content was equivalent to 100% relative humidity and thus some evaporation of the

injected salt solution could occur at the cell inlet, significantly increasing the ion concentration in solution and providing a higher diffusive driving force due to the large concentration gradient now established. Mitchell et al cell conditions were completed saturated to avoid any drying within the cell.²⁵ Typical GDLs are composed of a hydrophilic micro-porous layer to provide decreased contact resistance as well as provide a wicking effect removing water from the cathode catalyst layer, and a hydrophobic cloth/fiber layer with impregnated PTFE to move water droplets from the micro-porous layer to the gas channel. The presence of the hydrophobic layer may limit the formation of continuous water channels that would allow for ion transport from the injection liquid in the gas channel to the catalyst layer, especially under low concentrations which were used in these experiments. At low concentrations considered in this study it is important to establish continuous water channels from the catalyst layer to the gas channels.

As synergistic effects are of interest in studying mixed contamination as well as an understanding of single contaminant effects, gas phase contaminants currently being studied as part of the DOE air impurity project underway at HiSERF were considered for down selection for this study. One particular organic contaminant being studied was isopropanol. Isopropanol is a typical solvent and chemical intermediate, and is also a component of windshield de-icing solutions. Isopropanol has the propensity to change the wetting characteristics within the hydrophobic layer of the GDL, where previous studies show a reduction in the contact angle between water and PTFE and isopropanol and PTFE from 110 degrees to 20 degrees, respectively.³¹ This may aid in establishing continuous liquid diffusion paths for transport of the foreign cations by increasing wetting of the PTFE in the GDL. Also, from discussions with other HiSERF researchers on DOE airborne contaminants project, the observed performance impact at typical PEMFC operating conditions, was quite low (<3%) for concentrations below 1000ppm. Oxidation of the isopropanol is most likely occurring at typical PEMFC cathode potentials and concentrations are not high enough to cause significant blockage of the oxygen reduction reaction by the isopropanol reaction intermediates.³²⁻³⁴ Thus, with the possibility of decreasing the hydrophobicity of the GDL enhancing transport of the foreign cation to the ionomer, while not causing a significant performance impact, 100ppm isopropanol was used as the gas phase contaminant. The 100ppm level was selected in part based upon the available gas supply at the facility as well.

In this work, two constant current experiments were performed to evaluate possible mixed contaminant synergy and attempt to deconvolute the possible contaminant effects. After operating the cell on clean reactants to establish a baseline, the first experiment injected the liquid solution for 48 h, with the gas phase contaminant added after 24h of liquid injection. The second experiment injected the gas phase contaminant for 48h with the liquid injection added after 24h of impurity gas injection. After 48 h of contaminant introduction both the liquid and gas contaminant injections were stopped and the cells were run with clean reactants to evaluate any self-recovery.

The membrane/electrode assembly (MEA) was a GORE Select® 5150 type with 0.4mg cm⁻² Pt loading on both the anode and the cathode and an active area of 50cm². The gas diffusion layers utilized were SGL 25 BC which has a hydrophobized substrate (5wt% PTFE) with SGL's standard microporous layer (MPL). A new MEA was installed and conditioned for each test performed.

The single cell hardware utilized was a standard 50cm² cell from Fuel Cell Technologies. The cathode flow field was a triple serpentine while the anode a double serpentine. For the experiments the cell was operated horizontally with the cathode flow-field facing up. Reactant gases were operated in counter-flow mode. Temperature of the cell was controlled using a thermocouple in the cathode flow-field plate with 80W cartridge heaters inserted in each end plate for supplemental heating, and two 100 cubic feet per minute fans attached to each end plate, offset by 1.5 inch to provide cooling. The end plates were modified to allow for small bore tubing, connected to the liquid injection pump, to deliver the salt/acid solution directly into the cell/flow field without contacting any metallic parts. The layout of the injection port is shown in Figure 1.1.16. The liquid flow utilized in the study, 100μL min⁻¹, was low enough that additional heaters were not necessary and the conduction from the end plate would be sufficient to pre-heat the liquid.

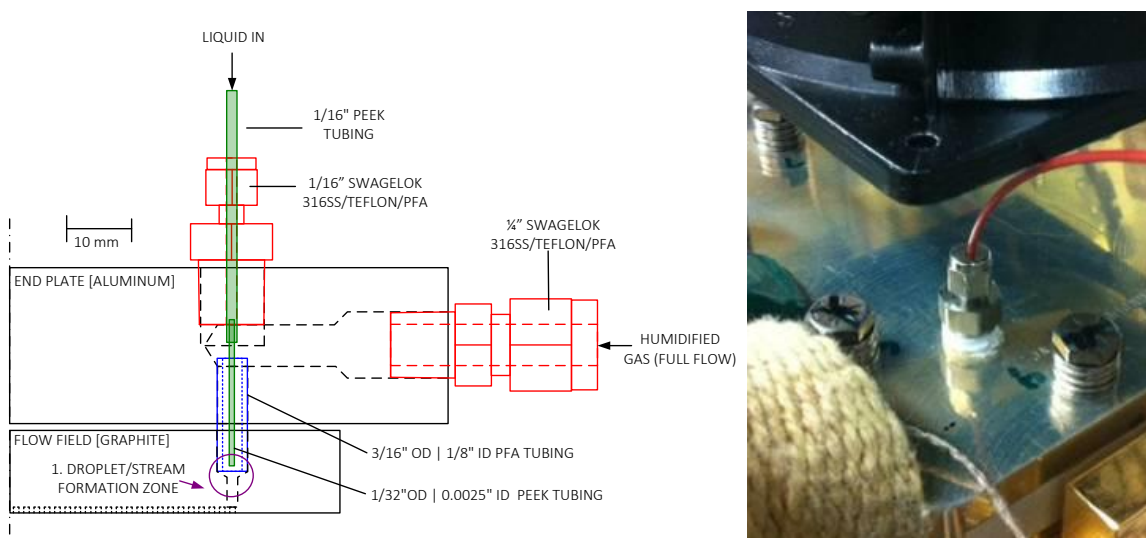


Figure 1.1.16 Cell hardware liquid injection modifications; drawing to scale (left), photo of end plate injection 1/16" outer diameter tube fitting (right)

The liquid supply and delivery system used in this study was designed and built for a past DOE project at HiSERF studying the effect of system contaminants. A review of the system components and design characteristics previously reported to the DOE is summarized here again. Figure 1.1.17 shows the schematic of the layout of the liquid delivery system supply. The system is based around a high pressure pump designed for liquid chromatography (Scientific Systems Inc. Series III Digital HPLC pump). The pump has a range from 0 to 10mL min⁻¹ in increments of 0.01mL. Polyether ether ketone (PEEK) was selected over stainless steel 316 for the pump body to minimize chemical incompatibility. The other wetted materials common to both head materials are synthetic ruby and sapphire and a fluorocarbon damper. The self-flushing pump head model was selected to avoid salt buildup in the pump internals behind the piston seals, although this option is really only necessary if pumping buffers, acids/bases, or any other inorganic solution near saturation. The source bottles are two 2 liter polypropylene (PP) Nalgene bottles with a small PTFE stir-bar at the bottom. Similar shaped PTFE/perfluoroalkoxy alkane (PFA) bottles were the more optimal choice, however they were not purchased due to the higher

cost and PP was sufficient for this application. Non-heating stir plates are used to avoid warming of the solutions. 10 to 20 micron PTFE/PEEK filters are used for the sparging gas and liquid suction lines (1/8" PFA or PTFE), with 1/8" PEEK bored-through bulkhead fittings sealed by Viton washers installed on the cap. The bored-through fitting allow for the option of using one piece of tubing on the suction side to minimize leakage points, or two pieces inside and outside the bottle with ferrules on each side. A PP 1/2" FNPT bulkhead seal in combination with a polyvinylidene fluoride (PVDF) 12mm electrode housing is installed for the option of inserting a pH, ion selective, or other electrode into the solution. To control the sparging gas flow, a micro-needle valve was installed on the outside of the cap, using a 1/4" PVDF bulkhead fitting. The micro-needle valve is constructed of PTFE, and was sized to allow flow control from 0-300mL min⁻¹ with a 2psi pressure drop. The ideal sparging gas is helium, as it has the lowest solubility of most inert gases. This helps prevent cavitation in the pump head on the suction side. The inlet pressure is set between 1-2psig to minimize bulging of the bottle. A PTFE gasket was added to the cap threads to aid in sealing. Two PEEK/PTFE 3-way micro valves are also utilized, one for bottle source switching, and one to change the pump outlet between a waste container for line purging and the injection point delivery line. When switching the bottle source from deionized water to the ion solution bottle at low flow rates the prime purge valve is used to flush the line between the 3-way valve and the pump head. This is necessary as the 1/8" tubing volume is quite large with respect to the flow rate. At the outlet of the pump this is not a concern as the 1/16" inner diameter tubing is shorter with a low volume. The outlet tubing material was PEEK. The majority of the parts were purchased from Valco Instruments Co.'s Cheminert LC division, with the bottles, needle valves, and stir plates coming from Cole Parmer. All components were mounted on the top and side surfaces of the HPLC pump for mobility from station to station. For automated flow control, the pump was accessorized with a 0-10V analog input which allows for flow rate adjustment.

The gas phase impurity was controlled by a separate mass flow controller and injected as a heated, dry gas downstream of the humidifier. The humidifier dew point was adjusted to achieve the desired relative humidity (RH) at the cell inlet. The inlet RH calculation did not include the amount of liquid water being injected into the cell. HiSERF flexible automation test stations, formerly purchased from UTC but now completely reconfigured and customized, were used for this testing. The new features including a new Labview based control software architecture recently developed and changes/upgrades to the hardware such that the stations are highly flexible and can change both software and hardware operating modes with very little time and effort (solid electrolyte batteries, flow batteries, PEMFC single cells or short stacks, high temperature fuel cells, electrolyzer cells, etc.).

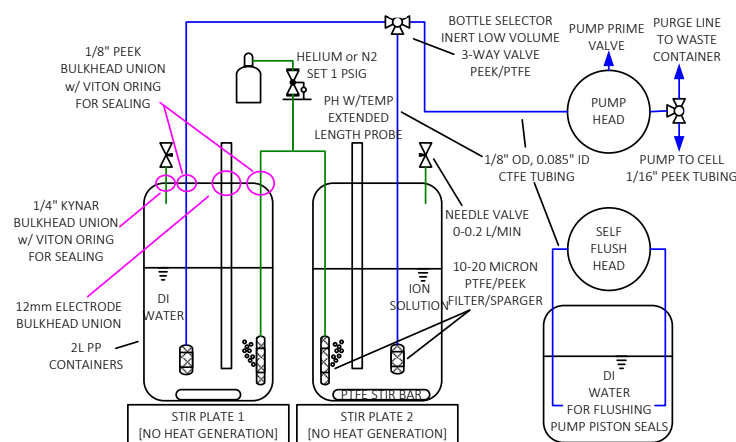


Figure 1.1.17 Schematic of liquid supply and delivery system (left) and photo of system (right)

The two contamination experiments were conducted in constant current discharge mode using a load bank. High frequency resistance (HFR) was measured using an Agilent 4338B milliohmmeter. The current density for both experiments was 0.2A cm^{-2} in an attempt to test while under load while minimizing water production. The other operating conditions were: 80°C cell temperature, 100/100% RH, $2/2\text{ H}_2/\text{air}$ stoichiometry, 150/150kPa back pressure control at the outlets. For both experiments, the liquid injection flow rate was set to $100\mu\text{L min}^{-1}$ with helium purged deionized water being injected when the 0.01M acid/salt solution was not being injected. The source of the isopropanol vapor was a 1000ppm isopropanol with zero grade air balance purchased from Matheson Tri-Gas. To maintain the stoichiometry on the cathode, the main air flow is reduced when the impurity gas flow is turned on. Both experiments started with a long duration clean reactant baseline phase. This phase was extended during the second experiment to evaluate any further changes in the baseline/clean reactant cell performance. As mentioned previously, the two impurities were injected in different orders to possibly assist in deconvoluting the various impacts of the single contaminants and mixed contaminants. A description of the timing and phases of the experiments are presented in Table 1.1.8. No additional diagnostics were performed as there was significant uncertainty as to whether the 100ppm isopropanol would affect the GDL wetting enough, along with other factors discussed earlier, that sodium ions could be transported to the catalyst layer. Thus the new MEAs were only conditioned overnight prior to the initiation of each contaminant experiment and no other diagnostics such as polarization curves were performed.

Table 1.1.8 Description of the different phases of each contamination experiment

| Phase | Experiment 1 | | Experiment 2 | |
|--|------------------|--|------------------|--|
| | Running time [h] | Reactants/Contaminants | Running time [h] | Reactants/Contaminants |
| Pre-poisoning | 66 | Neat air at 100% RH + 100 μ L min ⁻¹ DI Water | 93 | Neat air at 100% RH + 100 μ L min ⁻¹ DI Water |
| Single Contaminant [ion or organic] | 24 | Neat air at 100% RH + 100 μ L min ⁻¹ 0.01M HNO ₃ /Na ₂ SO ₄ | 24 | 100ppm isopropanol in air at 100% RH + 100 μ L min ⁻¹ DI Water |
| Mixed Contaminant [ion + organic] | 24 | 100ppm isopropanol in air at 100% RH + 100 μ L min ⁻¹ 0.01M HNO ₃ /Na ₂ SO ₄ | 24 | 100ppm isopropanol in air at 100% RH + 100 μ L/min ⁻¹ 0.01M HNO ₃ /Na ₂ SO ₄ |
| Self-Recovery | 30 | Neat air at 100% RH + 100 μ L min ⁻¹ DI Water | 24 | Neat air at 100% RH + 100 μ L/min ⁻¹ DI Water |

The voltage versus time behavior for both experiments is shown in Figure 1.1.18. Included in the data is the iR free voltage data as any Na⁺ ions displacing protons would cause an increase in the high frequency resistance which would be indicated by a deviation in the cell voltage versus iR free voltage (as HFR data is not plotted but can be inferred). The initial decrease between 0-10 h is primarily associated with the formation of an oxide layer, as voltages are well above the widely accepted potential of 0.7 V for the onset of Pt-O and Pt-OH oxide layer formation. The oxide formation proceeds rapidly then slows for the remainder of both experiments. Any observed voltage spikes down are due to the saturated conditions in the cell where water slugs might cause momentary current redistributions and voltage instabilities. The apparent noise in the data, which is on the order of +/- 1-2mV, is slightly higher than normally observed under dryer conditions. In both plots, it is apparent that very little ion contamination occurred. In the single contaminant phase, the first experiment shows very little change due to the acid solution. The corresponding phase in the second experiment, which starts with 100ppm isopropanol, shows about a 5-8mV decrease in both the cell voltage and iR free voltage. Thus no effect on the HFR is detected. In the mixed contaminant phase of the first experiment, the voltage decreases to the same levels and is attributed solely to the 100ppm isopropanol. In both these experiments the voltage drops were due to the impact of the oxidation of isopropanol resulting in small reduction in active sites for the ORR as indicated by the 5-8mV decrease in both the cell voltage and iR free voltage.

As no effect of the acid/salt solution was observed, there were discussions as to whether the solution even entered the cell. The flow fields are composed of a pyro-sealed porous graphite from POCO, such that only a small depth on the outer surface is gas/liquid tight, while the bulk of the material remains porous. The plates are machined after pyro-sealing and thus the break in the surface treatment can produce a leakage path, albeit a very restricted path, for gas or liquid to exit the cell. Shown in Figure 1.1.19 is a photo taken at the end of the first experiment of the thermocouple port, with a pile of salt evident on the opposite current collector. Thus, there was some minor leakage from the flow field out of the thermocouple port where the water evaporated leaving behind the precipitate. The leakage rate predicted to have occurred is significantly lower than the liquid injection rate which could be seen as evidence that the liquid solution was dispersed within the cell. In addition, salt deposits were also seen at the cathode outlet tubing after the cell, where the tubing is superheated to force evaporation.

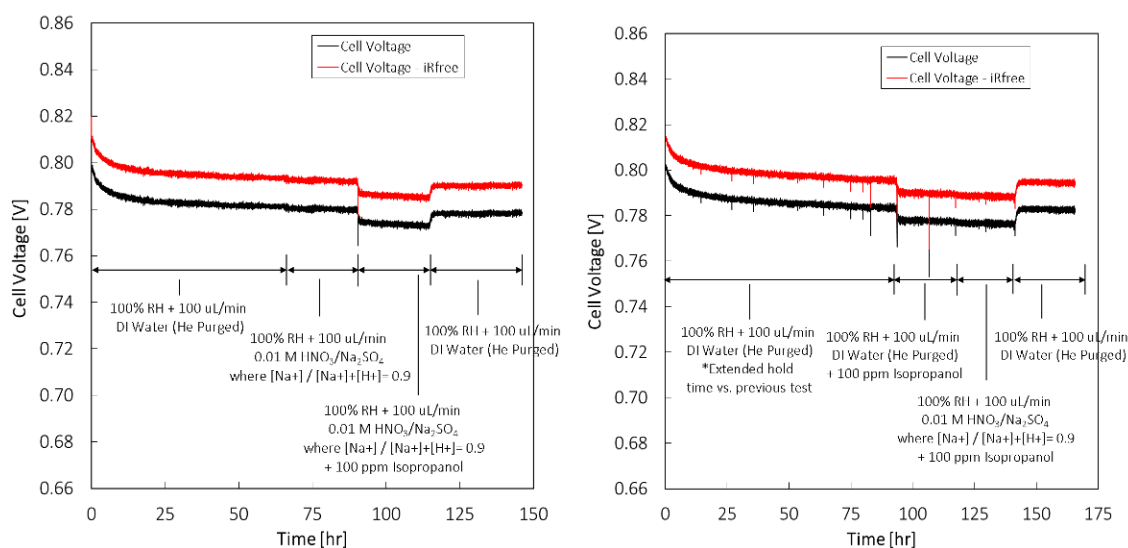


Figure 1.1.18 Cell voltage and iR-free cell voltage versus time for experiments listed in Table 1.1.8. Experiment 1 (left) and experiment 2 (right)

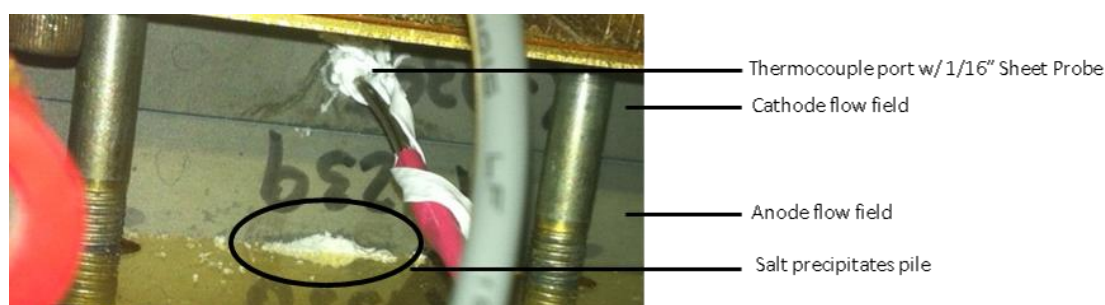


Figure 1.1.19 Photo of cell at end of experiment showing leakage and evaporation of liquid out of the thermocouple port resulting in salt precipitation

The experiments did not demonstrate a synergy between the two contaminants. In particular, foreign cation contamination was not achieved on the cathode either as a single contaminant or as a mixed contaminant with isopropanol vapor which caused only a 0.1% decrease in cell performance. One immediate option is to consider other organic contaminants, such as acetylene, that may induce a loss in phobicity. Increasing the isopropanol concentration might also be considered. For modeling purposes it is apparent that producing validation data of foreign ion contamination may be difficult to achieve without artificially altering the cell conditions from that used in typical operation. Running at low humidity/dry conditions where the acid/salt solution might evaporate and concentrate is one possible option, or even further considering incorporating accelerated degradation protocols such as RH cycling, used for determining mechanical stability of the membrane which might be beneficial to help induce cation contamination. Injecting the cation solution on the anode may also result in attraction of the cations towards the negative electrode. With all these options under consideration, one must remember that by concentrating the solution through increased injection concentrations or by evaporation within the cell may result in exceeding the Donnan exclusion limit of the ionomer preventing anion exchange and thus multiple ion contamination, through both anion and cation

exchange may occur. Further tests and experiments are under discussion and results from recent studies in other projects may provide additional guidance on how to proceed.

1.1.2 Fuel Cell Hardware-in-Loop and System Simulation

The performance of a novel partial (fuel cell/battery) hybrid UAV system was characterized. The new system was designed to reduce dynamic operations of the Ion Tiger UAV fuel cell stack (0.5kW_e) and improve its performance efficiency with the anticipation that its durability will also be extended. The partial hybrid system was also designed to minimize hybridization associated losses and prolong the mission duration of the UAV in comparison to most commonly used hybrid power systems.

In the previous study, detailed in the 2008 HEET report,³⁵ a partial hybrid (PH) UAV system simulation was used to design and test the new system concept and controller algorithm. The functionality of the controller algorithm was optimized by running the real time hardware-in-loop (HiL) system simulation with a Proton Exchange Membrane Fuel Cell (PEMFC) stack and some balance of plant (BoP) hardware and a simulated battery pack. For this present study, a prototype hardware controller was developed and tested on the HiL test station with a PEMFC stack, BoP and a battery pack. The focus of the HiL real time test of the PH UAV system under a 20 minutes load profile was to:

- Demonstrate the concept with a prototype hardware controller, PEMFC stack, battery pack and balance of plant (BoP) components
- Compare HiL measured versus simulation results
- Study the system performance with different operational strategies
- Estimate the UAV flight duration using the system energy balance

Figure 1.1.20 shows in more detail the features of the novel PH fuel cell/battery system. The system components specification are based on the non-hybrid Ion Tiger UAV system^{36,37} and consists of a 500W PEMFC stack and associated BoP components, a light-weight H₂ tank, a lithium ion battery pack, auxiliary loads and propulsion system. The PH system is designed specifically to minimize the system losses by using a smaller DC-DC converter for the battery charging process and allowing the fuel cell stack to operate at higher efficiencies and better controlled dynamics by sharing the peak power demand with a battery.

The system is also capable of switching to a non-hybrid mode of operation when the system demand is high for long periods or if the battery has failed or the state of charge (SoC) has decreased below a predetermined value. These operational modes are activated by different switches. Some of these switches are also designed to automatically restrict a reverse current with diodes having a very low voltage drop.

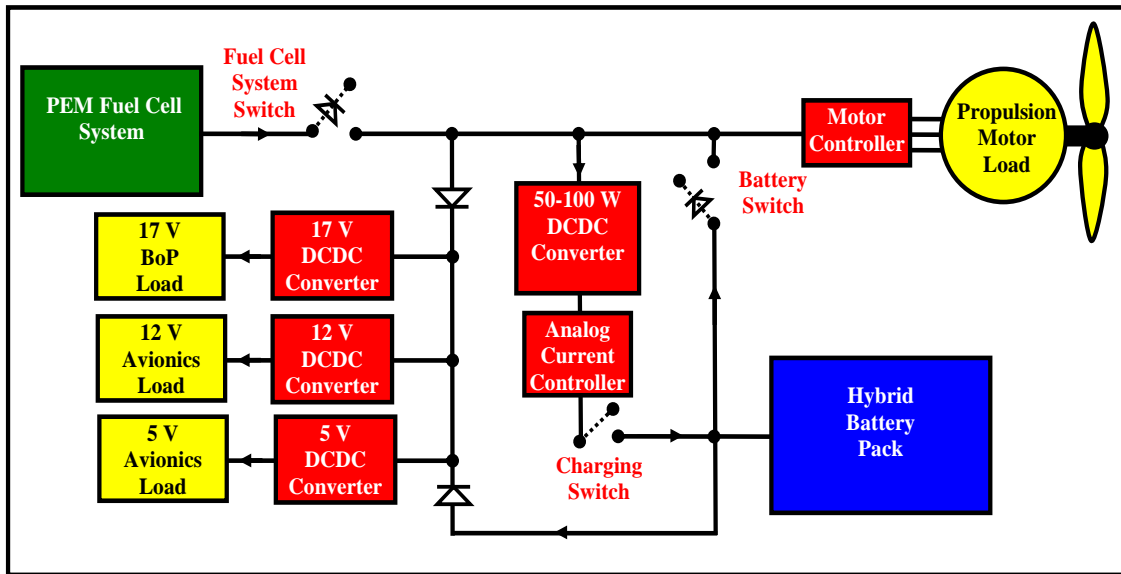


Figure 0-1.1.20 Schematic of a partial hybrid system

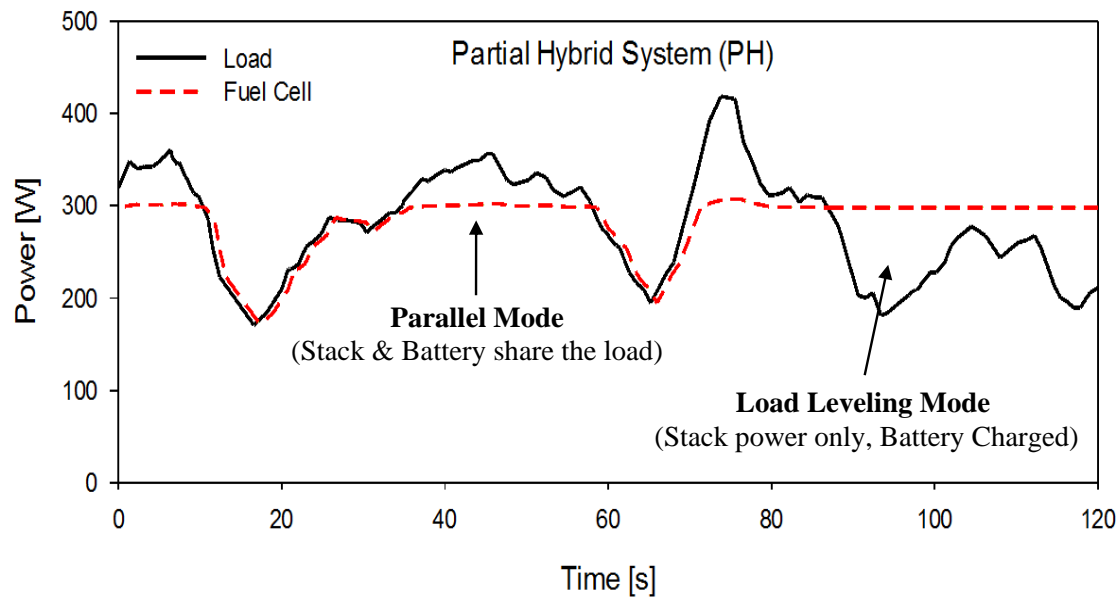


Figure 1.1.21 PEMFC stack response (theoretical) to a load demand for a PH System

The four modes of operation of the partial hybrid system are parallel, load leveling, charging and load following. Figure 1.1.21 shows the theoretical response of the PEMFC stack to load demand (part of an actual UAV mission load profile) for a partial hybrid system with two modes of operation highlighted. In parallel mode, both the fuel cell stack and the battery pack share the power demand according to their internal resistance. Hence, the battery pack (lower resistance) supplies the current above the fuel cell stack peak load. In the load leveling mode, the stack supplies all power to the system including the battery charging power, but the maximum stack power is limited (load leveled). Typically, in the load leveling mode, the stack power is higher than system load demand in order to support the battery pack charging (Figure 1.1.21). However, if the power demand goes above the fuel cell load level limit then the parallel mode is enabled.

The battery charging mode is enabled when the system load is low and the excess power is utilized to maintain the battery state of charge (SoC) within a predetermined range, for example 50–60% SoC. If the battery is completely discharged or damaged, the load following mode would be engaged where all system loads would be supplied by the fuel cell system.

A prototype hardware controller was designed and built to work in conjunction with the control algorithm of the partial hybrid system, enabling the use of a smaller charging DC/DC converter and “zero-Volt” diode control switches that reduce the overall system losses. Figure 1.1.22 shows the prototype controller which enables safe operation, the switching between different modes of operation, and the safe supply of the ancillary load to the fuel cell and/or battery (no power back flow). The controller consists of electrical circuits for the two “zero-Volt” diode switches, the DC-DC converter, the charging switch and voltage and current measurements for the battery SoC estimation. The “zero-Volt” diode and switches (Figure 1.1.20) are triggered by the control algorithm which determines the mode of operation according to the partial hybrid system operational strategy.

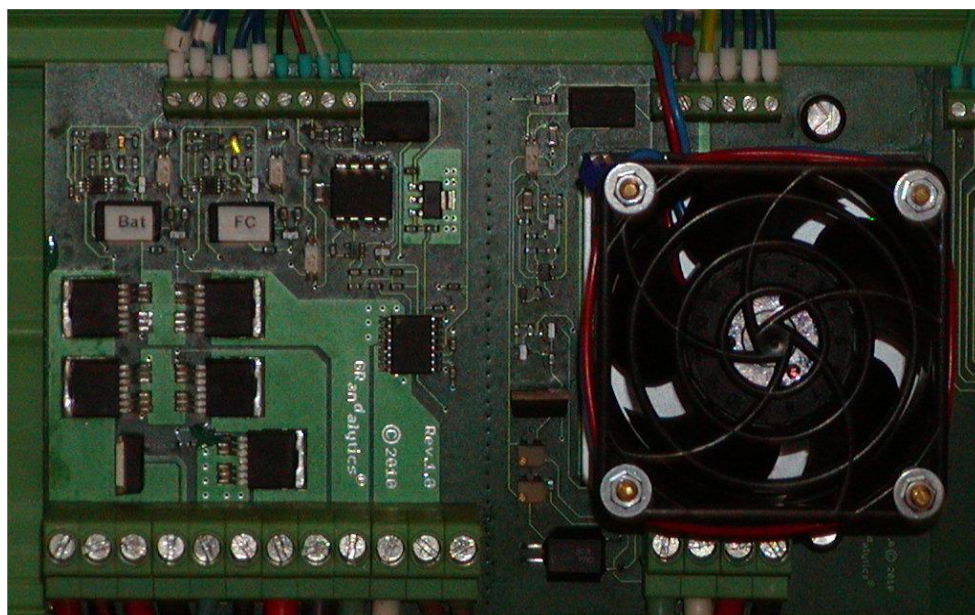


Figure 1.1.22 Prototype hardware controller

To study the performance of the PH system, the prototype controller hardware, a fuel cell stack, BoP components and a battery pack were coupled with the HiL test station. A HiL test station was specifically developed as a high speed simulator/measurement tool to support realistic simulations of various fuel cell applications and to derive optimal control strategies under a wide range of operating conditions. Figure 1.1.23 shows the HiL test station with different PH system hardware components.

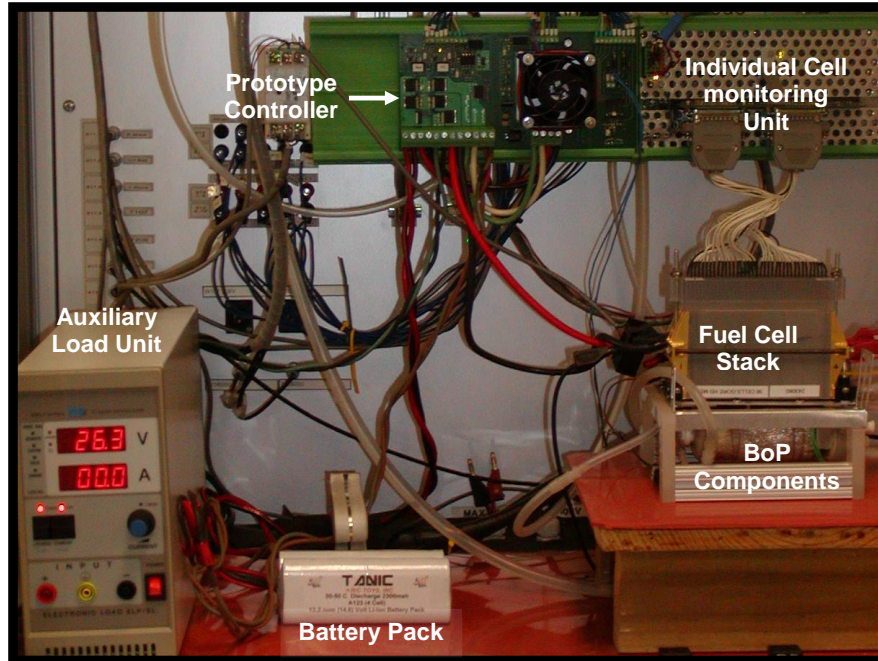


Figure 1.1.23 Partial fuel cell-battery hybrid system hardware components installed in the HiL test station

A PH system simulation with control algorithm was used along with hardware components embedded in the HiL test station to measure the performance of the system under a 20 minutes load profile. The following HiL simulation setup (Table 1.1.9) was used for the proof of concept demonstration test, performance test under different operational strategies and the UAV flight duration estimation.

Table 1.1.9 HiL simulation setup

| | |
|---------------------------|--|
| Load Demand | 20min UAV Load Profile |
| System Ancillary Load | Nominal Avionics (cruise) + BoP (~60W) |
| Fuel Cell : PEMFC Stack | Nominal Power: 500W, Anode Stoichiometry: 1.02, Temperature: 50–55°C and Cathode Stoichiometry: ~2.5 |
| Battery Pack: Lithium Ion | Capacity: 2.14Ah (7% de-rated), Nominal Voltage: 3.3 V/Cell (8 Cells) and Initial SoC: 100% |

The HiL simulation was designed to run in real time for 20 minutes under an actual UAV load (time versus power) profile with a nominal ancillary (~60W) load. The UAV had a tank with 0.5kg of hydrogen and a fully charged battery pack. The PH UAV's system simulation was converted into a real time simulation which was subsequently used to run the HiL test with the actual PEMFC stack operating on dry hydrogen with an anode purge system and air from the air blower and external humidifier. The air blower was designed to run at a cathode stoichiometry of ~2.5 and the external humidifier at 75% relative humidity. The battery pack size was optimized³⁵ and selected to meet the voltage range of the propulsion motor controller. The size of the DC-DC converter was also optimized to be large enough to maintain the battery state of charge (SoC)

between 50-60% and small enough to minimize both power losses and weight. The SoC of the battery was estimated by integrating the charge and discharge currents over time and was used by the control algorithm to run the prototype controller. A charging algorithm was implemented in order to charge the battery at a constant current and minimize current spikes by matching the current between the DC-DC converter and battery pack. Figure 1.1.24 shows the results of the demonstration test.

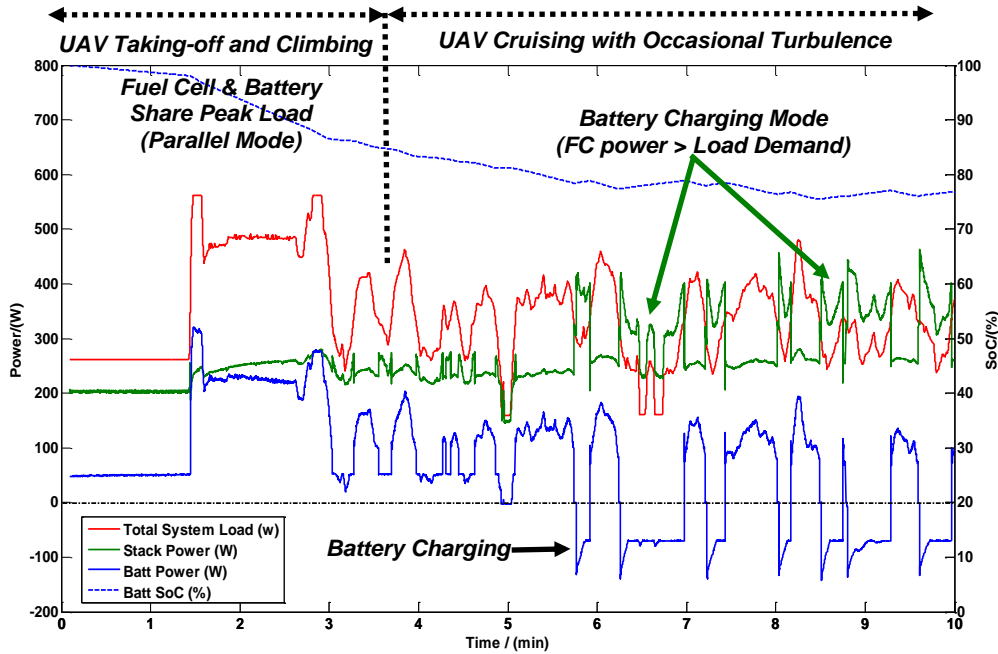


Figure 1.1.24 Partial hybrid system performance under a load demand

The test results in Figure 1.1.24 show that during the take off and landing phases of the flight the peak load is shared by the fuel cell stack and battery pack (parallel operation mode). In this mode of operation, the stack operates with a constant power output which is below the average power demand (355W). By comparison, the battery pack operates at a relatively higher power level under dynamic conditions. If the load demand is below 355W and the battery SoC is <80%, the battery charging mode is activated and the stack operates with a much higher power which is still less than the load leveling power of 475W. This result demonstrates the different modes of operation of the PH system that minimize stack dynamic operation and maximize its efficiency. The attractiveness of this design resides in the control algorithm that can be easily changed to further optimize stack operation and also manage the battery SoC and state of health (SoH). For example, adjustments would be necessary to accommodate a higher peak power for a longer period. During this specific phase of operation, the PH system would protect the battery pack by using the stack power so that the UAV would be able to complete its planned mission. For a hybrid system and during a continuous peak power demand, the battery would discharge more rapidly because the stack would not provide charging power. The UAV control system would either abort or cut the mission short to protect the fuel cell system and battery pack by safely landing the UAV.

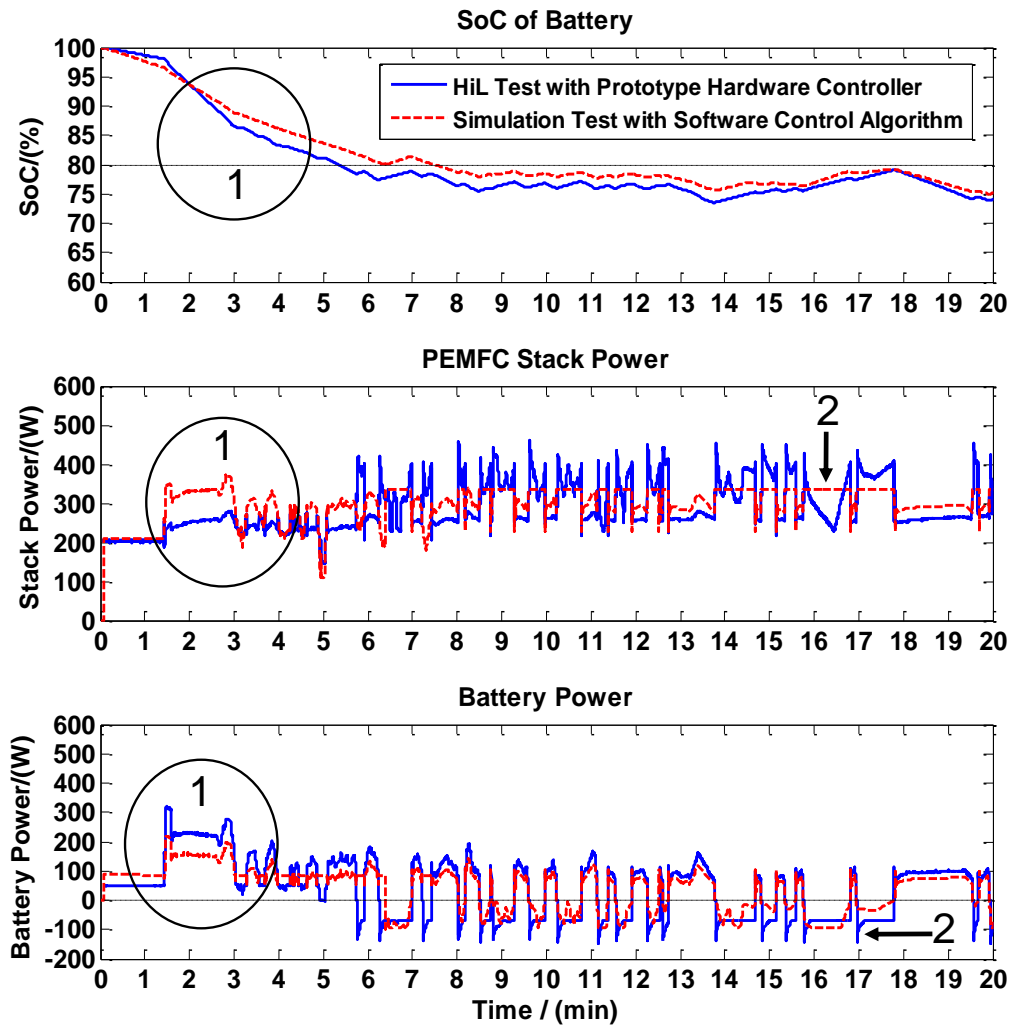


Figure 1.1.25 Comparison of HiL measured versus simulated results

The real time HiL results of the PH UAV system with prototype hardware controller under a 20 minute load profile were compared with the simulation test results (simulated software controller and system components under the same load profile). Figure 1.1.25 shows the performance comparison of the system in the HiL and simulation tests. Both results show very similar dynamic trends and mode switching over the 20 minutes test. However, the absolute values of the two set of results differ. This is mainly due to data used in the stack simulation model, the ideal software controller behavior and the battery charging current control.

In the simulation test, the fuel cell model uses static data which were measured when the stack was new (only a few hours under load) while in the HiL test the measured data are based on a stack with at least >150+ load hours. Therefore a difference in stack performance is observed as shown by the circle labeled 1 in the PEMFC stack power plot (Figure 1.1.25). This difference in stack performance also leads to more power being supplied by the stack during the parallel operation mode and a slower battery discharge in the simulation test in comparison to the HiL

test as shown by the circle labeled 1 in the SoC and battery power plots (Figure 1.1.25). Secondly, in the simulation test, an ideal software controller was used and therefore there is a much better control of the stack during the load leveling mode, as indicated by the stack power plot section labeled 2 in Figure 1.1.25, and a smoother battery charging power without spike (battery power plot section labeled 2 in Figure 1.1.25). The battery charging power spike is due to the iterative control. This effect will be minimized when the iterative control process will be modified by the use of an analog current controller in the prototype hardware controller.

The system performance was also investigated with different operational strategies. The main objectives of these tests were to demonstrate the capabilities and flexibility of the:

- HiL test system which can easily accommodate changes in operating conditions and/or control strategy without hardware modifications
- PH system with the use of redundant power sources to fulfill the UAV power demand when one power source degrades or fails

Due to the flexibility of the HiL, the SoC of the battery was easily changed from 100% to 50% and the performance of the PH system under this operating strategy was also measured. Figure 1.1.26 shows the results. For the 100% SoC test, a higher fraction of the battery charge was consumed and the stack operated at a lower power and higher efficiency as shown by the circle labeled 1. However, for the 50% SoC test, the reverse situation was observed due to a lower battery charge, and the stack provided a great share of the power demand during the parallel mode of operation. Furthermore, the battery starts to charge at the beginning of the mission profile and the control strategy maintains the battery SoC between 40–50% by ramping up the stack power whenever there was an opportunity to charge the battery (plot sections labeled 2 in Figure 1.1.26).

An energy balance was used to estimate the UAV flight duration using the measured data from the HiL test (20 minutes load profile) for non-hybrid (load following, LF), partial hybrid (PH) and full hybrid (FH) UAV system configurations. LF and FH system configurations were defined in the 2008 HEET report.³⁵ Figure 1.1.27 shows a UAV system schematic with all energy sources and losses which were considered in the energy balance. The energy balance is calculated by integrating the power into and out of each component over the 20 min load profile ($t_1=0$ s, $t_2=1200$ s) and the losses were estimated by the following equation (Equation 1.1.6, in kWh):

$$\frac{1}{3600} \times \left[\int_{t_1}^{t_2} P_{IN} dt - \int_{t_1}^{t_2} P_{OUT} dt - \int_{t_1}^{t_2} P_{LOSS} dt \right] = 0 \quad [1.1.6]$$

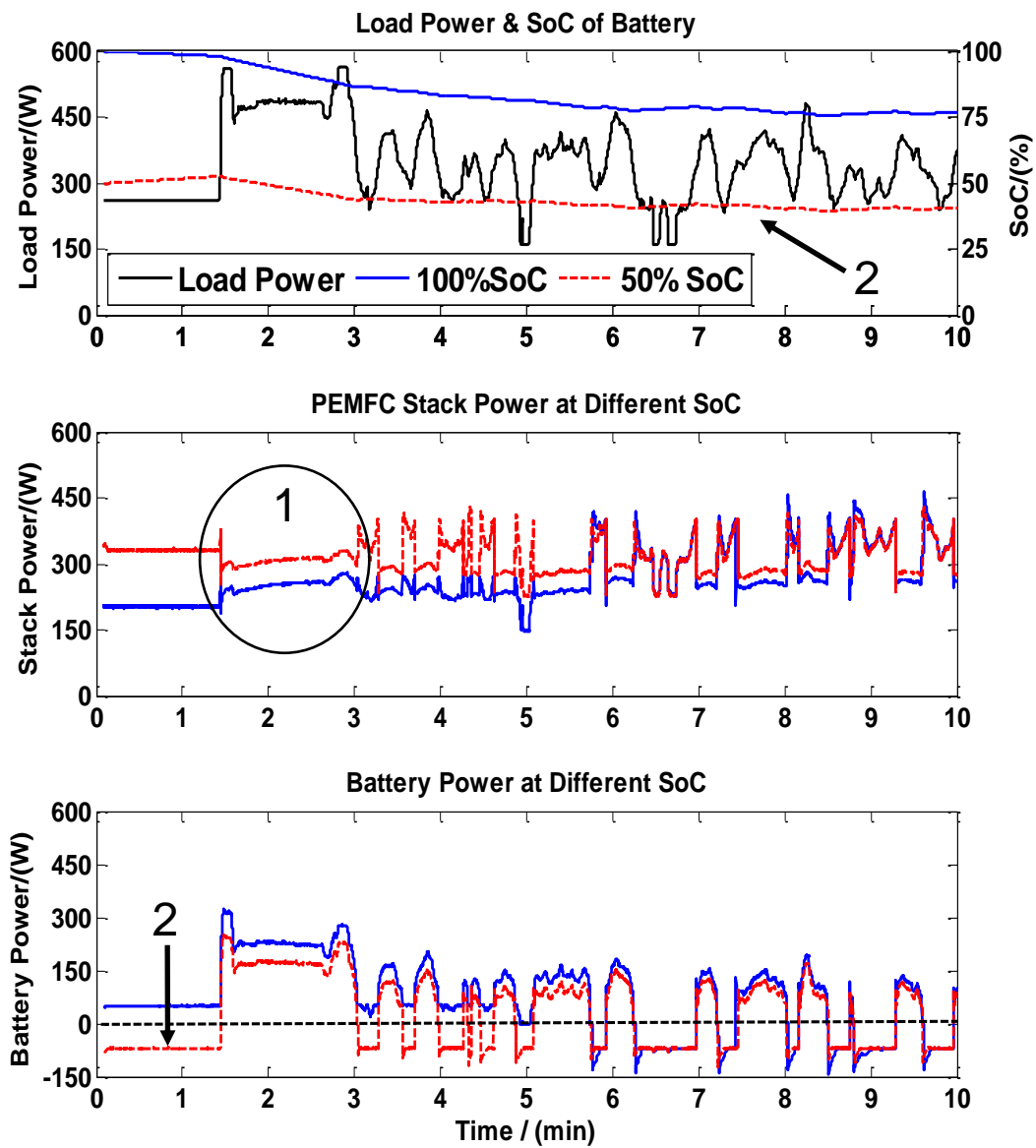


Figure 1.1.26 PH system performance at 50% and 100% initial battery SoC

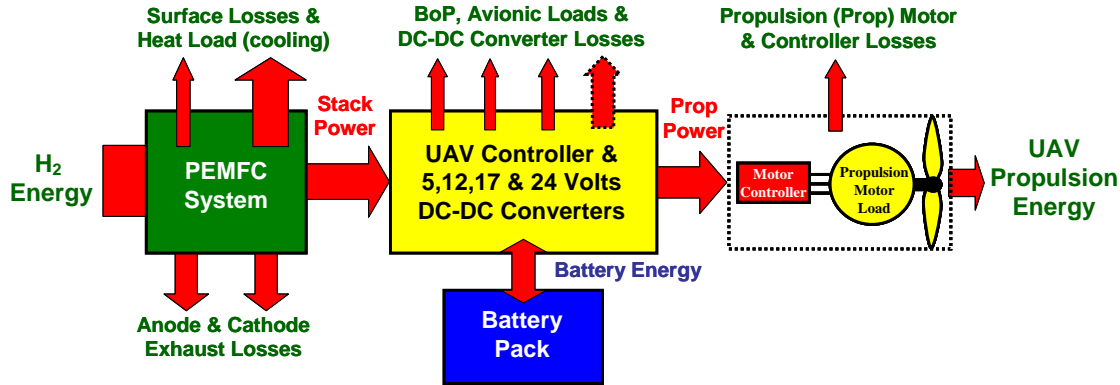


Figure 1.1.27 Schematic of energy balance over the UAV System

Energy balances were calculated with the following main assumptions:

- The stack energy balance is based on a 98% H_2 utilization and a fully charged battery pack
- The measured stack current, voltage, and, coolant and cathode exhaust temperatures were used to estimate the cathode losses and the heat load
- The measured current and voltage were used to estimate the energy utilization and losses in the battery pack

Figure 1.1.28 shows the percentage energy utilization and losses for each system estimated from the energy balance over the 20 minutes profile and normalized with the non-hybrid Ion Tiger UAV system.^{36,37} The non-hybrid system was used as a baseline to study the effect of hybridization and compare the performance of the new PH UAV system to a real functioning UAV fuel cell system. For the non-hybrid system, the energy balance results show that the system could not meet the system load due to a degraded stack performance which could not supply the peak power demand. The continuous stack operation at peak power and under highly dynamic conditions for the non-hybrid or load following UAV system, may have over time (>150+ load hours) lead to the performance degradation of the stack observed in this study. The FH system has the worst performance with higher stack losses because the stack operated at constant power even when the load demand was lower than the stack power. The PH system has the best performance of all the UAV systems, even the PH system with 50% initial SoC had a comparable performance to the non-hybrid but with enough power to complete the UAV mission. The main distinction between the two PH systems, a battery SoC of 100% and 50%, resulted in higher stack heat losses for the 50% SoC system as the fuel cell operated at a higher current density.

The energy balance data were also used to estimate the UAV flight duration for all three systems with a 0.5kg of hydrogen charge by extrapolating the amount of hydrogen consumed in the 20 minutes UAV flight. Figure 1.1.28 also shows the flight duration for each system normalized to the non-hybrid system. The novel PH system approximately has 10% and 30% longer flight duration than the non-hybrid and full hybrid respectively. These results demonstrate the greater benefit of the new system, even when one of the power sources is not optimally performing (PEMFC stack in this case). The new system was capable of completing the desired UAV mission.

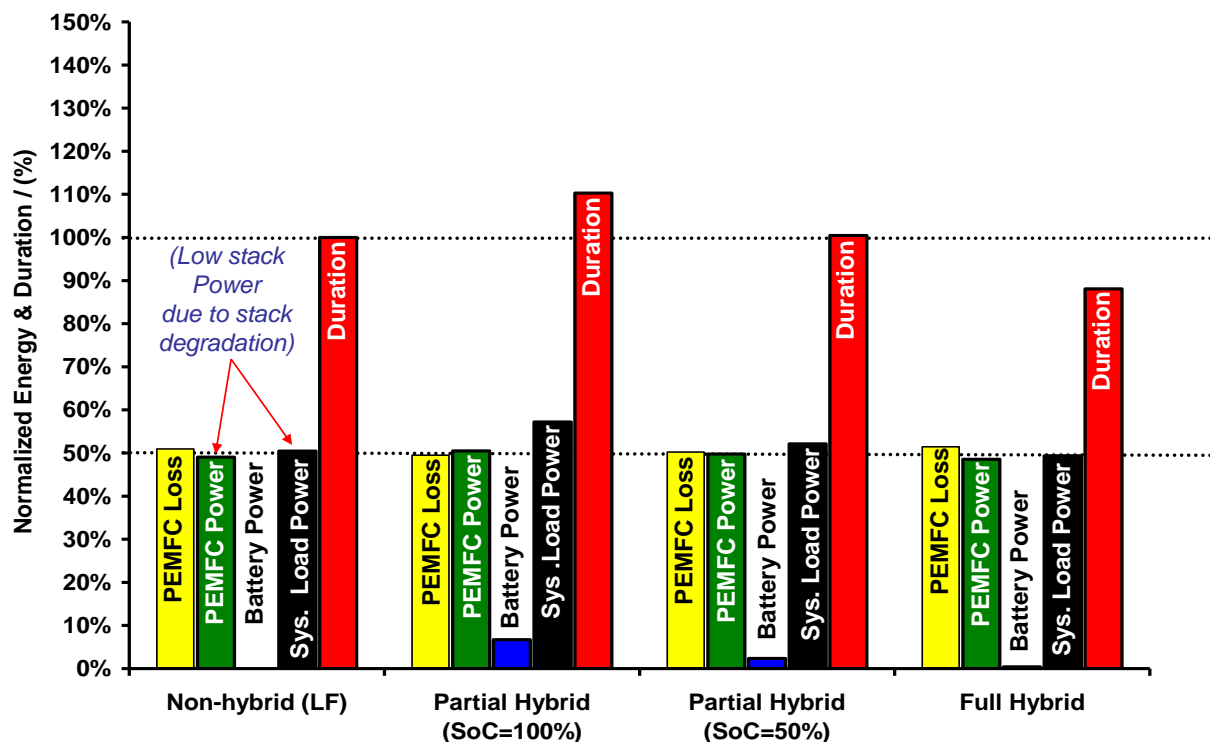


Figure 1.1.28 Energy balance performance of the three UAV systems

A novel partial hybrid system was designed and tested with a prototype hardware controller in the HiL test station. The system offers flexible modes of operation and lower power losses with the use of “zero-Volt” diode switches and a smaller DC-DC converter. The HiL study demonstrated that the system is capable of maximizing the use of battery energy to minimize the stack power and dynamics during peak demands by load sharing and utilizing the redundant power sources to support UAV power demands when one source degrades or fails. The energy balance analysis of the three systems considered also showed that the partial hybrid UAV system had 10% and 30% higher flight duration than the non-hybrid and full hybrid systems respectively under a 20 minutes UAV load profile. Improvement of the hardware controller would further reduce the stack operating power range and may increase its overall durability.^{38–40} This potential increase in stack durability due to a narrow operating power range will be further characterized with life tests.

References

1. F. Sapountzi, M. N. Tsampas, C. G. Vayenas, *Top. Catal.*, **44**, 461 (2007).
2. J. Zhang, R. Datta, *J. Electrochem. Soc.*, **149**, A1423 (2002).
3. J. Zhang, J. D. Fehriback, R. Datta, *J. Electrochem. Soc.*, **151**, A689 (2004).
4. A. Mota, P. P. Lopes, E. A. Ticianelli, E. R. Gonzales, H. Varela, *J. Electrochem. Soc.*, **157**, B1301 (2010).
5. P. P. Lopes, E. A. Ticianelli, H. Varela, *J. Power Sources*, **196**, 84 (2011).
6. G. Bender, M. Angelo, K. Bethune, S. Dorn, T. Thampan, R. Rocheleau, *J. Power Sources*, **193**, 713 (2009).

7. Y. Zhai, G. Bender, S. Dorn, R. Rocheleau, *J. Electrochem. Soc.*, **157**, B20 (2010).
8. R. Mohtadi, W.-K. Lee, J. W. Van Zee, *J. Power Sources*, **138**, 216 (2004).
9. J. St-Pierre, M. Angelo, Y. Zhai, *ECS Trans.*, **41**(1), 279 (2011).
10. J. St-Pierre, Y. Zhai, M. S. Angelo, *J. Electrochem. Soc.*, **161**, F280 (2014).
11. Y. Zhai, G. Bender, K. Bethune, R. Rocheleau, *J. Power Sources*, **247**, 40 (2014).
12. J. St-Pierre, in *Polymer Electrolyte Fuel Cell Durability*, F. N. Büchi, M. Inaba, T. J. Schmidt, Editors, p. 289, Springer, New York (2009).
13. V. A. Sethuraman, J. W. Weidner, A. T. Haug, S. Motupally, L. V. Protsailo, *J. Electrochem. Soc.*, **155**, B50 (2008).
14. J. Ge, J. St-Pierre, Y. Zhai, *Electrochim. Acta*, **134**, 272 (2014).
15. J. Ge, J. St-Pierre, Y. Zhai, *Electrochim. Acta*, **133**, 65 (2014).
16. J. Ge, J. St-Pierre, Y. Zhai, *Electrochim. Acta*, **138**, 437 (2014).
17. Y. Garsany, O. Baturina, J. Pietron, K. Swider-Lyons, *ECS Trans.*, **3**(1), 685 (2006).
18. Y. Garsany, O. A. Baturina, K. E. Swider-Lyons, *J. Electrochem. Soc.*, **154**, B670 (2007).
19. Y. Garsany, O. A. Baturina, K. E. Swider-Lyons, *J. Electrochem. Soc.*, **156**, B848 (2009).
20. F. Jing, M. Hou, W. Shi, J. Fu, H. Yu, P. Ming, B. Yi, *J. Power Sources*, **166**, 172 (2007).
21. W. Shi, B. Yi, M. Hou, Z. Shao, *Int. J. Hydrogen Energy*, **32**, 4412 (2007).
22. J. Biesdorf, N. Zamel, T. Kurz, *J. Power Sources*, **247**, 339 (2014).
23. J. St-Pierre, M. Angelo, K. Bethune, J. Ge, S. Higgins, T. Reshetenko, M. Virji, Y. Zhai, *ECS Trans.*, **61**(23), 1 (2014).
24. M. S. Mikkola, T. Rockward, F. A. Uribe, B. S. Pivovar, *Fuel Cells*, **7**, 153 (2007).
25. T. J. Schmidt, U. A. Paulus, H. A. Gasteiger, R. J. Behm, *J. Electroanal. Chem.*, **508**, 41 (2001).
26. J. St. Pierre, *Int. J. Hydrogen Energy*, **36**, 5527 (2011).
27. J. St. Pierre, *J. Power Sources*, **196**, 6274 (2011).
28. F. Helfferich, *Ion Exchange*, Dover Publications, New York (1995).
29. A. Lehmani, P. Turq, M. Périé, J. Périé, J.-P. Simonin, *J. Electroanal. Chem.*, **428**, 81 (1997).
30. H. Li, J. Gazzarri, K. Tsay, S. Wu, H. Wang, J. Zhang, S. Wessel, R. Abouatallah, N. Joos, J. Schrooten, *Electrochim. Acta*, **55**, 5823 (2010).
31. H. W. Fox, W. A. Zisman, *Rev. Sci. Instrum.*, **19**, 274 (1948).
32. S. S. Gupta, J. Datta, *J. Chem. Sci.*, **117**, 337 (2005).
33. S.-G. Sun, Y. Lin, *Electrochim. Acta*, **41**, 693 (1996).
34. S.-G. Sun, Y. Lin, *Electrochim. Acta*, **44**, 1153 (1998).
35. Hawaii Energy and Environmental Technologies (HEET) 2008 Report, December 2011, ONR Grant Award Number N00014-09-1-0709.
36. K. E. Swider-Lyons, R. O. Stroman, G. S. Page, J. F. Mackrell, J. A. Rodgers, M. W. Schuette, 'The Ion Tiger Fuel Cell Unmanned Air Vehicle', 44th Power Sources Conference, presentation 25.4, Las Vegas, NV, 14-17 June 2010.
37. D. McKinney, D. Thompson, D. Parry, K. Swider-Lyons, *NRL Spectra*, **2** (2010).
38. R. Borup, J. Meyers, B. Pivovar, et al, *Chem. Rev.*, **107**, 3904 (2007).
39. D. Liu, S. Case, *J. Power Sources*, **162**, 521 (2006).
40. D. P. Wilkinson, J. St-Pierre, in *Handbook of Fuel Cells - Fundamentals, Technology and Applications*, Vol. 3, Fuel Cell Technology and Applications, Part 1, Chapter 47, W. Vielstich, H. Gasteiger, A. Lamm, Editors, p. 611, John Wiley and Sons (2003).

Papers and Presentations Resulting from these Efforts

Conference Proceedings

- M. S. Angelo, J. St-Pierre, *ECS Trans.*, **64**(3), 773 (2014).
- M. Angelo, J. St-Pierre, K. Bethune, R. Rocheleau, *ECS Trans.*, **35**(32), 167 (2011).

Conference Presentations

- M. Angelo, J. St-Pierre, 'The Effect of Common Airborne Impurities and Mixtures on PEMFC Performance and Durability', in *Meeting Abstracts*, Electrochemical Society volume 2014-2, The Electrochemical Society, Pennington, NJ, 2014, abstract 1058.
- M. Virji, Knowledge Foundation's, 'A Novel Proton Exchange Membrane Fuel Cell-Battery Partial Hybrid System Design for Unmanned Aerial Vehicle (UAV) Application', 14th Annual International Symposium, Hybrid Small Fuel Cells 2012, Boston, MA, July 18, 2018.
- M. Angelo, J. St-Pierre, K. Bethune, R. Rocheleau, 'Gas Chromatography Study of Carbon Monoxide Reactions at Different Temperatures and a Trace Concentration Level within a PEMFC', in *Meeting Abstracts*, Electrochemical Society volume 2011-1, The Electrochemical Society, Pennington, NJ, 2011, abstract 285.

1.2 Bioactive Fuel Cells

Bioactive fuel cells are advanced electrochemical energy conversion cells that use electrobiocatalysis to promote the conversion of the chemical energy in biofuels into useful electrical energy. The overall objective in this subtask was to advance enzymatic biofuel cell technology through quantitative, *in situ* characterizations of the electrode properties and cell performance to enhance fundamental understanding of the underlying mechanism in electrobiocatalysis. Through this work, we:

- 1) Developed and characterized chitosan co-block polymers that immobilize multiple enzymes that can more fully oxidize complex energy fuels, and
- 2) Integrated *in situ* characterization methodology that comprises spectroscopic imaging ellipsometry, microgravimetric, and electrochemical techniques to investigate the dynamic interaction of enzyme-immobilized electrode surface and the bio-feedstock *in operando*, so the charge transfer process involved could be better understood by more direct measurements and correlations.

Development and characterization of chitosan co-block polymers scaffolds

Under past funding a method of fabricating chitosan polymer scaffolds was developed and used to fabricate working electrodes containing immobilized enzyme. To improve the activity of the immobilized enzymes it was postulated that immobilizing the enzymes in more hydrophobic microenvironments would be effective. In this funding period we 1) hydrophobically modifying

chitosan polymer with specific alkyl side chains (e.g., butyl, decyl...ect...) to create separate solutions of modified chitosan (i.e., C4-Chitosan, ALA-Chitosan, C8-Chitosan). These modified chitosan polymers provide a variety of amphiphilic environments that can be tailored to specific enzymes. With this system we fabricated co-block polymers comprised of the individual modified polymers in order to create a composite chitosan polymer that can immobilize and stabilize several enzymes that represent a pathway to more fully oxidize a complete energy fuel (i.e., glucose). The co-block polymers was fabricated into immobilization matrices using thin film coating using various spin and drop coating techniques as discussed above. To characterize the chemical microenvironments provided by the composite polymers we applied fluorescence emission spectroscopy to characterize the relative polarity and pH micro-environments provided by both native and hydrophobically modified chitosan co-block polymers. Additionally, fluorescence emission has been used to qualitatively characterize the extent to which hydrophobic modification of the chitosan polymer affect the relative polarity of the resultant amphiphilic micelles.

It has been proposed that the hydrophobically modified chitosan co-block polymers form amphiphilic micelles on the mesopore scale. These micelles become more hydrophobic due to the introduction of the hydrophobic side alkyl chains along an otherwise hydrophilic backbone. To test this theory, chitosan co-block polymer scaffolds were fabricated from solutions of unmodified and modified chitosan that also contained Nile Red, a fluorophore whose emission profile changes in both intensity and maximum in response to changes in the polarity of the surrounding solvent (Figure 1.2.1). Laser scanning confocal microscopy was used to image slices of the scaffolds, using filters that permitted light above 650nm (red region) and below (blue region) 620 nm (Figure 1.2.2) to be detected. In Figure 1.2.2, the top row of images presents the emission below 620 nm (A), above 650 nm (B) and their combined emission (C) for scaffolds fabricated from the unmodified chitosan. The bottom row of images presents the emission below 620 nm (A), above 650 nm (B), and their combined image (C) for scaffolds fabricated from the modified chitosan. Figure 1.2. 3 presents the distribution for the ratio of the emission intensity below 620 nm to the total emission intensity. The increase in the average from the unmodified, to modified chitosan (C4-chitosan) indicates an increase in the hydrophobic nature of the polymer.

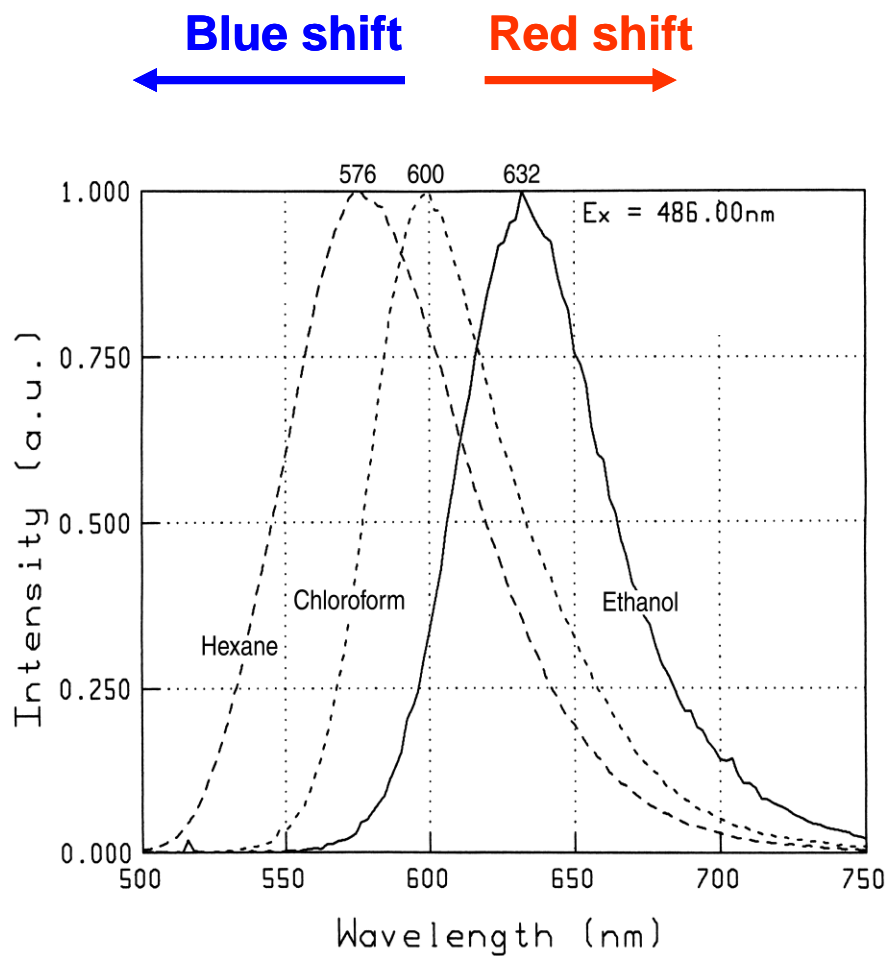


Figure 0-2.2.1: Normalized emission profile of Nile Red in solvents of varying polarity. Dielectric constants were 1.89 for hexane (at 20C), 4.8 for chloroform (at 20C) and 24.3 for ethanol (at 25C).

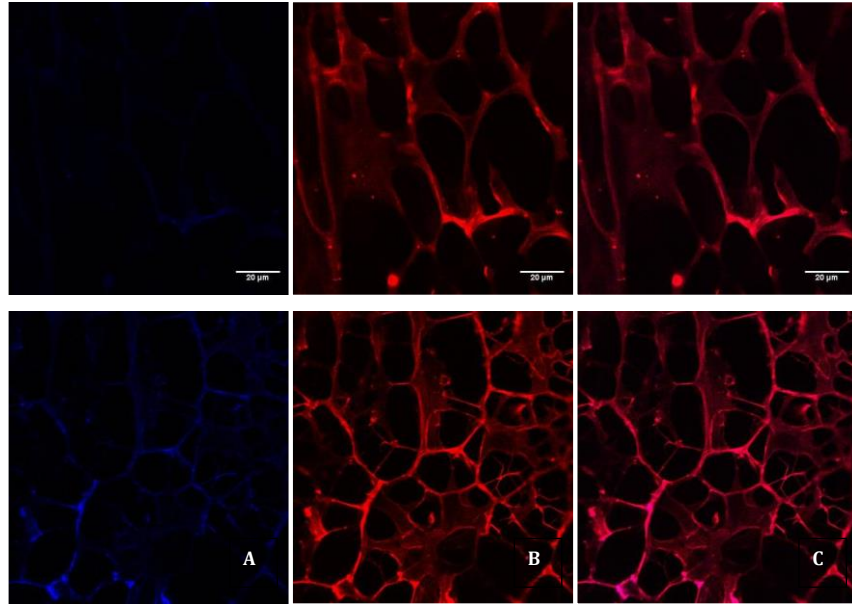


Figure 1.2.2: Laser scanning confocal microscopy images of chitosan scaffolds incorporating Nile Red fluorophore.

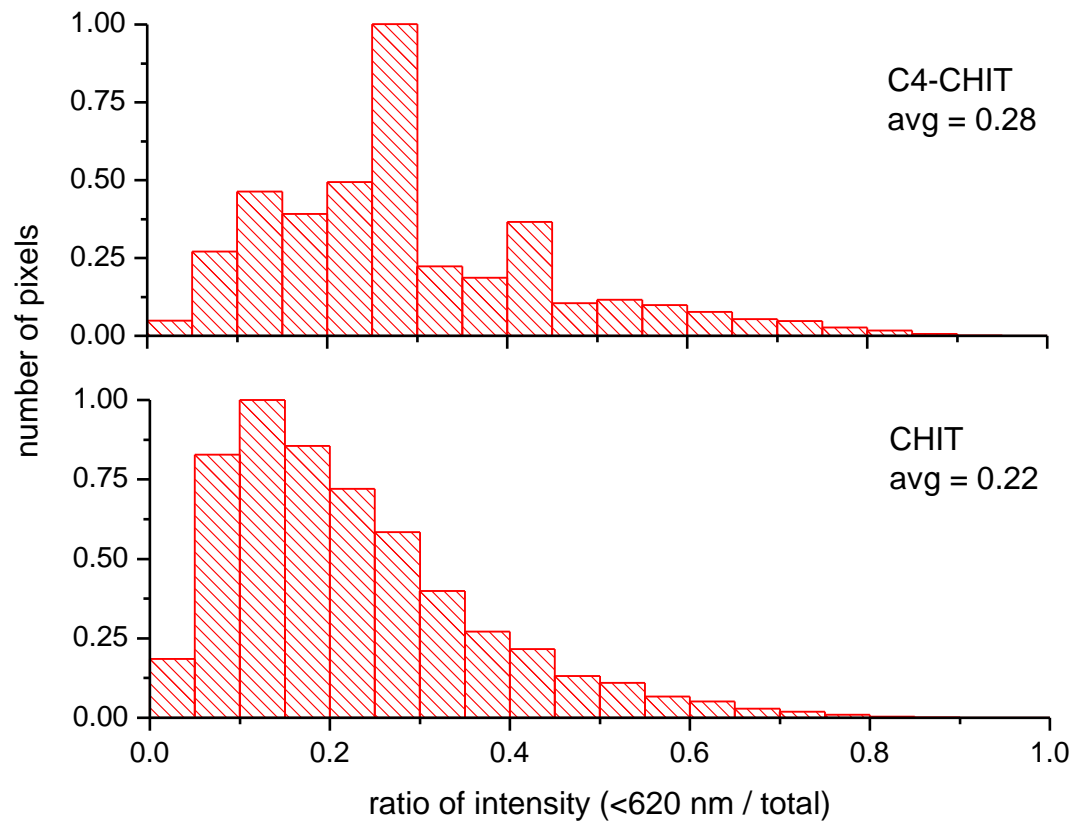


Figure 1.2.3. Ratio of the blue region intensity to the total emission intensity for modified and unmodified chitosan

The use of polar sensitive fluorophores in combination with fluorescent spectroscopy and microscopy provides a unique and informative tool for probing the chemical microenvironment provided by immobilization polymers. In this work, these techniques were used to probe the chemical microenvironments of native and hydrophobically modified chitosan polymer matrices used to immobilize enzymes. Our results indicate that electrostatic forces dominate the interaction between fluorophores and polymer when both are freely suspended in solution. Also, at least in the case of yeast alcohol dehydrogenase labeled with dansyl-chloride, there is no significant change in the local or global motion of the enzyme bound fluorophore when placed in the presence of either unmodified or butyl-modified chitosan. This suggests that the immobilization of enzyme into chitosan amphiphilic micelles does not occur in the aqueous phase, but more likely during the scaffold formation step. Introducing side alkyl chains of increasing carbon length (along the chitosan polymer backbone) results in a modified chitosan polymer that is more hydrophobic and amphiphilic [1].

Papers and Presentations Resulting from Efforts

- 2011** Martin, G., Minter, S., and M. J. Cooney[☒]. *Fluorescence characterization of immobilization induced enzyme aggregation*. Chemical Communications. Feb 21, 47(7):2083-5.
- 2010** Lau, C., Martin, G., Minter, S. D., and M. J., Cooney[☒]. *Development of a chitosan scaffold electrode for fuel cell applications*. Electroanalysis. 22(7-8):793-798.
- 2009** Martin, G. L., Ross, J. A., Minter, S. D., Jameson[☒], D. M., and M. J. Cooney[☒]. *Fluorescence characterization of polymer chemical microenvironments*. Carbohydrate Polymers. doi:10.1016/j.carbpol.2009.02.021
- 2009** Martin, G., Minter, S. D., and M. J. Cooney[☒]. *Spatial distribution of malate dehydrogenase in chitosan scaffolds*. Applied Materials & Interfaces, 1(2): 367 – 372.
- 2010** Cooney, M. J. *Modification and Characterization of Chemical Microenvironments for Enzyme Immobilization*. 240th American Chemical Society, August 22-26, Boston, MA.
- 2010** G. Martin, S. Minter and M. Cooney. *Fluorescence Characterization of Enzyme Aggregation in the Immobilized State*. 217th ECS Meeting in Vancouver, BC, Canada.
- 2010** G. Martin, C. Lau, S. Minter and M. Cooney. *Fluorescence Characterization of Immobilized Enzymes*. 217th ECS Meeting in Vancouver, BC, Canada.

References

- [1] Martin, G., M.J. Cooney, S.D. Minter, J.A. Ross, and D.A. Jameson, Fluorescence characterization of polymer chemical microenvironments in hydrophobically modified chitosan. *Carbohydrate Polymers*, 77, 695 - 702 (2009).

***In Situ* Characterization**

Under Subtask 1.2 we also studied the stability of mediators, such as methylene green (MG) and other azines, that are essential for power generation in reduced Nicotinamide Adenine Dinucleotide (NADH) dependent bioactive fuel cells. MG immobilization on Pt electrodes was investigated during electrode fabrication using *in situ* characterization techniques such as spectroscopic imaging ellipsometry (SIE), quartz crystal microbalance (QCM) and cyclic voltammetry (CV). The focus of the effort was to understand the underlying process in the immobilization of the mediators in order to develop effective working anodes for bioactive fuel cell applications.

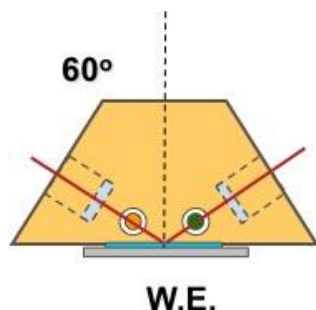


Figure 1.2.0-3: Schematic showing the cell assembly for the spectroscopic imaging ellipsometry and electrochemical studies.

The cross-section of the cell configuration for the SIE experiments is shown in Figure 1.2.0-3. The cell assembly is comprised of a working electrode (W.E.) made of thin film Pt (shown in gray) as substrate, deposited MG film (shown as the layer in blue), a vessel that contains the mediator solution (in yellow, which also serves as the electrolyte) for electrochemical study above the working electrode, two optical windows (dashed lines with white color lens) to allow laser light (red lines) to come in and exit to provide the access for the SIE studies simultaneously with electrochemical experiments. The green- and gold-colored circular objects (which are perpendicular to the plane of the drawing) are the counter and reference electrodes, respectively, in contact with the electrolyte in order to conduct electrochemical studies.

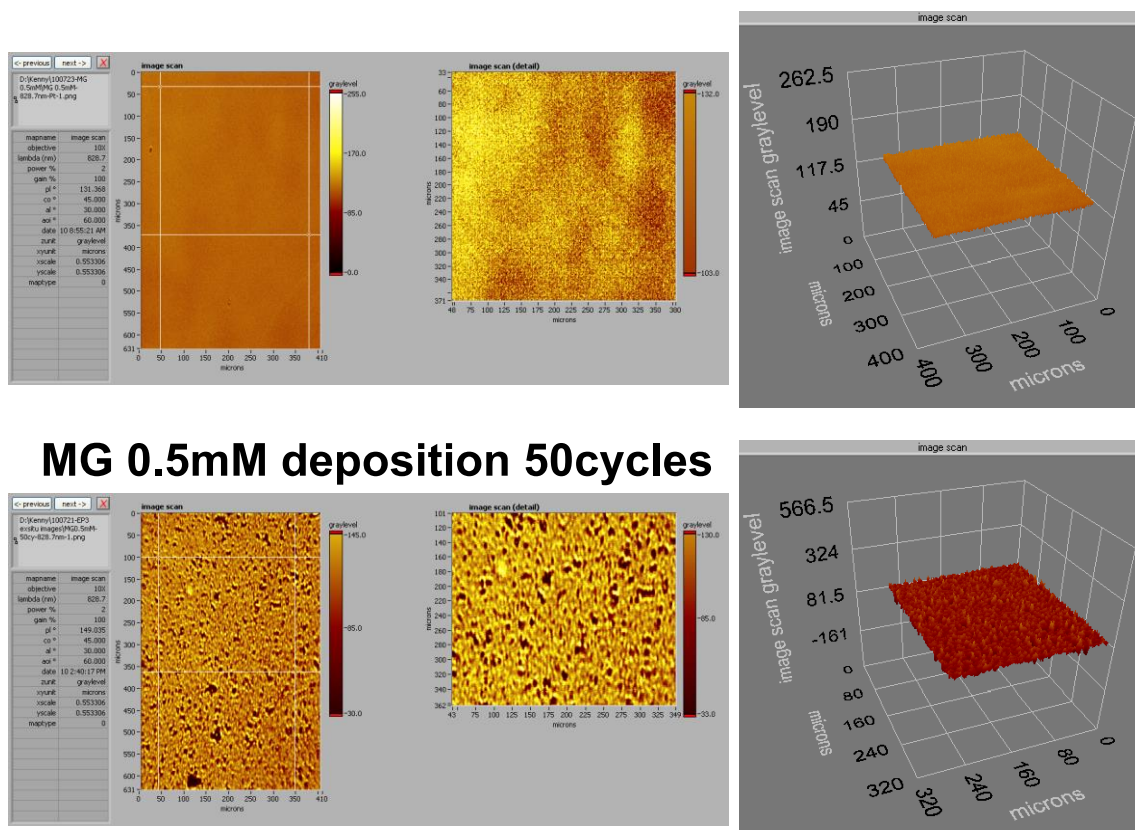
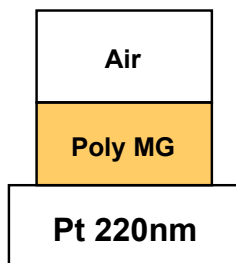


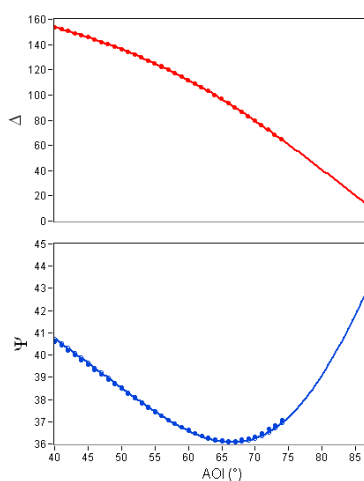
Figure 1.2.0-4: Imaging from SIE showing before and after the deposition of MG films on the Pt substrate.

Figure 1.2.0-4 shows the results of the MG film deposited on the Pt substrate using 0.5 mM MG solution and CV technique for deposition. The imaging capability of SIE clearly demonstrates the differences before and after the deposition of the MG film on Pt, with optical resolution sufficient to show the morphology (surface area on a scale of microns) and thickness of the film (nanometer scale). The images on the left are the scanned surfaces from the top of the sample, showing the entire sample and a section under higher resolution. The graph on the right is a three-dimensional plot to show the film thickness. The lateral 2-D resolution by the optical method is only about 1-2 microns (as labeled on the plot), but the perpendicular 1-D resolution of the imaging ellipsometry is in the nanometer range, depending on the optical property of the substance on the surface. As shown in the lower figure, the morphology and roughness of the as-deposited MG film has sufficient contrast to the smooth surface of the Pt substrate to reveal the surface roughness of the MG film. Since detectable, the roughness therefore must be above the detection limit, say a couple of microns, over a scanned area of 400×600 microns. The roughness makes determination of the film thickness a challenge. The interdependency of density and thickness makes determination of film thickness difficult using SIE. To resolve this difficulty in determining film thickness, additional precautions and validation needs to be taken into account to derive reliable interpretation of the data.

0.5mM MG solution

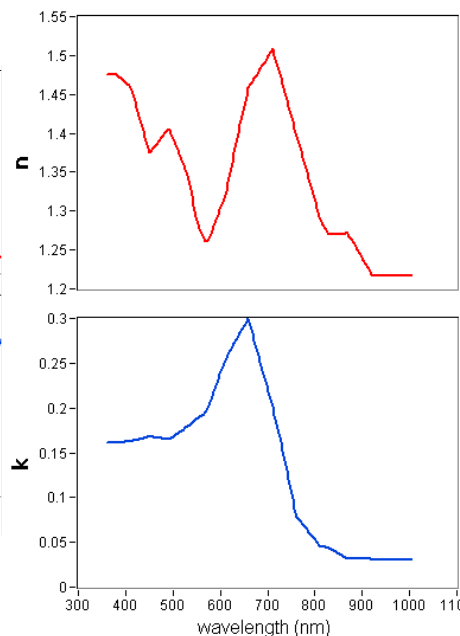


Rinse sample by
pure water after
deposition



$\lambda = 531.9 \text{ nm}$

- $n = 1.345$
- $k = 0.180$
- $t = 48.4 \text{ nm}$



$\lambda = 380.3\text{-}920.6 \text{ nm}$

Figure 1.2.0-5: Optical parameters derived from the SIE measurements to show the refractive index of the MG film deposited on the Pt substrate. The film thickness was estimated to be about 48 nm using a solution of 0.5 mM MG with 50 CV cycles of deposition.

We tried to resolve the thickness of the deposited MG film using the optical model of the SIE (Figure 1.2.0-5). Here the ellipsometric angles, Δ and Ψ , were measured using a single wavelength laser beam at 532 nm. The variations of Δ and Ψ as a function of incident beam angle were measured by the analyzer of the SIE. Although SIE is a powerful characterization technique for a variety of needs, including the monitoring of film growth and the determination of the optical properties of thin film and bulk materials, the data obtained from an SIE measurement is not useful by itself. One must first model the near-surface region of the sample and obtain the complex reflection coefficients (CRC) from the optical model. The CRCs must then be compared with the ellipsometric data, which involves some assumptions concerning the nature of the light interaction with the surface. Another problem associated with the interpretation of SIE measurements taken on thin film systems is that often the optical properties of thin-film material are quite different from those of the bulk material; moreover, these optical properties will often be a very strong function of the deposition process. A major advantage of SIE is that it is sensitive to the details of the deposition process and can therefore be used to monitor and control the process. However, this sensitivity of the optical functions means that we begin the modeling having only a rough idea of the values of the thin-film optical functions, which must then either be measured or parameterized. Since the optical properties of MG or its polymeric films are unknown in the literature, we tried to approach this issue with direct measurement of the optical properties of the deposited film. One should bear in mind that controlling the deposition conditions would be too complicated to do to yield consistent and reliable film properties. Therefore, careful repetition of the experimental conditions and reliable

reproducibility of mediator film properties are a significant part of this study, as shown below.

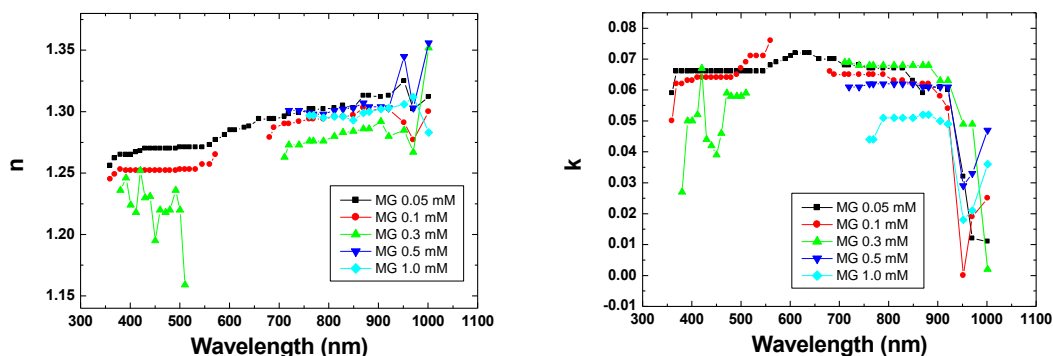


Figure 1.2.0-6. Optical properties refractive index n and extinction coefficient k for the MG solutions with different MG concentrations obtained from the SIE experiments in the liquid cell shown in Figure 1.2.0-3.

Figure 1.2.0-6 shows the CRCs derived from the optical model used in the SIE analysis, where the refractive index n and extinction coefficient k for the MG solution of different concentrations could be determined. As the MG concentration varied from 0.05 mM to 1.0 mM, the n and k did not vary in any significant manner scanning from 350 nm to >1,000 nm wavelength. The values of n varied from only about 1.25 at 400 nm to about 1.30 at 950 nm, and the extinction coefficient k stayed in the range of 0.06 – 0.07 in the same wavelength scan. Taking into account the possible experimental errors in the SIE measurements and the variations in opaqueness (i.e. affecting the degree of incident light penetration at various wavelengths) of the MG solution with different concentrations, the variations in the n and k are considered relatively small, as anticipated for liquid samples. The weak dependence of n and k values with wavelength and MG concentration makes the determination of the optical properties of the MG film easier, since we do not need to consider this dependency in a complicated manner during the fitting of the SIE data using the optical model. As shown in Figure 1.2.0-7, when MG films were deposited using the CV cycling technique and 0.5 mM MG solution, the n and k values are very different from those of the solution itself. There are distinct transitions from $n = 1.40 - 1.55$ (where $\lambda = 400-600$ nm) to $1.85 - 1.95$ (where $\lambda = 700$ nm) and then to $1.60 - 1.75$ (where $\lambda = 1,000$ nm) for the refractive index. Likewise, the extinction coefficient k has similar transitions as a function of wavelength in the same range. These wavelength dependent curves are very different from those of the solution.

The three samples of different film thicknesses at 10, 20 and 50 CV cycles also showed additional information for the optical parameters of the MG films with thickness dependence. For n , the shift from short to longer wavelengths, the depth of the incident beam penetration does affect the index value in the thicker film. Such impact is also reflected in the extinction coefficient k as a function of thickness and wavelength. These effects gave us confidence in the n and k values for the thickness calculations. One simple assumption we made is that the density of the film does not change with cycle number.

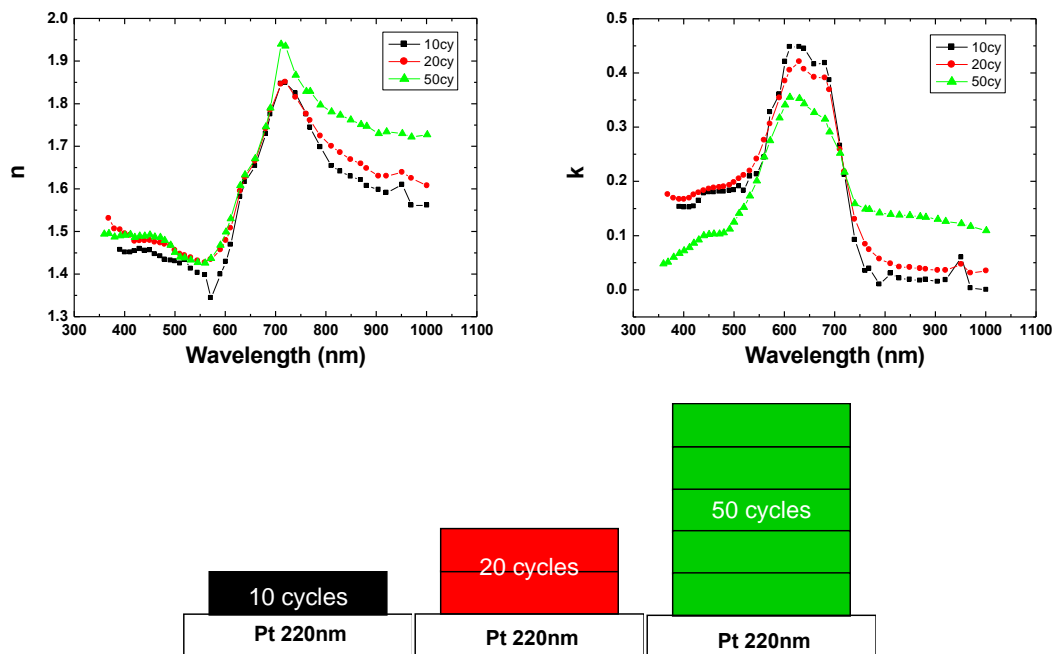


Figure 1.2.0-7: Optical properties of the MG films determined by SIE and the optical model. As the film thickness increased, the refractive index and extinction coefficient changed as a function of CV cycle number.

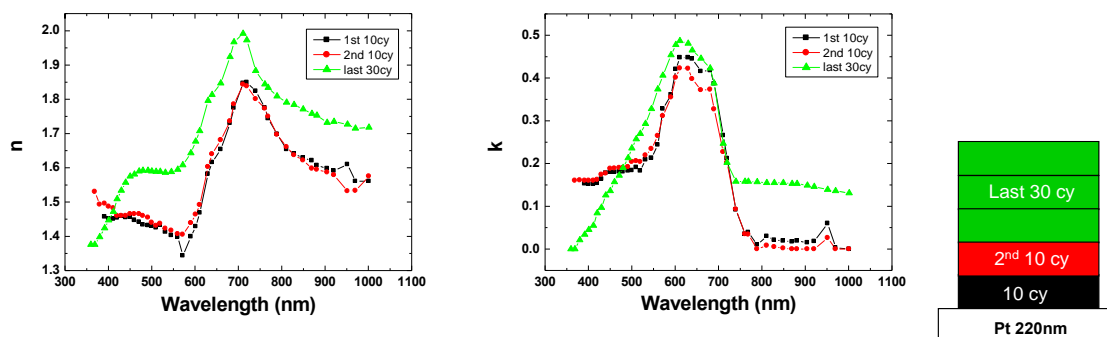


Figure 1.2.0-8: Optical properties of an MG film determined by SIE and the optical model as the film thickness was measured progressively at the end of the first 10 cycles, the second 10 cycles, and the last 30 cycles.

In the analysis summarized in Figure 1.2.0-7, the entire film at different stages of the deposition was considered a homogeneous body in the optical model simulation. So, the optical properties, i.e. the n and k values of the film, were derived for the entire film as the thickness varied in the CV cycles. In contrast, in Figure 1.2.0-8, the experiments and the data analysis were conducted differently. Here, a series of SIE measurements and optical model simulations were performed on the same sample, as an MG film was progressively deposited. The SIE measurements and

optical model simulations were made at the end of the first 10 cycles, the second 10 cycles and the last 30 cycles, as shown in Figure 1.2.0-8. In these experiments, the newly deposited film was considered a different layer of materials from the prior one. Therefore in the optical model, the new layer was simulated on top of the old ones. In other words, different from those in Figure 1.2.0-7, those curves in Figure 1.2.0-8 were derived by subtracting the background optical signals from the prior cycles in the simulation. This approach and illustration provide an interesting way for validation. First, interestingly, the n and k versus wavelength curves are almost identical between the first two sets of 10 cycles; i.e. in the first 20 cycles, the same n and k values and properties were reproduced. This result validated that when the thickness is relatively thin (on the order of 10 nm) in the first two 10 cycles, the measured optical properties of such thin films were quite reproducible, implying that the density of the film was also consistent within experimental errors. However, as the thickness increased, the curves for the next 30 cycles are different from the first two 10 cycles. The exact reason for such a disparity is still under investigation. There is no indication that the density of the film changed. Thus, thicker films might have less intensity of the incident light to allow accurate fitting of the optical properties of the films through model simulation.

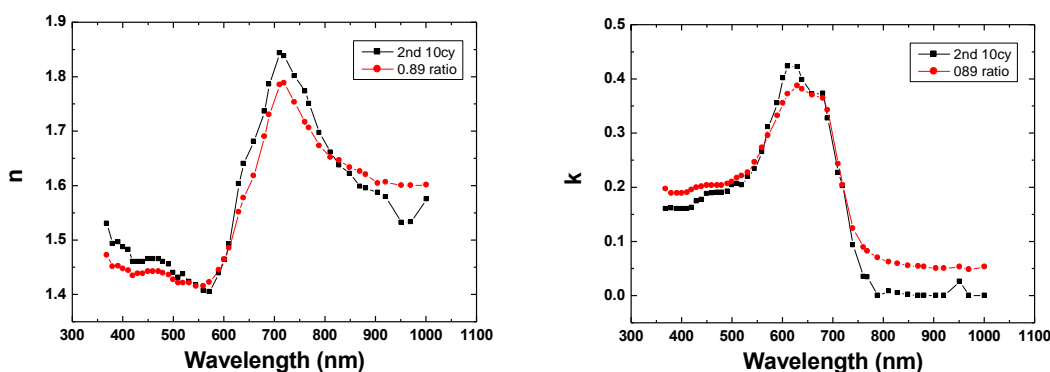


Figure 1.2.0-9: Simulation of variations in density and impacts on the optical properties.

To test this assumption we conducted some additional simulations as shown in Figure 1.2.0-9. In this simulation, the n and k properties were estimated assuming a variation in porosity, simulating a change in the density of the film. In the optical model simulation, the matrix of the film was assumed to have 11% porosity, thus comprising 89% dense MG and 11% MG solution. The simplest way to emulate the CRCs of this matrix would be assuming a dense, thinner MG film with the n and k values of the first 10 cycles of deposition (as shown in Figure 1.2.0-7) and the corresponding values of the MG solution (in Figure 1.2.0-6). This approach would avoid the complex calculation of the CMCs directly from the porous matrix of the same formulation. The results showed complicated impacts on the n and k properties and comparisons of the results with those derived in Figure 1.2.0-8. Such comparisons need additional work to quantify and validate why such differences exist or if the differences are artifacts. For example, in a study with three different types of MG samples: as deposited MG film (poly-MG), 0.5 mM MG solution in contact with the Pt, and a thin liquid MG film sprayed on the Pt surface; the n and k curves showed noticeable differences among the three in the wavelength scans (Figure 1.2.0-10). What caused such variations in optical properties is not fully understood yet. But, it is clear that the

dispersion of MG in condensed polymerized film, dispersed in liquid droplets, and in bulk solution, may have different chemical forms, compositions, and concentration distributions in the matrices (as interpreted from the evidence illustrated in Figure 1.2.0-10). It remains as a challenge to quantify such effects and their influences on optical properties.

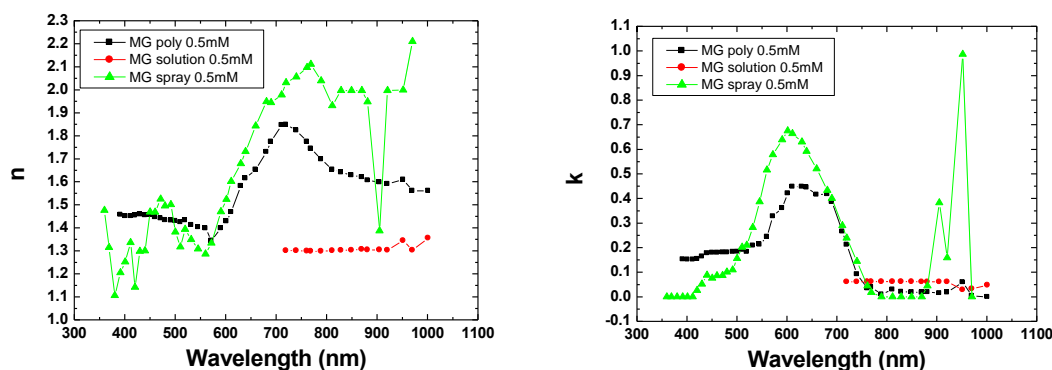


Figure 1.2.0-10: Comparison of the optical properties of the Pt surface with three different matrices of MG materials: poly-MG film, MG solution of 0.5 mM, and a liquid film of spray of the same solution.

In summary, as mediators play a critical role in the charge transfer process during biofuel cell operation, the important questions to be answered are the concentration and its distribution, the chemical formula of the mediator on the surface of the electrode where the charge transfer takes place, and the method used in preparing the proper form of mediator to facilitate such a charge transfer with better efficiency and durability. Thus, the *in situ, operando* investigation of mediator interactions with the electrode surfaces remains of interest in developing a full understanding of the charge transfer phenomenon and behavior. We have demonstrated some unique capabilities of using the SIE and electrochemical techniques to study such processes and resulting properties.

TASK 2. TECHNOLOGY FOR SYNTHETIC FUELS PRODUCTION

Biofuel products start from a variety of primary sources of plant or animal material to produce four main intermediate products; oil, starch, sugar, and/or fiber. These intermediate products are in turn converted to fuels, chemicals, biomaterials, or power depending on the intended use. The primary sources of biomass material have the potential to impact the end product and are likely to depend not only on the plant species but also the location of crop production, the conversion method employed, and its history between point of production and point of use. For the Navy application there is particular interest in liquid biofuels that can be introduced into the current supply chain. However, the introduction of biofuels with varying properties into systems developed for fossil fuels can present additional operational challenges. Biofuels are likely to be delivered as neat fuels by the supplier and can be consumed in this form or in blends with

petroleum products. Acceptance testing and monitoring of fuel quality through the supply chain – from storage to blending to use are important. This task seeks to identify and address issues related to fuel variability caused by primary feedstock sources, conversion methods, storage methods, or the presence of contaminants.

2.1 Biofuel Characterization Planning

As the Navy moves toward greater use of alternative fuels blended with petroleum F76 diesel and JP5 jet fuel, there is imminent need to understand how these blends will compare with conventional petroleum products. Two general areas of comparison are of interest, (1) the combustion characteristics and (2) the broader area termed “fit-for-purpose.” This latter group includes compatibility with materials commonly found in fuel tanks and piping, compatibility with elastomer seals (o-rings) used in engines and fuel delivery equipment, and susceptibility of the fuel blends to maintain levels of microbial and corrosion activity comparable to, or lower than, petroleum fuels in current use.

Under a previous award, HNEI conducted an assessment of a variety of biofuel components that could support Navy operations in tropical island settings, including primary sources of potential supply for identified biofuel components, critical material quality monitoring points along the supply chain, appropriate tests for each of these critical monitoring points, and equipment, personnel, and lab facilities and associated costs that would be required to conduct testing. Under the proposed activities for this subtask, high priority, critical testing capabilities identified in the previous phase, including equipment, personnel, and lab facilities, will be developed and interfaced with the supply chain.

Previous phases of this task identified the methods in Tables 2.1.1 as those needed to conduct fuel quality testing. This list was down-selected in this phase to focus on storage stability test capabilities. For fuel stability tests, the most widely accepted methods in US are Active Oxygen Method ASTM D4625, ASTM D2274, and ASTM D5304. Standard test method ASTM D4625 is the most widely used test method for assessing the storage stability of middle distillate petroleum fuels [1-4], and distilled and undistilled biodiesels [5-11]. In this method, the fuel is stored at 43°C for selected periods up to 24 weeks, and 1 week of storage is roughly equivalent to a month of storage at normal (environmental) ambient temperatures, 21°C. Typically, samples are analyzed to determine the amount of filterable and adherent insolubles formed every 4 or 6 weeks. Standard test method ASTM D5304 is also developed to study middle distillate fuel [12] storage stability under elevated temperature and pressure conditions, 90°C and 800 kPa, with pure oxygen, and the 16 hour test yields approximately the same amount of insolubles as 20°C storage for 27 months under atmospheric air pressure. This method has also been employed as ASTM D4625 method to study the storage stability of biodiesels. [13-15] Standard test method ASTM D2274 requires even higher temperature, 95°C, and more oxygen exposure, 3L/h, compared to the ASTM D4625, and is originally developed to investigate the oxidation stability of distillate fuel oil [1-3]. Although it hasn't yet been validated for biodiesel, results of this method have been reported for biodiesel and its blends [7-11, 16].

To further plan for conducting these tests, the lab equipment and lab space requirements were assessed. Vendors were identified for the major pieces of equipment and lab infrastructure deemed necessary to support equipment operations was assessed.

Table 2.1.1 Summary of special equipment requirements for fuel quality research program needs.

| ASTM ID No. | Required Equipment |
|-------------|--|
| D93 | Pensky-Martens closed cup flash test apparatus |
| D130 | Copper strip corrosion pressure vessel |
| D445 | Viscometer |
| D1160 | Vacuum distillation apparatus |
| D1298 | Hydrometer |
| D1401 | Water separability test station |
| D1500 | Fuel Color Comparator |
| D2500 | Cloud Point Analyzer |
| D4294 | Energy dispersive X-ray fluorescence analyzer |
| D5304 | Storage stability testing apparatus |
| D5453 | Sulfur by UV-fluorescence analyzer |
| D6079 | High-frequency reciprocating rig apparatus |

References

1. Marshman, S. J. In *A rapid colorimetric method for predicting the storage stability of middle distillate fuels*, 1995; National Technical Information Service: 1995; pp 377-89.
2. Waynick, J. A.; Taskila, S. M. In *A comparison of low and high sulfur middle distillate fuels in the United States*, 1995; National Technical Information Service: 1995; pp 697-723.
3. White, E. W. In *A bit of history - the development of storage stability tests for middle distillate fuels since World War II*, 1998; National Technical Information Service: 1998; pp 717-730.
4. Muzikova, Z.; Prochaska, F.; Pospisil, M., Storage stability of FCC light cycle oil. *Fuel* 2010, 89, (11), 3534-3539.
5. Obadiah, A.; Kannan, R.; Ramasubbu, A.; Kumar, S. V., Studies on the effect of antioxidants on the long-term storage and oxidation stability of Pongamia pinnata (L.) Pierre biodiesel. *Fuel Process Technol* 2012, 99, 56-63.
6. Bondioli, P.; Gasparoli, A.; della Bella, L.; Tagliabue, S.; Lacoste, F.; Lagardere, L., The prediction of biodiesel storage stability. Proposal for a quick test. *Eur J Lipid Sci Tech* 2004, 106, (12), 822-830.
7. Bondioli, P.; Gasparoli, A.; Della Bella, L.; Tagliabue, S., Evaluation of biodiesel storage stability using reference methods. *Eur J Lipid Sci Tech* 2002, 104, (12), 777-784.
8. Westbrook, S. R.; Stavinocha, L. L. In *Biodiesel and B20 blends: stability test methods and stability characteristics*, 2003; International Association for Stability, Handling and Use of Liquid Fuels: 2003; pp 271-298.
9. Waynick, J. A. In *Evaluation of the stability, lubricity, and cold flow properties of biodiesel fuel*, 1998; National Technical Information Service: 1998; pp 805-829.

10. McCormick, R. L.; Westbrook, S. R., Storage Stability of Biodiesel and Biodiesel Blends. *Energ Fuel* 2010, 24, 690-698.
11. Dinkov, R.; Hristov, G.; Stratiev, D.; Aldayri, V. B., Effect of commercially available antioxidants over biodiesel/diesel blends stability. *Fuel* 2009, 88, (4), 732-737.
12. Aksoy, P.; Gul, O.; Cetiner, R.; Fonseca, D. A.; Sobkowiak, M.; Falcone-Miller, S.; Miller, B. G.; Beaver, B., Insight into the Mechanisms of Middle Distillate Fuel Oxidative Degradation. Part 2: On the Relationship between Jet Fuel Thermal Oxidative Deposit, Soluble Macromolecular Oxidatively Reactive Species, and Smoke Point. *Energ Fuel* 2009, 23, 2047-2051.
13. Mushrush, G. W.; Willauer, H. D.; Wynne, J. H.; Lloyd, C. T.; Bauserman, J. W., Storage Tank Stability of Soybean-derived Biodiesel. *Energ Source Part A* 2011, 33, (24), 2303-2308.
14. Mushrush, G. W.; Beal, E. J.; Hughes, J. M.; Wynne, J. H.; Sakran, J. V.; Hardy, D. R., Biodiesel fuels: Use of soy oil as a blending stock for middle distillate petroleum fuels. *Ind Eng Chem Res* 2000, 39, (10), 3945-3948.
15. Hilten, R. N.; Das, K. C., Comparison of three accelerated aging procedures to assess bio-oil stability. *Fuel* 2010, 89, (10), 2741-2749.
16. McCormick, R. L.; Ratcliff, M.; Moens, L.; Lawrence, R., Several factors affecting the stability of biodiesel in standard accelerated tests. *Fuel Process. Technol.* 2007, 88, (7), 651-657.

2.2 Plasma Arc Processing

Recently, the alternative energy sector has experienced rapid growth because of increasing pressure from climate change awareness, rising fuel costs, and a need for domestic energy security [1, 2]. New technologies have focused on producing energy that is accessible, environmental friendly, sustainable, secure, and can meet current and future projected energy needs [3]. Hydrogen is expected to play a large role in the energy economy of the future as it can be utilized in fuel cell applications, and in the synthesis of alternative fuels [1, 3, 4]. This work explored the use of a non-thermal reverse vortex flow (RVF) gliding-arc reformer for liquid fuels. Tests were conducted using dodecane as a model diesel compound and hydroprocessed renewable diesel fuel. Parametric tests determined the effects of various system parameters, while factorial tests were utilized for system optimization.

Hydrogen is expected to be a prominent fuel in the future [1, 3, 4]. However current production methods are expensive, require complex and large machinery or costly catalysts, and require an expensive distribution infrastructure [1, 3, 5]. Steam, partial oxidation, and autothermal reforming constitute the major reforming technologies [2, 3]. Hydrogen production via steam reforming of natural gas utilizes roughly one third of the fuel to support the parasitic energy requirement of the process. Ultimately this leads to an specific energy requirement (SER) of 325 to 354 kJ mol⁻¹ of hydrogen produced [6, 7].

Since the late 90's, interest in plasma reforming has grown [8]. Plasma reformers can operate in thermal equilibrium or non-thermal equilibrium. Thermal plasma reformers operate at high temperatures (5,000 – 10,000 K) [9], require power inputs of 1 kW to 50 MW [9, 10], require

extensive measures to prevent electrode wear [9], and are most commonly used for metallurgical applications [11].

Non-thermal reformers can utilize various plasma forms such as glow discharge, corona discharge, silent discharge, dielectric barrier discharge, gliding arc, etc. Non-thermal plasma can operate near room temperature, at lower power inputs than thermal plasmas, and at or near atmospheric pressure [10]. They commonly have a much smaller physical foot print than traditional reforming technologies and can be used in onboard applications [12], all while maintaining high energy densities required for hydrocarbon reforming [13]. Within a non-thermal plasma, electrons exist at high temperatures, ranging from 10,000 to 100,000 K [2], while the protons and neutrons remain near room temperature [10, 13]. Intermediate, ‘warm’ plasmas, however, with gas temperatures ranging from 2,000 to 4,000 K can also be utilized for controlled gas reforming [11]. Petitpas et al. produced an extensive comparison of plasma technologies highlighting various reformer efficiencies, fuel conversion rates, and energy requirements [2]. Gutsol et. al.’s review of reforming technologies concluded that hydrogen must be produced for less than 109 kJ mol⁻¹ [6] to be economically feasible. Many technologies are approaching this point [2].

Previous work explored parameters affecting the performance and optimization of non-thermal, reverse vortex flow, stabilized gliding-arc plasma reforming of methane [14]. Under this subtask, the performance and optimization of the same system adapted for the reforming of selected liquid fuels. Liquid fuels can be distributed via existing fuel infrastructure and then reformed to produce hydrogen on site.

The two fuels of particular interest for ship board applications are marine diesel (F-76) and hydroprocessed renewable diesel (HRD-76). Dodecane was chosen as a model liquid diesel compound in the development of a liquid fuel injection system. HRD-76 was the primary biofuel used in the recent Great Green Fleet exercises [15]. Reforming F-76, HRD-76, or their blends, could allow the Navy to transport a liquid fuel that could be reformed into hydrogen rich gas for shipboard applications.

Materials and Methods: Figure 2.2.0-1 shows the test bed for RVF non-thermal, gliding-arc plasma reforming of liquid fuels. The system used for methane reforming previously described [14] was modified to accommodate liquid fuels. Changes to the three major component groups, reactant delivery, reformer and power supply, and product conditioning, are highlighted below. A piston pump (SmoothFlow Pump 100 (LF), Microfluidica, Glendale, WI) provided precise fuel flow control to a nozzle injection system. The fuel is atomized upon injection at the top of the reaction chamber by an ultrasonic nozzle system powered by a digital signal generator (model HT40K50T, Sonaer Ultrasonics, Farmingdale, NY). The system atomized liquid fuel into 25 µm diameter droplets using 1.15 to 2.25 W power input over a range of fuel flow rates from 0.44 to 1.65 ml min⁻¹. Droplet sizes were measured using a phase-Doppler particle sizing system (Aerometrics, Sunnyvale, CA). Increasing power to the nozzle tip decreased the mean droplet diameter while increasing axial and radial droplet velocity, and resulted in liquid accumulation on the reactor walls and/or excessive unreacted fuel directly exiting the reactor. Particles with 25 µm diameter were entrained within the interior vortex of the reverse vortex flow, and were transported along the flow lines through the plasma arc.

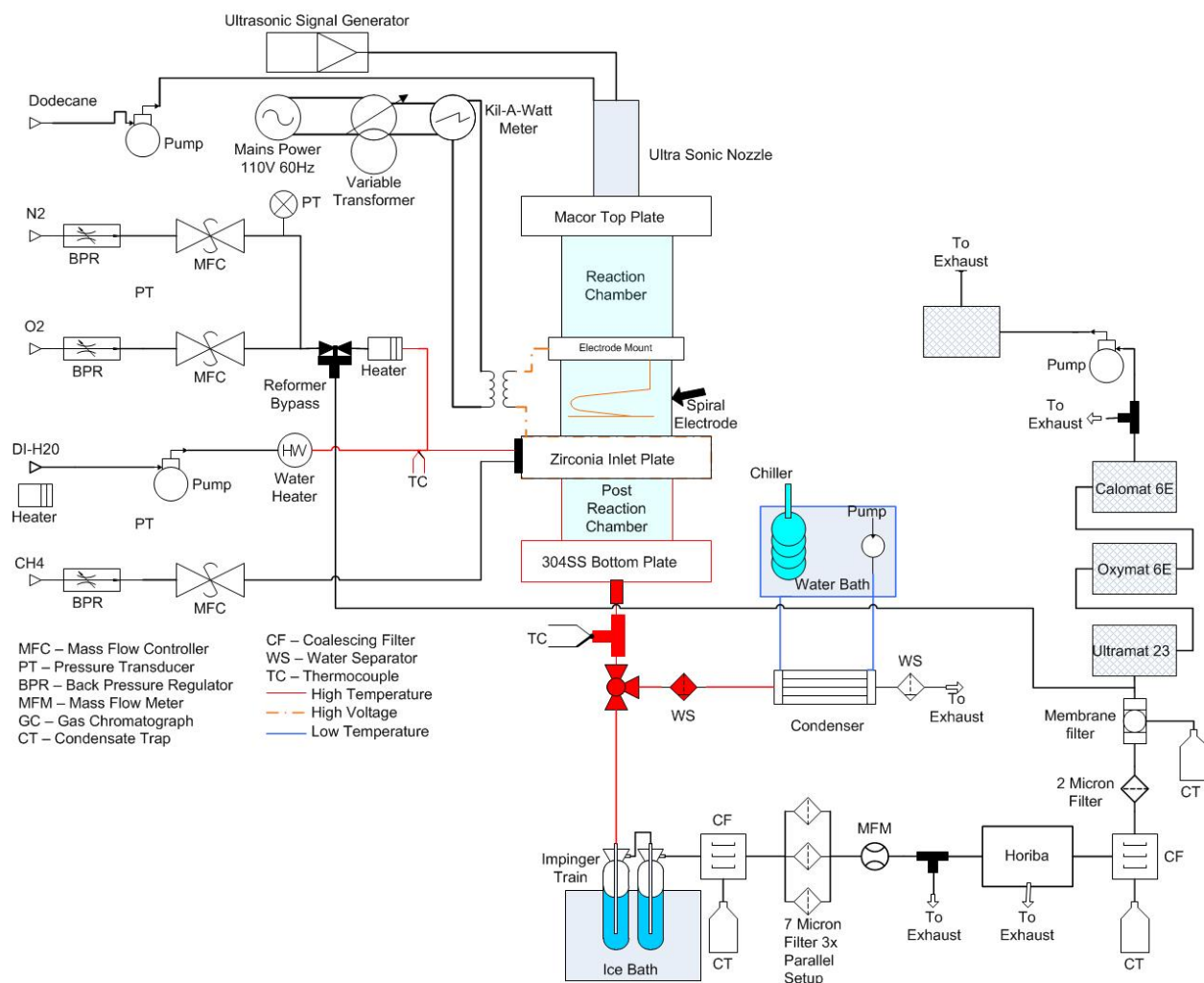


Figure 2.2.0-1 - RVF non-thermal plasma reformer for liquid fuels test bed diagram

The power supply for the reactor underwent minor changes when the reformer was adapted for use with liquid fuels. The only change to the power supply section was the substitution of an updated variable transformer (Model 3PN1510B-DVAM, ISE, Inc., Cleveland, OH).

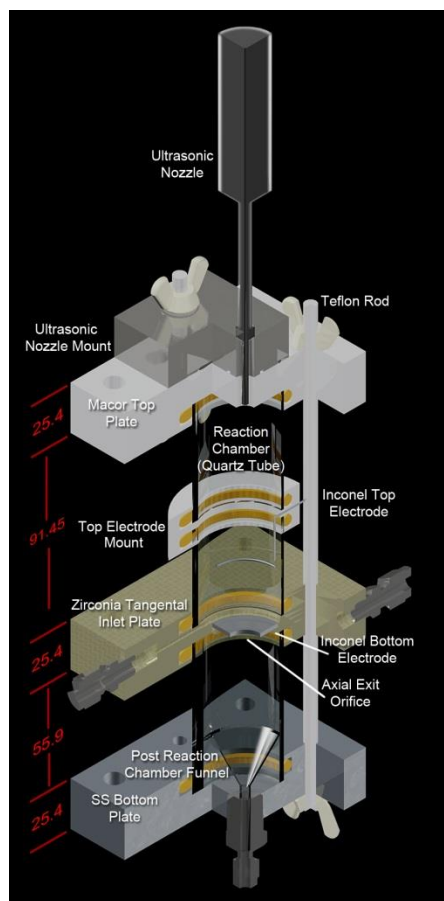


Figure 2.2.0-2 - Non-thermal gliding arc plasma RVC reformer (42 mm internal diameter) for liquid fuels, dimension in mm.

Figure 2.2.0-2 shows the updated reformer, modified for the introduction of liquid fuels into the reaction chamber. A non-conducting, top electrode mount made from zirconia ceramic (AmZirOx 86, Astro Met Zirconium Oxide, Cincinnati, OH) electrically insulated the ultrasonic nozzle from the upper electrode. AmZirOx 86 zirconia ceramic was chosen due to its electrical resistivity, low thermal expansion, and chemical inertness. Removing the upper electrode mount from the Macor top plate allowed radial insertion of the upper electrode into the reaction chamber. The 42 mm ID quartz tube reactor body is sealed at all mounting points with silicone O-rings.

The stainless steel tangential inlet plate used in the earlier study was replaced by one made of zirconia (AmZirOx 86, Astro Met Zirconium Oxide, Cincinnati, OH) to avoid electrical discharge between it and the top electrode. The bottom electrode lead was inserted through a pilot hole on the side of the plate (not shown in Figure 2.2.2) and made radial contact with the Inconel bottom electrode. All gas ports were 316 stainless steel Swagelok fittings inserted into the ceramic with pipe thread connections.

The ultrasonic nozzle was attached to an aluminum mounting plate fixed to the Macor™ top plate with PTFE threaded rods and sealed with a Kalrez® o-ring.

A funnel shape was added to the bottom of the quartz post reaction chamber to drain any unreformed liquids out of the reactor. A high temperature three-way valve (model MPT100-SS-T-SSS-N-15, Control Resources, Salisbury NC) at the reactor exit directed the product stream into the reformat conditioning and analysis section or into a bypass to exhaust during non-steady state periods. This allowed the system to come to steady state without contaminating the impinger train used for liquid analysis.

The gas phase analysis section of the test bed remained unchanged. The reformat conditioning system was modified to accommodate liquid fuels. Unreformed liquid fuel and liquid byproducts were condensed, trapped, and removed from the reformat stream exiting the reactor. Following the post reaction chamber and the bypass valve, the product stream flowed into a set of four, 500 ml stainless steel impingers in series (SN-5C set, Apex Instruments, Apex, NC). The first three contained 100 ml of isopropyl alcohol (A416 2-Propanol Certified ACS Plus, Fisher Scientific, Hanover Park, IL) and the fourth impinger was left empty. Upon exiting the impinger train, the gaseous reformat passed through a coalescing filter (Model 31G, Balston, Haverhill, MA) to remove any remaining aerosol or particulate matter.

For each operating condition the system was allowed to come to steady state with the reformat bypassing the analysis section. Once steady state was reached, reformat was directed through the analysis section for 40 minutes. The reformat stream was analyzed for CH₄, CO, CO₂ (Ultramat 23, Siemens, Washington, D.C.), O₂ (Oxymat 6E, Siemens, Washington, D.C.), and H₂ (Calomat 6E, Siemens, Washington, D.C.) by three on-line gas analyzers. Reformat was analyzed every ten minutes by an on-line gas chromatograph (GC) (Model 14A, Shimadzu, Columbia, MD) equipped with a 1.52 m x 3 mm Carbonex™ 1000 column (SUPELCO, Bellefonte, PA) and a thermal conductivity detector in accordance with ASTM D1946-90 [16]. After a 40 minute sampling period the flow was diverted to the bypass and exhaust. The impinger train could be removed and replaced prior to characterizing a different reactor operating point.

The final mass and volume of liquid recovered from the impingers was recorded and a sample of the liquid stored for later analysis using a GC (Autosystem GC, Perkin Elmer, Waltham, MA) equipped with a 60 meter capillary column (Rtx-1, 60m-0.53-7μm, Restek Corporation, Bellefonte, PA) and a flame ionization detector.

Dodecane and HRD-76 were used to test the liquid reforming performance of the reactor. Dodecane (99.9% purity, Arcos Organics No. 117595000, Fisher Scientific, Hanover Park, IL) was chosen as a model compound for diesel [17, 18]. Parametric tests with dodecane were conducted to determine the effects of system parameters. Factorial tests were used to approach optimal operating conditions for dodecane and HRD-76.

HRD-76 was provided by the Naval Fuels and Lubricants Cross Functional Team. It was shipped with a bulk composition by mass of 84.63% carbon and 15.37% hydrogen, and a density of 0.781 g ml⁻¹. Figure 2.2.0-3 shows the GC mass spectrometry (MS) analysis of HRD with the y-axis truncated. 3% of the peak area is octane, but the large majority of the fuel's components fall between pentadecane and octadecane. Heptadecane composes 24% of the peak area, and octadecane 18%. Gowdagiri et.al report that HRD-76 has an equivalent hydrocarbon formula of C_{15.4}H_{32.7} [19] and molecular weight of 218 g mol⁻¹, which corresponds well with the GCMS

data. Higher heating value was measured with an adiabatic bomb calorimeter (Model 6200, Parr Instruments, Moline, IL) and found to be $46.7 \pm 0.3 \text{ MJ kg}^{-1}$ (95% confidence interval), with a calculated lower heating value of 43.40 MJ kg^{-1} .

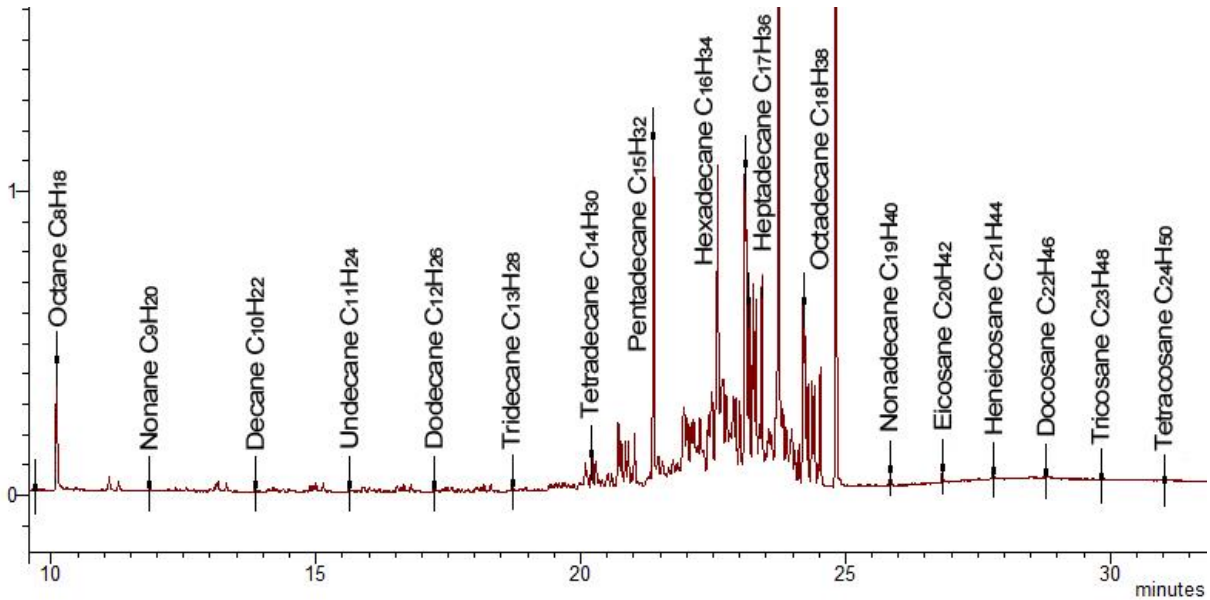


Figure 2.2.0-3 - GCMS chromatograph of HRD components

Dodecane input was varied from 0.44 ml min^{-1} to 1.32 ml min^{-1} , corresponding to equivalence ratios of 0.70 to 0.26. Subsequent HRD test conditions were based on dodecane test equivalence ratios. The equivalence ratio is defined as the oxygen to fuel ratio of the reaction divided by the stoichiometric oxygen to fuel ratio (Equation 2.2.1) where \dot{n} is the species molar flow rate.

$$\text{Equivalence Ratio} = \frac{\left(\frac{\dot{n}_{O_2}}{\dot{n}_{fuel}} \right)_{\text{Reaction}}}{\left(\frac{\dot{n}_{O_2}}{\dot{n}_{fuel}} \right)_{\text{Stoich.}}} \quad (2.2.1)$$

Parametric tests on dodecane investigated the system response while altering one independent variable at a time. Equivalence ratio, power input, and steam to carbon ratio were investigated. Initial set points and their range for the parametric tests are presented in

Table 2.2.1.

Table 2.2.1 - Independent variables, initial conditions, and value ranges for parametric tests.

| Parameter | Initial Set Point | Parametric Range of Values |
|----------------------------|---------------------------|-----------------------------------|
| Reactor Length | 112.4 mm | fixed |
| Reactor Diameter | 40 mm | fixed |
| Axial Exit Diameter | 12.7 mm | fixed |
| Electrode Gap | 35 mm | fixed |
| Nitrogen Flow | 2 slpm | fixed |
| Oxygen Flow | 0.56 slpm | fixed |
| Dodecane Flow | 0.66 ml min ⁻¹ | 0.44 to 1.32 ml min ⁻¹ |
| Equivalence Ratio | 0.47 | 0.70 to 0.23 |
| Steam Input | 0.6 g min ⁻¹ | 0.1 to 0.6 g min ⁻¹ |
| Steam : Carbon Molar Ratio | 0.96 | 0.16 to 0.96 |
| Power Input | 180 W | 140 to 250 W |

A 2³ factorial experimental design (8 points per test) was used to optimize dodecane reforming using SER (see definition in Equation (2.2.2)) as the performance variable, i.e. identifying the minimum SER operating point of the process. The SER definition in Equation (2.2.2) is based on the assumption that CO in the product gas can be used to produce additional H₂ using the water gas shift reaction. The input power is measured in kW, and \dot{n} is the molar flow rate in mol s⁻¹.

$$SER = \frac{\text{Input Plasma Power}}{(\dot{n}_{CO} + \dot{n}_{H_2})_{produced}} \quad (\text{kJ mol}^{-1}\text{H}_2 \text{ produced}) \quad (2.2.2)$$

High and low values of operating parameters were selected using the results from the parametric tests as a center point (Table 2.2.2). The factorial tests also identified system operating limits and higher order interaction effects between the independent variables. The order of individual test points was randomized and data at each test point were collected four times to provide an average value and estimate error. Reported error and error bars on charts reflect a 95% confidence interval.

Based on the optimal operating conditions for dodecane a 2² factorial test investigated HRD-76 reforming while minimizing SER. For the HRD factorial treatments, power input was held constant at the maximum value identified from the dodecane factorial tests. The operating values are summarized in Table 2.2.2.

Table 2.2.2 - Center points and step sizes for dodecane and HRD-76 factorial tests

| | 1st Dodecane Factorial Test | | 2nd Dodecane Factorial Test | | HRD-76 Factorial Test | |
|-------------|-----------------------------|---------------------------|-----------------------------|---------------------------|---------------------------|---------------------------|
| Parameter | Center Pt. | Step Size | Center Pt. | Step Size | Center Pt. | Step Size |
| Fuel Input | 0.66 ml min ⁻¹ | 0.11 ml min ⁻¹ | 1.32 ml min ⁻¹ | 0.11 ml min ⁻¹ | 1.27 ml min ⁻¹ | 0.11 ml min ⁻¹ |
| Steam Input | 0.4 g min ⁻¹ | 0.1 g min ⁻¹ | 1.1 g min ⁻¹ | 0.1 g min ⁻¹ | 1.1 g min ⁻¹ | 0.1 g min ⁻¹ |
| Power Input | 220 W | 20 W | 240 W | 20 W | 260 W | NA |

Calculation of performance indicators from experimental data conformed to those used by Petitpas et al. [2]. System performance for dodecane parametric tests and factorial tests were characterized by hydrogen yield, fuel conversion, hydrogen selectivity, efficiency, and specific energy requirements. Differentiating reaction products from original fuel components in HRD was not possible, as higher hydrocarbons present in the fuel could react to form smaller molecules also present in the original fuel, eg. octadecane reformed to heptadecane. Therefore system performance indicators for HRD omitted fuel conversion and selectivity.

Hydrogen yield is defined by the number of hydrogen atoms in hydrogen gas in the reformat divided by the total amount of hydrogen atoms in the reactant fuel (Equation 2.2.3) [2].

$$\text{Hydrogen Yield} = \frac{\text{Hydrogen Atoms in } H_2 \text{ in reformat}}{\text{Hydrogen Atoms in Feed Fuel}} (\%) \quad (2.2.3)$$

Fuel conversion is defined as the amount of fuel converted in the reactor divided by the total fuel input to the system (Equation 2.2.4).

$$\text{Dodecane Conversion} = \frac{\dot{n}_{\text{dodecane in fuel}} - \dot{n}_{\text{dodecane in reformat}}}{\dot{n}_{\text{dodecane in fuel}}} * 100 (\%) \quad (2.2.4)$$

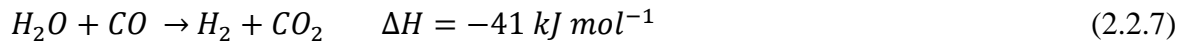
Selectivity is defined as the hydrogen yield divided by the fuel conversion as shown in Equation 2.2.5. This provides an index of the system's ability to reform the fuel into hydrogen with the assumption that unreformed fuel could be recovered, utilized by other processes, or reintroduced into the reformer.

$$\text{Selectivity} = \frac{\text{moles of } H_2 \text{ produced}}{13(\text{moles of dodecane converted})} * 100 (\%) \quad (2.2.5)$$

Efficiency is defined in Equation 2.2.6 as the amount of hydrogen energy in the reformat divided by the total system energy input from both the plasma and reactant fuel [2].

$$\text{Efficiency } \eta = \frac{LHV_{H_2 \text{ gas}} * (\dot{m}_{H_2} + \dot{m}_{CO})_{\text{reformat}}}{\text{Plasma Power} + LHV_{\text{fuel input}} * \dot{m}_{\text{fuel input}}} \quad (2.2.6)$$

LHV is the lower heating value (MJ kg^{-1}) and \dot{m} is the mass flow rate of a given species. The efficiency definition assumes, according to convention [2, 21], that any CO present in the reformat could be converted to H_2 by the exothermic water gas shift reaction (Equation 2.2.7) [22].



Results and Discussion: Results from the parametric and factorial tests of dodecane and HRD-76 are summarized below.

Dodecane testing: Power input was varied parametrically from 120 to 225 W in nominal 20 W increments. The highest point was 225 W instead of 220 due to the sensitivity of power input controls. Below 120 W, a continuous arc could not be maintained.

Parametrically increasing power input had very little effect on hydrogen yield, hydrogen selectivity, fuel conversion, and efficiency as seen in Figure 2.2.0-4. As the power increased the fuel conversion remained relatively constant at ~90%. Gains in hydrogen yield, which rose from 32.1 to 35.73%, and selectivity, which rose from 35.7 to 42.6%, were realized. Increases in H₂ and CO yields maintained efficiency at near constant values of ~19% across all power input levels. At 120 W power input, the plasma power corresponded to 23% of the total energy input (plasma plus fuel), increasing to 37% at 225W. The increasing power input to the system yielded increasing specific energy requirements, ranging from 319.9 to 486.0 kJ mol⁻¹ of H₂ produced. Therefore the lower the plasma power input to the system the better the reformer performed as measured by SER.

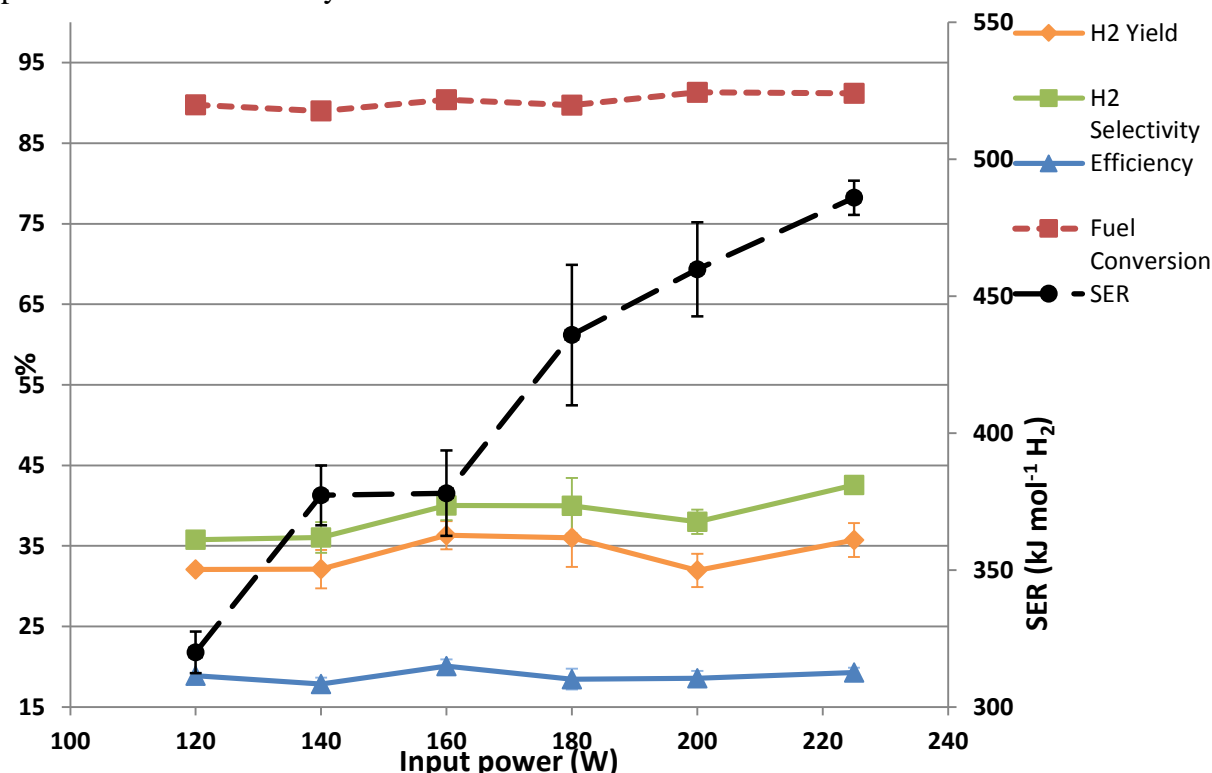


Figure 2.2.0-4 - Dodecane parametric test results for power input. Error bars indicate 95% confidence interval. Error bars that are not visible are equal in size to the data point symbol.

The fuel input tests effectively decreased the equivalence ratio by increasing the fuel input (Equation 2.2.1). Soot formation occurred when the equivalence ratio decreased below 0.25.

Figure 2.2.0-5 shows fuel conversion remained constant at ~95% while the equivalence ratio decreased. As the fuel input increased the hydrogen yield and selectivity both increased from 34 to 47% and 36 to 49% respectively. At 0.29 equivalence ratio, both the hydrogen yield and selectivity were slightly higher than at 0.25 equivalence ratio. Over the equivalence ratio test range, the efficiency varied from 13 to 30.3% with the latter value measured at equivalence ratio of 0.29. This is strongly due to the large increase of H₂ and CO production. At an equivalence ratio of 0.29 and efficiency of 33.2%, the reformate contains H₂ (17.0%) and CO (16.2%). A significant rise in SER resulted from increasing fuel input while the fuel conversion percentage remained constant. The SER of 763 kJ mol⁻¹ of H₂ produced at an equivalence ratio of 0.71 decreases to 184 kJ mol⁻¹ at 0.25. However these gains have diminishing returns and approach a lower limit as the equivalence ratio drops below 0.30.

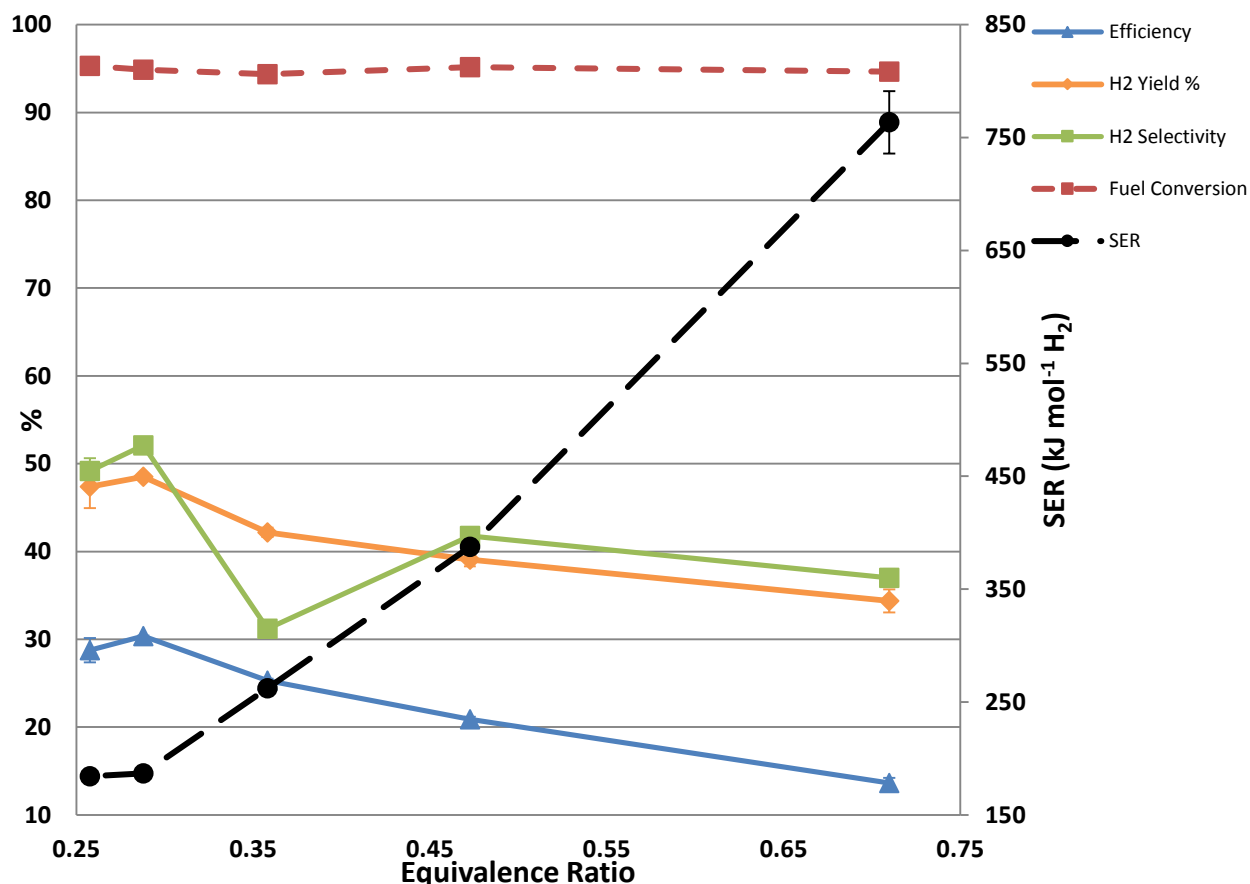


Figure 2.2.0-5 – Dodecane parametric test results for equivalence ratio. Error bars indicate 95% confidence interval. Error bars that are not visible are equal in size to the data point symbol.

Steam input helps prevent soot formation within the reactor, however the excess water molecules absorb energy introduced to the system [23]. Steam input to the system was varied from 0.1 to 0.6 g min⁻¹ corresponding to a steam:carbon molar ratios of 0.16 to 0.96, respectively.

Figure 2.2.0-6 shows the effects of increasing steam input to the reformer. The increase in steam does little to change the fuel conversion, which remains near 94%, and efficiency, which remains around 17%. Slight gains are realized in hydrogen yield and hydrogen selectivity as the steam input increases. Hydrogen yield increases 18% (relative) from 28.3 to 33.5%, while selectivity increases by 14% (relative) from 31.2 to 36.4%. Gains realized over this low range of steam input indicate that steam was a limiting reactant in some H₂ producing reactions. Further increases in steam input dilute the plasma power with negative results [14]. These gains are reflected in the SER which decreased from 493 to 434 kJ mol⁻¹ of H₂ produced. The effect of steam input was further investigated in the factorial treatments.

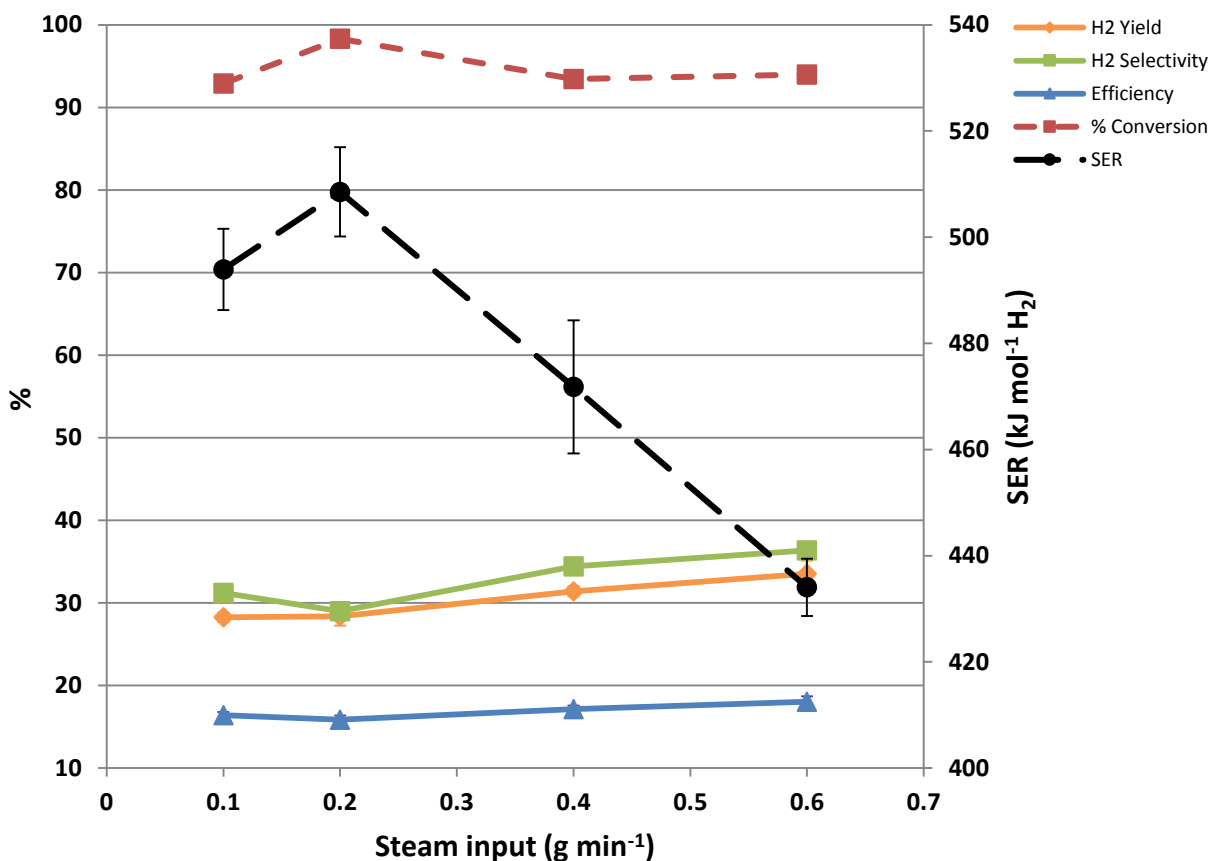


Figure 2.2.0-6 – Dodecane parametric test results for steam input. Error bars indicate 95% confidence interval. Error bars that are not visible are equal in size to the data point symbol.

Dodecane reforming was further investigated using a 2^3 factorial experiment design which investigated effects of plasma power input, fuel input, and steam input. The center point and step sizes for the first factorial test were chosen to ensure the reactor system operated (i.e. no soot formation or arc extinction) and to produce measureable differences in the dependent variables. Data from the factorial tests allowed a path of steepest descent to be mapped across the operating response surface toward a set of independent variable control points that minimized SER.

Table 2.2.3 shows the effects of independent variables changing between high and low values. Third order effects (ABC) are assumed to be an estimate of the error [24] thus first and second order effects of greater magnitude are significant. None of the control parameters have a significant effect on dodecane conversion, confirming the parametric test results. Increasing power did not affect the performance metrics except for its negative effect on SER; a 20 W increase in power input increased the SER by $60 \text{ kJ mol}^{-1} \text{ H}_2$. Dodecane input significantly increased both hydrogen yield and selectivity, however it did not have a significant effect on either efficiency or SER. Steam input had the greatest effect on all of the metrics. The increase from 0.3 to 0.5 g min^{-1} improved both hydrogen yield and selectivity by 13%, and increased efficiency by 10.5%. The greatest performance gains came in the SER, decreasing by $276 \text{ kJ mol}^{-1} \text{ H}_2$ produced.

Table 2.2.3 – Summary of first dodecane factorial test results

| | Control Parameter | Performance Indicator | | | | |
|---|----------------------|-----------------------|--------------------|--------------------|--------------------|--------------------------------|
| | | Dodecane | Hydrogen | Hydrogen | | |
| | | Conversion | Yield | Selectivity | Efficiency | SER |
| | | change in % | change in % | change in % | change in % | change in kJ mol ⁻¹ |
| 1 st Order Effects | A (Power) | 0.45 | 0.70 | 0.54 | -1.35 | 60.16 ¹ |
| | B (Steam) | 0.36 | 13.25 ¹ | 13.75 ¹ | 10.47 ¹ | -276.51 ¹ |
| | C (Fuel) | 1.27 | 4.81 ¹ | 4.45 ¹ | 1.45 | -39.44 |
| 2 nd Order Effects | AB | -1.16 | -2.47 | -1.97 | -1.64 | 3.07 |
| | AC | 0.98 | 2.39 | 2.07 | 1.15 | -39.48 |
| | BC | -1.18 | -1.77 | -1.33 | -0.80 | 32.76 |
| 3 rd | ABC | -1.25 | -2.34 | -1.85 | -1.32 | 42.32 |
| ¹ Indicates significant effect | | | | | | |

To move toward operating conditions that improve (reduce) the SER, a path of steepest descent was calculated from the results of the first factorial test. As shown in Table 2.2.2, the path pointed toward a center point for the second factorial tests characterized by increased steam input, increased dodecane input, and a slight increase in arc power input.

The second factorial test point with high dodecane and steam inputs, and low power input, experienced multiple failures due to arc extinction. While the arc was extinguished, unreformed fuel passed through the reactor and into the impingers. Therefore the impinger data needed to calculate dodecane conversion and selectivity was not available. However, the GC and online gas analyzers provided reformat gas stream composition when the arc was established and the remaining metrics could be calculated.

Table 2.2.4 shows the system responses from the second factorial test. Only dodecane input continued to have a significant effect on the system performance. Changing levels of power and steam input with respect to the center point no longer had an effect on system performance. Based on the results of the second factorial test, the path of steepest descent for SER required increasing dodecane input with constant steam and power inputs.

Table 2.2.4 - Second dodecane factorial test results

| | Control Parameter | Performance Indicator | | | | |
|---|----------------------|-----------------------|-------------|-------------|-------------|--------------------------------|
| | | Dodecane | Hydrogen | Hydrogen | | |
| | | Conversion | Yield | Selectivity | Efficiency | SER |
| | | change in % | change in % | change in % | change in % | change in kJ mol ⁻¹ |
| 1 st Order Effects | A (Power) | NA | 3.88 | NA | 0.34 | 18.85 |
| | B (Steam) | NA | -3.07 | NA | -2.35 | 13.87 |
| | C (Fuel) | NA | 3.66 | NA | 3.30 | -37.79 ¹ |
| 2 nd Order Effects | AB | NA | -2.85 | NA | -1.56 | 5.30 |
| | AC | NA | -3.36 | NA | -1.90 | 9.47 |
| | BC | NA | -0.14 | NA | -0.09 | -0.12 |
| 3 rd | ABC | NA | -6.36 | NA | -3.52 | 17.57 |
| ¹ Indicates significant effect | | | | | | |

Figure 2.2.0-7 shows the last path of steepest descent, which terminated at the optimal operating condition for dodecane reforming. The optimal reactor operating point was defined by an input of 2 slpm N₂ and 0.26 slpm O₂, power input of 240 W, fuel input of 1.65 ml min⁻¹ of dodecane (EQ ratio = 0.18), and steam input of 1.0 g min⁻¹ (S:C ratio =0.63). These inputs yielded a SER of 134.1 kJ mol⁻¹ H₂ produced, a hydrogen yield of 65%, and an efficiency of 37%. Throughout the path of steepest descent the SER continually dropped while the hydrogen yield and efficiency remained nearly constant. Continuing beyond this point on the path of steepest descent was unsuccessful due to extinction of the arc.

The 37% efficiency at the operating conditions identified by minimizing SER can be compared to the efficiency predicted by thermodynamic equilibrium. The state of the reactant system was described using the N₂, O₂, C₁₂H₂₆, and H₂O input flowrates detailed above, a mass averaged input temperature of 50 °C, and 0.1 MPa pressure. The change in enthalpy between reactants and products was based on the 240 W power input to the plasma arc. Reactant flow rates and arc power were converted to units of moles and Joules using a common time basis. The product composition at equilibrium, calculated using FactSageTM (CRCT, Montreal, Quebec, Canada), yielded an efficiency of 77%, with 86% of the input carbon predicted to be present as CO and the remainder (>13%) largely present as CH₄, CO₂, and solid C. Differences between the measured and equilibrium efficiencies are the result of non-idealities in the plasma system such as heat loss, incomplete mixing of reactants, and inadequate reaction time. This single-pass reactor efficiency would be improved by recovering and recycling unreacted liquid hydrocarbons (described in the next section) as might be expected to occur in a fully integrated reformer unit. Gallagher et al. [21] reported ~35% efficiency for a lab scale plasmatron reformer using n-tetradecane at an oxygen to carbon reactant ratio of 0.9, similar to the conditions reported here as optimal conditions.

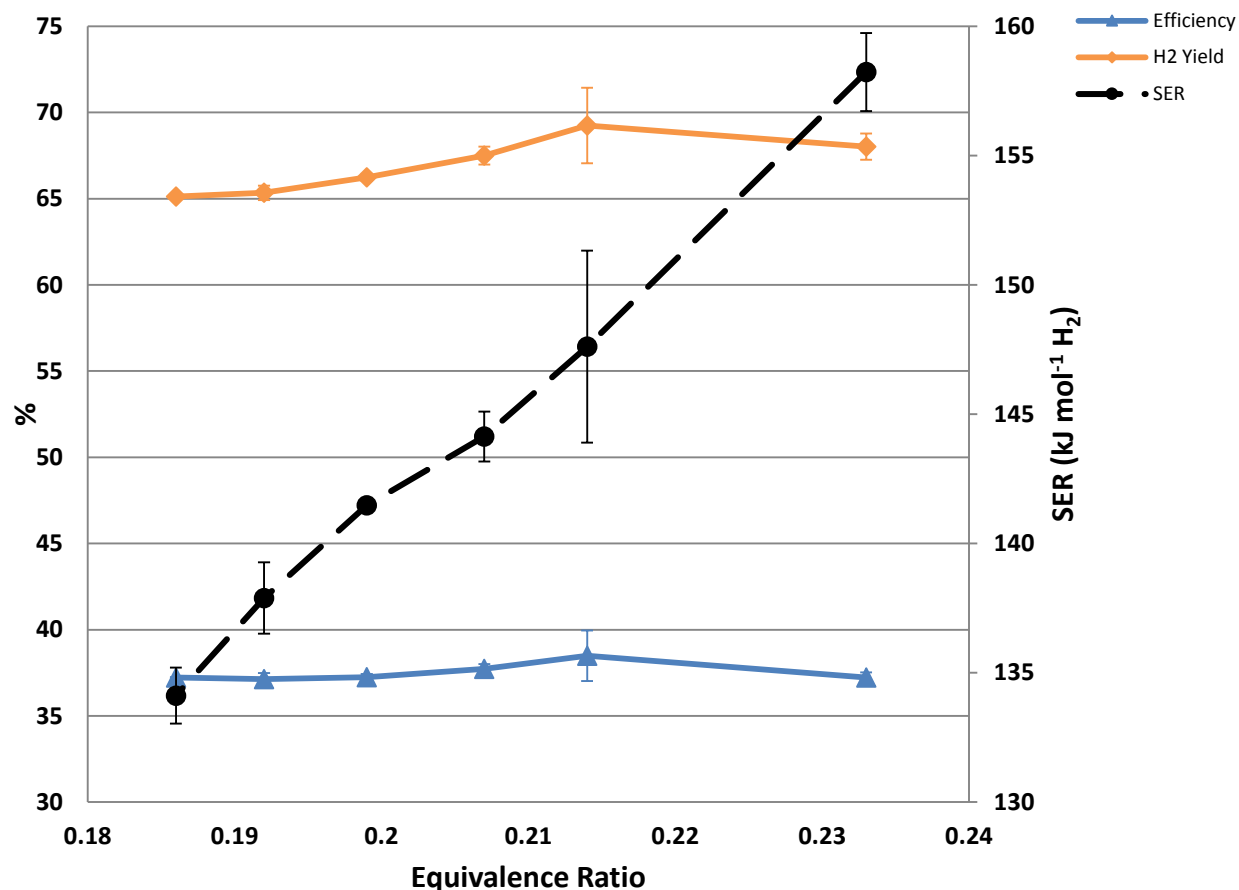


Figure 2.2.0-7 - Final dodecane path of steepest descent and optimal operating condition based on minimized SER. Error bars indicate 95% confidence interval. Error bars that are not visible are equal in size to the data point symbol.

Analysis results of the liquid product recovered from impingers downstream of the reactor for test conditions of 0.55 ml dodecane min⁻¹, steam input of 0.3 g min⁻¹, and power input of 200 W, are presented in Figure 2.2.0-8. In addition to unreacted dodecane, six alkenes from 1-hexene to 1-undecene were identified and quantified. Concentrations determined from the GC-FID analysis and the impinger liquid volumes were used to calculate analyte mass. Figure 2.2.0-9 summarizes the distribution of dodecane input carbon among reforming products. The alkene species from Figure 2.2.0-8 as a group (Alkenes) in Figure 2.2.9 account for 1.3% of the input carbon. Identified products accounted for 96.3% of the carbon input to the system. C3 to C5 hydrocarbons were not measured in either the GC-TCD or GC-FID analysis due to co-elusion with the IPA/acetone trapping solution.

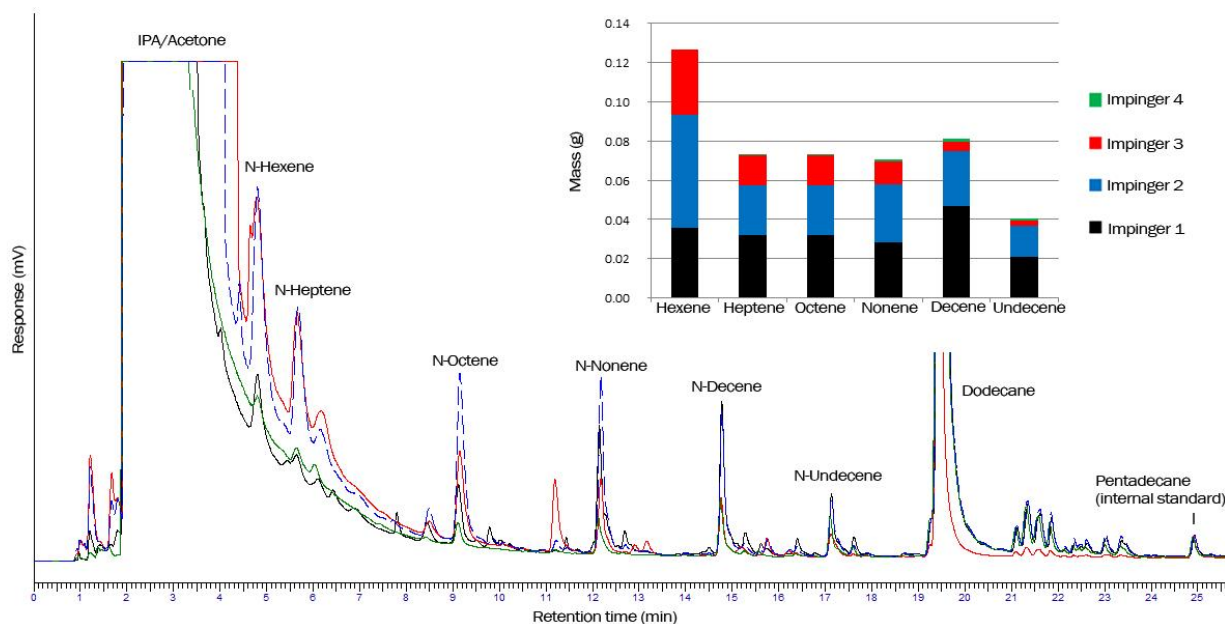


Figure 2.2.0-8 - TCD analysis of liquid samples from impingers 1 - 4. IPA/acetone and dodecane saturated the detector. 1.54 g of unreformed dodecane was recovered in the impingers, analysis was performed at 10% dilution.

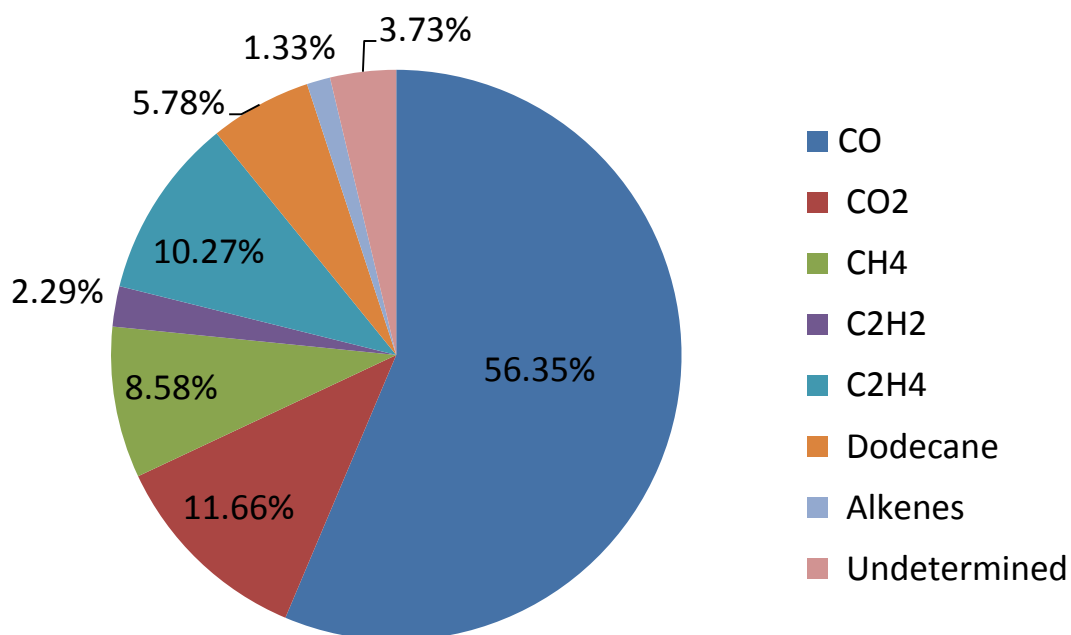


Figure 2.2.0-9 – Distribution of dodecane input carbon among measured products.

HRD-76 testing

Based on the parametric and factorial test results for dodecane, a factorial test was performed to identify the optimal SER reactor operating conditions for HRD-76.

During the preliminary HRD-76 tests a cloud of fuel vapor was observed in the top of the reaction chamber. Insulation was added to the top section of the reaction chamber, above the upper electrode mount to improve vaporization. Tests were conducted before and after the insulation was added to the reaction chamber with operating conditions of 260 W, 1 g min⁻¹ of steam input, and 1.16 ml min⁻¹ of HRD. Prior to adding insulation, the average SER was 218.7 ± 2.5 kJ mol⁻¹ of H₂. With the added insulation on the reactor, this operating point was revisited intermittently throughout the ensuing test campaign to provide an indicator of performance repeatability. Using SER data from 12 independent measurements yielded an average value of 183.3 ± 4.5 kJ mol⁻¹ of H₂ produced or 2.5% error.

Based on dodecane test results, a 2³ factorial experiment was designed for the HRD-76 optimization with power input centered at 240 W and a 20 W step size. However, the system could not operate at 220 W due to arc extinction. Power input was removed as a variable in the optimization and the factorial test redesigned to investigate steam and HRD-76 (equivalence ratio) inputs while holding power constant at 260 W (see Table 2.2.2).

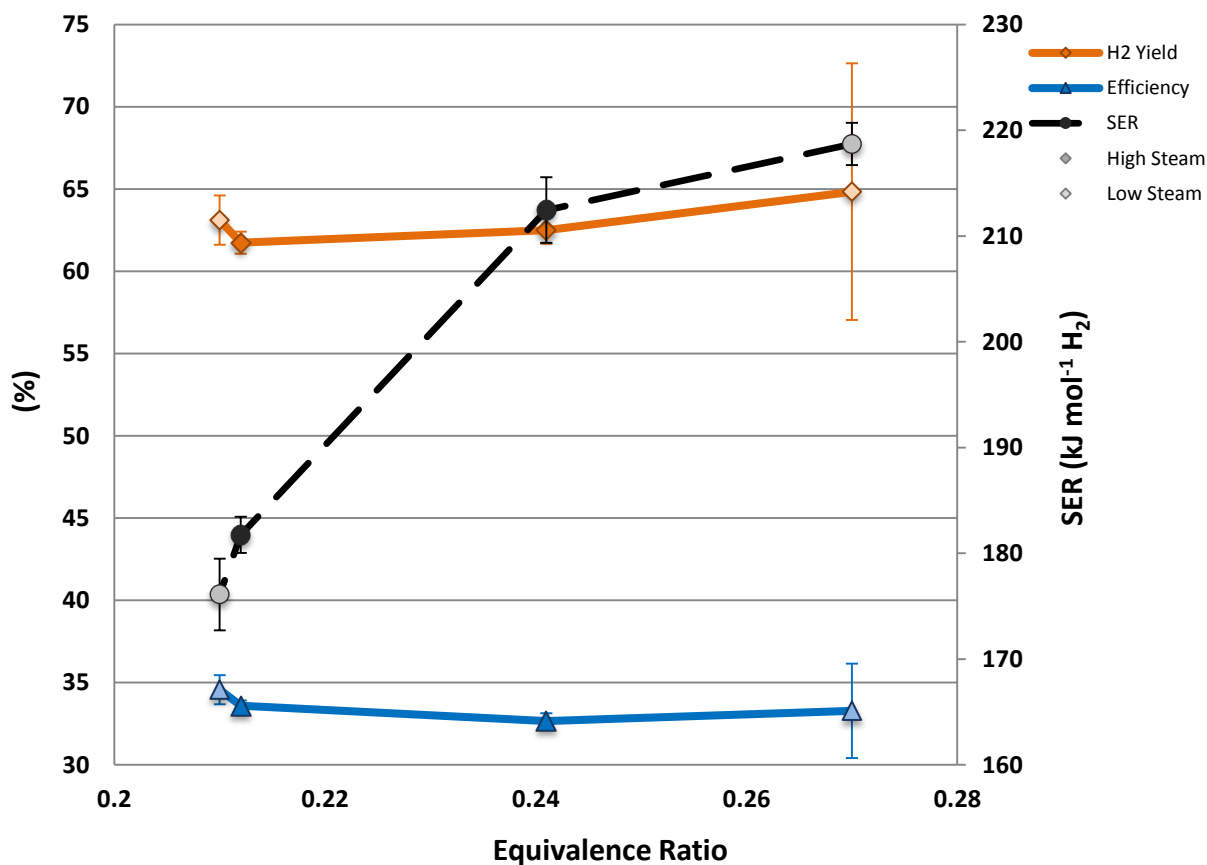


Figure 2.2.0-10 - Results of first factorial test for HRD. The darkened symbols show the high steam input points and lighter symbols show the low steam input points. Error bars indicate 95% confidence interval. Error bars that are not visible are equal in size to the data point symbol.

Figure 2.2.0-10 and Table 2.2.5 present the results from the HRD-76 factorial tests. In general the efficiency for the system does not vary greatly from point to point, but trends lower than the efficiency of dodecane at similar equivalence ratios. Increasing fuel input greatly improves system SER performance.

To interpret the data in Table 2.2.5, second order effects (AB) were used as indicators of error to judge the significance of lower order effects [20]. The system appears to be operating near an optimum for steam input, as changes to steam input no longer significantly affect the SER. However, increasing steam input has a negative impact on both hydrogen yield and efficiency. Fuel input has a significant effect on SER and efficiency. Increasing fuel input from 1.16 ml min⁻¹ to 1.38 ml min⁻¹ (decreasing equivalence ratio from 0.26 to 0.22) improves both the efficiency and SER, but reduces hydrogen yield.

Table 2.2.5 – HRD-76 first factorial treatment system responses

| Control Parameter | Performance Indicator | | |
|-------------------|----------------------------|------------------------|------------------------------------|
| | Hydrogen Yield change in % | Efficiency change in % | SER change in kJ mol ⁻¹ |
| A(Steam) | -3.12 ¹ | -1.28 ¹ | -0.45 |
| B(HRD) | -0.04 | 1.62 ¹ | -36.50 ¹ |
| AB | 1.72 | 0.29 | 6.09 |

¹ indicates significant effect

The path of steepest descent from the first factorial test held both power and steam at constant values, while increasing fuel input. The power was set at 260 W in order to ensure reactor operation, while steam was held constant at an input of 1.0 g min⁻¹. As the fuel was increased past 1.38 ml min⁻¹, at an equivalence ratio of 0.22, soot and liquids deposited on the reactor walls, the latter appearing as a tacky brown film. With increasing deposit mass the arc discharged to the deposited material instead of the lower electrode and the test was terminated. Thus optimal operating conditions for minimum SER were identified at inputs of 2 slpm of N₂, 0.56 slpm of O₂, 1.0 g min⁻¹ of steam, 1.38 ml min⁻¹ of HRD-76, and 260 W of power. At these conditions the reactor operated with an H₂O:C ratio of 0.70, equivalence ratio of 0.21, SER of 176.1 kJ mol⁻¹ of H₂ produced, an efficiency of 35.0%, and a hydrogen yield of 64.2%.

Modifications to the non-thermal plasma reverse vortex flow methane reformer allowed for the reformation of liquid fuels. Ultrasonic atomization of the fuel was used to axially inject fuel into the reformer. Injected fuel vaporized due to elevated temperatures in the reactor, and vapor clouds were eliminated by insulating the upper half of the reaction chamber.

Parametric and factorial tests investigated the effects of varying the power input, dodecane input, and steam input to the system. Dodecane conversion remained fairly constant across all of the tests while the selectivity, hydrogen yield, efficiency, and SER of the system varied greatly. The system was optimized for SER. Decreasing power input, increasing fuel input, and increasing steam input up to a steam:carbon ratio of 0.73 decreased the SER and improved system performance. Optimal SER of 134.1 ± 1.08 kJ mol⁻¹ H₂ produced, with accompanying hydrogen yield of 65.0 ± 0.02 %, and efficiency of 37.0 ± 0.02 % was achieved for dodecane at inputs of 2

slpm N₂, 0.26 slpm O₂, 240 W, 1.65 ml min⁻¹ of dodecane (equivalence ratio = 0.18), with a steam input of 1.0 g min⁻¹ (H₂O:C ratio = 0.63).

HRD-76 reforming was optimized at SER of 176.1 ± 3.8 kJ mol⁻¹ of H₂ produced, a hydrogen yield of $64.2 \pm 1.7\%$, and efficiency of $35.0 \pm 1.0\%$, using operating parameters of 2.0 slpm of N₂, 0.56 slpm of O₂, HRD input of 1.38 ml min⁻¹ (equivalence ratio = 0.21), and steam input of 1.0 g min⁻¹ (H₂O:C ratio of 0.73).

SER values obtained for both fuels were below the ~340 kJ mol⁻¹ H₂ benchmark for steam reforming of natural gas but above the ~110 kJ mol⁻¹ H₂ identified as competitive for plasma based systems. SER could be improved by reducing heat loss, recovering and recycling unreacted liquid and gas phase hydrocarbons, and operating the reformer as a fully integrated industrial package.

References

- [1] Andrews J, Shabani B. Re-envisioning the role of hydrogen in a sustainable energy economy. *International Journal of Hydrogen Energy*. 2012;37:1184-203.
- [2] Petitpas G, Rollier JD, Darmon A, Gonzalez-Aguilar J, Metkemeijer R, Fulcheri L. A comparative study of non-thermal plasma assisted reforming technologies. *International Journal of Hydrogen Energy*. 2007;32:2848-67.
- [3] Mueller-Langer F, Tzimas E, Kaltschmitt M, Peteves S. Techno-economic assessment of hydrogen production processes for the hydrogen economy for the short and medium term. *International Journal of Hydrogen Energy*. 2007;32:3797-810.
- [4] Kothari R, Buddhi D, Sawhney RL. Comparison of environmental and economic aspects of various hydrogen production methods. *Renewable and Sustainable Energy Reviews*. 2008;12:553-63.
- [5] Yang C, Ogden J. Determining the lowest-cost hydrogen delivery mode. *International Journal of Hydrogen Energy*. 2007;32:268-86.
- [6] Gutsol A, Rabinovich A, Fridman A. Combustion-assisted plasma in fuel conversion. *Journal of Physics D: Applied Physics*. 2011;44:274001.
- [7] Reddy EL, Biju VM, Subrahmanyam C. Production of hydrogen from hydrogen sulfide assisted by dielectric barrier discharge. *Int J Hydrogen Energy*. 2012;37:2204-9.
- [8] Mutaf-Yardimci O, Saveliev AV, Fridman AA, Kennedy LA. Thermal and nonthermal regimes of gliding arc discharge in air flow. *Journal of Applied Physics*. 2000;87:1632-41.
- [9] Paulmier T, Fulcheri L. Use of non-thermal plasma for hydrocarbon reforming. *Chemical Engineering Journal*. 2005;106:59-71.
- [10] Fridman A, Nester S, Kennedy LA, Saveliev A, Mutaf-Yardimci O. Gliding arc gas discharge. *Progress in Energy and Combustion Science*. 1998;25:211-31.
- [11] Nunnally T, Gutsol K, Rabinovich A, Fridman A, Starikovskiy A, Gutsol A, et al. Dissociation of H₂S in non-equilibrium gliding arc “tornado” discharge. *International Journal of Hydrogen Energy*. 2009;34:7618-25.
- [12] Gallagher MJ, Geiger R, Polevich A, Rabinovich A, Gutsol A, Fridman A. On-board plasma-assisted conversion of heavy hydrocarbons into synthesis gas. *Fuel*. 2010;89:1187-92.
- [13] Kalra CS, Cho YI, Gutsol A, Fridman A, Rufael TS. Gliding arc in tornado using a reverse vortex flow. *Review of Scientific Instruments*. 2005;76:0251101 - 7.

- [14] Piavis W, Turn S. An experimental investigation of reverse vortex flow plasma reforming of methane. *International Journal of Hydrogen Energy*. 2012;37:17078-92.
- [15] Great Green Fleet. 2013. <http://greenfleet.dodlive.mil/energy/great-green-fleet/>. Accessed: May 7, 2014
- [16] ASTM. D 1946 - 90 Standard Practice for Analysis of Reformed Gas by Gas Chromatography. ASTM International. 2006.
- [17] Lee S-w, Kusaka J, Daisho Y. Spray characteristics of alternative fuels in constant volume chamber (comparison of the spray characteristics of LPG, DME and n-dodecane). *JSAE Review*. 2001;22:271-6.
- [18] Som S. Advancement in Fuel Spray and Combustion Modeling for Compression Ignition Engine Applications. In: Longman DE, editor. Argonne National Laboratory 2012.
- [19] Gowdagiri S, Wang W, Oehlschlaeger MA. A shock tube ignition delay study of conventional diesel fuel and hydroprocessed renewable diesel fuel from algal oil. *Fuel*. 2014;128:21-9.
- [20] Kalra CS, Kossitsyn M, Iskenderova K, Chirokov A, Cho YI, A.Gutsol, et al. Electrical discharges in the reverse vortex flow – tornado discharges. 2003. <http://plasma.mem.drexel.edu/publications/documents/ISPC-16-565-Tornado.pdf>. Accessed: 8/6/2008
- [21] Rollier J-D, Gonzalez-Aguilar Jx, Petitpas G, Darmon A, Fulcheri L, Metkemeijer R. Experimental study on gasoline reforming assisted by nonthermal arc discharge. *Energy Fuels*. 2008;22:556-60.
- [22] Galvita V, Messerle VE, Ustimenko AB. Hydrogen production by coal plasma gasification for fuel cell technology. *International Journal of Hydrogen Energy*. 2007;32:3899-906.
- [23] Pietruszka B, Heintze M. Methane conversion at low temperature: the combined application of catalysis and non-equilibrium plasma. *Catalysis Today*. 2004;90:151-8.
- [24] Box GEP, Hunter WG, Hunter JS. *Statistics for Experimenters*. 1st ed. New York, NY: John Wiley & Sons. Inc; 1978.

2.3 Thermocatalytic Conversion of Synthesis Gas into Liquid Fuels

Catalyst characterization and activity of Zr or Mn containing Ru/Q10 were investigated for Fischer–Tropsch synthesis in a stirred slurry tank reactor. The addition of Zr or Mn in Ru/Q10 enhanced CO conversion, C₅₊ selectivity and space time yield at 503 K, 5.0 MPa and 1800 h⁻¹, and the catalyst activity was highly stable during the reaction. The addition of Zr or Mn can inhibit the oxidation of Ru species and maintain the active, reduced Ru atoms on the catalyst surface. Ru/Q10 showed lower activity compared to Zr or Mn containing catalysts and it was deactivated due to the oxidation of active and reduced Ru species. Catalyst characterization results of BET, BJH, XRD, TPR, H₂ chemisorption, TEM, EDS and XPS suggest that a small amount of Zr or Mn addition can increase the surface atomic concentration of Ru and inhibit the oxidation of Ru species. ZrO₂ in Ru/Zr/Q10 and MnO in Ru/Mn/Q10 were formed on the catalyst surface, and appear to play a role in maintaining Ru species in a reduced state, resulting in enhanced catalyst activity and stability. Complete details of this study can be found at <http://www.sciencedirect.com/science/article/pii/S0378382015300552>.

2.4 Novel Solvent Based Extraction of Bio-oils and Protein from Biomass

The overall objective of this project was to optimize methods and compositions of co-solvent mixtures for the one-step extraction of bio-oils and protein from biomass, and to further develop the outlines of unit operations that fractionates and purifies both products. Outcomes from this research will be used to develop the chemistry underlying the extraction and fractionation of protein, as well as to investigate the extraction efficiency, and the impact of the co-solvent has on the quality of the extracted protein. Biomass sources to be investigated will include corn and oil-seeds such as jatropha. The solvent system to be investigated will comprise a co-solvent mixture of an ionic liquid (e.g., 1-ethyl-3-methylimidazolium methyl sulfate) and a polar covalent molecules\ (e.g., alcohols) that have been previously shown to facilitate one-step extractions of both bio-oils and proteins at low pressure and moderate temperature. A number of co-solvent compositions will be tested and their efficiency correlated to their polarity.

To execute the overall objective, the follow specific tasks were pursued: 1) Quantify the degree to which a 1-step extraction using a hydrophilic co-solvent system (comprised of an ionic liquid and an polar covalent molecule) extracts protein from corn and oil seeds; 2) Determine the extent to which protein denatures in the co-solvent system; and 3) optimize the composition (i.e. choice of ionic liquid, polar covalent molecule, and their ratio) of the co-solvent for protein extraction.

With respect to 1) work has been completed that has tracked the fate of biomass protein throughout a multi-phase extraction process applied to jatropha bio-oil bearing seed. The extraction applied our ionic liquid based co-solvent system and demonstrated pathways to recover jatropha seed bio-oil, phorbol esters and a protein rich biomass. Results demonstrated that the majority of protein (~ 86%) tracked with the biomass while approximately 12% was lost to the co-solvent, with the remaining 2% lost to methanol washes. A significant portion of the ionic liquid was lost to the biomass phase, indicating aggressive washing with methanol or water to recover. Preliminary analysis suggests that the advantages gained from protein retention in the biomass are undermined by the cost of solvent recovery.

The full treatment of Jatropha biomass was executed across multiple steps (Figure 2.4.1). The final distribution of products in respective final phases is presented in Table 2.4.1. To our surprise only about half (~55% w/w) of the total lipid available in the jatropha biomass was extracted during the initial extraction step (5, Figure 2.4.1) which represents a deviation from previous studies wherein almost all of the available bio-oil was extracted and recovered from the biomass during the initial extraction step (Table 2.4.2). This discrepancy is attributed to a modification of the method used in those studies that was made to accommodate this paper's focus on the tracking of biomass protein. Specifically, this experiment used 25 ml instead of 5 ml of methanol in the transfer of extracted material (4, Figure 2.4.1) to the centrifuge tube (5, Figure 2.4.1). This likely caused a greater portion of the oil to remain with the bottoms biomass phase as lipids are denser than methanol. The majority of this bio-oil was then recovered by a combination of washes (19, 27 Figure 2.4.1) of the delipidified biomass. In a typical application of this solvent system, however, full recovery of the lipid is expected.

With respect to 2) our internal results have indicated that the protein does denature to some extent owing to the interaction of the protein outer shell with the amphiphilic solvent. The

denatured nature of the protein is hypothesized to be a major factor in the protein binding to the treated and delipified jatropha biomass and the cause of it remaining bound to the biomass during the subsequent washing steps.

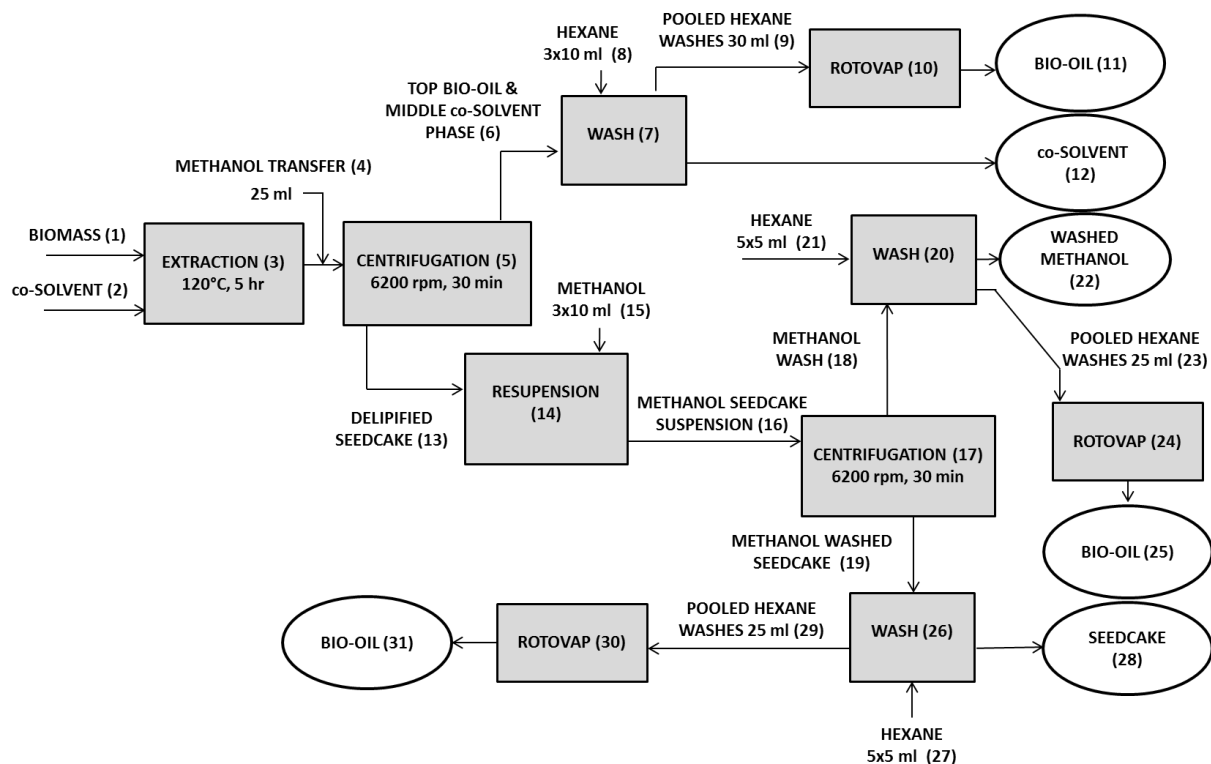


Figure 2.4.1. Jatropha oil-seed treatment pathway

Table 2.4.1. Percent of Starting Material in End Phases

| | Bio-oil (11) | Co-solvent (12) | Washed Methanol (22) | Bio-oil (25) | Bio-oil (31) | Seed (28) | Cake | Total |
|---------------------------------------|-----------------|--------------------|-------------------------|-----------------|-----------------|--------------|------|-------|
| Protein (BM) (%) ¹ : | 0 | 12 | 1.3 | 0 | 0.004 | 86.6 | | 99.9 |
| Lipid (BM) (%): | 55 | 0 | 0 | 14.9 | 20.6 | 0 | | 90.5 |
| Ionic liquid (CS) (%): | 0.04 | 59.4 | 9.4 | 0.04 | 0 | 31 | | 99.88 |

¹The percent yield of protein in the various phases are relative to the total amount of protein in the jatropha seed prior to pretreatment

With respect to 3) our work has indicated a clear optimum in relative concentrations of the ionic liquid to co-solvent in terms of extraction of bio-oil and value added amphiphilic compounds

such as phorbol esters. Phorbol esters are toxic compounds that cannot be deactivated by heat treatment and cause a variety of biological effects including tumor promotion and inflammation, even at very low concentrations. The co-extraction of both phorbol esters and bio-oil, however, requires that the highest possible yield of extracted bio-oil also be achieved. To optimize this two component extraction the relative concentration of [C2mim][MeSO₄] and [C2mim][Ac] was increased from 0 to 100 wt% whilst keeping all other extraction parameters consistent (i.e., extraction time and temperature identical at 22 hours and 64°C, respectively). The results for [C2mim][MeSO₄] are presented in Figure 2.4.2. In general no correlation was observed until the IL concentration reached 60 wt% after which both yields gradually decreased with increasing IL concentration. The key result from Figure 2.4.2, however, was the observation that the bio-oil yield is highly non-linear, with a maximum achieved at IL concentrations between 20 and 55 wt%. A similar bio-oil trend was also observed with [C2mim][Ac], Figure 2.4.3, even though the bio-oil yields are less than those with [C2mim][MeSO₄]. Accordingly, the [C2mim][MeSO₄] concentration range for optimum simultaneous extraction of phorbol ester and bio-oil lies between the range of 30-50 wt %, with 30 wt % level preferred as it minimizes the cost of ionic liquids and lowers the solution viscosity.

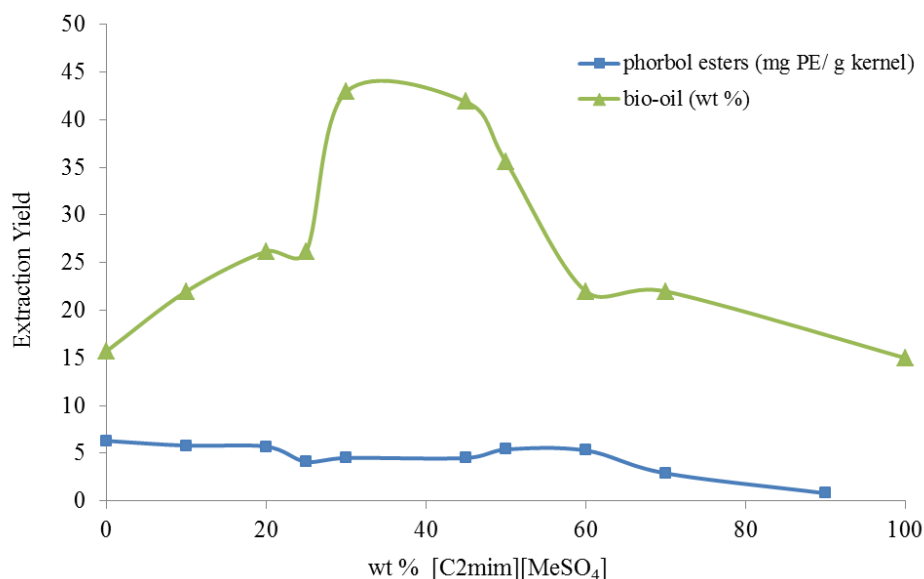


Figure 2.4.2. Yields of extracted phorbol esters and bio-oil as a function of [C2mim][MeSO₄] weight %.

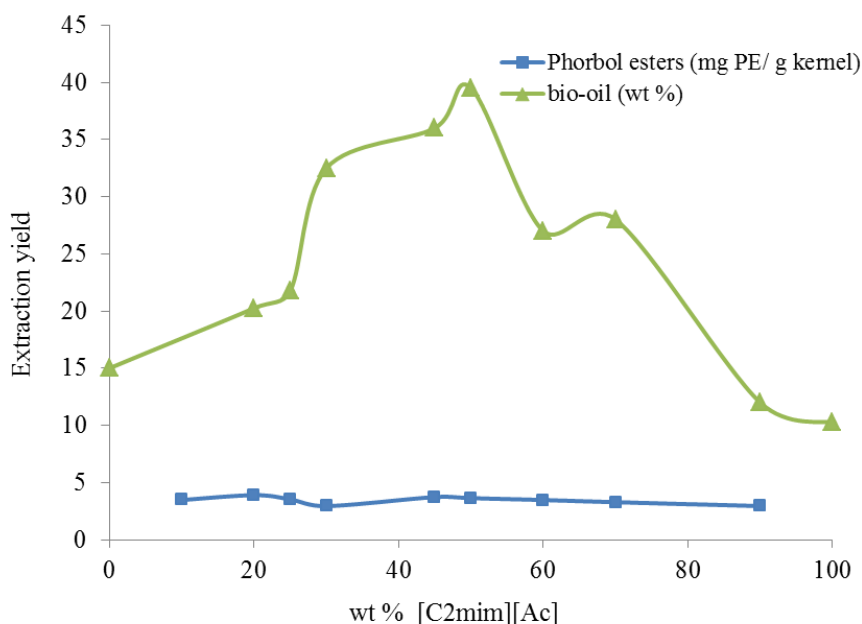


Figure 2.4.3. Yields of extracted phorbol esters and bio-oil as a function of [C2mim][Ac] weight %.

In this work [1], an ionic liquid – methanol co-solvent was shown for the first time to effectively co-extract phorbol esters and bio-oil from *jatropha* kernel biomass in a single extraction step. Under optimized conditions for simultaneous extraction of bio-oil and phorbol esters, 30 wt% [C2mim][MeSO₄] and 70 wt% methanol, nearly all the bio-oil was extracted and auto-partitioned to separate immiscible phase and approximately 98% of the phorbol esters were extracted from the original biomass. In keeping with the work discussed above in 1) e, the co-solvent did not extract significant amounts of protein which remained with the *jatropha* biomass even after washing steps. In addition to achieving effective co-extraction of both bio-oil and phorbol esters, the low phorbol esters - high protein content of the de-lipified biomass also possessed high potential as an animal feed.

References

[1] Godwin Severa, Kumar G., Troung, M., Young, G., and Michael J. Cooney[✉], **2013**. *Ionic liquid co-solvent assisted extraction of phorbol esters from jatropha biomass*. Separation and Purification Technology. 116:265-270.

2.5 Biochemical Conversion of Synthesis Gas into Liquid Fuels

Biomass gasification produces a synthesis gas or syngas that contains primarily H₂, CO₂ and CO. A hydrogen-oxidizing bacterium has been found to convert CO₂ and H₂ into a biopolyester that

can be conveniently liquefied into bio-oil. The effect of CO on the strain, however, was not clear. In this work, the effect of CO on microbial activity was investigated in a gas tight bioreactor, revealing the toxicity of CO in a typical biomass syngas (CO>10%). A thermal reactor with Cu/ZnO catalyst was developed to convert CO into CO₂ and H₂. A dual reactor system was built up for continuous gas circulation between the bioreactor and the catalytic reactor to reach a very high CO conversion (> 90%).

A dual reactor system consisting of a gas-tight bioreactor and a thermal catalytic reactor was set up for the research. A gas mixture of H₂, CO₂ and CO at predetermined composition was used to grow a hydrogen-oxidizing bacterium in the bioreactor to investigate the effect of CO on microbial activity. The overhead gas in the bioreactor was circulated through the thermal catalytic reactor and the gas composition was monitored with time.

Bioreactor and operation: Figure 2.5.1 is the schematic structure of a dual reactor system. The bioreactor (left) is a gas tight reactor (Parr 5500, Parr Instrument Co., Moline, IL) for microbial gas cultures. It consisted of a stainless steel vessel (6.4 cm in diameter, 600 mL working volume) equipped with a stirrer of two 4-blade impellers (3.5 cm in diameter) and a controller for agitation speed and temperature. The reactor (Figure 2.5.2) designed for gas-tight up to 200 atm was run at 3 atm and 35 °C. The gas pressure was measured by a high accuracy digital gauge (accuracy $\pm 0.05\%$ full scale, resolution 0.0007 atm, Cole-Parmer, IL). A gas mixture of pre-determined composition was prepared from cylinders of H₂, O₂, CO₂ and CO, respectively, through a gas proportioner and the composition was determined with a gas chromatography (GC). Samples of gas and liquid medium could be collected from the bioreactor independently.

A laboratory strain of hydrogen-oxidizing bacterium was cultivated in a mineral medium solution.^[1] The strain was first cultivated in 100 mL mineral solution in a closed bottle culture till an optical density (OD) around 2 (0.8 g dry cell mass/L). The bioreactor was filled with 200 mL mineral solution and sterilized at 120 °C. Once cooled to 35 °C, the bottle culture was aseptically transferred into the reactor, resulting in an equal volume (300 mL) of gas and liquid solution. The system was flushed with about 1.5 L of a gas with

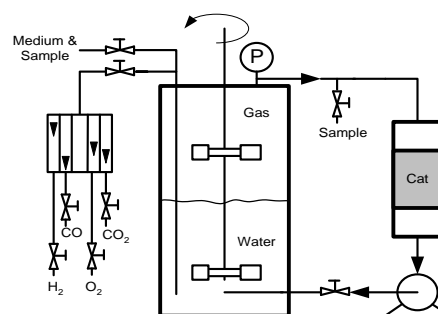


Fig 2.5.1. Schematic dual reactor system for microbial gas culture: a gas-tight bioreactor (left) and a thermal catalytic reactor (right) for water shift reaction. The overhead gas in bioreactor was circulated through the catalytic reactor.



Fig 2.5.2. Laboratory setup of the dual reactor system

pre-determined composition and then filled to an initial pressure (P_0) of around 3 atm (absolute). The pressure of the closed reactor declined with time because of microbial gas consumption. Without the microbes, the pressure drop over 12 hours was negligible ($P/P_0 = 1.0 \pm 0.001$).

Dual reactor system and metal oxide catalyst: As shown in Fig. 2.5.1, the overhead gas in the bioreactor could be circulated between two reactors via a peristaltic pump. When the gas flew through the catalyst bed at a high temperature, water shift reaction occurred: $\text{CO} + \text{H}_2\text{O} \rightarrow \text{CO}_2 + \text{H}_2$. A catalyst of Cu/ZnO was prepared in the laboratory: a solution of 100 mL $\text{CuN}_2\text{O}_6 \cdot 2.5\text{H}_2\text{O}$ (0.2 M) and 100 mL $\text{ZnN}_2\text{O}_6 \cdot 6\text{H}_2\text{O}$ (0.2 M) was stirred and slowly titrated with a solution of NaOH (10M) till pH 6.2. The precipitates were collected with vacuum filtration and oven-dried at 80 °C. After calcined at 300 °C for 3 hours, the brownish black solid (CuO) was treated under H_2 at 240 °C till reddish color (Cu_2O): $2\text{CuO} + \text{H}_2 \rightarrow \text{Cu}_2\text{O} + \text{H}_2\text{O}$. Copper (I) oxide was the active form of copper oxides for water shift reaction. About 5 g catalyst was added into a glass tube to form a fixed bed (40 mm height). The reactor was heated and maintained at a desired temperature, which was monitored with a thermal probe at the middle of the catalyst bed.

Technical accomplishments under this task are described below.

Microbial gas consumption and CO toxicity: The gas in the bioreactor was consumed by microbial cells, causing pressure drop with time as shown in Fig. 2.5.3. Without CO, the pressure dropped linearly with time and the gas consumption rate was 2.42 mmole per hour by one gram of dry cell mass (DCM) as shown in Table 2.5.1. The rate was not affected very much at 5 mole% of CO, but declined to zero at 10 mole% of CO. This result indicates that the strain has a good tolerance to CO, but cannot work on syngas since a typical biomass syngas contains 10-30% of CO. Because CO is a feedstock of Fisher-Tropsch process, the residual gas would contain much less CO (<5%) and hence can be used as the gas feedstock for microbial conversion. The biochemical conversion of the gas waste is therefore a promising clean technology for biomass refining. In order to use the syngas directly, this work also explored a dual reactor technology to convert CO into CO_2 and H_2 .

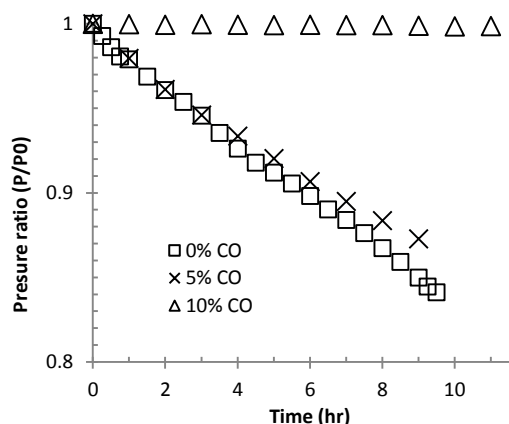


Fig. 2.5.3. Effect of CO on microbial gas consumption: 0, 5 and 10 mole% of CO in a mixed gas ($\text{H}_2:\text{O}_2:\text{CO}_2 = 74:21:5$).

Table 2.5.1. Microbial gas consumption in a gas-tight bioreactor

| CO content (mole%) | Pressure drop rate (hr^{-1}) | Gas consumption ^a (mmole. hr^{-1}) | Specific rate ^b (mmole.gDCM ⁻¹ . hr^{-1}) |
|--------------------|---|---|---|
| 0 | 0.0161 | 0.58 | 2.42 |
| 5 | 0.0138 | 0.50 | 2.08 |
| 10 | 0 | 0 | 0 |

a. Initial 36 mmole gas in bioreactor (0.3L, 3 atm and 30 °C)

b. Gas consumption rate by dry cell mass (DCM)

Initiation of water shift reaction: On Cu/ZnO catalyst, CO could be converted into CO₂ and H₂ when the reaction temperature was raised to 200 °C or above as shown in Fig. 2.5.4. In the experiments, the thermal reactor temperature was controlled at 270-280 °C. Importantly, the high gas temperature did not cause difficulty in maintaining the bioreactor at 30-35 °C, because of the high heating capacity of aqueous medium and a slow gas flow rate (50 mL/min).

CO conversion into CO₂ and H₂: In a single pass operation mode, a gas stream containing 10-20 mole% CO flew through the thermal catalytic reactor without circulation and only 2-4 mole% of CO was converted, depending on the flow rate (20-80 mL/min). When the gas was circulated between two reactors (Fig. 2.5.1), however, CO conversion was improved significantly with time. In an extreme case of pure CO, more than 90% of CO was converted into CO₂ and H₂ in about two hours (Fig. 2.5.5). This result indicates that the dual reactor system can work effectively on synthesis gas. It was also noticed that a stoichiometric amount of CO₂ was formed and measured according to the water shift reaction, but only about 70% H₂ was formed and detected. This needs to be further investigated.

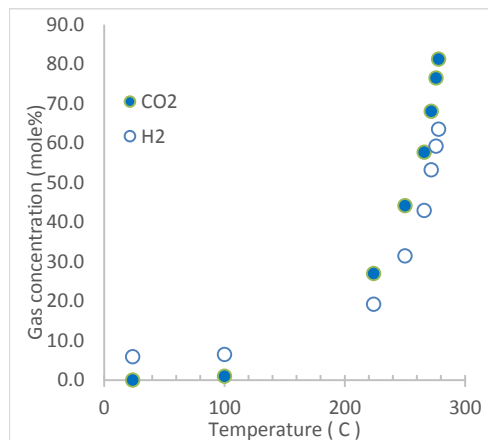


Fig. 2.5.4. Initiation of catalytic CO

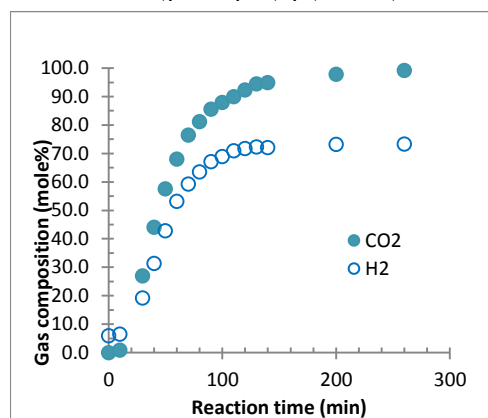


Fig. 2.5.5. Catalytic conversion of CO into CO₂ and H₂ in dual reactors at 280 °C

Three major conclusions were drawn from the work:

- The microbial strain cannot work directly on syngas because of the high CO content (>10%) and its toxicity to microbes;
- The strain can work on residual gas from other processes if CO content is 5% or below;
- A dual reactor system can effectively reduce the CO content of syngas for its direct utilization and conversion into biopolyester by the microbes.

Publications and presentations from the research

- [1] Jian Yu, Alex Dow, Sricanth Pingali (2013). The energy efficiency of carbon dioxide fixation by a hydrogen-oxidizing bacterium. *Int. J Hydrogen Energy* 38: 8683-8690.
- [2] Jian Yu (2013). Direct conversion of CO₂ into biopolyester with solar energy and water. American Chemical Society National Meeting, September 8-12, Indianapolis, Indiana.
- [3] Jian Yu (2012). Clean production of bioplastics and bio-oil from solar energy and carbon dioxide. CleanTech Conference & Showcase 2012, June 18-21, Santa Clara, California.

2.6 Biocontamination of Fuels

Analysis, control and mitigation of microbial contamination of biofuels are important operational considerations. Such contamination may reduce fuel stability, enhance biofouling, and induce corrosion of fuel-related components. Biodiesel is also more likely to be contaminated by microbes than is petroleum diesel (Zhang *et al.*, 1998; Lee *et al.*, 2009; Achten *et al.*, 2010; Stamper *et al.*, 2011). Diverse *Fungi* and *Bacteria* have been implicated in biofuel contamination (Chao *et al.*, 2010; Bucker *et al.* 2011), a phenomenon directly attributed to biodiesel's hygroscopicity (Passman *et al.* 2009). Biodiesel's water adsorption and subsequent phase separation promotes microbial growth. Moreover, biodiesel's chemical and biological hydrolysis to fatty acids provides labile carbon for sustained growth, which in turn results in acidification and microbiologically induced corrosion (MIC) (Passman, 2003; Leung *et al.*, 2006; Corseuil *et al.*, 2011; Passman, 2013). Enhanced oxidation rates through formation of anoxic environments and biofilms exacerbate MIC (Dzierzewicz *et al.*, 1997; Rajasekar, 2010; Satoh *et al.*, 2009; Stamper *et al.*, 2011). To advocate the use of biofuels it is important to isolate microbiological contaminants and study how to reduce fuel oxidation rates and MIC.

Previously, extracted samples of DNA from contaminated field samples have been used for molecular characterization of biofilms using bacterial 16S and specific sulfate reducing primers that target the dissimilatory sulfite reductase gene for estimation of diversity. We had also investigated the use of *Arthrobacter* sp. P1-1 and *Burkholderia* sp. C3 to study the degradation of dibenzothiophene, a compound inherently present in all diesel fuels. Results indicate that the biodegradation of dibenzothiophene by the two isolates is regulated by sulfate. Dibenzothiophene is a typical model chemical for biodegradation studies of sulfur-containing chemicals. Our studies indicated that both *Arthrobacter* sp. P1-1 and *Burkholderia* sp. C3 can efficiently degrade dibenzothiophene and other polycyclic aromatic hydrocarbons (PAHs).

During our last report we proposed to continue with the development of a field detection method and have been working toward the determination of a metabolism inhibitor. Under this subtask, development focused on a DNA based rapid molecular detection method and continued the investigation of microbiologically induced corrosion.

Characterization of Moniliella wahieum Y12^T – During the current effort we further described a putatively novel basidiomycete, *Moniliella wahieum* Y12^T that was isolated from a 20% biodiesel blend (B20), and this strain's impact on biodiesel stability, and '1018' steel corrosion. The filamentous fungus was cultivated from a biofilm at the interface of fuel and aqueous layers in a contaminated biodiesel (B20) obtained from the City and County of Honolulu. A BLAST comparison of a 565 nt fragment of the D1/D2 region of the 26S rRNA showed the strain shared 98% sequence identity with its nearest described relative, *Moniliella suaveolens* var. *nigra* CBS 542.78^T (AF335524) (Altschul *et al.*, 1997). Strain Y12 has been tentatively assigned to the genus *Moniliella* as the type strain of *M. wahieum* Y12^T and has been deposited into repository with the identifier, ATCC MYA-4962 (Fig. 2.6.1). This will allow public access and further other biofuel degradation studies.

Biodiesel degradation during cultivation of Y12^T was determined through loss of chromatographic peaks from a B100 biodiesel obtained from a local manufacturer (Pacific

Biodiesel, 1003 Makepono St., Honolulu, Hawaii). Degradation was determined by loss of chromatographic peaks and plotted against cell density. Specifically, hexadecanoic acid methyl ester; 9,12- octadecenoic acid methyl ester and 9-octadecenoic methyl ester; methyl stearate and 9, 12, 15- octadecatrienoic acid methyl ester, were dominant fuel constituents that were biologically oxidized at equal rates. A maximum degradation rate of 3.56×10^{-2} mg/h was observed during log phase growth.

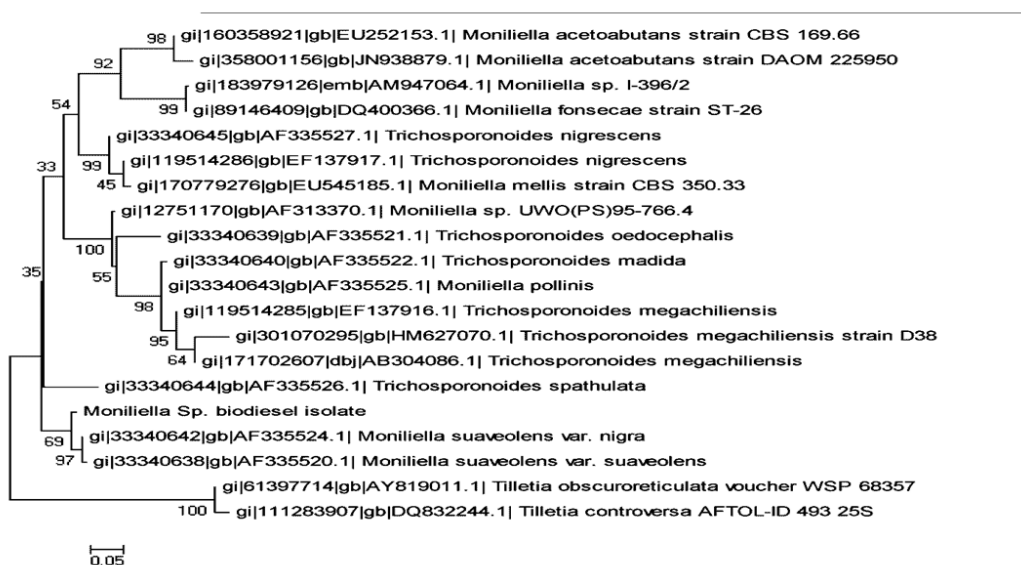


Fig. 2.6.1. Maximum likelihood tree showing the relationship of *Moniliella wahieum* Y12^T with type strains of species in the same and related genera on the basis approximately 90% of the 26S D1/D2 region. Sequences from two *Tilletia* species were used as outgroups. Bootstrap values for 500 replicates are shown at each branch. Scale bar represents 5 substitutions per 100 nt.

Oxidation of '1018' metal coupons – Composition and carbon content of '1018' steel coupons approximately matches that of material used to build many fuel containment vessels. Our data show this carbon steel is oxidized at an elevated rate during biodiesel degradation in the presence of *M. wahieum* Y12^T (Fig. 2.6.2). Metal coupons in the presence of only biodiesel and medium showed an average mass reduction of 0.49 ± 0.22 mg after 30 d, and 0.85 ± 0.07 mg after 60 days. Mass loss from coupons in the same medium in the presence of Y12^T exceeded that observed in control tests by 70% after 30 days, and 50% after 60 days (mass reduction of 0.85 ± 0.06 mg, and 1.30 ± 0.14 mg after 60 days).

Oxidation and acidification are typically observed during diesel fuel degradation (Prankl and Schindlbauer, 1998), and biofilm formation is also recognized as a contributory factor in metal corrosion (Achten *et al.*, 2010, Damon, 1941). A reduction in pH was observed during Y12^T growth, with medium pH falling from 7.0 to 5.3 after 30 days; this may arise through products of beta-oxidation including acetic acid, smaller fatty acids and ultimately CO₂. We also observed biofilm formation at the fuel/water interface on the metal coupon, and on inner surfaces of the jar (Fig. 2.6.2).

Biological contamination of fuels has been reported for some time (cf. Gaylarde *et al.* 1999). The

fundamental interaction in such contamination is the ability of a microorganism to utilize a chemical component as a growth substrate. Transfer of carbon through the production of metabolites can further support other metabolisms, and also chemically impact the local environment (Passman, 2013). We investigated the ability of *M. wahieum* Y12^T to utilize FAMEs as sole carbon sources, and its subsequent impact on corrosion. The degree and rate of biodiesel degradation usually depends on the component hydrocarbons' saturation and fatty acid chain length (Knothe, 2005). *M. wahieum* Y12^T did not appear to prefer a specific hydrocarbon, and complete utilization of both saturated and unsaturated FAMEs was observed at nearly identical rates.

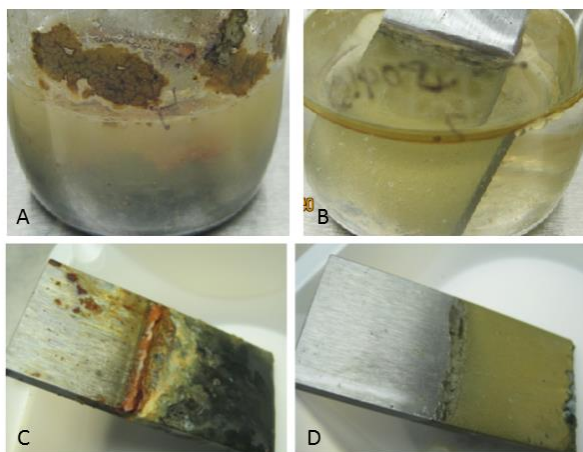


Fig. 2.6.2. Microbiologically induced corrosion of a '1018' metal coupon by *Moniliella wahieum* Y12^T, with biodiesel as the carbon source. A) Inoculated sample containing 2 ml biodiesel and 40 ml modified M9 minimal medium. Significant growth was observed on the side of the containers and occurs also on the '1018' coupon. B) Control sample and fuel layer after 60 days incubation. C) Visible MIC on the metal coupon after 60 days incubation. D) Chemical oxidation of the control coupon after 60 days incubation.

Comparative mass spectrometry-based metabolomics and proteomics showed putative catabolic networks and pathways of the aromatics in C3. The addition of glycerol was found to enhance biodegradation of the aromatics including dibenzothiophene. This result indicated that glycerol induces C3 to secrete rhamnolipids that enhance PAH and dibenzothiophene biodegradation. Rhamnolipids are non-toxic and biodegradable glycolipid biosurfactants with a wide range of commercial applications. The relevant proteins profiled and genes (i.e., *rhl* genes) detected and cloned allow further understanding of metabolism of PAHs and biosynthesis of rhamnolipids. These results provided insights into bacterial adaptation to overcome stress conditions and might lead us to the improvement of bioremediation technologies and prevention of fuel biocontamination.

Our current direction still maintains its original purpose for finding a rapid and accurate molecular detection method. Previous research along with our results, suggest that corrosion also occurs due to the direct metabolism of FAMEs. This metabolism can provide basal support for the development of complex microbiological communities that include sulfate reducing bacteria and others that may also play a role in biofouling and corrosion. Detection of this specific

metabolic pathway is fundamental to development of an effective control methodology. Due to these results, our research direction is now focused on finding specific genetic elements that are expressed during FAMES metabolisms using *Moniliella wahieum* Y12^T as a model. Prokaryotic isolates have also been obtained and will be included in subsequent work.

References

1. Achten, W.M.J., Almeida, J., Fobelets, V., Bolle, E., Mathijs, E., Singh, V.P., Tewari, D.N., Verchot, L.V., Muys, B. 2010. Life cycle assessment of Jatropha biodiesel as transportation fuel in rural India. *Applied Energy* 87(12), 3652–3660
2. Altschul, S.F., Madden, T.L., Schäffer, A.A., Zhang, J., Zhang, Z., Miller, W. & Lipman, D.J. 1997. Gapped BLAST and PSI-BLAST: a new generation of protein database search programs. *Nucleic Acids Research* 25, 3389-3402
3. Bücker, F., Santestevan, N.A., Roesch, L.F., Jacques, R.J.S., Peralba, M.C.R., Camargo, F.A.O., Bento, F.M. 2011. Impact of biodiesel on biodeterioration of stored Brazilian diesel oil. *International Biodeterioration & Biodegradation* 6, 172-178.
4. Chao, Y., Liua, N., Zhanga, T., Chen, S. 2010. Isolation and characterization of bacteria from engine sludge generated from biodiesel-diesel blends. *Fuel* 89(11), 3358-3364.
5. Corseuil, H.X., Monier, A.L., Gomes, A.P.N., Chiaranda, H.S., Rosario, M.D., Alvarez, P.J.J. 2011. Biodegradation of soybean and castor oil biodiesel: implications on the natural attenuation of monoaromatic hydrocarbons in groundwater. *Groundwater Monitoring and Remediation* 31(3), 111-118
6. Damon, G.H. 1941. Acid corrosion of steel. *Indust Eng Chem* 33(1), 67–69.
7. Dzierzewicz, Z., Cwalina, B., Chodurek, E., Wilczok, T. 1997. The relationship between microbial metabolic activity and biocorrosion of carbon steel. *Research in Microbiology* 148(9), 785–793
8. Knothe, G. 2005. Dependence of biodiesel fuel properties on the structure of fatty acid
9. Lee, J.S., Ray, R.I., Little, B.J. 2009. Microbiological and corrosivity characterizations of biodiesels and Advanced Diesel Fuels DTIC Document. <http://www.dtic.mil/dtic/tr/fulltext/u2/a503602.pdf>
10. Leung, D.Y., Koo, B.C., Guo, Y. 2006. Degradation of biodiesel under different storage conditions. *Biores Technol.* 97(2), 250-6
11. Passman, F. J., 2003. Introduction to fuel microbiology. In: Passman, F. J. (Ed.), *Manual 47 - Fuel and fuel system microbiology: fundamentals, diagnosis and contamination control*, ASTM International, West Conshohocken, pp. 1- 13.
12. Passman, F.J., Lewis, R.P., Palmer, J.L., Reid, H. 2009. Effect of ethanol on microbial proliferation in unleaded gasoline microcosms. In: Morris, R.E. (Ed.), *Proceedings of the 11th International Conference on the Stability and Handling of Liquid Fuels*; Prague, Czech Republic.
13. Passman, F.J. 2013. Microbial contamination and its control in fuels and fuel systems since 1980-a review. *International Biodeterioration and Biodegradation* 81, 88-104

14. Satoh, H., Odagiri, M., Ito, T., Okabe, S. 2009. Microbial community structures and in situ sulfate-reducing and sulfur-oxidizing activities in biofilms developed on mortar specimens in a corroded sewer system. *Water Research* 43(18), 4729–4739
15. Stamper, D., Montgomery, M., Morris, R. 2011. Biofouling of Several Marine Diesel Fuels. DTIC Document. <http://www.dtic.mil/docs/citations/ADA546379>
16. Zhang, X., Peterson, C., Reece, D., Haws, R., Moller, G. 1998. Biodegradability of biodiesel in the aquatic environment. *Transactions of the ASAE* 41, 1423–1430.

2.7 Biofuel Corrosion

Under this subtask, static immersion tests were conducted in water/biodiesel (B100 and B20) mixtures using unfiltered and filtered fuels in the anaerobic, sterile aerobic, and aerobic conditions. The results indicated that presence of microorganisms in the unfiltered B100 resulted in the most severe corrosion rate of steel after 6 months in the anaerobic condition. The microorganism responsible for the accelerated corrosion rate could not be cultured and identified. The corrosion products on steel immersed in the biodiesel phase were identified as mainly iron formate hydrate and iron oxalate hydrate. The formation of iron formate and iron oxalate suggests the presence of organic acids (i.e., formic acid and oxalic acid) in the B100 fuel.

Biodiesel fuels have emerged as alternative fuels of petroleum diesel worldwide. Cleaner emissions and wide availability are known advantages of using biodiesels. Biodiesels are essentially ester-based fuels derived from vegetable oils or animal fats through a transesterification process [1]. Biodiesel, in comparison to petroleum diesel, has the advantage of being biodegradable and non-toxic, having higher flash point, and causing reduced emissions. However, the major cons of biodiesel include its oxidative instability, poorer low-temperature properties, slightly lower power and torque generation, and higher fuel consumption [2].

The compatibility of various automotive engine materials with biodiesel, such as carbon steel [3-9], copper/brass/bronze [6, 10-15], aluminum [6, 9, 11, 12, 15-17], cast iron [12], as stainless steel [6, 11], has been widely investigated. Generally, the studies showed that copper/brass/bronze was more prone to corrosion than ferrous alloys [6]. Carbon steel, aluminum, and cast iron also experienced significant corrosion, while stainless steel barely corroded in biodiesel environments. The biodiesel fuels that were investigated include those made from palm oil [5, 8, 10-12, 14], rapeseed oil [6, 15], soybean oil [3, 4, 7], sunflower oil [4], other seed oil [9, 16], and animal fats [3, 18]. Biodiesel fuels with different origins might have different effects on the corrosion of metallic materials. Maru et al. found that soybean-based biodiesel was less reactive to the metal than the sunflower-based biodiesel [4]. Kaul et al. discovered that biodiesel originating from *Salvadora* oil was the most aggressive to piston metal and piston liner metal among four biodiesel fuels from different seed oils, i.e., *Pongamia glabra*, *Salvadora oleoides*, *Madhuca Indica*, and *Jatropha curcas* [16].

The effects of biodiesel fuels on the corrosion behavior of metallic materials have been compared to that of petrodiesel. Generally, it has been reported that that pure biodiesel fuels

(i.e., B100) are more corrosive to metallic materials as compared to pure petrodiesel (i.e., B0) [8, 10-12, 18]. Fazal et al. believed that this is likely caused by the presence of oxygen moieties, auto-oxidation, increased polarity in biodiesel, and its hygroscopic nature [14]. The high sulfur content in some biodiesel fuels is also a reason for high corrosion rates in biodiesel [16]. Besides B100 and B0 fuels, other biodiesel/petrodiesel blends were also studied, such as B50, B30, and B10 with 50%, 30%, and 10% of petrodiesel, respectively. Lu et al. found that B100 was the most corrosive fuel to various engine materials followed by the emulsions of B30 and B10 [19]. Haseeb et al. [5, 10] and Akhabue et al. [9] also found that the increase of biodiesel contents (i.e., from 0% to 50% and 100%) in biodiesel/petrodiesel blends increased the corrosion rates of metallic materials.

Despite extensive studies on the corrosion performance of metallic materials in various biodiesel fuels or biodiesel/petrodiesel mixtures, very few studies have focused on water/biodiesel and/or seawater/biodiesel mixtures. Wire beam electrode (WBE) has been used to investigate the corrosion behavior of carbon steel in water/biodiesel, with aims to evaluate the effect of water contamination on the corrosion of biodiesel storage containers [20, 21]. The water phase in biodiesel was found to induce corrosion because it can concentrate corrosive species over time [21]. Seawater/biodiesel mixtures were also studied to simulate the fuel tank environment in ships [22, 23]. However, the static immersion tests of metallic materials in water/biodiesel mixtures have not been conducted. The present study aims to investigate the corrosion behavior of carbon steel in both water/B100 and water/B20 mixtures.

Plain carbon 1018 steel was chosen as the material to be investigated based on its similar chemical compositions to that of ASTM A36 steel and API Spec 5L X60, which are often used for fuel tank storage and pipelines, respectively. The 1018 steel coupons were machined to the following dimensions: 2.25 in \times 1 in \times 0.125 in. A BenchMark 320 marking system was used to pin stamp the coupons for identification. The coupons were then acetone washed to remove any oil residue and weighed to obtain an initial mass. To prevent oxidation of the steel, the coupons were kept in a dry box (1% RH) prior to performing any experiments.

The types of fuels that were selected for this study were 100% biodiesel (B100) and 20% biodiesel (B20). These fuels were obtained locally from gas stations (i.e., 76 and Aloha Petroleum gas stations). Sterilized versions of the aforementioned fuels were also used. Sterility of the B100 and B20 fuels were achieved via vacuum filter sterilization by a 0.22 μ m Millipore membrane filter. Nanopure water (40 mL) was added to the biodiesel fuels (40 mL) in 100 mL glass Pyrex media bottles to facilitate water contamination whereupon biofouling could occur. The 1018 steel coupon samples were placed in these water/biodiesel mixtures at an approximate angle of 45° with respect to the horizon. Triplicates of each water/biodiesel mixture and 1018 steel coupon were exposed outdoors under the three following environmental conditions: anaerobic, aerobic, and sterile aerobic. UV exposure from the sun and rain water contamination was kept to a minimum by encasing samples in boxes under a protective alcove.

Figure 2.7.0-11 depicts the environmental systems. The bottle with an orange cap are sealed air-tight to simulate an anaerobic environment. The uncapped bottle simulates an aerobic environment, while the one with a gray cap simulates a “sterile” aerobic environment. The gray cap is fitted with a 0.22 μ m filter at the top to allow only air to be exchanged into and out of the

bottle. Contamination from the outside environment will not be able to enter the bottle. Exposure time periods of 6 months and 1 year were chosen for this experiment to compare and contrast the corrosion of the steel samples.

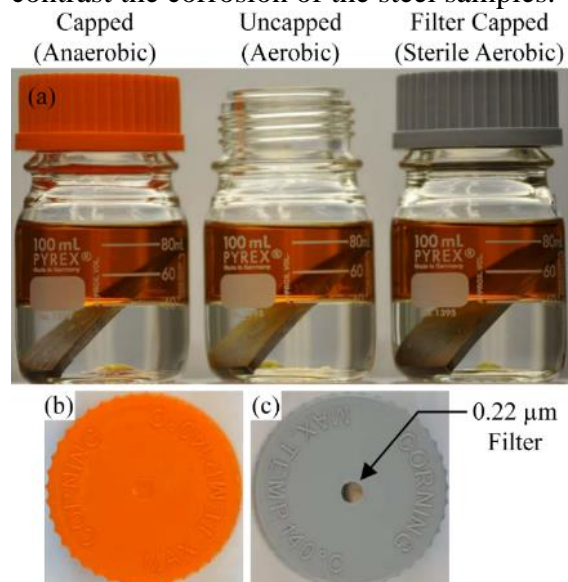


Figure 2.7.0-11. (a) Water/biodiesel mixtures depicting anaerobic, aerobic, and sterile aerobic environments; (b) a normal cap; and (c) a cap with 0.22 µm Millipore membrane filter.

Figure 0-12 depicts the coded system of numbers and characters denoting the fuel type (B100 or B20), filtration status (unfiltered or filtered), environmental condition (aerobic, sterile aerobic, or anaerobic), exposure duration (6 months or 1 year), and sample number (1, 2, or 3).

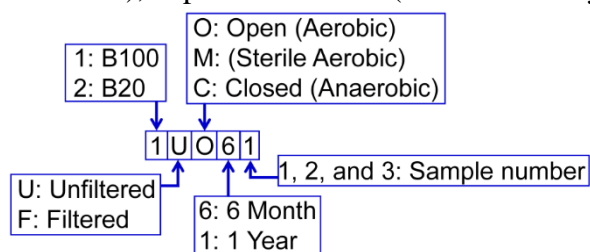


Figure 0-12.7.2. Notation for sample names.

The coupons were removed from the water/biodiesel mixtures after 6-month and 1-year immersion. Then the coupons were lightly washed using acetone to remove oil residue and stored in a dry box (1% RH) prior to digital imaging and corrosion product analysis.

A Nicolet Almega XR dispersive Raman Spectrometer (Thermo Scientific Corp.) equipped with multiple Olympus objectives and a Peltier-cold charge-coupled device (CCD) detector was used for the experiments. An objective with a magnification of 50× with an estimated spatial resolution of 1.6 µm was used. The instrument was operated with laser sources of a green Nd:YAG laser with 532 nm wavelength excitation and an infrared diode laser with 780 nm wavelength excitation. The maximum spectra resolution was up to 2.2 – 2.6 cm⁻¹ using a 25 µm pinhole or slit, which requires longer acquisition time and reduces signal-to-noise ratio. To

reduce the collecting time, an aperture of 100 μm pinhole was used, giving an estimated resolution in the range of 8.4 – 10.2 cm^{-1} . The accumulation time was 120 seconds.

To obtain the total mass loss, the steel coupons were cleaned with an acid wash (ISO 8407) to remove any corrosion product. After acid washing and drying in the dry box (1% RH) for at least one hour, the steel coupons were weighed and compared to their respective initial mass values to obtain the total mass loss. The penetration rate in mm/year or mpy was then calculated based on the total mass loss results.

Corrosion morphology: The typical corrosion morphologies of the 6-month and 1-year 1018 steel coupons retrieved from specified environments is shown in Figure 2.7.0-13 and 2.7.4. Notice that all coupons were lightly acetone washed to remove oil residue prior to digital imaging, therefore, the loose corrosion products on steel were removed before images were taken. Generally, more corrosion products formed on steel immersed in the biodiesel phase in the water/B100 mixtures (Figure 2.7.0-13) than the water/B20 mixtures (Figure 2.7.0-14).

Regarding the corrosion on steel immersed in biodiesel phase, while most triplicates had similar corrosion morphologies among the three samples, there are a few exceptions, such as the 1FC6, 2UM6, and 1FC1 triplicates. One sample from the 1FC6 triplicate does not have rust formation on the upper region exposed to the fuel (similar as that shown in Figure 2.7.0-13d), but the other two samples have thick layers of orange rust on upper region, such as the sample 1FC62 shown in Figure 2.7.0-13b. One sample from the 2UM6 triplicate and one sample from the 1FC1 triplicate showed thick layers of yellow rust on steel immersed in biodiesel, while the other two triplicates look pristine, such as samples 2UM61 and 1FC12 shown in Figure 2.7.0-14e and Figure 2.7.0-13h, respectively.

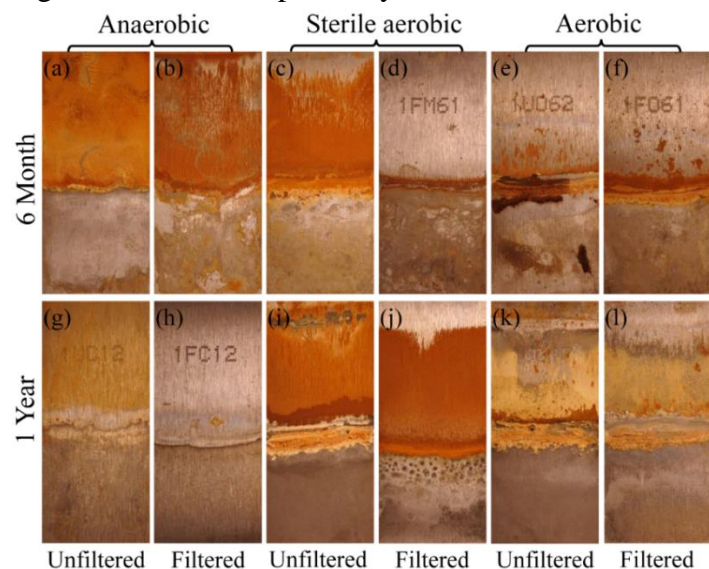


Figure 2.7.0-13. Corrosion morphologies of 1018 steel samples exposed in anaerobic, sterile aerobic, and aerobic environments for 6 months and 1 year in unfiltered and filtered water/B100 mixtures.

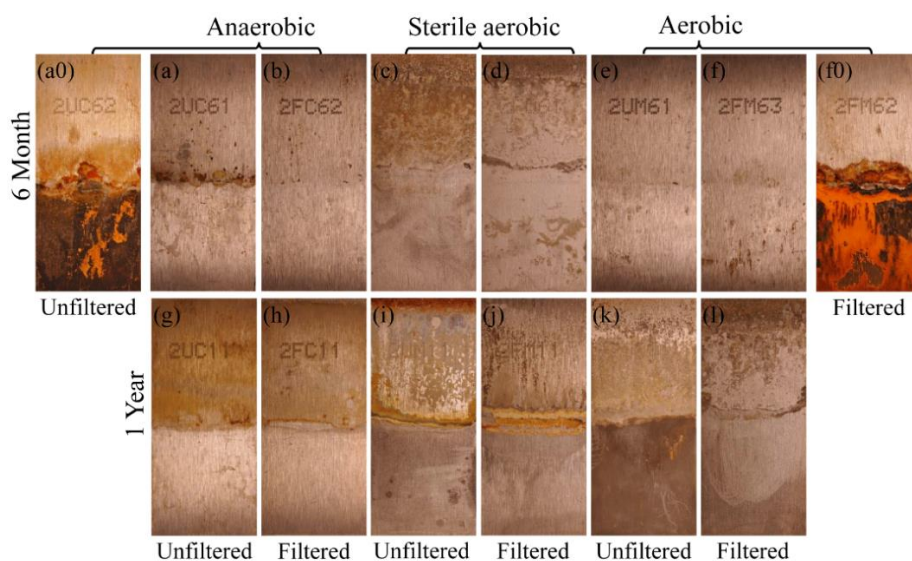


Figure 2.7.0-14. Corrosion morphologies of 1018 steel samples exposed in anaerobic, sterile aerobic, and aerobic environments for 6 months and 1 year in unfiltered and filtered water/B20 mixtures.

Another inconsistency in corrosion morphology occurred on steel immersed in the water phase. For example, one of the 2UC6 samples (i.e., Figure 2.7.0-14a0), two of the 2FC6 samples, and two of the 2FM6 samples (e.g., Figure 2.7.0-14f0) suffered severe corrosion in the water phase, with the formation of black and yellow/red rust. However, the other steel samples from these three triplicates look pristine, both in the water and biodiesel phases. This phenomenon is believed to be related to the air-formed surface iron oxide film on the steel surface. If the air-formed film remains intact, the steel samples can remain pristine when immersed in ultrapure water even for prolonged periods. If the air-form film is breached, for example by scratching, corrosion will initiate. Once corrosion initiates, the formation of corrosion products and the concomitant development of pH gradients can cause corrosion to propagate. This was confirmed with immersion experiments of steel in ultrapure water. It is likely, therefore that any defects on the steel surface such as unintentional scratches formed during sample handling or changes in pH of the water layer due to reaction with the fuel or due to byproducts from microbial activity could initiate corrosion on steel.

The other 12 triplicates showed relatively consistent corrosion morphology among the three samples. Generally, corrosion products formed on the top section of the steel coupon in the fuel layer and at the water/fuel interface, but not on the bottom section in the water layer. One exception is the 1FM6 triplicate, which did not have visible corrosion product on the top section, possibly due to the effect of filtration. Among the samples with corrosion products on the top section in the fuel layer, the 1UC6, 1UM6, 1UO1, 1FO1, 1UM1, and 1FM1 triplicates showed the formation of thick layers of corrosion products. These corrosion products appear light yellow on the 1UO1 and 1FO1 triplicates but are orange on others.

Generally, according to the above observations, it can be observed that steel suffered more severe corrosion in B100 than in B20. In addition, the aerobic and sterile aerobic conditions resulted in more severe corrosion of carbon steel than the anaerobic conditions. Significant corrosion does not always occur on steel in the water phase; and a few exceptions was possibly

caused by defects in the air-formed iron oxide film on steel surface. Finally, the corrosion morphology was featured by the formation of thick corrosion products on steel immersed in water/diesel interface.

XRD analysis: The steel samples immersed in aerobic and sterile aerobic water/B100 mixtures for 1 year had the largest amount of corrosion products on the face-up sides. Typical XRD patterns from these corrosion products (Figure 2.7.0-15a and b) suggest iron formate hydrate ($\text{Fe}(\text{HCOO})_2 \cdot 2\text{H}_2\text{O}$, PDF: #01-074-6933) and iron oxalate hydrate ($\text{FeC}_2\text{O}_4 \cdot 2\text{H}_2\text{O}$, PDF: #00-001-0292) as the major components. However, on the face-down sides of these samples, goethite ($\gamma\text{-FeOOH}$) and lepidocrocite ($\alpha\text{-FeOOH}$) were identified as the corrosion products (Figure 2.7.0-15c). As mentioned earlier, one sample from the anaerobic water/B100 mixture (i.e., 1FC13) showed the formation of a thick layer of orange corrosion products, which was identified as iron formate hydrate (Figure 2.7.0-15d). The relatively weak peaks of Fe as compared to those of iron formate hydrate indicate that the iron formate hydrate had a high coverage on steel.

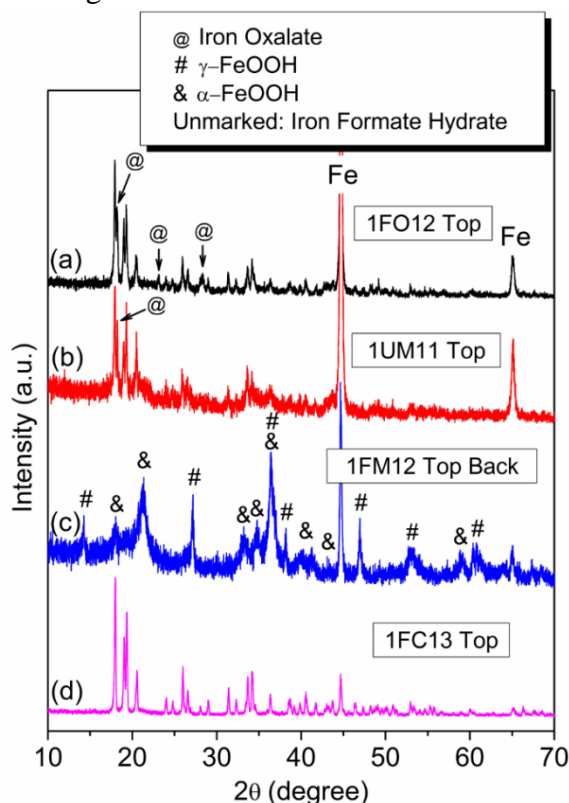


Figure 2.7.0-15. Typical XRD patterns from the corrosion products on steel samples immersed in (a) aerobic, (b) and (c) sterile aerobic, and (d) anaerobic water/B100 mixtures for 1 year.

As mentioned in section 3.1, steel samples in the water/B20 mixtures generally had less corrosion than those in the water/B100 mixtures. The top section of the samples from the water/B20 mixtures had very less corrosion products which usually did not generate strong XRD peaks. However, the sample 2UM63 was an exception, which had a thin layer of iron formate hydrate (Figure 2.7.0-16a) similar to those formed on steel samples immersed in the biodiesel phase of the water/B100 mixtures (Figure 2.7.0-15). Regarding the bottom section of the steel

samples, there were five exceptions (all from the 6-month immersion) which had black and yellow/red rust on steel. One XRD pattern from these corrosion products (Figure 2.7.0-16b) suggests the presence of magnetite (Fe_3O_4) and lepidocrocite. As an example, Figure 2.7.0-16c shows the formation of iron formate hydrate on the top parts of the 1-year samples from the water/B20 mixtures. Notice that the formation of iron formate hydrate occurred on both sides of the top parts of steel samples immersed in water/B20 mixtures, but only the XRD result from the back side is shown in Figure 2.7.0-16c.

The XRD analysis results showed that the orange or light yellow corrosion products formed on steel immersed in the B100 fuel consisted mainly of iron formate hydrate and sometimes accompanied by iron oxalate hydrate. While most samples do not have corrosion products on the bottom sections, a few exceptions showed the formation of magnetite and lepidocrocite on steel immersed in the water phase.

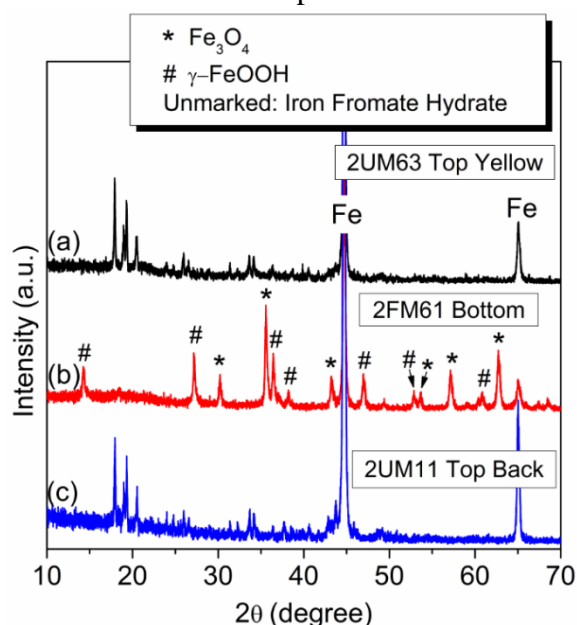


Figure 2.7.0-16. Typical XRD patterns from the corrosion products on steel immersed in water/B20 mixtures for 6 month and 1 year.

Raman analysis: Figure 2.7.0-17 and 2.7.8 present typical Raman spectra from steel samples which had relatively large amount of corrosion products. On the sample 1FO12 that was immersed in an aerobic water/B100 mixture, the orange corrosion products which were identified as iron formate hydrate using XRD did not show any prominent Raman peaks (Figure 2.7.0-17a). The reason might be due to the small amount of this corrosion products. Some white corrosion product coexisting with the orange product showed Raman peaks at 578 and 921 cm^{-1} (Figure 2.7.0-17b), which are possibly from iron oxalate [24, 25]. The orange/white corrosion products formed on steel immersed in the water/B100 interface showed Raman peaks at 287 and 1088 cm^{-1} (Figure 2.7.0-17c), which can be attributed to carbonates that usually precipitates in the cathodic regions [26].

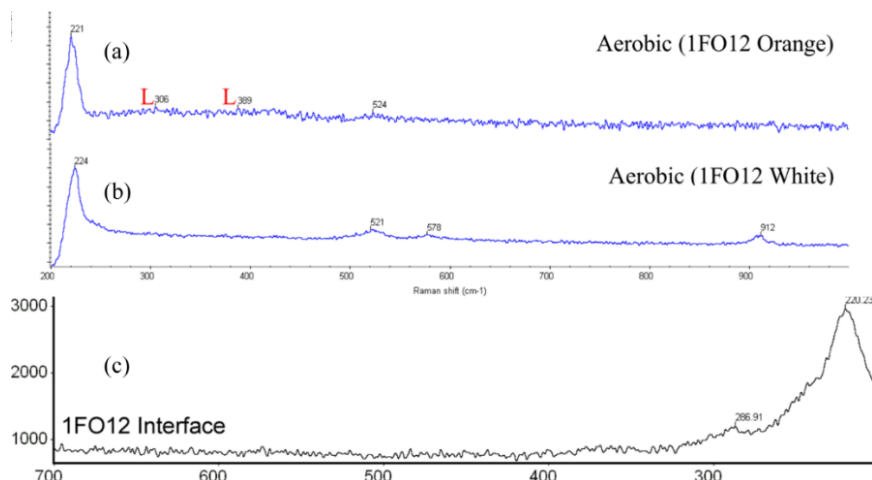


Figure 2.7.0-17. Raman spectra obtained from the corrosion products on the top part of a steel sample (1FO12) immersed in aerobic water/B100 mixture for 1 year.

The orange corrosion products on the top part of a sample immersed in sterile aerobic water/B100 mixture (1UM11) also did not show prominent Raman peaks (Figure 2.7.0-18a). The thick white corrosion products formed on steel immersed in the water/diesel interface generated Raman peaks at 300 and 385 cm^{-1} (Figure 2.7.0-18b). Another sample from the sterile aerobic water/B100 mixture (1FM12) also had orange corrosion product which showed peaks at 295 and 390 cm^{-1} (Figure 2.7.0-18c). These peaks at approximately 300 and 390 cm^{-1} are possibly caused by iron formate hydrate, because the same corrosion products were identified as iron formate hydrate using XRD (Figure 2.7.0-15b).

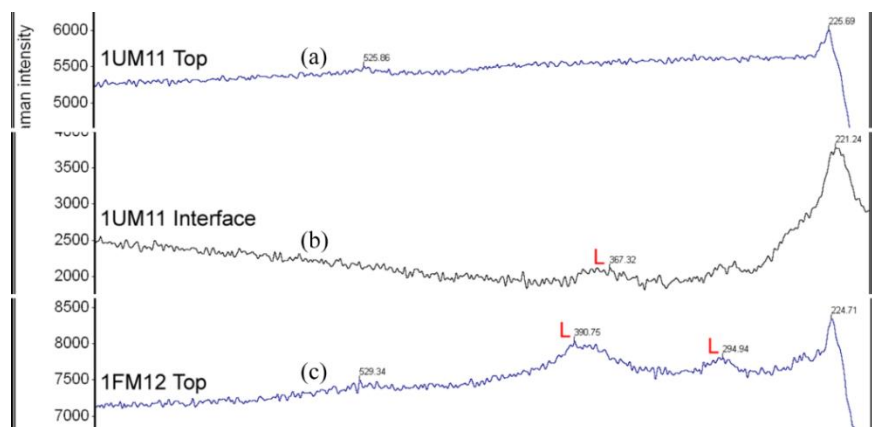


Figure 2.7.0-18. Raman spectra obtained from the corrosion products on the top parts of two steel samples (1UM11 and 1FM12) immersed in sterile aerobic water/B100 mixtures for 1 year.

As mentioned in section 3.1, corrosion occurred on the bottom section of five samples which were immersed in sterile aerobic and anaerobic water/B20 mixtures for 6 months. A Raman spectrum from the orange corrosion product (Figure 2.7.0-19a) indicates the formation of lepidocrocite with major peaks at 247, 304, 345, 373, 525, and 644 cm^{-1} , while that from the black corrosion products (Figure 2.7.0-19b) suggests the presence of magnetite with a peak at 666 cm^{-1} [27-29].

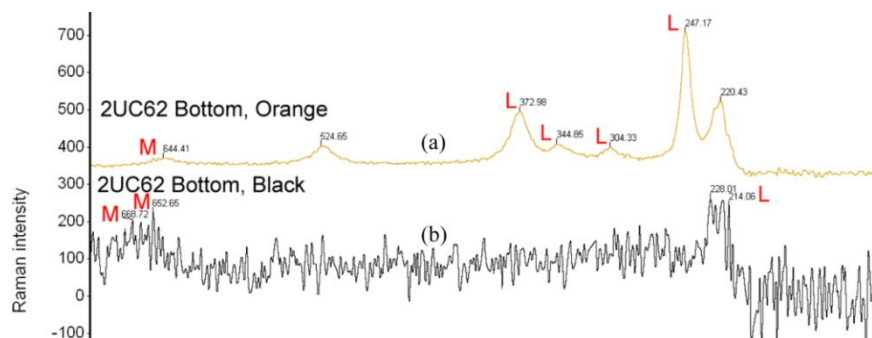


Figure 2.7.0-19. Raman spectra from the corrosion products formed on the bottom of a steel sample (2UC62) immersed in water/B20 mixture for 6 months.

Generally, the Raman spectroscopic analysis of the corrosion products agreed well with the XRD results. Notice that the steel samples exposed in an aerobic environment are missing XRD and Raman analysis since upon sludge removal on the coupons via acetone washing, no corrosion product was detected.

Weight loss analysis: Effect of immersion duration – Generally, the corrosion rates of steel in the four water/diesel mixtures, i.e., water/unfiltered (UF)-B100, water/filtered (F)-B100, water/UF-B20, and water/F-B20, did not change significantly from 6-month to 1-year immersion. This phenomenon was likely due to the relatively low corrosion rates of steel caused by the high solution resistance and very low conductivity of the water/diesel mixtures. However, as an exception, the average corrosion rate of steel samples after 6-month immersion in anaerobic water/UF-B100 mixtures (i.e., 0.0276 ± 0.0012 mpy) was more than 5 times than that of steel samples experienced 1-year immersion (i.e., 0.0008 ± 0.0004 mpy). The huge difference could have been caused by two reasons. Firstly, because the 1-year immersion experiments were started approximately 1 month after the 6-month experiments using the same B100 fuel from the same lot, it is plausible that the population of active bacteria changed during this 1 month period. Secondly, the 1-year samples might have thicker and more protective surface iron oxide films than the 6-month samples due to prolonged storage (1 month) in the dry box [30], and therefore suffered less significant corrosion in the water/biodiesel environments.

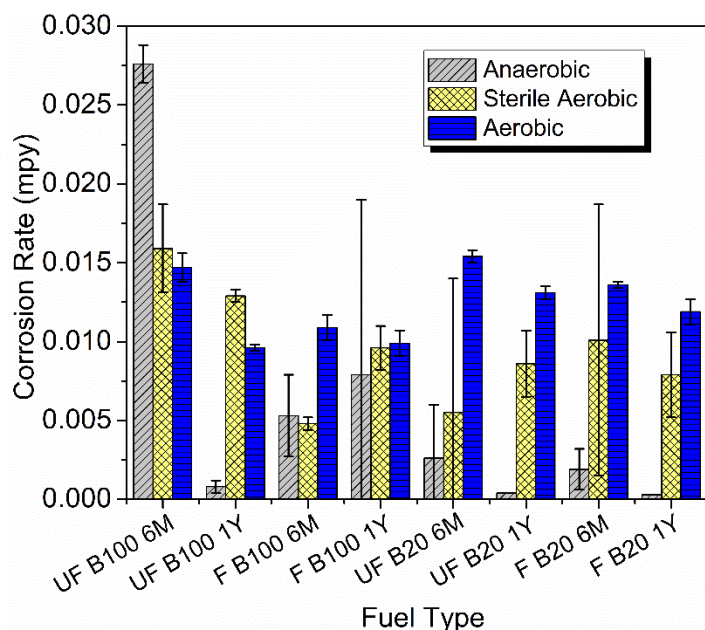


Figure 2.7.0-20. The corrosion rates of 1018 steel samples exposed in water/biodiesel mixtures for 6 months and 1 year.

Effect of fuel types – The corrosion rates of steel samples immersed in aerobic water/B20 mixtures are higher than those immersed in aerobic water/B100 mixtures (Figure 2.7.0-20). This phenomenon is possibly caused by the contamination from outside atmosphere, which appeared to have more significant effects in the water/B20 mixtures than the water/B100 mixtures. No direct correlations could be made between the corrosion rates of steel samples and the other water/fuel types, because there are many exceptional cases where only one or two samples among the triplicate corroded while the others did not. This is indicated by the relatively large error bars in some data in Figure 2.7.0-20, such as the data for anaerobic F-B100-1Y, sterile aerobic UF-B20-6M, and sterile aerobic F-B20-6M. For the sterile aerobic conditions, if taking the exceptional samples out of consideration, the water/B100 mixtures lead to higher corrosion rates of steel than the water/B20 mixtures. For the anaerobic conditions, the corrosion rates of steel samples were usually extremely low in both water/B100 and water/B20 mixtures, with that from anaerobic UF-B100-6M as an extreme exception. As discussed above, the extremely high corrosion rate of steel in anaerobic UF-B100-6M was likely caused by the presence of microorganisms and the non-protective iron oxide film on steel surface.

Effect of filtration – Generally, in aerobic and sterile aerobic conditions, the water/diesel mixtures containing unfiltered biodiesel resulted in higher corrosion rates of steel than the corresponding mixtures with filtered biodiesel, with a few exceptions from the sterile aerobic conditions. However, the change of corrosion rates was not significant, except the UF-B100-6M samples which had much higher corrosion rates than the F-B100-6M samples, for all three environments. As discussed in the above sections, the presence of microorganisms in the B100 diesel was likely the reason for higher corrosion rates. Filtration did not seem to affect the corrosion rates of steel in the anaerobic water/diesel mixtures (UF-B100-6M as an extreme exception), because the anaerobic conditions resulted only in extremely lower corrosion as

compared to the other two aerobic conditions. In the absence of microbial activity that is conducive to corrosion, anaerobic conditions should result in much lower corrosion rates than aerobic conditions since hydrogen-evolution kinetics in the anaerobic environments is slower than oxygen-reduction kinetics in aerated environments.

Effect of different environments (anaerobic, sterile aerobic, and aerobic) – The effect of different environments, i.e., anaerobic, sterile aerobic, and aerobic, on the corrosion rates of steel was more apparent than the effects of immersion duration, fuel types, and filtration. Except the UF-B100 samples, all other combinations in Figure 2.7.0-20 showed that steel samples had the highest corrosion rates in aerobic water/diesel mixtures and relatively lower corrosion rates in sterile aerobic conditions, which indicates that pollutions from the outside atmosphere accelerated the corrosion rates of steel to some extent. The anaerobic conditions resulted the lowest corrosion rates of steel (except UF-B100-6M) among the three conditions, possibly due to the lack of oxygen in the air-tight system. Notice that there are a few samples with virtually no corrosion from both sterile aerobic and anaerobic conditions, all from the 6-month experiments.

Microbial analysis: Bacteria – No microorganisms were detected in any part of the fuel layer of the water/fuel mixtures used in these experiments. This agrees well with literature as microorganisms are only capable of growth when fuels have been contaminated with water [31]. Microbial contamination was only observed in a few fuel samples such as the water/B20 mixtures. All microbial contamination was found within the water/fuel interface or within the water layer itself. Although no direct evidence of bacteria was found in the B100 fuels, the formation of sediments in the fuel within approximately 1 week of dispensing fuel from the pump indicated microbial activity. In addition, filtered B100 fuel did not form sediments and remained lucid for over one year.

The length of duration for the time the samples were exposed most likely decreased the amount of “culturable” microorganisms [32]. According to literature, bacteria seldom experience environmental conditions that allow prolonged continuous growth [33]. On contrary, due to their fast exponential growth cycles, bacteria often consume required nutrients efficiently and because of this, are nutritionally starved most of the time [33]. Bacteria that are nutritionally starved can then enter a stationary phase in which metabolic activities begin to slow down until nutrients are again available [33]. Some bacteria however are unable to survive such extended periods of starvation and die off [33]. In most cases, bacteria are known to enter a viable but nonculturable (VBNC) state [32]. Bacteria in this state fail to grow on routine bacteriological media on which they would normally grow and develop into colonies, but are alive and capable of renewed metabolic activity [32]. Thus, in the case of the 6-month and 1-year experiments, a hypothesis can be made that the majority of microorganisms died off and/or entered into the VBNC state.

Fungi – For the case of the 6-month exposure experiments, a fungi was successfully isolated and identified. This particular fungi was found only within the water/fuel interface regions of the 1018 steel coupons exposed in anaerobic (2UC63) and sterile aerobic (2UM62) unfiltered water/B20 mixtures.



Figure 2.7.0-21. Fungi culture, 18S rRNA sequencing yields a 99% match to the fungi *Paecilomyces saturatus*.

Figure 2.7.0-21 depicts the isolated fungus cultured on specialized fungi media sab dex agar. Successful identification of this fungi was possible through 18S rRNA sequencing. A BLAST database search was performed to identify the specific species of fungi cultured. The BLAST results obtained revealed a 99% match identity to the fungi *Paecilomyces saturatus*. According to literature, *Paecilomyces variotti*, which closely resembles *Paecilomyces saturatus*, is the most commonly occurring species within this genus and is often found in foods, soil, indoor air, and wood [34]. *Paecilomyces* strains are also often heat resistant and may produce mycotoxins in contaminated pasteurized foods [35].

For the case of the 1-year exposure experiment, the same fungi was isolated and cultured from the water/interface regions of the 1018 steel coupons exposed in unfiltered B20 water/fuel mixtures set in an anaerobic environment (2UC13). However this time, no fungi was found in the B20 fuel/water mixtures set in a sterile aerobic environment as was the case in the 6-month exposure.

The fungi and bacteria were the only two types of microorganisms that were isolated from both 6-month and 1-year exposures. Little is known whether or not they play a role in corrosion.

Effects of microorganisms on corrosion of steel – Although few microorganisms were successfully cultured in the lab, their effects on corrosion of 1018 steel can still be noted. Strong evidence for this can be found on the 1018 steel coupons exposed to the water/B100 mixture for the 6 months. As mentioned earlier, the corrosion rate of steel in unfiltered water/B100 mixture in the anaerobic environment was more than 5 times than that in the anaerobic filtered water/B100 mixture. The corrosion rate in the anaerobic unfiltered water/B100 mixture was also approximately 2 times of that in the aerobic unfiltered water/B100 mixture. In the absence of oxygen and microbial activity, the corrosion rate of steel should be lower in the deaerated case compared to the aerated case; hence, the higher rates of corrosion in the anaerobic unfiltered

water/B100 mixture compared to the aerobic case strongly suggest that microbial activity in the deaerated case was the cause of accelerated corrosion. Interestingly, for the 1 year exposure period, the unfiltered and filtered water/B100 mixtures shared similar trends in the corrosion behavior, where the corrosion rates in the anaerobic environment was significantly lower than the aerated environments. This was likely caused by dead or dormant bacteria in the unfiltered B100 fuel. The 1 year exposure experiments were started approximately 1 month after the 6 month exposure experiments using the same B100 fuel from the same lot. It is plausible that the population of active bacteria dwindled during this 1 month period.

Other evidence of microbial activity was observed in both filtered and unfiltered water/B20 mixtures exposed in aerobic conditions. These steel coupons taken from the 6-month and 1-year exposure times all revealed a thick sludge layer characteristic of microbial contamination in the form of biofouling [5, 17, 19]. Figure 2.7.0-22 shows images of a steel coupon before and after acetone washing. Clearly, little to very little corrosion products remain upon acetone washing which indicates that the corrosion products was embedded within the sludge layer. Although numerous attempts of culturing microorganisms from the sludge failed, the sludge formation could be indicative of microbiological activity.

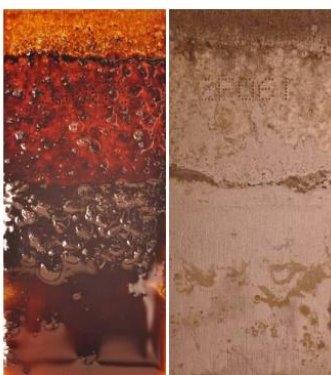
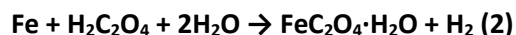
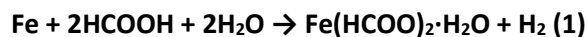


Figure 2.7.0-22. Before and after acetone wash images of 1018 steel samples exposed in aerobic B20 water/diesel mixture.

Corrosion mechanism

As discussed above, most of the steel samples immersed in B100 had a large amount of corrosion products which are either orange or light yellow. These corrosion products were identified as mainly iron formate hydrate and sometimes mixed with iron oxalate hydrate. The formation of iron formate and iron oxalate suggests the presence of organic acids-formic acid and oxalic acid in the B100 fuel, as indicated in equations 1 and 2, respectively.



Generally, the corrosion of steel immersed in water phase did not suffer severe corrosion. The corrosion products were easily removed by acetone washing, indicating only superficial corrosion. Some of the samples after immersion in the water/B20 mixtures even look pristine on the bottom regions of the samples. Only a few exceptions (i.e., Figure 2.7.0-14a0 and 2.7.4f0) had severe corrosion on the bottom regions of the steel samples, with the formation of lepidocrocite and magnetite. Lepidocrocite is always the initial form of corrosion product of steel in aqueous environment [27, 36, 37], while magnetite forms in environments with less oxygen [38-40].

The following was concluded based on the results from the static immersion tests of carbon steel in water/biodiesel mixtures with different environments:

1. According to the corrosion morphology, in both anaerobic and sterile aerobic conditions, carbon steel generally suffered more severe corrosion in water/B100 mixtures than in water/B20 mixtures. Corrosion rates, however, showed contrary results due to a few exceptional examples that experienced severe corrosion in the water phase. The corrosion rates also showed that, in aerobic conditions, all water/B20 mixtures resulted in more significant corrosion of carbon steel than the water/B100 mixtures, which was not obvious from visual observation due to the removal of loose corrosion products by acetone washing.
2. The orange corrosion products formed on steel immersed in the B100 phase were identified as mainly iron formate hydrate which sometimes coexist with iron oxalate hydrate. The orange and black corrosion products formed on some steel samples in the water phase were identified as lepidocrocite and magnetite, respectively.
3. The effect of filtrating microorganisms on the corrosion of carbon steel were significant for the 6-month water/B100 mixtures in all three environments, but not for other combinations. The possible presence of microorganisms in the unfiltered B100 fuel resulted in steel samples immersed in unfiltered water/B100 mixtures for 6 months having corrosion rates more than 5 times of those from the filtered water/B100 mixtures.
4. Steel samples had the highest corrosion rates in aerobic water/diesel mixtures, relatively lower corrosion rates in sterile aerobic conditions, and the lowest corrosion rates in anaerobic conditions due to the lack of oxygen to drive that cathodic oxygen-reduction reaction. The opposite trend found in steel in unfiltered water/B100 mixture in the anaerobic environment indicating the presence of microbial activity that was conducive to accelerating corrosion.

References

- [1] P. McCarthy, M.G. Rasul, S. Moazzem, Analysis and comparison of performance and emissions of an internal combustion engine fuelled with petroleum diesel and different bio-diesels, *Fuel*, 90 (2011) 2147-2157.
- [2] A.S.M.A. Haseeb, M.A. Fazal, M.I. Jahirul, H.H. Masjuki, Compatibility of automotive materials in biodiesel: A review, *Fuel*, 90 (2011) 922-931.

- [3] M.A. Jakab, S.R. Westbrook, S.A. Hutzler, Testing for compatibility of steel with biodiesel, SwRI® Project No. 08.13070, Southwest Research Institute, (2008).
- [4] M.M. Maru, M.M. Lucchese, C. Legnani, W.G. Quirino, A. Balbo, I.B. Aranha, L.T. Costa, C. Vilani, L.Á. de Sena, J.C. Damasceno, T. dos Santos Cruz, L.R. Lidizio, R. Ferreira e Silva, A. Jorio, C.A. Achete, Biodiesel compatibility with carbon steel and HDPE parts, *Fuel Processing Technology*, 90 (2009) 1175-1182.
- [5] M.A. Fazal, A.S.M.A. Haseeb, H.H. Masjuki, Effect of temperature on the corrosion behavior of mild steel upon exposure to palm biodiesel, *Energy*, 36 (2011) 3328-3334.
- [6] E. Hu, Y. Xu, X. Hu, L. Pan, S. Jiang, Corrosion behaviors of metals in biodiesel from rapeseed oil and methanol, *Renewable Energy*, 37 (2012) 371-378.
- [7] D.M. Fernandes, R.H.O. Montes, E.S. Almeida, A.N. Nascimento, P.V. Oliveira, E.M. Richter, R.A.A. Muñoz, Storage stability and corrosive character of stabilised biodiesel exposed to carbon and galvanised steels, *Fuel*, 107 (2013) 609-614.
- [8] D. Jin, X. Zhou, P. Wu, L. Jiang, H. Ge, Corrosion behavior of ASTM 1045 mild steel in palm biodiesel, *Renewable Energy*, 81 (2015) 457-463.
- [9] C.E. Akhabue, F.A. Aisien, C.O. Ojo, The effect of Jatropha oil biodiesel on the corrosion rates of aluminium and mild carbon steel, *Biofuels*, 5 (2014) 545-550.
- [10] A.S.M.A. Haseeb, H.H. Masjuki, L.J. Ann, M.A. Fazal, Corrosion characteristics of copper and leaded bronze in palm biodiesel, *Fuel Processing Technology*, 91 (2010) 329-334.
- [11] M.A. Fazal, A.S.M.A. Haseeb, H.H. Masjuki, Comparative corrosive characteristics of petroleum diesel and palm biodiesel for automotive materials, *Fuel Processing Technology*, 91 (2010) 1308-1315.
- [12] M.A. Fazal, A.S.M.A. Haseeb, H.H. Masjuki, Degradation of automotive materials in palm biodiesel, *Energy*, 40 (2012) 76-83.
- [13] I.P. Aquino, R.P.B. Hernandez, D.L. Chicoma, H.P.F. Pinto, I.V. Aoki, Influence of light, temperature and metallic ions on biodiesel degradation and corrosiveness to copper and brass, *Fuel*, 102 (2012) 795-807.
- [14] M.A. Fazal, A.S.M.A. Haseeb, H.H. Masjuki, Corrosion mechanism of copper in palm biodiesel, *Corrosion Science*, 67 (2013) 50-59.
- [15] S. Norouzi, K. Hazeri, M.L. Wyszynski, A. Tsolakis, Investigation on the effects of temperature, dissolved oxygen and water on corrosion behaviour of aluminium and copper exposed to diesel-type liquid fuels, *Fuel Processing Technology*, 128 (2014) 220-231.
- [16] S. Kaul, R.C. Saxena, A. Kumar, M.S. Negi, A.K. Bhatnagar, H.B. Goyal, A.K. Gupta, Corrosion behavior of biodiesel from seed oils of Indian origin on diesel engine parts, *Fuel Processing Technology*, 88 (2007) 303-307.
- [17] L. Díaz-Ballote, J.F. López-Sansores, L. Maldonado-López, L.F. Garfias-Mesias, Corrosion behavior of aluminum exposed to a biodiesel, *Electrochemistry Communications*, 11 (2009) 41-44.
- [18] D.P. Geller, T.T. Adams, J.W. Goodrum, J. Pendergrass, Storage stability of poultry fat and diesel fuel mixtures: Specific gravity and viscosity, *Fuel*, 87 (2008) 92-102.
- [19] Q. Lu, J. Zhang, X. Zhu, Corrosion properties of bio-oil and its emulsions with diesel, *Chin. Sci. Bull.*, 53 (2008) 3726-3734.
- [20] W. Wang, P.E. Jenkins, Z. Ren, Heterogeneous corrosion behaviour of carbon steel in water contaminated biodiesel, *Corrosion Science*, 53 (2011) 845-849.
- [21] F. Gui, J. James, N. Sridhar, Corrosion Study of Carbon Steel in Biodiesel and Water Mixture Using Multielectrode Array, *Corrosion*, 68 (2012) 827-834.
- [22] W. Wang, P.E. Jenkins, Z. Ren, Electrochemical corrosion of carbon steel exposed to biodiesel/simulated seawater mixture, *Corrosion Science*, 57 (2012) 215-219.
- [23] D.F. Aktas, J.S. Lee, B.J. Little, R.I. Ray, I.A. Davidova, C.N. Lyles, J.M. Suflita, Anaerobic Metabolism of Biodiesel and Its Impact on Metal Corrosion, *Energy & Fuels*, 24 (2010) 2924-2928.
- [24] R.L. Frost, Raman spectroscopy of natural oxalates, *Analytica Chimica Acta*, 517 (2004) 207-214.
- [25] Q. Ma, H. He, C. Liu, Hygroscopic properties of oxalic acid and atmospherically relevant oxalates, *Atmospheric Environment*, 69 (2013) 281-288.

- [26] S. Li, J. Kealoha, L.H. Hihara, Corrosion of Low-Carbon Steel in Seawater/Biodiesel Mixtures – a Study Related to the Corrosion of Fuel Tanks in Ships, in: CORROSION 2015, NACE International, Dallas, TX, 2015.
- [27] S. Li, L.H. Hihara, In situ Raman spectroscopic study of NaCl particle-induced marine atmospheric corrosion of carbon steel, J. Electrochem. Soc., 159 (2012) C147-C154.
- [28] S. Li, L.H. Hihara, In situ Raman spectroscopic identification of rust formation in Evans' droplet experiments, Electrochem. Commun., 18 (2012) 48-50.
- [29] S. Li, L.H. Hihara, Aerosol salt particle deposition on metals exposed to marine environments: a study related to marine atmospheric corrosion, J. Electrochem. Soc., 161 (2014) C268-C275.
- [30] S. Li, L.H. Hihara, Atmospheric-Corrosion Electrochemistry of NaCl Droplets on Carbon Steel, J. Electrochem. Soc., 159 (2012) C461-C468.
- [31] B. Klotfutar, J. Golob, Microorganisms in Diesel and in Biodiesel Fuels, Anglais, 54 (2007) 744-748.
- [32] J.D. Oliver, The viable but nonculturable state in bacteria, J Microbiol., 43(S) (2005) 93-100.
- [33] R. Kolter, D.A. Siegle, A. Tormo, The stationary phase of the bacterial life cycle, Annual review of microbiology, 47 (1993) 855-874.
- [34] J. Houbraken, P.E. Verweij, A.J. Rijs, A.M. Borman, R.A. Samson, Identification of *Paecilomyces variotii* in clinical samples and settings, Journal of clinical microbiology, 48 (2010) 2754-2761.
- [35] R.A. Samson, J. Houbraken, J. Varga, J.C. Frisvad, Polyphasic taxonomy of the heat resistant ascomycete genus *Byssosclamyces* and its *Paecilomyces* anamorphs, Persoonia, 22 (2009) 14-27.
- [36] J. Kassim, T. Baird, J.R. Fryer, Electron microscope studies of iron corrosion products in water at room temperature, Corrosion Science, 22 (1982) 147-158.
- [37] J.G. Castaño, C.A. Botero, A.H. Restrepo, E.A. Agudelo, E. Correa, F. Echeverría, Atmospheric corrosion of carbon steel in Colombia, Corrosion Science, 52 (2010) 216-223.
- [38] T. Misawa, K. Asami, K. Hashimoto, S. Shimodaira, The mechanism of atmospheric rusting and the protective amorphous rust on low alloy steel, Corrosion Science, 14 (1974) 279-289.
- [39] K. Rösler, H. Baum, O. Kukurs, A. Upite, D. Knotkova, Character and behavior of a layer of corrosion products on low-alloy steels in natural conditions, Protection of Metals, 17 (1981) 514-522.
- [40] S. Li, L.H. Hihara, A Micro-Raman Spectroscopic Study of Marine Atmospheric Corrosion of Carbon Steel: The Effect of Akaganeite, J. Electrochem. Soc., 162 (2015) C495-C502.

2.8 Waste Management Using the Flash-Carbonization™ Process

Past efforts under this task studied the Flash Carbonization™ process applied to various waste products and the characterization and use of the resulting biocarbons for downstream applications including carbon fuel cells. The present study continued this work and reports on fundamental measurements of the specific heat of water at elevated temperature and pressure to produce data needed to inform carbon fuel cell system design.

Scope of Work and Approach

The present work reports experimental results concerning the specific isobaric heat capacity of pure water at elevated pressure. Experiments were performed using a Tian-Calvet differential scanning calorimeter (Setaram Model BT2.15), at temperatures ranging from 298.15 to 465.65 K and at a constant pressure of 4.0 MPa. The aim of this study is to compare the new experimental results with values predicted by the IAPWS-95 formulation, which is generally accepted as reliable by the scientific community despite the fact that, in this formulation, nearly all the data for the isobaric heat capacity of water are based on measurements of Sirota's group in the former

Soviet Union in the period from 1956 to 1970. The present calorimetric results for the specific heat capacity of pure water were found to be substantially in disagreement with the values obtained using the IAPWS-95 formulation, especially at high temperatures, where the differences were greater than 20%.

Technical Accomplishments

The calorimetric results obtained for the specific heat capacity of pure water at 4.0 MPa are clearly in disagreement with the values obtained using the IAPWS-95 formulation, especially at high temperatures. On the basis of these findings, the need for the research community to revisit the calorimetric measurements of the heat capacity of liquid water at high temperatures and pressures is emphasized.

The results reported should be confirmed independently. The stepwise heating program adopted in the present study involves a certain degree of uncertainty because the experimental time consumed between two isotherms is not enough to completely stabilize the heat flow signal. In addition, the theoretical correction of the vapor contribution, by means of an approximate form of the Clausius-Clapeyron equation, might add a certain level of uncertainty to the heat capacity values reported in the present study. Nevertheless, this correction accounts for only a small portion of the disagreement between the present data and those reported in the literature. Conducting more extensive experimental studies, focused on the measurement of the specific heat of pure water at different pressures and temperatures, should be a priority for the international research community in order to confirm the trends found in this work. In the short term, it seems advisable to perform a round-robin study, for the measurement of the specific heat capacity of pure water, involving several different types of calorimeters (and cells) and different heat flow quantification techniques. Complete details of this subtask are presented in the publication:

Manyà, J.J., M.J. Antal, Jr. C.K. Kinoshita, and S.M. Masutani. 2011. Specific heat capacity of pure water at 4.0 MPa between 298.15 and 465.65 K. *Industrial & Engineering Chemistry Research*. 50, pp. 6470-6484.

The full manuscript is available at:

<http://pubs.acs.org/doi/abs/10.1021/ie102462g>

TASK 3. METHANE HYDRATES

Objectives

Methane hydrates in ocean sediments constitute an enormous energy reservoir that is estimated to exceed the energy content of all known coal, oil, and conventional natural gas resources. Located on continental margins throughout the world, methane hydrates offer unique opportunities as an onsite source of fuel for various marine applications and are believed to play a major role in seafloor stability and global climate.

National R&D programs on methane hydrates were initiated in Japan and India in the mid-1990's with the goal of commercial gas production within a 20 year time horizon. The U.S. established its own program in May 2000. The Methane Hydrate Research and Development Act of 2000 (Public Law 106-193) included seven technical areas of focus: (1) identification, exploration, assessment, and development of methane hydrate as a source of energy; (2) technology development for efficient and environmentally sound recovery of methane from hydrates; (3) transport and storage of methane produced from methane hydrates; (4) education and training related to methane hydrate resource R&D; (5) assessment and mitigation of environmental impacts of natural and purposeful hydrate degassing; (6) development of technologies to reduce the risks of drilling through methane hydrates; and (7) support of exploratory drilling projects. The objectives of the Methane Hydrates Task of the HEET initiative, which was initiated in 2001, reflect most of the priorities of P.L. 106-193, but emphasize those areas of particular relevance to the Office of Naval Research (ONR) and which are consistent to the overall goals of HEET. Specifically, the development of hydrates and related sources of seafloor methane as logistical fuels for Naval applications and related marine environmental issues, have been the principal areas of interest; exploratory drilling projects and seafloor stability/safety have received limited attention. Work also has been initiated to explore engineering applications of hydrates such as desalination and hydrogen storage. Task objectives were devised to fully leverage hydrate R&D expertise and infrastructure that had been developed at HNEI during previous research programs on CO₂ ocean sequestration and deep oil spills.

The goals of the HEET09 Methane Hydrates Task were:

- Pursue development of methods to recover methane gas from hydrates.
- Investigate the microbial processes in sediment and the water column that generate and modulate methane levels.
- Investigate engineering applications of hydrate.
- In cooperation with NRL and ONR Global (previously ONR-IFO), promote international collaborative research on methane hydrates.

Specific technical initiatives that were pursued to attain the above goals included:

- Conduct laboratory experiments on hydrate destabilization using chemical inhibitors using differential scanning calorimetry (DSC).
- Investigate hydrate stability in porous media.
- Continue development of a 3D model of methane transport through the ocean water column and construct submodels of methane production and oxidation that can be incorporated into an ocean general circulation model.
- Investigate the mechanisms of microbial methane metabolism in ocean sediment; and methane generation and consumption in the water column.
- Conduct experiments to assess the feasibility of hydrate biofiltration.
- Organize workshops to promote international collaboration on methane hydrate R&D.

Scope of Work and Approach

Pursuant to the goals and technical objectives identified in the preceding section, work on the HEET09 Methane Hydrates Task focused on four primary areas which are described below.

Subtask 3.1 Hydrate Energy

A major priority of this subtask was to elucidate the fundamental mechanism of methane hydrate destabilization for the purpose of producing fuel gas and, to a lesser extent, to clear hydrate blockages that can form in natural gas conduits or deep ocean oil wells (such as occurred during the 2010 Deepwater Horizon incident in the Gulf of Mexico). Toward that end, we continued our experimental studies of hydrate destabilization by reagent injection. In a departure from our earlier work, we focused on non-conventional hydrate inhibitors. Specifically, DSC) was employed to explore the effects of transition metal salts, which can be found in seawater, on the behavior of clathrate hydrates. Work also was continued on investigating the stability of hydrates in porous media such as seafloor sediment and Arctic permafrost.

Subtask 3.2 Environmental Impacts of Methane Release from Seafloor Hydrates

This subtask is a continuation of activities pursued in previous years to: (1) assess the consequences of inadvertent or purposeful releases of methane from seafloor hydrates via the development of a model of methane transport through the ocean water column to the atmosphere; and (2) elucidate the mechanisms by which microbes generate and consume methane in seafloor sediment, the oceanic water column, and arctic permafrost.

Subtask 3.3 Hydrate Engineering Applications

The major priority of this subtask was to conduct exploratory studies of the use of gas hydrates for various engineering applications relevant to DOD interests. Previously, we investigated desalination and H₂ storage. During the present phase of the HEET Initiative, experiments were performed to assess the feasibility of employing hydrates to remove biological contaminants from drinking or process water.

Subtask 3.4 International Collaborative Research and Development

To promote international R&D cooperation on methane hydrates in order to accelerate development of this energy resource, HNEI has sponsored and helped to organize a series of workshops on methane hydrates that was started under the HEET initiative in 2001. During the current phase, the objective of this subtask was to provide logistical and organizational support for the 8th Workshop held in Sapporo, Japan.

Technical Accomplishments

The principal technical accomplishments of the HEET09 Methane Hydrates Task for each of the components identified above are described in the following sections.

3.1 Hydrate Energy

The primary accomplishments of this subtask were: (1) completed an initial set of experiments to investigate the effects of transition metal salts on the behavior of clathrate hydrates; and (2) completed a study of hydrate formation and dissociation in sand matrices. The investigation of hydrate kinetics and equilibrium in sand comprised the M.S. thesis research of a graduate student in the Department of Ocean and Resources Engineering at UH.

Reagent Destabilization of Methane Hydrates

Formation of clathrate hydrates has been prevented by thermodynamic inhibitors such as alcohols and salts. These inhibitors shift the equilibrium between the three phases, hydrate (H), liquid water (Lw), and guest molecular vapor (V), to lower temperature or higher pressure (Sloan & Koh, 2008). Per the Gibb's Phase Rule, a second intensive variable (in addition to either pressure or temperature) is needed to specify the three-phase binary system with an inhibitor. The concentration of the inhibitor is typically employed as the second intensive variable; therefore, alcohols and salts, which have considerable solubility in the aqueous phase, have the potential to be effective inhibitors of hydrate formation. It has been posited that dissolved inhibitors tie up water molecules needed for hydrate formation through hydrogen bonding in the case of alcohols and glycols, or via Coulombic forces for salt ions (Sloan & Koh 2008).

Alcohols frequently are employed by the oil industry to avoid hydrate blockages in natural gas pipelines since the potential for undesirable side reactions (such as corrosion) is low relative to salts; however, amounts needed may reach 50 wt% (aq), leading to high costs and disposal problems (Kelland, 1995; Dholabhai *et al.*, 1997). In addition to alcohols and ionic salts, other inhibitors include kinetic inhibitors, like polyvinyl caprolactam (PVCap) or polyvinylpyrrolidone (PVP) and ionic liquids, e.g., dialkylimidazolium halide compounds, which have been studied more recently (Sloan *et al.*, 1996; Xiao & Adidharma, 2009). Kinetic inhibitors are quite effective in delaying the crystallization of gas hydrates (Sloan *et al.*, 1996), whereas ionic liquids exhibit both thermodynamic and kinetic inhibition features (Xiao & Adidharma, 2009).

Studies have been conducted to investigate the roles played by cations and anions in the inhibition of hydrate formation (Lu *et al.*, 2001; Sabil *et al.*, 2010). Lu *et al.* (2001) compared the effects of salts with different cations and anions on hydrate phase equilibria of CO₂, CH₄, and C₃H₈ hydrates. In particular, they compared CH₃CO₂Na versus CH₃CO₂H at different concentrations and found that the stability of CO₂ hydrate was affected by the concentration of CH₃CO₂⁻ and CH₃CO₂H but not Na⁺. In addition, it was observed that there was a larger shift in the equilibrium temperature of methane hydrate with MgSO₄ versus MgCl₂, but not a very large difference between NaCl versus KCl and CaCl₂. They concluded that the anion has a greater influence on hydrate stability than the cation, and posited that difference was due to interactions between liquid water molecules and ions (i.e., hydration effects)

Sabil *et al.* (2010) compared the effects of salts with different cations and anions on hydrate phase equilibria of mixed CO₂/THF hydrates using a Caillettet apparatus. Their observations did not support the conclusions of Lu *et al.* (2001). They found that the inhibiting effect increased in the following order: NaF < KBr < NaCl < NaBr < CaCl₂ < MgCl₂, and concluded that the inhibition of the hydrate increased with the charge of the cation, and the radius of the anion. They proposed that this trend was the result of the strength of the ion-hydrogen bonds which acts either to disrupt or to reinforce the ambient water networks. In their study, it was noted that the electrolyte inhibitors completely negate the hydrate-promoting effect of THF.

The mechanism underlying the influence of salts on hydrate stability has not been clearly identified and warrants additional study, insofar as this has relevance to a host of engineering and scientific issues including the development of new reagents for flow assurance in natural gas

pipelines and the formation and dissociation of hydrates in the seafloor and in permafrost. Toward this end, we conducted experiments to explore the behavior of clathrate hydrates in the presence of transition metal salts using DSC (Kharrat & Dalmazzone, 2003; Koh *et al.*, 2009; Jager *et al.*, 2002; Gupta *et al.*, 2008; Lafond *et al.*, 2012). Specifically, DSC was employed to determine the onset temperature for methane hydrate decomposition in the presence of ferric chloride hexahydrate, $[\text{FeCl}_2(\text{H}_2\text{O})_4]\text{Cl}\cdot 2\text{H}_2\text{O}$ (Lind, 1967), anhydrous ferric chloride, FeCl_3 , MnSO_4 , FeSO_4 , and CuSO_4 , and to compare the inhibiting properties of these transition metal salts with NaCl and CaCl_2 , two well-known salt inhibitors.

Experimental Materials and Methods

Shown in Figure 3.1 is a schematic diagram of the system used to perform the experiments. The primary component of the system is a Multi-Cell μDSC . This DSC has the capability of testing three samples simultaneously and has a detection limit of $0.2\ \mu\text{W}$ over an operating temperature range of about 233K to 433K ($-40.0\ ^\circ\text{C}$ to $160.0\ ^\circ\text{C}$) and pressures up to 40 MPa. The Hastelloy sample cells have a volume of 0.5 ml.

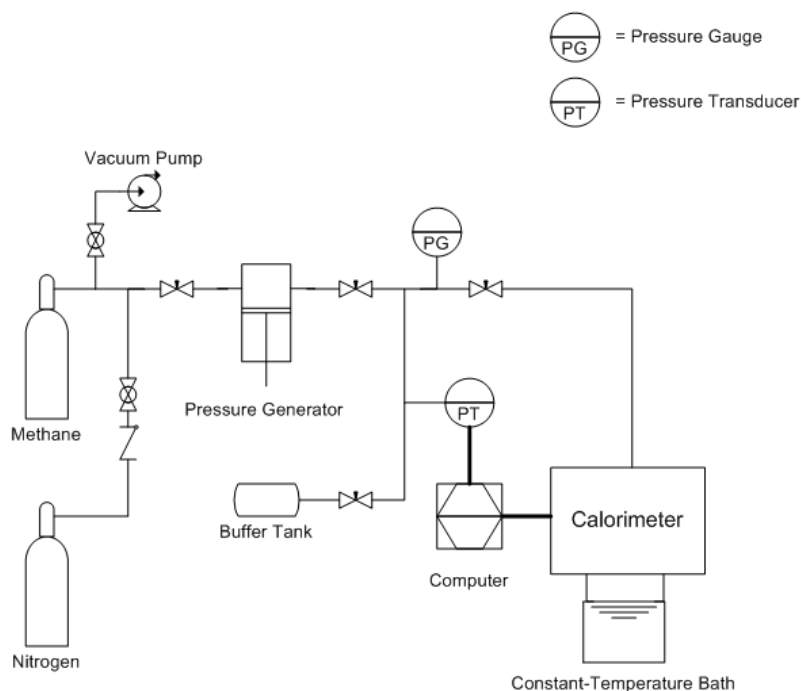


Figure 3.1 Schematic diagram of the Multi-Cell Differential Scanning Calorimeter system.

The sample cells are pressurized through capillary tubing attached to the cell closures. The capillary tubing is connected to the gas supply system which provides either Grade 4.0 (99.99% purity) methane or nitrogen (for purging). Gas pressure in the cells can be adjusted with a manually-operated, piston screw pump pressure generator and is monitored using a pressure transducer with an accuracy of 0.0345 MPa. To prevent significant pressure swings from occurring during hydrate formation and decomposition, a small gas reservoir is integrated into the supply system to act as a buffer tank.

Prior to running experiments, the calorimeter temperature was calibrated against the freezing point of pure water. Aqueous solutions of the salts were then prepared gravimetrically using an analytical balance (accuracy 0.0001 g). Sodium chloride (99.8% assay) and anhydrous ferric chloride (laboratory grade) were mixed with distilled and deionized water to the appropriate molar concentrations. Due to the hygroscopic nature of anhydrous ferric chloride, the ferric chloride samples were prepared in a nitrogen-filled glove bag. The solutions were then transferred into the high pressure sample cells, and the cells were placed in the calorimeter. A vacuum pump was employed to evacuate the gas lines which were then purged with nitrogen, vacuum evacuated again, and pressurized with methane. The cells were cooled from 298K to 243K (25°C to -30°C) at a rate of 2K/minute and held at 243K for 30 minutes to ensure complete crystallization. The cells were then slowly warmed from 243K to 298K at a rate of 0.25K/minute. This temperature cycle was repeated at least 2 times for each test.

Figure 3.2 shows representative thermograms of water and methane at different pressures as the samples were slowly heated from about 248K to 293K. The large negative (endothermic) peak corresponds to the melting of ice. The smaller peaks that occur at higher temperatures are due to the dissociation of the methane hydrate. As indicated in the insert, the onset temperature of dissociation of the methane hydrate is determined by the intersection of the local (horizontal) baseline of the thermogram and a best-fit line whose slope matches the rate of descent of the thermogram. This approach was employed to compare the methane hydrate dissociation temperature shifts induced by the different salts employed in this investigation.

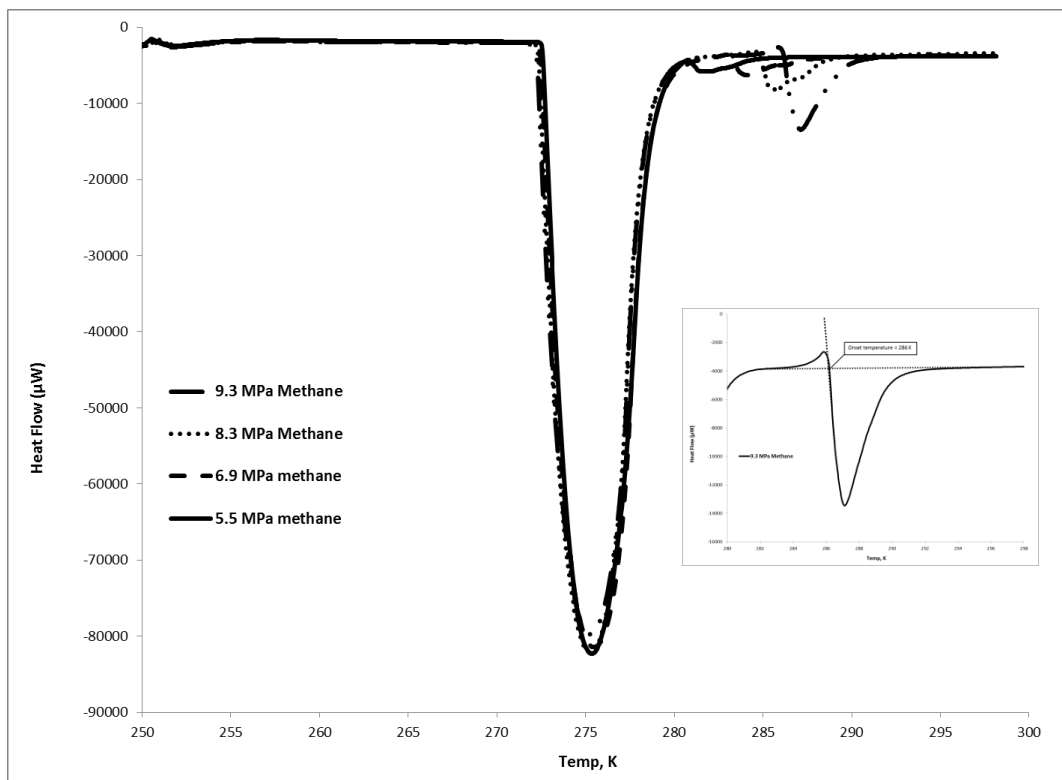


Figure 3.2 Representative thermograms of water and methane at different pressures.

Results

To assess the ability of the DSC method accurately to measure hydrate phase transitions, the dissociation temperatures of methane hydrate determined in replicate experiments conducted with our DSC are compared with data provided in Sloan and Koh (2008) in Figure 3.3. The DSC results appear to agree reasonably well with those data.

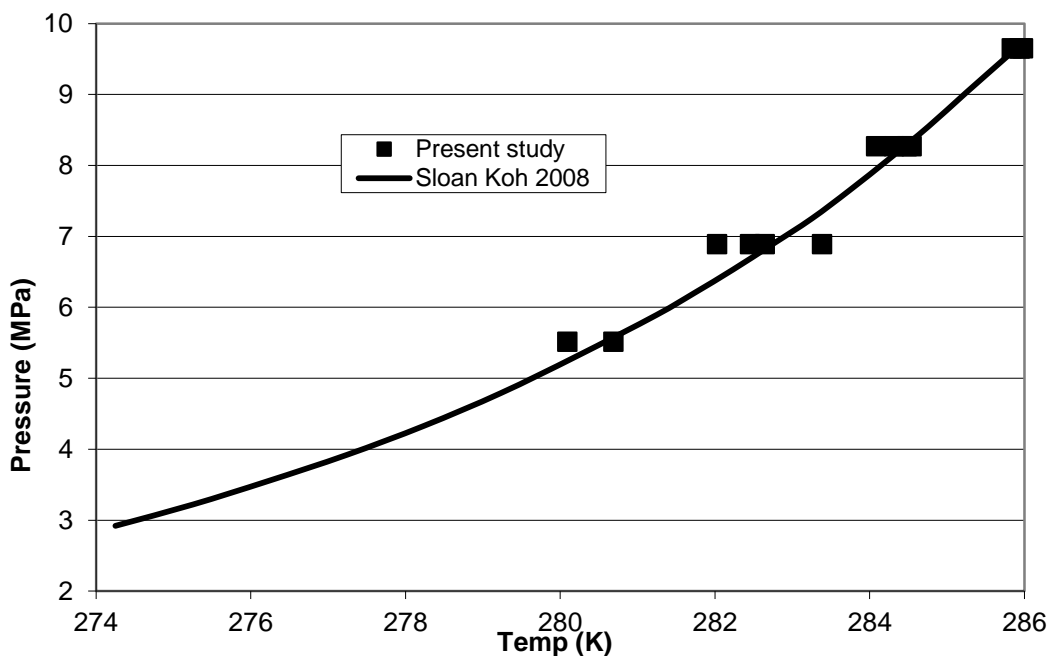


Figure 3.3 Comparison of data on methane hydrate stability boundary obtained in this investigation with earlier results published by Sloan & Koh (2008).

Table 3.1 summarizes the measured onset temperatures of methane hydrate dissociation at 5.51, 6.89, 8.27, and 9.65 MPa for solutions containing different concentrations of the inhibitors examined in this study. The NaCl results are shown in Figure 3.4, along with the published data from Roo *et al.* (1983). Good agreement is observed for 3.94 mol% NaCl.

Table 3.1 Onset Temperature for Dissociation of Methane Hydrate at Different Pressures

| | CH ₄ Pressure (MPa) | 5.51 | | 6.89 | | 8.27 | | 9.65 | |
|-----------|--------------------------------|-----------------------|-----|-----------------------|-----|-----------------------|-----|-----------------------|----|
| Inhibitor | Inhibitor (mol%) | T _{diss} (K) | ΔT | T _{diss} (K) | ΔT | T _{diss} (K) | ΔT | T _{diss} (K) | ΔT |
| None | 0 | 280.7 | - | 282.6 | - | 284.3 | - | 286 | - |
| NaCl | 0.5 | 279.8 | 0.9 | 282.2 | 0.4 | 283.7 | 0.6 | 285 | 1 |

| | | | | | | | | | |
|-------------------|------|-------|------|-------|------|-------|------|-------|------|
| | 1 | 279.1 | 1.6 | 281.4 | 1.2 | 283.2 | 0.9 | 277 | 3.7 |
| | 2 | 277 | 3.7 | 279.4 | 3.2 | 281.2 | 3.2 | 282.6 | 3.8 |
| | 3.94 | 275.8 | 4.9 | 276.8 | 5.8 | 278.6 | 5.7 | - | - |
| FeCl ₃ | 0.5 | 281.9 | 0.7 | 283.5 | 0.8 | 284.8 | 0.5 | 277.3 | 3.4 |
| | 1 | 277.3 | 3.4 | 279 | 3.6 | 281.1 | 3.2 | 283.4 | 3.9 |
| | 2 | 273.1 | 7.6 | 273.1 | 9.5 | 275.1 | 9.3 | 275.4 | 10.6 |
| | 3.94 | - | - | - | - | - | - | - | - |
| MnSO ₄ | 0.5 | 281.0 | -0.3 | 283.0 | -0.4 | 284.5 | -0.2 | 286.2 | -0.2 |
| | 1 | 280.2 | 0.5 | 282.3 | 0.3 | 283.6 | 0.7 | 285.3 | 0.7 |
| | 2 | 279.2 | 1.5 | 281.5 | 1.1 | 283.2 | 1.1 | 284.1 | 1.9 |
| FeSO ₄ | 0.5 | 281.2 | -0.5 | 283.3 | -0.7 | 285.2 | -0.9 | 286.0 | 0.0 |
| | 1 | 280.4 | 0.3 | 282.6 | 0 | 284.5 | -0.2 | 285.5 | 0.5 |
| | 2 | 280.3 | 0.4 | 282.2 | 0.4 | 284.3 | 0 | 285.3 | 0.7 |
| CuSO ₄ | 0.5 | 280.7 | 0 | 283.4 | -0.8 | 285.0 | -0.7 | 286.5 | -0.5 |
| | 1 | 280.7 | 0 | 282.8 | -0.2 | 284.6 | -0.3 | 286.0 | 0 |
| | 2 | 280.4 | 0.3 | 282.5 | 0.1 | 284.2 | 0.1 | 285.4 | 0.6 |
| CaCl ₂ | 0.5 | 280.6 | 0.1 | 283 | -0.4 | 284.6 | -0.3 | 282.6 | 3.4 |
| | 1 | 279.5 | 1.2 | 281.9 | 0.7 | 283.6 | 0.7 | 281.9 | 4.1 |
| | 2 | 279.3 | 1.4 | 281.6 | 1 | 283.3 | 1 | 281.2 | 4.8 |

Notes:

$$\Delta T = T_{\text{diss}} (\text{no inhibitor}) - T_{\text{diss}} (\text{inhibitor})$$

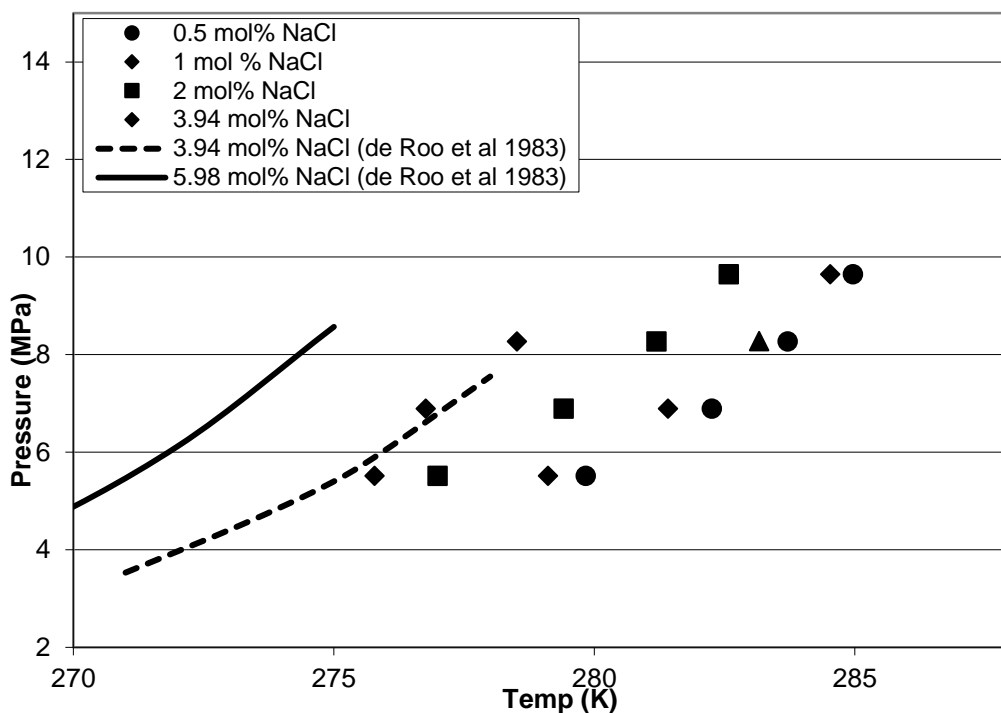


Figure 3.4 Methane hydrate dissociation temperatures and pressures for different concentrations of NaCl. The solid lines are the results of Roo et al. (1983).

Figure 3.5 compares shifts in the methane hydrate P-T phase boundary arising from the presence of sodium chloride and ferric chloride salt. The data indicate that, at a given pressure and inhibitor concentration, dissociation of methane hydrate occurs at lower temperatures for ferric chloride compared to sodium chloride. Dissociation onset temperatures were measured for concentrations ranging from 0.5 mol% to 3.94 mol% of inhibitor. No hydrate is detected at 3.94 mol% FeCl_3 , but hydrate formation does occur in the presence of 3.94 mol% NaCl.

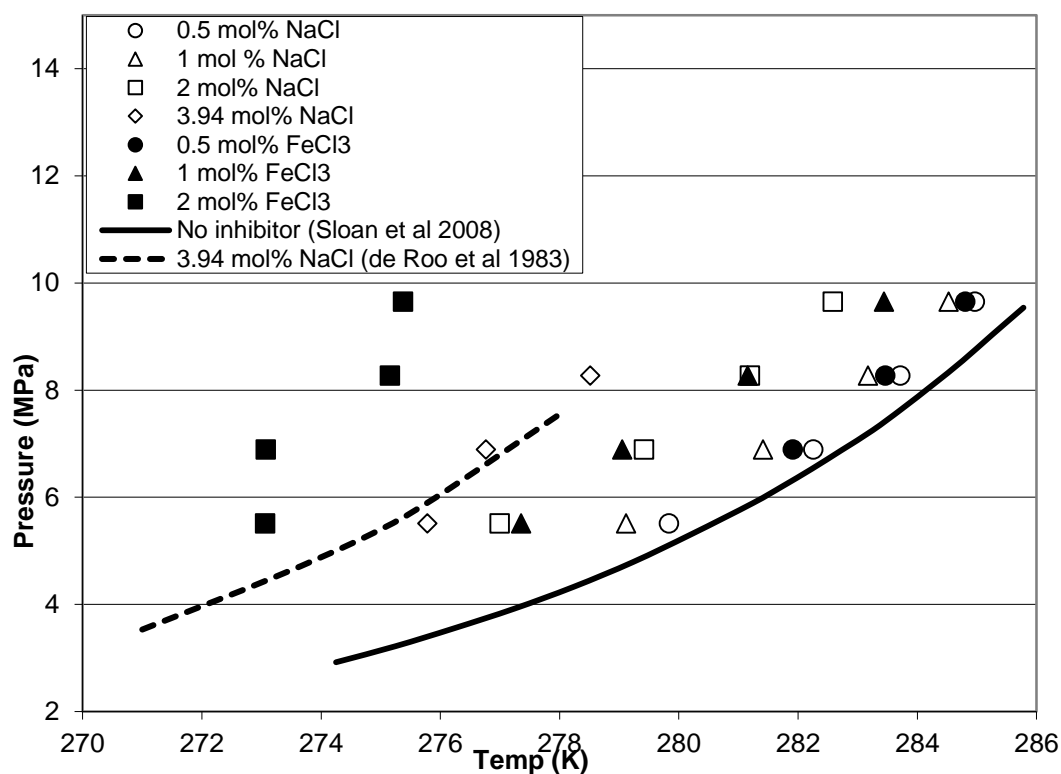


Figure 3.5 Methane hydrate dissociation temperatures and pressures for different concentrations of NaCl. The solid lines are the results of Roo et al. (1983).

The effect of other metal salts investigated in this study (FeSO₄, MnSO₄, CuSO₄, and AgNO₃.) on methane hydrate stability is shown in Figure 3.6. That figure also includes data for NaCl, and CaCl₂. The concentrations of the salts was 2 mol%. With the exception of FeCl₃, none of the tested salts were able to induce a reduction of the hydrate dissociation temperature to the extent that NaCl could.

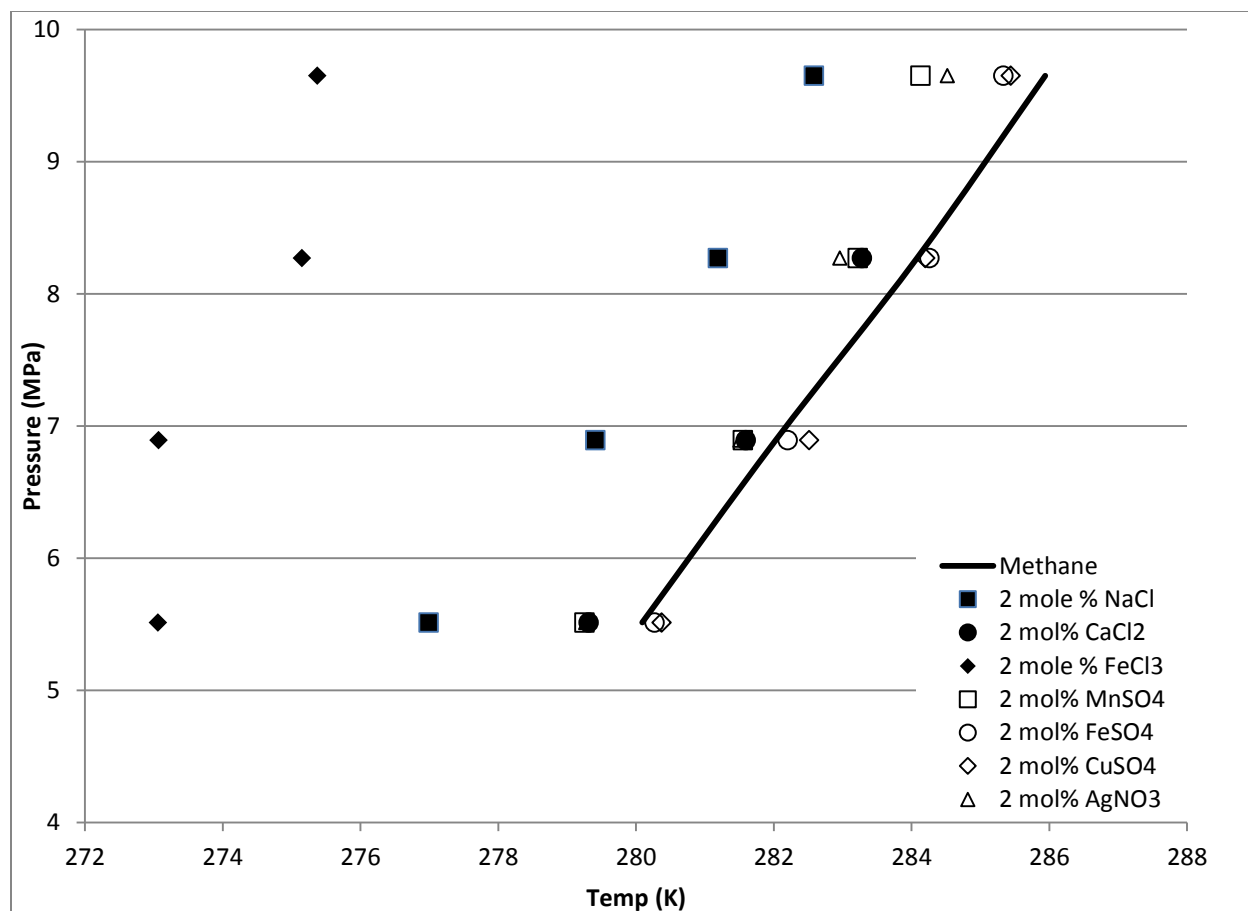


Figure 3.6 Methane hydrate dissociation temperatures and pressures for different salts at 2 mol%. The solid line is for pure methane hydrate with no added inhibitors.

Discussion and Conclusions

Most of the transition metal salts investigated in the present study inhibited methane hydrate formation at high concentrations but none to the extent of sodium chloride, except for ferric chloride. FeSO_4 and CuSO_4 at concentrations up to 2 mol% were observed to have minimal impact on hydrate stability. At lower concentrations (0.5 mol %), some of the salts appeared to promote hydrate formation, an effect that is also observed with alcohols.

The present results appear to confirm the assertion of Sabil *et al.* (2010) that the inhibitor effect increases with increasing charge on the cation; however, the results contradict the assertion that greater inhibition results from a larger anion. One possible explanation for the behavior observed in this and previous studies is that, when salts dissolve, the ions interact with the dipoles of the water molecules. The stronger interaction between water with salt ions (versus hydrate guest molecules) interferes with the organization of the water lattice around the clathrate hydrate guest molecule, and thus inhibits hydrate formation. The strength of the salt ion-dipole bond between the metal ion and water molecules may correlate with the degree of inhibition of hydrate formation. The strength of the ion-dipole bond in the primary solvation shell is expected to increase with the electrical charge, z , on the metal ion and decrease as its radius, r , increases. Therefore, higher charged metal ions, such as Ca^{2+} and Fe^{3+} would be expected to have a greater

attraction to the water molecules and thus more effectively impede hydrate formation. Furthermore, larger polyatomic anions, such as SO_4^{2-} would have a weaker attraction to the water molecules and would be less effective inhibitors.

The degree of methane hydrate inhibition induced by the salts that were studied (as indicated by the reduction in dissociation temperature at a given pressure), when compared between mixtures with the same mole percentages of the salt, increases in the following order: $\text{FeSO}_4 \approx \text{CuSO}_4 < \text{MnSO}_4 \approx \text{AgNO}_3 \approx \text{CaCl}_2 < \text{NaCl} < \text{FeCl}_3$. Consideration of the charge and size characteristics of the anion and cation components of the tested salts appears to support the mechanism posited above to explain this behavior

Methane Hydrates in Porous Media

Understanding the mechanisms of hydrate formation and dissociation in porous media is critical in order to devise viable methane extraction and carbon sequestration methods and to assess the associated environmental consequences. For example, Uchida *et al.* (2004) investigated the effects of porosity on the decomposition of methane hydrate formed in sediments and concluded: 1) that dissociation is mainly affected by intergranular pore size; and 2) that the hydrate phase equilibrium curves in porous media may be slightly different from those found in the literature which corresponds to simple binary methane-water samples. Their study, and other similar previous investigations, did not measure associated energy flows (e.g., heat of fusion; specific heat), which are important parameters for well production and environmental models. To investigate the mechanisms and energetics of methane hydrate formation and decomposition in porous media, experiments were conducted employing calorimetry and Raman spectroscopy. Two types of sands which are representative of deep ocean methane hydrate sediments, and which are employed as standards in the Japanese and U.S. national methane hydrates research programs, were tested. Sandy sediments represent the most viable scenario for methane extraction. Measured phase transition temperatures of hydrates in these sands were compared with the phase diagram for the simple binary methane-water system.

The technical objective of this study was:

- Conduct experiments of methane hydrate formation and dissociation in sand matrices using our Raman calorimeter to determine if hydrate stability is affected by the presence of the sand.

The primary hypothesis tested was:

- Pressure-temperature phase boundaries of methane hydrate change when formation and dissociation occur in porous media.

Experimental Facility

Hydrate was formed as a simple two-component water-methane system and also in porous media employing the HNEI experimental facility which couples calorimetry with Raman spectroscopy. High pressure sample cells of a Setaram BT2.15 DSC have been modified to provide access for a fiberoptic probe to perform Raman measurements of the sample in the cell as it undergoes a user-defined thermal process. The calorimeter allows samples (up to about 8 ml) to be cooled or heated, according to a user-selected process, between -196°C and 200°C at pressures up to ~ 10 MPa. The calorimeter can detect heat transfer to or from the sample as low as $0.10 \mu\text{W}$ and can

be used to determine thermodynamic properties such as specific heats, heats of reaction, heats of fusion, and phase boundaries. Figure 3.7 is a cutaway drawing of the DSC that shows its primary components. A photograph and schematic drawing of the experimental facility are shown in Figures 3.8 and 3.9, respectively.

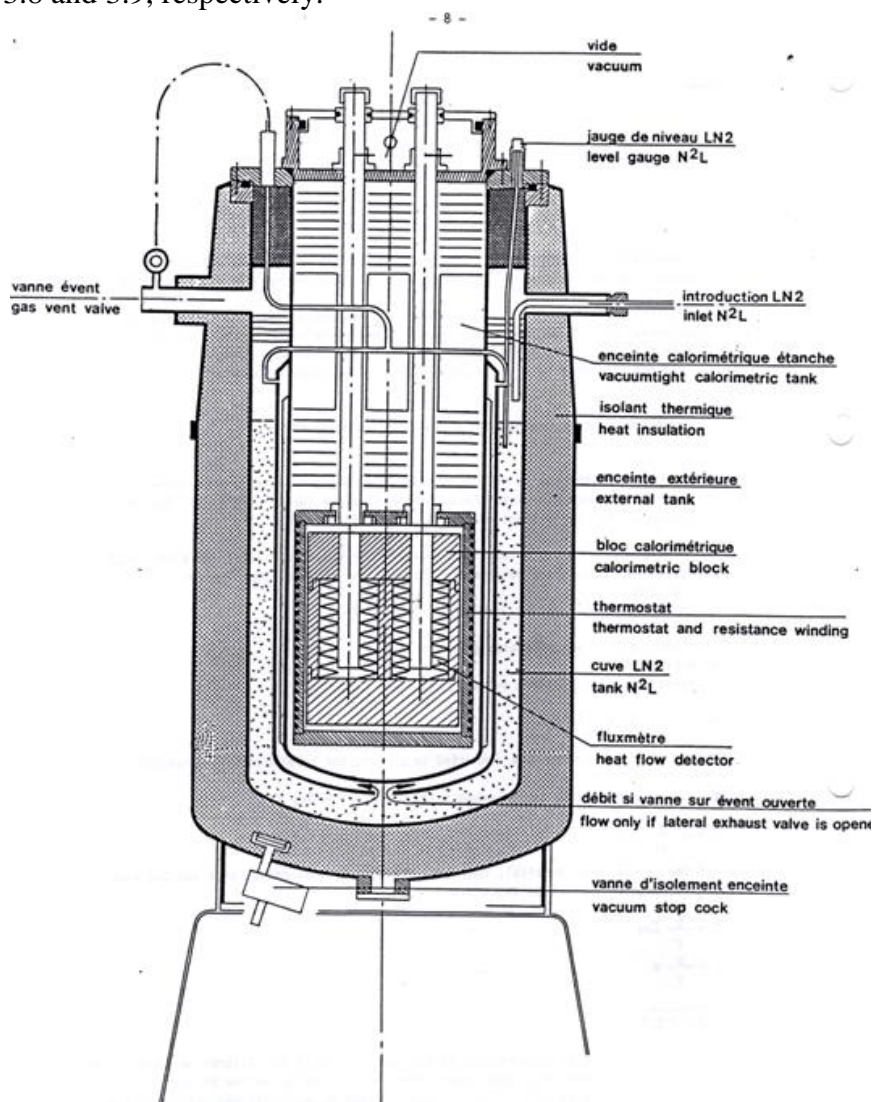


Figure 3.7 Cutaway drawing of the Setaram BT2.15 DSC.

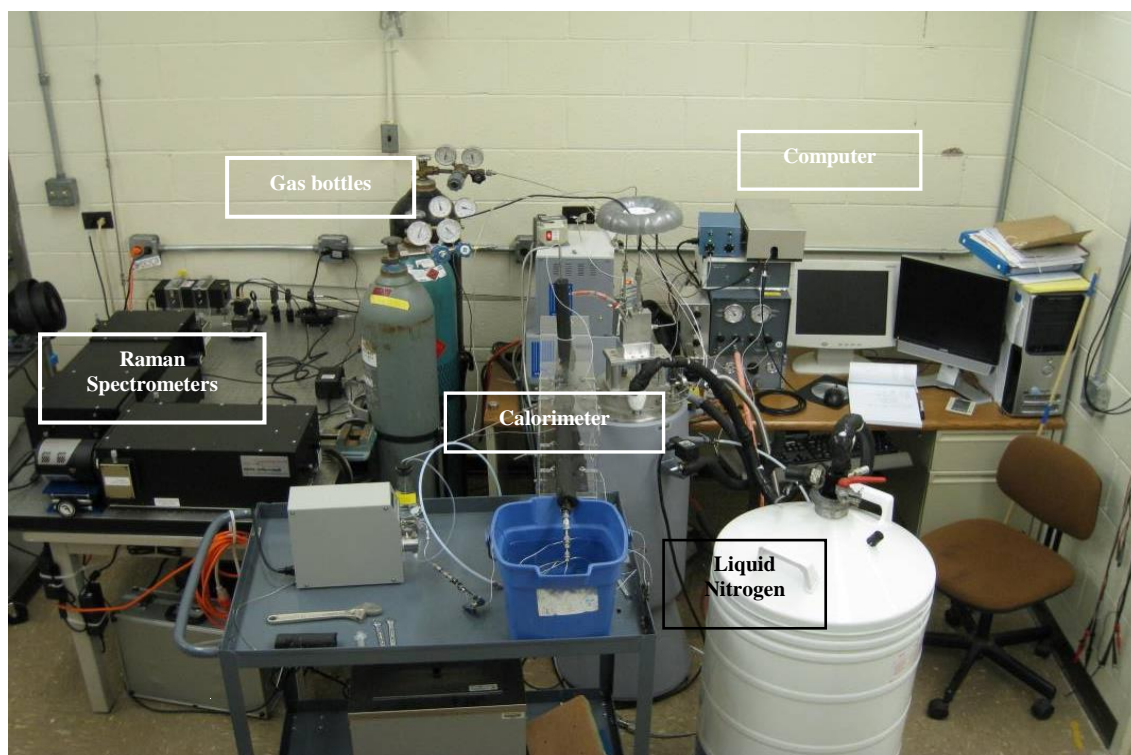


Figure 3.8 Photograph of the experimental facility.

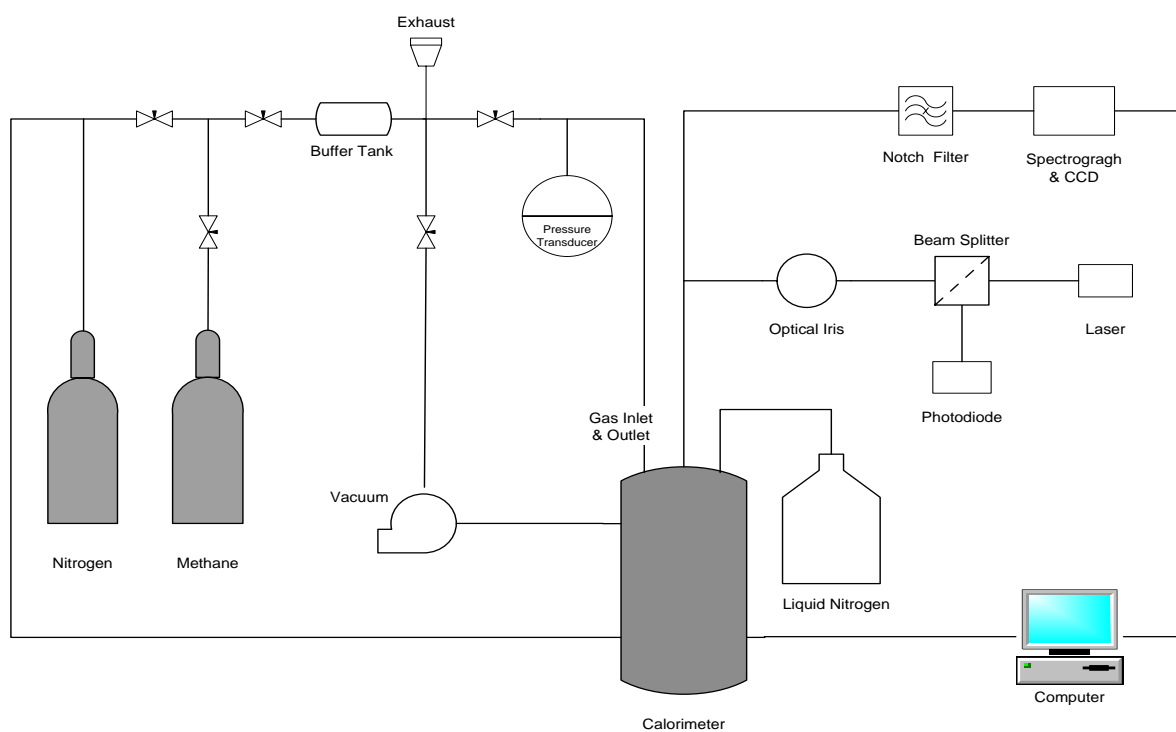


Figure 3.9 Schematic diagram of the experimental facility.

The DSC monitors the difference in thermal energy required to change the temperature of a sample and a reference. The material being investigated is contained in closed cylindrical sample cell, which is inserted into a well in the DSC as shown in Figure 3.7. An identical empty sample cell is used as the reference and is inserted into a second adjacent well. The cells are completely surrounded by an array of thermocouples that detects the heat flow to or from each cell as temperature is changed with a combination of an electric furnace and a liquid N₂ cooling system.

Figure 3.10 shows a photograph of the fiberoptic probe assembly that extends into the pressurized sample cell through a compression fitting welded to its top closure. The 0.125 inch (3.175 mm) o.d. probe is inserted into a 0.250 inch (6.35 mm) o.d., 0.18 inch (4.57 mm) i.d., stainless steel tube that attaches to the compression fitting. This tube also provides access to the inside of the sample cell to add or remove gases. Raman spectroscopy is used to confirm the existence of methane hydrates in the sample during the experiment. The Raman system shown in Figures 3.8 and 3.9 comprises a solid state laser, the fiberoptic probe, and a spectrometer. Laser radiation at 532 nm is transmitted by a 200 μ m core UV silica optical fiber into the cell to excite molecules in the sample to a virtual energy state. A portion of these excited molecules relax down to different rotation or vibrational levels than where they originally existed, with the emission of a photon. The frequency of the photon is shifted from the laser radiation. This Raman shift is determined by the structure of the molecule; i.e., its particular rotational and vibrational levels. Six 200 μ m core optical fibers positioned around the transmitting fiber in the probe are used to collect the emitted Raman shifted light and bring it into a Princeton Instruments SpectraPro-2750 spectrograph equipped with a Princeton Instruments PIXIS ccd detector. The spectrograph has a focal length of 0.750 m.



Figure 3.10 Photograph of the fiberoptic probe assembly

The sample cell can be evacuated with a vacuum pump and purged with dry N₂ gas. Research grade methane gas is used to form hydrate in the sample cell during an experiment. A buffer tank filled with methane is connected to the gas supply line to minimize changes in sample pressure that occurs when hydrate forms or decomposes. With this system, pressure can generally be maintained to within $\pm 1\%$. An electronic pressure transducer is employed to continuously monitor and record sample pressure.

Two kinds of sand representative of deep ocean methane hydrate sediment were investigated: Toyoura sand, which has been adopted as the “standard” sand for the Japanese national methane hydrate R&D program (Hyodo *et al.*, 2005) and Ottawa sand, which is the standard sand of the U.S. national program (Waite *et al.*, 2004). The properties of these sands, including composition, grain size distribution, void ratio and fraction,

water saturation, and grain porosity, were determined to characterize the samples tested with the calorimeter. The general procedures that were employed are discussed below.

Procedures

Properties of Porous Media. Natural water content, specific gravity, and grain size distribution of the porous media employed in this investigation were determined following the respective standard procedures: ASTM D2216, ASTM D 854, and ASTM D 422. Scanning Electron Microscopy (SEM), mercury intrusion porosimetry, and gas sorption analysis were used to characterize sand particle surfaces.

Calorimeter Experiments. Sand-water samples were prepared which have the desired porosity and specific water saturation for a particular experiment. The amount of sand needed to attain the target porosity was calculated based on the results of the specific gravity test. Next, distilled and deionized water was added to the sand. The amount of water was calculated considering the measured natural water content of the sand. The sand and water were mixed well and loaded into the calorimeter sample cell. The cell was closed and inserted into the calorimeter well before being purged with dry N₂ and vacuum evacuated. Methane gas was then added to the cell to achieve the desired pressure. The sample was then subjected to a user-selected thermal cycle to form and decompose hydrate and the thermal transfers indicative of phase transitions were monitored and recorded. Raman spectra were taken at selected points during the experiment to confirm the presence of methane hydrate.

Results

SAND PROPERTIES. The results of the natural water content test (ASTM D2216), the specific gravity test (ASTM D 854), and the grain size distribution test (ASTM D 422) for Toyoura and Ottawa sands are shown in Table 3.2. A portion of the Ottawa sand was sieved to remove fine particles and is identified as Ottawa* in the table. For comparison, the specific gravity of laboratory silica sand also is provided. The cumulative particle size distribution curves for the Toyoura, Ottawa, and Ottawa* sands are plotted in Figure 3.11.

Table 3.2 Sand Properties

| | Natural water content (%): ω_n | Specific gravity (g/cm^3): G_s | Grain size distribution by weight (%) | |
|---------|---------------------------------------|--|---------------------------------------|------------------------|
| | | | 140–425 (μm) | < 75 (μm) |
| Toyoura | 0.3267 | 2.656 | 99.85 | 0.01 |
| Ottawa | 0.3010 | 2.671 | 81.81 | 3.54 |
| Ottawa* | 0.2277 | 2.672 | 84.81 | 0 |
| Silica | – | ≈ 2.700 | – | – |

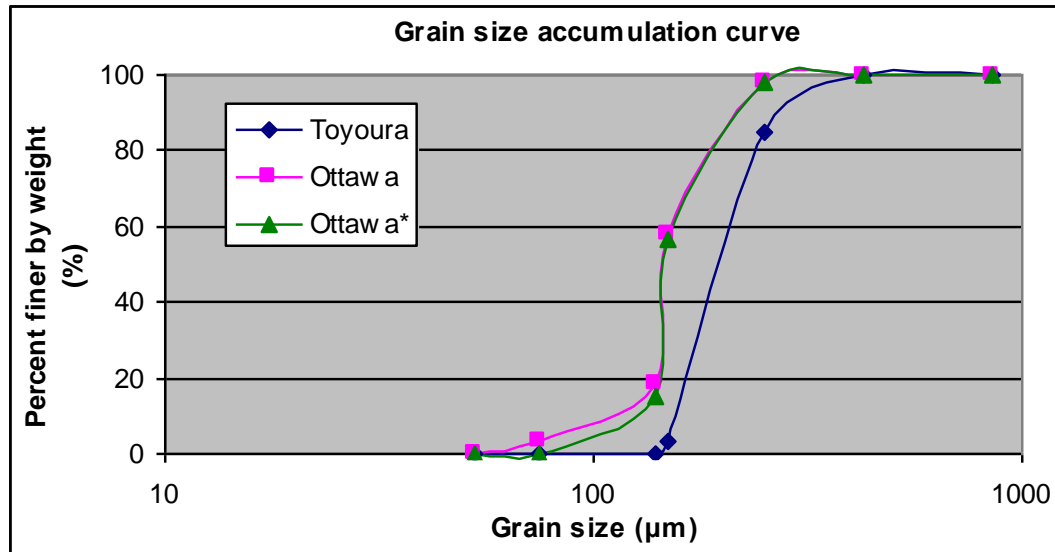


Figure 3.11 Cumulative particle size distributions for Toyoura and Ottawa sands.

The water content tests for all sands were conducted on the same day in order to ensure similar ambient conditions. Both Ottawa sand and Ottawa* sand have slightly lower water content than Toyoura sand. This may be related to their higher silt content. Fine silt particles reduce the void space between particles where moisture collects. The specific gravity of Toyoura and Ottawa sand are given in Table 3.2 appear reasonable, since they are silicates whose specific gravity is typically around 2.700 g/cm^3 . The small differences in specific gravities may again be due to fine particles that fill voids between the larger particles in the Ottawa and Ottawa* sands.

Figures 3.12 and 3.13 are representative SEM images of, respectively, the Ottawa and Toyoura sands at different magnifications. A Hitachi S-4800 field emission SEM operated by the Biological Electron Microscope Facility located at the University of Hawaii at Manoa was employed to document the topographical features of the sand particles. This instrument is also equipped with an Oxford INCA Energy 250 energy-dispersive X-ray spectroscopy system for elemental analysis.

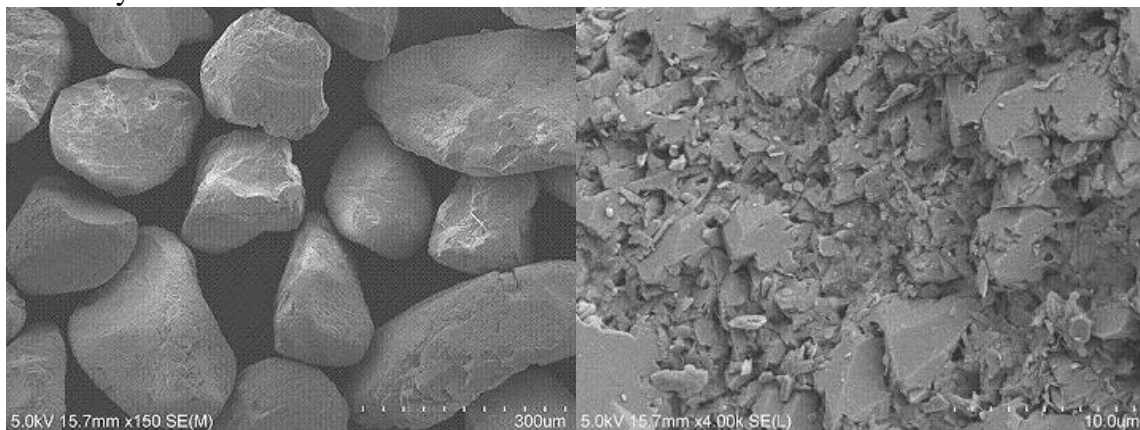


Figure 3.12 SEM images of Ottawa sand at two magnifications (see scale)

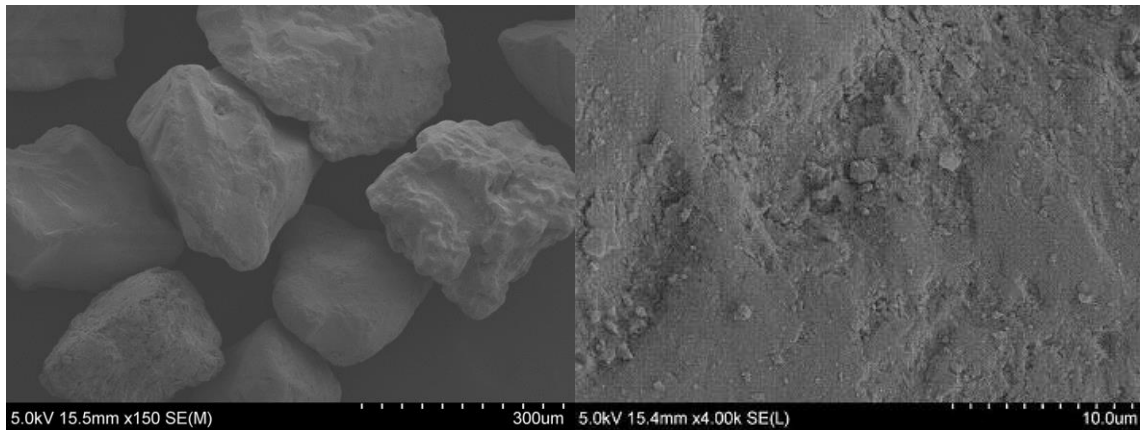


Figure 3.13 SEM images of Toyoura sand at two magnifications (see scale).

Both sands have relatively smooth surfaces and are primarily composed of aluminum silicates, which is typical of silicate sand. As seen in the SEM X-ray spectroscopy images (Figures 3.14 and 3.15), Toyoura sand appears to have more iron than Ottawa sand. In these figures, silicate is colored green, aluminum is blue, and iron is red. These three are the most prominent elements detected in the analysis.

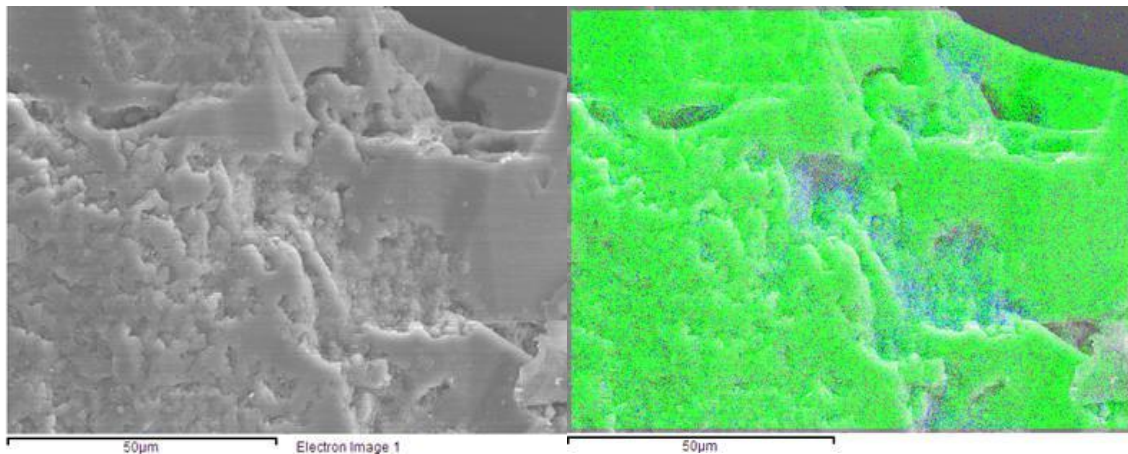


Figure 3.14 SEM image of Ottawa sand and overlay view of three elements.

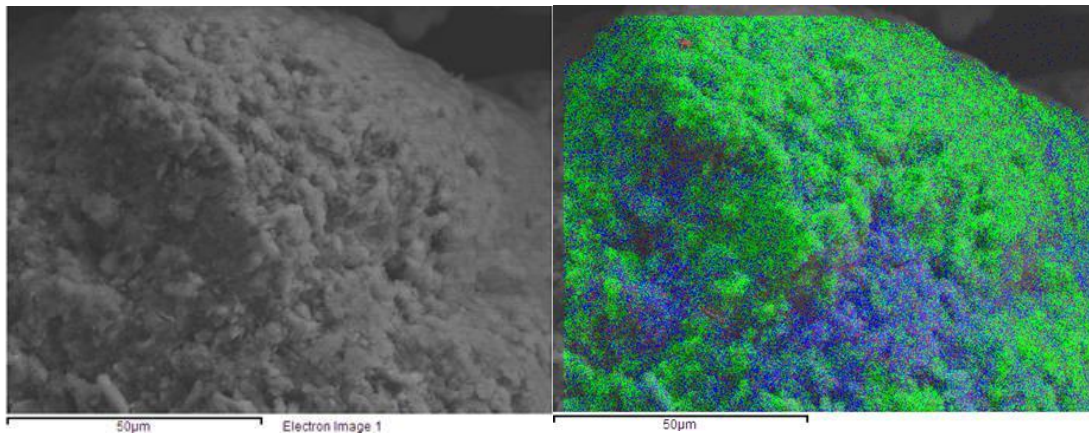


Figure 3.15 SEM image of Toyoura sand and overlay view of three elements.

In order to determine void fraction and grain porosity, Particle Technology Labs (Downers Grove, IL) performed mercury intrusion porosimetry on replicate aliquots of the sand. The primary results of these analyses are summarized in Table 3.3. These data only consider surface pores $< 6 \mu\text{m}$. Additional information on sand grain porosity was obtained with a gas adsorption instrument (Micromeritics TriStar 3000). Those data are summarized in Table 3.4.

Table 3.3 Mercury intrusion porosimetry results for Toyoura and Ottawa sands

| Sample | Total Intrusion Volume [cm ³ /g] | Total Pore Area [m ² /g] | Volume Median Pore Diameter [μm] | Bulk Density [g/cm ³] | Apparent Density [g/cm ³] | Percent Porosity $n_{\text{int}}[\%]$ |
|-------------|---|-------------------------------------|----------------------------------|-----------------------------------|---------------------------------------|---------------------------------------|
| Toyourea #1 | 0.0082 | 0.38 | 0.32 | 1.41 | 1.43 | 1.15 |
| Toyourea #2 | 0.0060 | 0.11 | 0.51 | 1.47 | 1.49 | 0.88 |
| Ottawa #1 | 0.0032 | 0.25 | 1.60 | 1.49 | 1.49 | 0.47 |
| Ottawa #2 | 0.0005 | 0.003 | 0.88 | 1.56 | 1.56 | 0.07 |

Table 3.4 Gas sorption analysis of Toyoura and Ottawa sands.

| Sand | Specific surface area (m ² /g) |
|----------|---|
| Ottawa | 0.11 |
| Toyourea | 0.74 |

The results of the mercury intrusion porosimetry and gas sorption analyses of the two sands indicate that they have very low grain porosity. The mercury porosimetry data exhibit significant variations between samples of the same sand because of the extremely low measured intrusion volumes that result from the low porosity of the material. The gas sorption data indicate that the specific surface area of the Toyoura sand is larger than that of Ottawa sand; however, both of the sands have very low specific surface areas, indicating that they are essentially non-porous.

CALORIMETRY. A series of calorimetry experiments were performed at different pressures between about 450 psig (3.2 MPa) and 1100 psig (7.7 MPa), which correspond to ocean depths between approximately 300 m and 750 m. The primary outcome of these experiments was the measured phase change temperatures for the hydrate at these pressures.

Figures 3.16 and 3.17 are representative thermograms from a calorimetry experiment using Ottawa sand. The pressure was set at $P = 1000$ psi (7.00 MPa) and held constant ($\pm 1\%$) throughout the test. Figure 3.16 shows the portion of the process where temperature is slowly reduced over a period of about 5 hours from 23°C (room temperature in the lab) to 1°C . The blue line in the figure is heat flow to or from the sample (mW) as a function of time, the red line is sample temperature ($^{\circ}\text{C}$), and the purple line is the temperature of the furnace ($^{\circ}\text{C}$) that is used to supply or remove heat. Heat flow is positive when energy is transferred from the sample cell towards the reference cell, indicating an exothermic process, and negative during an endothermic process. The steep positive peak in the heat flow curve seen in Figure 3.16 occurs as a result of hydrate formation. Note that sample temperature is above the ice point.

Figure 3.17 shows the portion of the process where sample temperature is very slowly raised from 1°C to 12°C over 16 hours. The large negative (endothermic) heat flow peak that begins at around the 12 hour mark is due to dissociation of the hydrate in the sand. The heat flow peaks in the thermograms at temperatures above the freezing point of water provided substantial evidence of hydrate formation and dissociation.

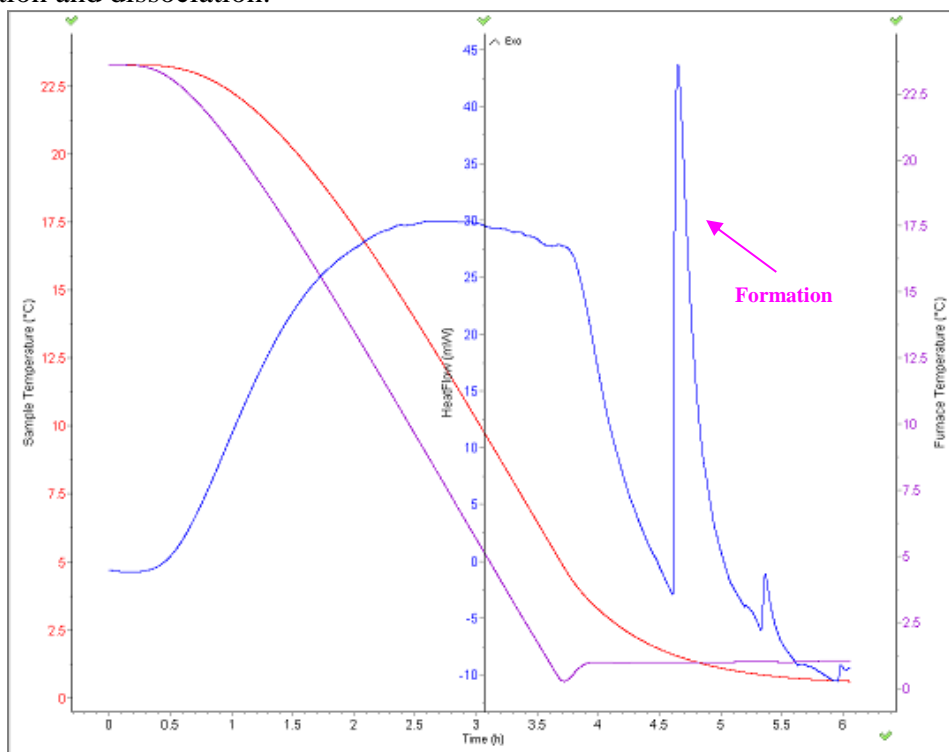


Figure 3.16 Calorimetry thermogram of methane hydrate formation in Ottawa sand

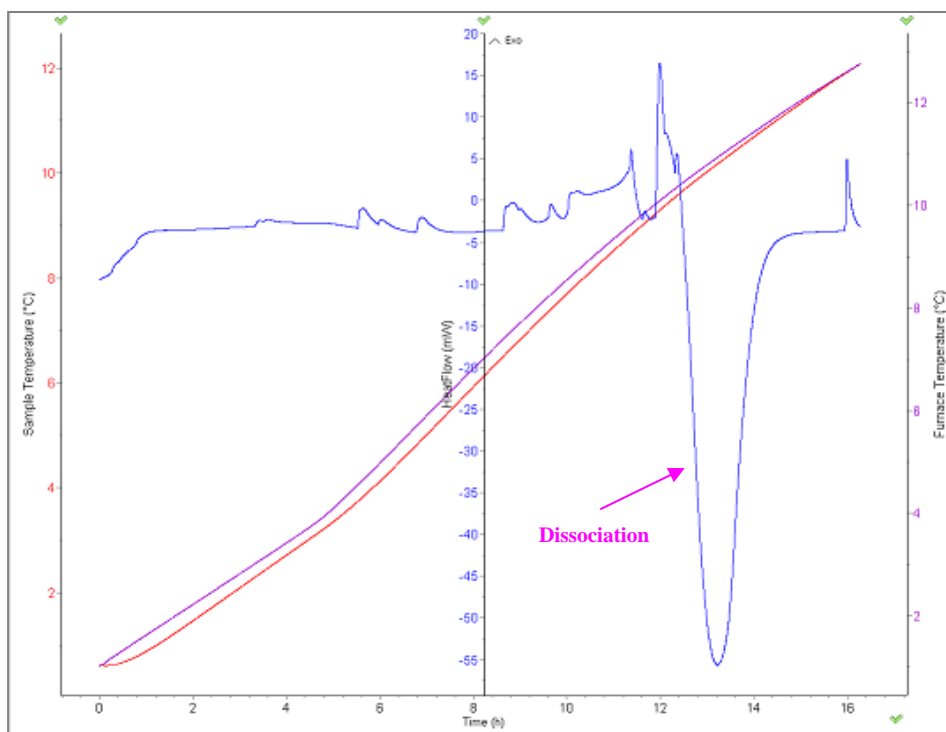


Figure 3.17 Calorimetry thermogram of methane hydrate dissociation in Ottawa sand. The presence of hydrate in the sample was confirmed using Raman spectroscopy. An example of the Raman spectra obtained during the experiments with the fiberoptic probe system is shown in Figure 3.18. The spectrum exhibits two peaks: the smaller peak to the left (633.90 nm) corresponds to methane hydrate and larger peak (634.31 nm) to methane gas overlying the sample in the calorimeter cell.

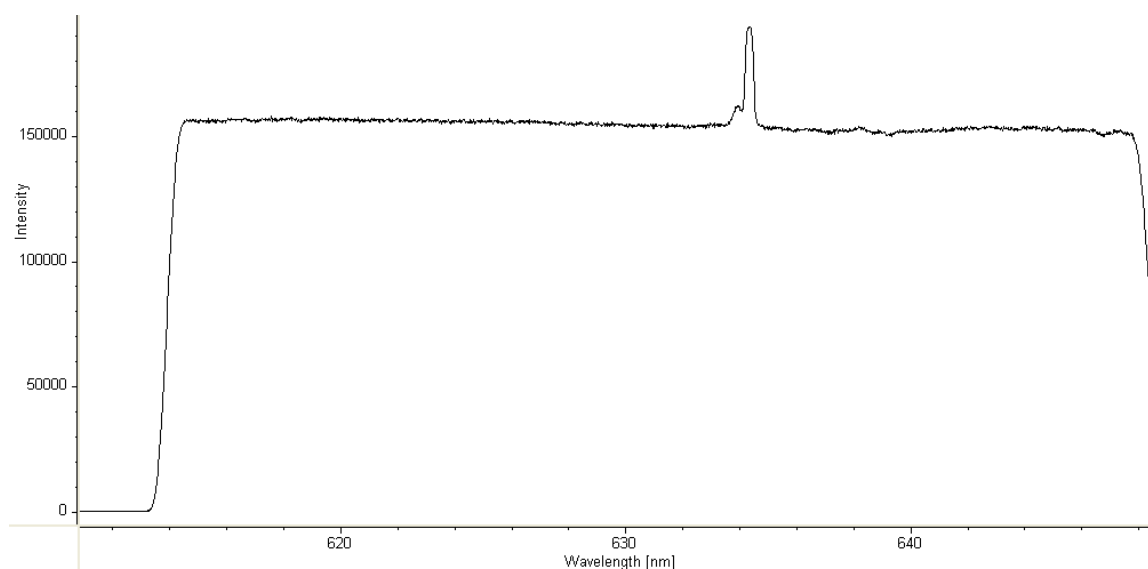


Figure 3.18 Raman spectra of the sample in the calorimeter.

Hydrate formation is a crystallization process and therefore involves nucleation and growth. Sub-cooling frequently is observed and phase transition data can exhibit significant scatter. Dissociation, on the other hand, is less sensitive to random experimental factors, so the phase transition temperatures were determined from the hydrate decomposition data. The process that was employed to identify melting point temperatures from the calorimetry thermograms is described below by reference to Figure 3.19:

- i. Extend the baselines of heat flow before and after the hydrate dissociation peak since the temperature ramping rate is constant.
- ii. Calculate the average value of the heat flow at the two points of intersection of the curve with these baselines, shown in the figure as green dots, and find the time that corresponds to this average value.
- iii. Determine the sample temperature at the time identified in step ii.

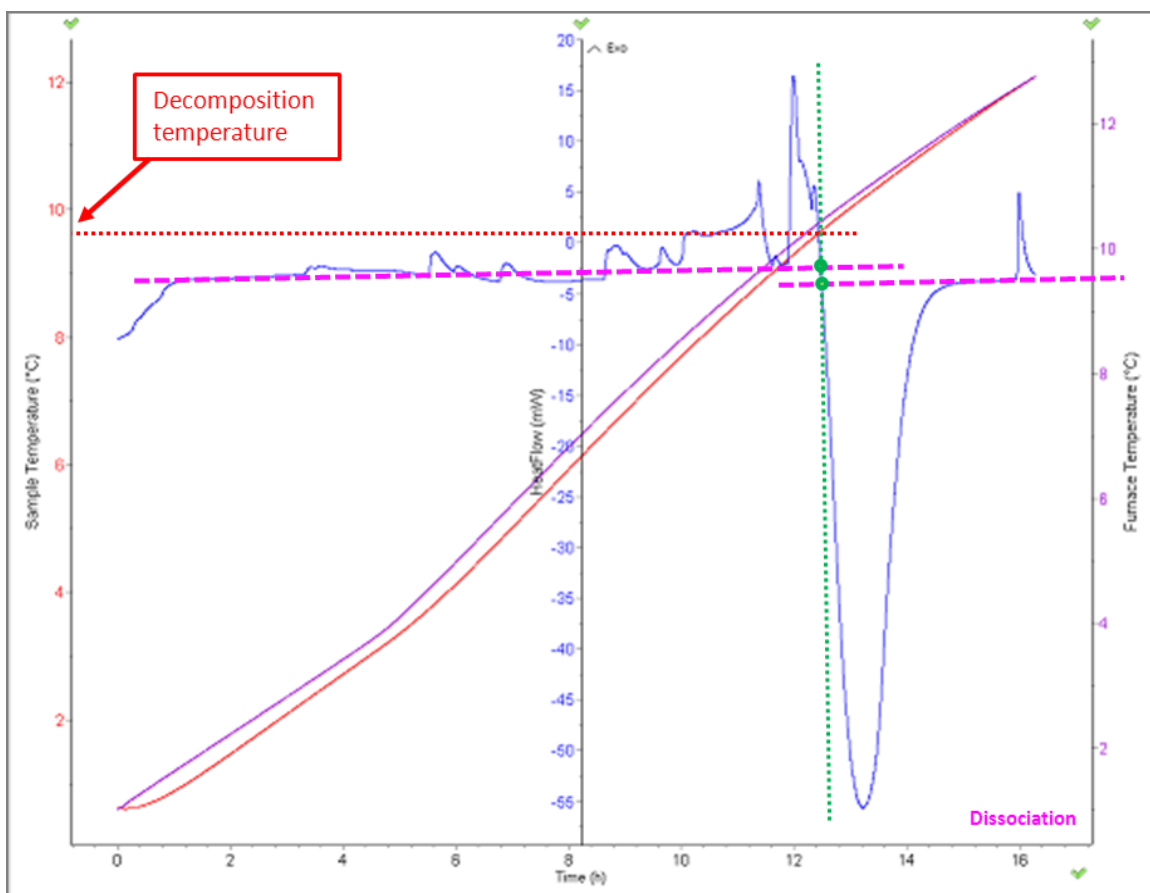


Figure 3.19 Determination of the hydrate dissociation temperature.

Table 3.5 summarizes the calorimeter experiments that were performed in this investigation. Figure 3.20 presents the results for the Ottawa and sieved Ottawa* sands. The solid line is the phase boundary for bulk hydrate (no porous media). Although there is significant scatter in the data, measured dissociation temperatures were consistently lower than the values for bulk hydrate at the same pressure. Differences typically fell between 1 and 2°C.

Table 3.5 Measured dissociation temperatures for different sands and pressures.

| Sand | Mass of sand (g) | Mass of water (g) | Porosity n(%) | Sr (%) | Pressure(psi) | Dissociation temperature (°C) |
|---------|------------------|-------------------|---------------|--------|---------------|-------------------------------|
| Ottawa | 10.9 | 2.17 | 40 | 80 | 1001.94 | 9.5 |
| | 10.9 | 2.17 | | | 999.12 | 9.29 |
| | 1.95 | 0.39 | | | 631.47 | 5.00 |
| | 1.95 | 0.39 | | | 628.16 | 4.90 |
| Ottawa* | 10.91 | 2.17 | | | 1012.36 | 9.75 |
| | 10.91 | 2.17 | | | 1011.01 | 9.68 |
| | 10.91 | 2.17 | | | 1010.00 | 9.40 |
| | 5.84 | 1.16 | | | 1042.00 | 9.08 |
| | 2.43 | 0.48 | | | 994.95 | 9.75 |
| | 2.43 | 0.48 | | | 864.83 | 10.50 |
| | 2.43 | 0.48 | | | 1006.11 | 9.6 |
| Toyoura | 10.84 | 2.17 | | | 1013.71 | 9.25 |
| | 10.86 | 2.17 | | | 442.74 | 0.79 |
| | 2.42 | 0.48 | | | 940.25 | 7.85 |
| | 2.42 | 0.48 | | | 1055.53 | 10.00 |
| | 4.48 | 0.97 | | | | |

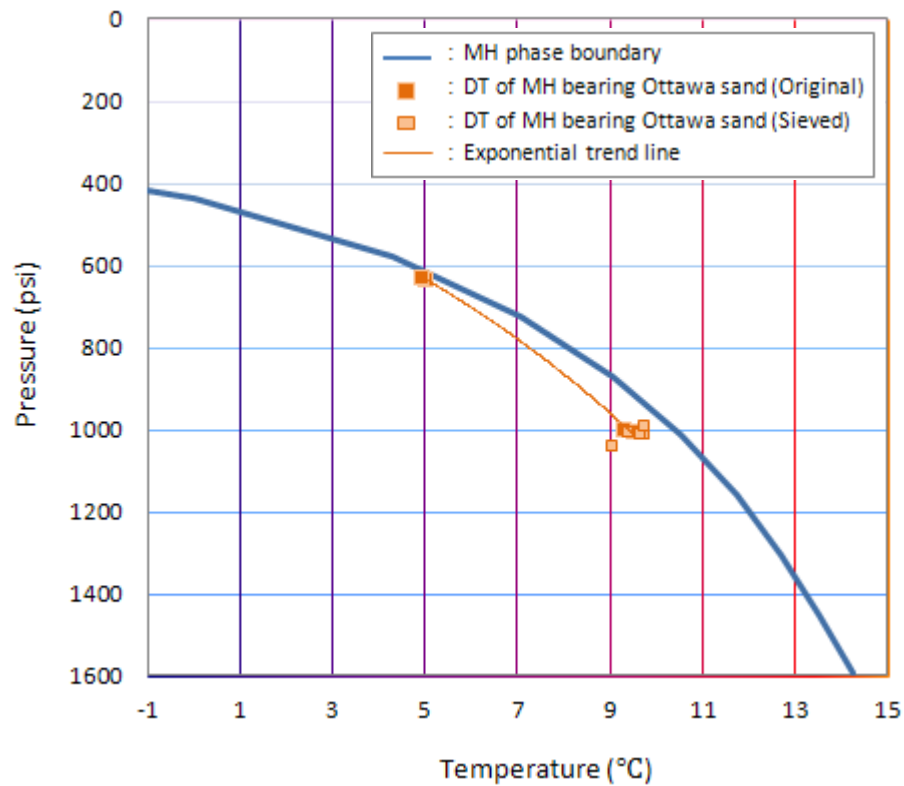


Figure 3.20 Measured dissociation temperatures for Ottawa sand.

From a different perspective, at a given temperature, the data suggest that methane hydrate in sand dissociates at pressures 15 to 200 psi lower than expected, which is greater than the uncertainty in the pressure data. Figure 3.20 also includes a trend line calculated from all the data points. Finally, the results for the Ottawa and sieved Ottawa* sands do not exhibit any significant differences.

Figure 3.21 shows the results for Toyoura sand. With the exception of the single data point at $P = 440$ psi (3.14 MPa), measured dissociation temperatures were again consistently lower than the values for bulk hydrate at the same pressure. The differences also typically fell between 1 and 2°C (although there is one data point where the difference is significantly larger). The corresponding pressure offsets were > 100 psi. The plotted trend line appears to confirm the shift in the phase boundary. All the experimental data are plotted in Figure 3.22.

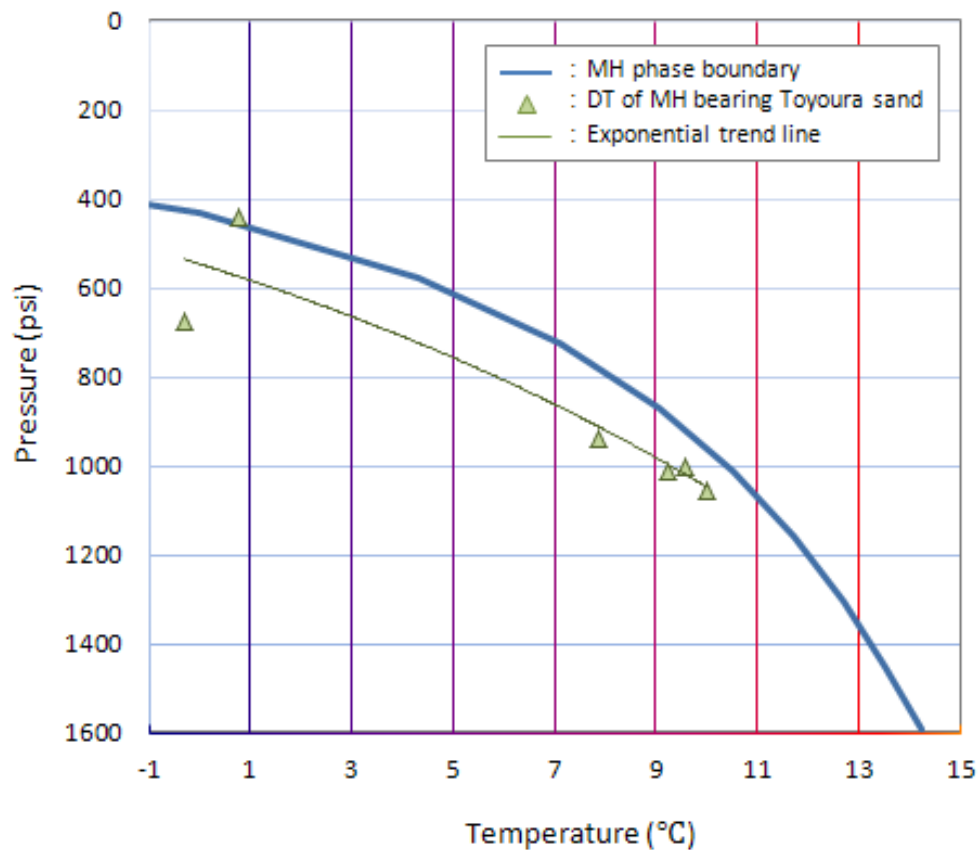


Figure 3.21 Measured dissociation temperatures for Toyoura sand.

Strategies to recover methane from marine hydrate deposits by thermal stimulation or depressurization, estimates of the volume of the hydrate stability zone in marine sediments to assess reservoir inventories, and assessments of the sensitivity to these reservoirs to changes in deep water temperature typically employ the phase diagram for simple methane-water systems.

The results of Uchida *et al.* (2004) and the present investigation suggest this may not be appropriate since methane hydrates appear to form and dissociate at lower temperatures in sand than bulk hydrate.

Conclusions

Calorimetric experiments were performed to test the hypothesis that the pressure-temperature phase boundaries of methane hydrate change when formation and dissociation occur in porous media. Two “standard” sands selected by the national methane hydrate R&D programs in Japan and the U.S. were employed in these experiments. The data suggest that a small shift in the phase boundary of hydrates might occur in porous media. The measured change is of the order of scatter in the experimental data but is consistent. For both sands, and over a range of pressures relevant to deep ocean sediments, the phase boundary for a simple water-methane binary system tends to overpredict hydrate melting temperature.

Lower melting temperatures imply that natural hydrate deposits in seafloor sediment are more vulnerable to purposeful or inadvertent increases in temperature. While this can be advantageous for certain methane recovery strategies, it raises concerns about outgassing and seafloor stability in a warming climate. Additional experiments appear to be warranted to confirm this phenomenon for a broader range of porous media properties and to more definitively quantify the shift in the phase boundary and to understand the underlying mechanism.

3.2 Environmental Impacts of Methane Release from Seafloor Hydrates

The long-term goal of this subtask is to develop a robust three-dimensional numerical model of methane in the ocean. Methane is a potent greenhouse gas with a significantly higher Global Warming Potential than CO₂, but much lower levels of emissions into the atmosphere. Whereas the oceans currently are a net sink for atmospheric CO₂, they represent a net source of CH₄. Moreover, the historical record contains evidence of massive methane outgassing from marine and permafrost hydrate reservoirs that may have greatly exacerbated earlier episodes of global warming. Methane models have also become a subject of intense R&D interest in the wake of the 2010 Macondo Prospect oil spill in the Gulf of Mexico which released an estimated 2.5×10^8 standard m³ of natural gas from the broken wellhead at a depth of about 1,500 m.

The target model will need to consider the production, oxidation, and transport of CH₄ and will require an understanding of processes that affect the exchange of methane between the atmosphere, ocean, and seafloor sediment. Work focused on field and laboratory experimental investigations of the role of microbes in methane production and consumption.

Methane Microbiology

Studies have been ongoing as part of this Task to investigate methane cycling in both sediments and the water column. To date, the sediment work has focused on understanding biological formation and the anaerobic oxidation of methane. Anaerobic oxidation of methane (AOM) occurs through an undefined process and is potentially the largest sink for methane in sediments. Biological AOM is thought to be mediated by a consortium of micro-organisms composed of

sulfate reducing bacteria and methanogenic *Archaea*. Geochemical data suggests that the majority of methane produced in sediments is oxidized anaerobically within a narrow depth range called the sulfate methane interface (SMI). The sediment depth of the SMI is influenced by the rates of methane flux. Stronger methane flux results in shallower SMIs, and the possibility of methane releases into the water column.

In terrestrial environments, biological methane oxidation typically occurs as an obligate aerobic process mediated by methanotrophic bacteria. This suggests that a methane sink could also exist at the sediment-water interface in the ocean where there is dissolved oxygen. In consideration of this, we have recently expanded our research scope to investigate aerobic as well as anaerobic methane oxidation at this interface, as well as the associated prokaryotic methanotrophic populations.

Molecular analyses of the microbial community that utilize 16S rRNA and *pmoA* phylogenies have been performed in different environments that include the Kuroshima Knoll (Inagaki *et al.*, 2004), Gulf of Mexico (Yan *et al.*, 2006), Haakon-Mosby mud volcano (Niemann *et al.*, 2006), and the East Pacific rise and Mid Atlantic vent fields (Nercessian *et al.*, 2005). While this approach can be employed to evaluate the potential for bacterial aerobic methane oxidation in marine sediments, it generally does not provide estimates of the methane oxidation rates.

In mid-September 2009, we participated in a 12 day oceanographic research cruise on the U.S. Coast Guard Cutter Polar Sea in the Beaufort Sea off the North Slope of Alaska. This cruise was organized by the Naval Research Laboratory. There were 34 international participants, including scientists from university and government research agencies from the U.S., Netherlands, Belgium, Germany and Canada.

The Arctic Ocean expedition provided a unique opportunity to study the microbial communities and aerobic C1 metabolisms in shallow and cold water environments in methane-rich areas. Comparative analysis of collected samples utilizing data that includes concentrations of C1 metabolizing prokaryotes and sediment and water chemistries could yield important information about the methane sink at the sediment-water interface.

Geochemical data collected during the cruise was used to investigate spatial variations from different methane sources impacted by vertical methane flux in shallow sediments (<10mbsf), and methane contributions to shallow sediment carbon cycling. Results from the expedition represent one of the most comprehensive studies of methane source(s) and vertical methane flux in shallow sediments of the U.S. Alaskan Beaufort Shelf. Results show that sediment methane flux that is highly influenced spatially by the geophysical environment. This data has resulted in a joint publication (Coffin *et al.* 2013)

To elucidate the aerobic biological metabolisms by which microbes can regulate methane level in both the water column and near-surface, the combined use of molecular analysis, chromatography and microcalorimetry was attempted using samples collected during the 2009 Beaufort Sea Cruise.

Six multicore samples were collected during the Beaufort Sea cruise. Multicore samples are better suited for the analysis of methanotrophic bacteria than the piston cores collected in

previous expeditions as there is less disturbance of the upper sediment layer. The multicores unfortunately were not geochemically profiled, which would have provided useful information to interpret the biological data. It originally was planned to employ the multicorer at mounds where with high methane fluxes may exist; however, no samples ultimately were obtained from active seeps. In comparison to the rates typically observed in investigations of AOM (0.7fmol CH₄/cell/24hrs), aerobic oxidation rates may be considerably larger in methane-rich environments (Nauhaus *et al.* 2005).

As previously reported, DNA was extracted shipboard during the Beaufort Sea cruise in 2009 immediately after collection. DNA extraction was performed using a commercially available kit from a homogenate of the uppermost 1 cm of sediment from the core. Upon returning to the laboratory it was determined through 16S rRNA analysis using specific primers that 5 of the 6 samples had methanotrophic DNA signatures. Using these same samples it was determined through micro-DSC calorimetry that the metabolic rates were too low to be measured in a methane enriched atmosphere.

During the cruise, 1 g core samples were weighed and placed into sterilized Hungate tubes containing a seawater-based enrichment media and 1 gram of silica to increase the porosity of the often clay-like sediments (Holmes *et al.*, 1995; Whittenbury *et al.*, 1970). An artificial atmosphere containing 10% methane in air was infused into the tubes after inoculation. Methane concentrations were measured using a head space method (Kiene and Capone, 1985) with a gas chromatograph equipped with an FID detector. The extent of methane consumption in these experiments, however, was insufficient to determine oxidation rates on the ship probably due to low cell density since we were unable to collect cores from areas stimulated by high methane gas fluxes. These results were verified by the micro-DSC analysis previously mentioned.

The enrichments that were performed shipboard were maintained and sent back to our laboratory for long term incubation. After six months, there were no observable changes within the samples. Analysis of methane headspace composition using the same gas chromatograph and methodology revealed no significant differences when compared with controls. The triplicate 10 g frozen samples that were brought back to our laboratory for analysis will be used, in a subsequent investigation, for the isolation of single cells and genetic amplification.

Modeling Methane in the Ocean

In prior work funded by the HEET program, we began to construct a 3D model of methane transport in the ocean water column from seafloor sources. We have contacted colleagues at UH and MIT who specialize in OGCM (ocean general circulation model) coding and solicited their cooperation. Under the present award, we pursued this collaborative strategy to develop our 3D model. The focus of our efforts was to construct submodels of methane production and oxidation in the water column that will be incorporated into the OGCM.

The identification of key elements of a methane cycle that could be incorporated in an Ocean General Circulation Model (OGCM) was performed. *MITgcm* was selected as the reference OGCM (<http://mitgcm.org/public/docs.html>), with little loss of generality. This open-source code

is one of the most sophisticated to date, and its users can participate in an active forum for specific problem solving. Aside from direct communication with MIT colleagues, significant experience running *MITgcm* also could be leveraged from different research projects involving active team members (c.f., for example, Rajagopalan and Nihous, 2012 and 2013; Jia *et al.*, 2012). A unique feature of *MITgcm* is the option of efficiently solving the non-hydrostatic Navier-Stokes equations (Marshall *et al.*, 1998). This would allow, in particular, the modeling of phenomena at smaller scales (sub-mesoscale, perhaps in the vicinity of concentrated methane sources and sinks on the seafloor), where the vertical momentum equation should not be reduced to a simple balance between hydrostatic pressure and gravity. The inclusion of a methane cycle in an OGCM rests on the addition of methane concentration as a passive non-conservative tracer.

Provisions for the formal representation of such tracers (i.e., the advection diffusion equations and generic input format) already exist in *MITgcm*, e.g., in connection to a basic carbon cycle (with the calculation of pH as a goal). This step was not implemented at such a preliminary stage, although the characterization of specific methane sources and sinks was initiated. One diffuse methane source within the mixed layer was well described (Nihous and Masutani, 2006), while other aspects of methanogenesis were not sufficiently characterized yet from an OGCM modeling perspective. More work was performed on methane oxidation since this methane sink involves the representation of an additional non-conservative tracer, in the form of a methanotroph concentration.

As outlined in Nihous and Masutani (2007), this is a clear departure from simple first-order reactions, since the methane oxidation reaction constant must be proportional to the methanotroph population density, subject to a typical limit (e.g., half saturation constant in Michaelis-Menten kinetics). In the absence of a detailed knowledge of methanotrophic bacterial populations, and without the inclusion of additional trophic levels (prey-predator hierarchy), a mortality sink proportional to the square of methanotroph concentration was envisioned for closure, as in some food chain models of planktonic growth (e.g., Kawamiya *et al.*, 1995 and 1997). There are obvious drawbacks when adding modeling parameters since their calibration may be difficult, while their variability under the influence of external factors (e.g., temperature, pressure) is likely to be unknown, or may require additional sensitivity constants. Another issue with the modeling of any tracer imbedded in OGCMs is the required computational intensity. If specific regions are spatially limited, as could be the case with seafloor methane-rich hydrothermal vents, then a domain nesting strategy may be economical, with the representation of local momentum and dispersion effects (jets and plumes) greatly simplified using empirically derived algorithms. This approach was tested in a different project, and proved to be numerical efficient (Jia *et al.*, 2012), although the treatment of open boundaries in the nested-domain architecture requires special care.

During the present phase of HEET, a formalism for incorporating microbial methane sources and sinks in the *MITgcm* was devised and some preliminary testing was undertaken. Integration of these submodels is ongoing.

3.3 Hydrate Engineering Applications

The availability of sufficient supplies of potable water is an important consideration for a host of DOD activities. Local water supplies may be contaminated with chemicals and pathogenic bacteria and viruses, necessitating burdensome transport-to-site of large quantities of safe water or the installation and operation of complicated purification facilities. Contamination can be particularly bad in developing countries where over 90% of raw sewage and 70% of untreated industrial wastes are dumped into surface waters (UN-Water & UNEP, Clean Water for a Healthy World, 2010).

The two most common water purification techniques currently in use are multi-stage flash (MSF) and reverse osmosis. MSF is employed extensively in countries of the Middle East and accounts for approximately 40% of the world's desalination capacity (Miller, 2003). MSF operates by flashing (i.e., evaporating) seawater or saline water into steam, which is then collected and condensed into clean water (Bruggen & Vandecasteele, 2002). The energy required to evaporate the saline water usually is waste heat from a combustion power plant burning fossil fuel. Specific power requirement of state-of-the-art MSF plants is about $4.4\text{kW}\cdot\text{hr}/\text{m}^3$ (Darwish & Al-Najem, 2000). Larger systems can produce up to $5680\text{ m}^3/\text{day}$ (Darwish & Al-Najem, 2000). Figure 3.22 presents a schematic diagram of a typical MSF facility.

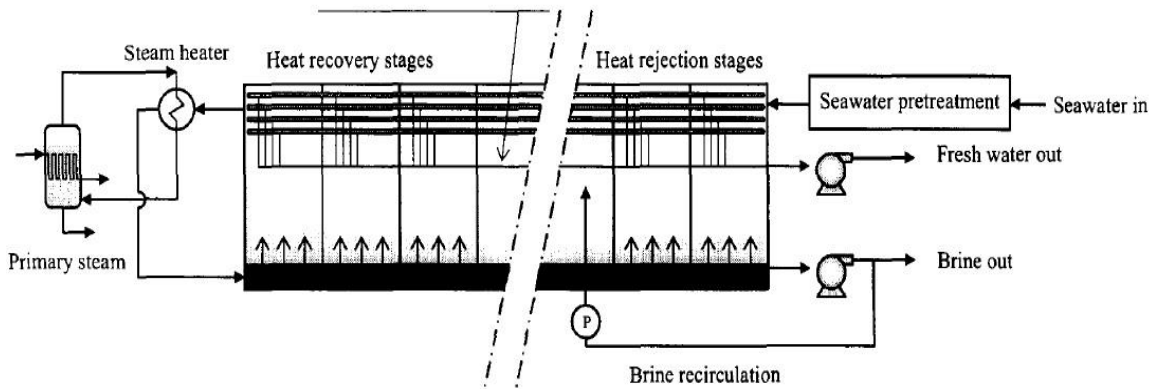


Figure 3.22 Schematic diagram of a MSF plant; from (Bruggen & Vandecasteele (2002).

While MSF is a popular desalination technique, it does have several drawbacks, including low recovery ratio and high costs (URS, 2002). Recovery ratio is the fraction of feed water that is converted to (desalinated) product water. A low recovery ratio means that large quantities of unconverted brine must be discharged, usually into rivers, lakes, or the ocean (Bleninger & Jirka, 2010).

Another technology commonly employed to purify water is reverse osmosis (RO). RO operates by forcing water through a semipermeable membrane, which filters out ions; contaminants are retained on the pressurized side of the membrane and pure water on the other side (Bruggen & Vandecasteele, 2002). Figure 3.23 shows a diagram of an RO system.

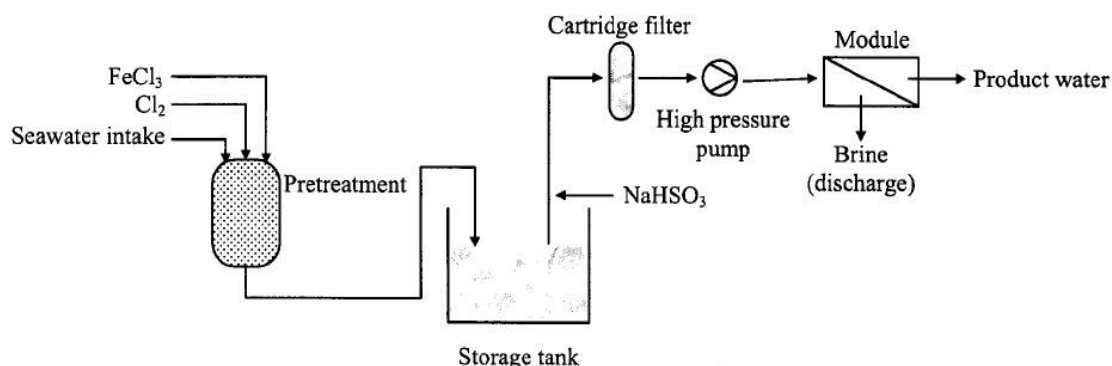


Figure 3.23 Schematic diagram of an RO plant; from (Bruggen & Vandecasteele (2002).

RO systems tend to be energy-intensive due to the high pressures (~50-80 bars) required to force seawater through the membrane. Typical energy requirements range from 2.91- 7.45kW-hr/m³ (Dashtpour & Al-Zubaidy, 2012). Also, reverse osmosis membranes deteriorate over time due to the accumulation of solid impurities (Bruggen & Vandecasteele, 2002).

Clathrate hydrates offer the potential to remove contaminants from water. Since only specific molecules (e.g., CO₂, CH₄) can fit in the interstitial spaces of the crystal water lattice, solid hydrates that form from contaminated water will tend to exclude everything but those (hydrate guest) molecules. Furthermore, because some types of hydrates form at lower temperatures than those required by MSF systems, and at lower pressures than RO, this approach could be less energy intensive.

In the 1960's, the U.S. Department of Interior's Office of Saline Water funded the construction of a number of "freeze" desalination pilot plants (Barduhn, 1982). Two of these plants used hydrates rather than ice. The two plants, however, were unsuccessful because the hydrate crystals were too small to be separated from the brine (Bruggen & Vandecasteele, 2002).

More recently, the Bureau of Reclamation sponsored a preliminary study of clathrate hydrate desalinization (McCormack & Anderson, Clathrate Desalination Plant Preliminary Research Study, 1995). This was followed by a pilot-scale test of hydrate desalinization which was conducted at the Natural Energy Laboratory of Hawaii Authority in Kona, Hawaii (McCormack & Niblock, Build and Operate a Clathrate Desalination Pilot Plant, 1998). The test was a partial success insofar as it demonstrated that hydrates can be formed from seawater with minimal inclusions; however, the project was terminated before viable methods were identified to collect, wash and decompose the hydrate crystals. Termination was due to unconfirmed reports of environmental violations during experiments.

While studies have been conducted on hydrate desalinization, removal of biological material from water by hydrate crystallization has not been investigated. Toward this end, exploratory laboratory experiments were conducted to assess the potential of using hydrates to filter out cell-scale contaminants. Bovine serum albumen (BSA), a 6.6kda protein, was used in these tests as a proxy for actual water-borne microbial pathogens. Hydrate desalination experiments also were performed. Successful separation of these contaminants would demonstrate the utility of hydrate

formation for both desalination and for the removal of higher molecular weight metabolites from previously treated water that was biologically contaminated.

R-134A (DuPont Suva; 1,1,1,2 Tetrafluoroethane), a common refrigerant, was employed in this investigation since R-134A hydrate forms at lower pressures and/or higher temperatures than other candidate hydrate forming gases. For example, R-134A hydrate will form at 35 psig (~3.4 bar absolute) and 5°C, while methane hydrate forms at approximately 435 psig (~31 bar absolute) at 5°C. R-134A also has a relatively benign safety profile. Refrigerants have been considered or used in previous hydrate desalination studies (Liang *et al.*, 2001; Nikbakht *et al.*, 2011).

Experimental Materials and Methods

Figure 3.24 shows a schematic diagram of the system employed in this study. The primary component of the system is the reactor where hydrate crystals are formed from contaminated water solutions. A diagram of the reactor is presented in Figure 3.25. The reactor consists of an acrylic cylinder closed on both ends with high-density polyethylene (HDPE) caps. The internal diameter of the reactor is 76.2 mm (3.0 inches). It has an internal volume of 1.6 liters. A wire basket is inserted into the reactor to collect the hydrate that forms. The reactor is immersed in a tank, which is typically held at -1°C using a constant temperature bath.

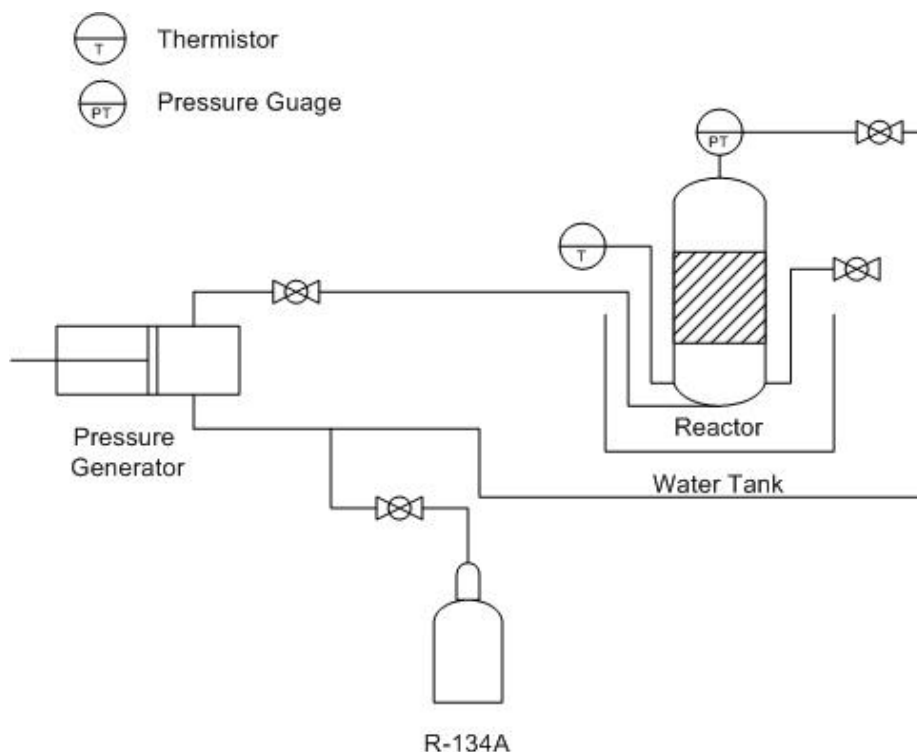


Figure 3.24 Schematic diagram of the hydrate water purification facility.

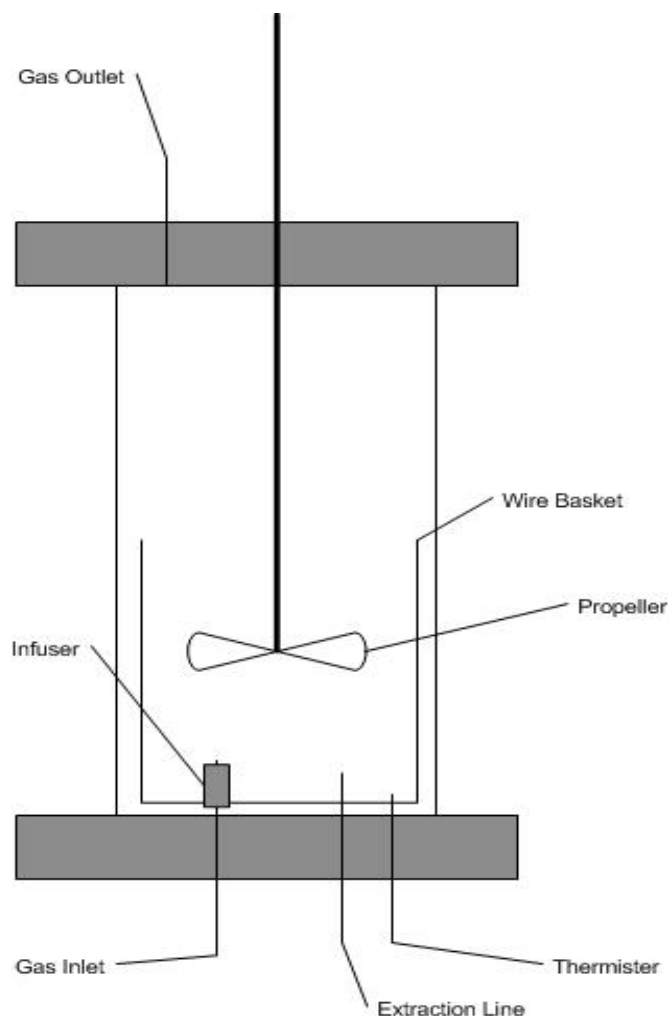


Figure 3.25 Diagram of the reactor.

Hydrate forming gas is bubbled through water in the reactor from a tube extending through a fitting in the bottom cap. An infuser (i.e., aquarium stone) is attached to the end of the tube to create small gas bubbles that dissolve rapidly and agitate the water. A propeller or auger is also employed to stir the solution and promote hydrate formation. An extraction port in the bottom cap is used to remove liquid after hydrate has formed for analysis to determine the concentration of salt and/or biological contaminants.

R-134A is supplied from a small canister. The gas from the canister passes through a series of valves and a piston-cylinder pressure generator where it is compressed to a selected operating pressure and injected into the bottom of the reactor. Excess R-134A gas in the reactor headspace is extracted from the top of the reactor and re-pressurized and infused back into the bottom of the reactor. This circulation loop is employed to minimize the amount of R-134A used (since the refrigerant must be collected for disposal) and to ensure that the solution is saturated.

Temperature in the reactor is monitored continuously with a thermistor (accuracy $\pm 0.02^{\circ}\text{C}$ at 25°C). Due to heat transfer from the ambient air, water temperature inside the reactor was

determined to be approximately 5°C when the bath temperature is set at -1°C. A pressure transducer (accuracy $\pm 0.25\%$) connected to the gas extraction line monitors the pressure in the reactor.

Concentrations of dissolved NaCl in the solution before and after hydrate formation, and in the product water released after decomposing the collected hydrate, were measured with an Omega CDH45 salinity meter. A spectrophotometer (Shimadzu UV-160) was used to determine the concentration of BSA in our water samples. Absorption at 280 nm was monitored since the BSA has a strong signature at this wavelength.

Solutions were prepared by adding reagent grade NaCl or BSA to 500 g of distilled, deionized water. When the impurities were completely dissolved, approximately 10 ml of solution was extracted and stored in a stoppered test tube. This reference sample was used to determine the initial concentration of contaminants. The reactor was filled with the remaining liquid, closed, and immersed in the temperature bath.

After the temperature of the solution in the reactor equilibrated, the reactor was pressurized with R-134A to approximately 30 psig (~ 3.1 bar absolute). The propeller was activated typically three times each day for approximately 30 seconds total to agitate the water to promote hydrate formation.

Most of the hydrate forms within 24-48 hours after the start of an experiment. The remaining solution eventually becomes too saline for hydrate to form (Ruppel *et al.*, 2005). At this point, remaining liquid is purged from the reactor and collected by opening the valve in the extraction line. During this process, additional R-134A gas is added to the reactor to keep pressure within the hydrate stability zone. The R-134A is then collected for recycling and the reactor top cap is removed and the hydrate is lifted out using the wire basket and placed in a beaker where it is allowed to melt.

Residual liquid removed from the reactor and water remaining after the collected hydrate melts were analyzed, along with the 10 ml reference sample, to determine the extent of contaminant removal. Portions of the reference sample, hydrate water, and residual liquid were placed in three separate cuvettes using a 5 ml syringe equipped with a 0.2 μm syringe filter. The filter was used to remove any large impurities that would alter the spectrophotometer results. The baseline for the spectrophotometer was established using distilled, deionized water before the samples were analyzed.

Results

Results from the desalination and biological contaminant removal experiments are summarized in Tables 3.6 and 3.7, respectively. The tables compare the measured levels of dissolved NaCl or bovine serum albumin in the solution in the reactor prior to hydrate formation and in the water recovered from the melted R-134A hydrates.

Table 3.6 Hydrate desalination results.

| Test 1 | Salt % (ppt) |
|---------------|--------------|
| Initial | 2.6 |
| Purified | 2.2 |
| | |
| Reduction (%) | 15 |

| Test 2 | Salt % (ppt) |
|---------------|--------------|
| Initial | 2.6 |
| Purified | 1.7 |
| | |
| Reduction (%) | 35 |

| Test 3 | Salt % (ppt) |
|---------------|--------------|
| Initial | 2.6 |
| Purified | 1.5 |
| | |
| Reduction (%) | 42 |

Table 3.7 Albumen removal results.

| Test 1 | |
|---------------|------|
| Initial | 0.64 |
| Purified | 0.60 |
| | |
| Reduction (%) | 6.7 |

| Test 2 | |
|---------------|------|
| Initial | 0.71 |
| Purified | 0.69 |
| | |
| Reduction (%) | 2.0 |

| Test 3 | |
|---------------|------|
| Initial | 0.70 |
| Purified | 0.66 |
| | |
| Reduction (%) | 5.5 |

The data suggest that hydrates can be used substantially to decrease the salt content of low salinity water. The salinity of the water collected after decomposition of the R-134A hydrate

was $31 \pm 14\%$ lower than the solution containing 2.6 ppt of NaCl. On the other hand, the BSA concentration in decomposed hydrate water was reduced by only about $4.7 \pm 2.4\%$.

Test conditions (e.g., temperature; pressure; etc.) during the experiments were well-controlled and are not believed to be responsible for the large standard deviations. In our reactor, hydrate formation likely initiated from multiple nucleation points and the resulting pockets that occurred within the hydrate mass may have trapped unpurified water. The observed low level of removal of proteins may also be due to inclusions of unconverted solution within the hydrate slush. Since larger molecules have reduced Van der Waals interactions with the water molecules in hydrates (Lu *et al.*, 2000), the size of the BSA contaminant may have inhibited crystallization and growth, resulting in numerous pockets of BSA-rich water in the collected hydrate mass. Additional experiments are needed to confirm the present, preliminary results.

3.4 International Collaborative Research and Development

The 8th International Workshop on Methane Hydrate R&D was held in Sapporo, Japan on 28 May-1 June 2012. This series of meetings was initiated as part of HEET and HNEI has served on the organizing committee and as a sponsor for all of the past workshops. The 8th Workshop was attended by 101 scientists, engineers, and other stakeholder from 16 countries. The workshop comprised three overview lectures (two keynote speeches and the banquet talk), 13 national reports, six breakout sessions and 50 individual research presentations consisting of 15 oral and 35 poster presentations.

Immediately following completion of the Sapporo workshop, planning commenced for the 9th workshop that will be held in Hyderabad, India from 9-12 November 2014. CSIR-National Geophysical Research Institute is taking the lead for this workshop and HNEI will once again serve on the organizing committee and provide sponsorship.

Publications Resulting from Efforts

R&D conducted as part of the HEET09 Methane Hydrates Task has produced one journal publication:

Coffin R.B, Smith J.P, Plummer R.E., Yoza B., Larsen R.K., Millholland L.C., Montgomery M.T. (2013) Spatial variation in shallow sediment methane sources and cycling on the Alaskan Beaufort Sea Shelf/Slope. *Marine and Petroleum Geology* 45: 186-197

A second manuscript on the effects of transition metal salts on hydrate formation has been revised and will be re-submitted for review. In addition, the work on hydrate formation in sand matrices and hydrate water purification resulted in an M.S. thesis in Ocean and Resources Engineering and a B.S. Honors thesis in Global Environmental Science, respectively.

References

- Boswell, R. & Collett, S.T. 2011. Current perspectives on gas hydrate resources. *Energy & Environmental Science*, **4**, 1206-1215.
- Coffin R.B, Smith J.P, Plummer R.E., Yoza B., Larsen R.K., Millholland L.C., Montgomery M.T. (2013) Spatial variation in shallow sediment methane sources and cycling on the Alaskan Beaufort Sea Shelf/Slope. *Marine and Petroleum Geology* **45**: 186-197
- de Roo, J.L., Peters, C.J., Lichtenthaler, R.N., Diepen, G.A.M. 1986. Occurrence of methane hydrate in saturated and unsaturated solutions of sodium chloride and water in dependence of temperature and pressure. *AIChE Journal*, **29**(4), 651-657.
- Dholabhai, P.D., Parent, J.S., Bishnoi, P.R. 1997. Equilibrium conditions for hydrate formation from binary mixtures of methane and carbon dioxide in the presence of electrolytes, methanol and ethylene glycol. *Fluid Phase Equilibria*, **141**, 235-246.
- Gupta, A., Lachance, J., Sloan Jr., E.D., and Koh, C.A., 2008. Measurement of methane hydrate heat of dissociation using high pressure differential scanning calorimetry. *Chemical Engineering Science* **63**, 5848-5853.
- Handa, Y. P. 1986. Compositions, enthalpies of dissociation, and heat capacities in the range 85 to 270 K for clathrate hydrates of methane, ethane, and propane, and enthalpy of dissociation of isobutane hydrate, as determined by a heat-flow calorimeter. *Journal of Chemical Thermodynamics*, **18**, 915-921.
- Holmes, A.J., Costello, A., Lidstrom, M.E. and Murrell, J.C. 1995. Evidence that particulate methane monooxygenase and ammonia monooxygenase may be evolutionarily related. *FEMS Microbiol. Lett.* **132**: 203-208
- Hyodo, M., Nakata, Y., Yoshimoto, N., Ebinuma, T. 2005. Basic research on the mechanical behavior of methane hydrate-sediments mixture. *Soils and Foundations*, **45**(1), 75-85.
- Inagaki F., Tsunogai U., Suzuki M., Kosaka A., Machiyama H., Takai K., Nunoura T., Nealson K.H., Horikoshi K. 2004. Characterization of C1-metabolizing prokaryotic communities in methane seep habitats at the Kuroshima Knoll, southern Ryukyu Arc, by analyzing pmoA, mmoX, mxaF, mcrA, and 16S rRNA genes. *Appl Environ Microbiol.* **70**(12): 7445-55.
- Jia, Y., G.C. Nihous and K.J. Richards. 2012. Effects of Ocean Thermal Energy Conversion systems on near and far field seawater properties - a case study for Hawaii. *Journal of Renewable and Sustainable Energy*, **4**, 063104, doi: 10.1063/1.4766820, 13 p.
- Kawamiya, M., Kishi, M. J., Yamanaka, Y. and Suginochara, M. 1995. An ecological-physical coupled model applied to Station Papa. *Journal of Oceanography*, **51**, 635-664.

Kawamiya, M., Kishi, M. J., Yamanaka, Y. and Suginoara, M. 1997. Obtaining reasonable results in different oceanic regimes with the same ecological-physical coupled model. *Journal of Oceanography*, **53**, 397-402.

Kiene, R. P., and D. G. Capone. 1985. Degassing of pore water methane during sediment incubations. *Appl. Environ. Microbiol.* **49**: 143-147.

Kharrat, M. and Dalmazzone, D., 2003. Experimental determination of stability conditions of methane hydrate in aqueous calcium chloride solutions using high pressure differential scanning calorimetry. *J. Chem. Thermodynamics*, **35**, 1489-1505.

Lafond, P.G., Olcott, K.A., Sloan, E.D., Koh, C.A., Sum, A.K. 2012. Measurements of methane hydrate equilibrium in systems inhibited with NaCl and methanol. *J. Chem. Thermodynamics*, **48**, 1-6.

Liang, D., Wang, R., Guo, K., & Fan, S. 2001. Prediction of refrigerant gas hydrates formation conditions. *Journal of Thermal Science*, 64-68.

Nikbakht, F., Izadpanah, A. A., & Varaminian, F. 2011. *Modeling of Hydrate Formation Conditions for Refrigerant R-134A, R141B and R152A Using the CPA Equation of State and Obtaining the Kihara Potential Parameters for these Refrigerants*. Bushehr: Persian Gulf University.

Lind, M.D., 1967. Crystal structure of ferric chloride hexahydrate. *Journal of Chemical Physics* **47**, 990-993.

Lu, H., Matsumoto, R., Tsuji, Y., & Oda, H. 2000. Anion plays a important role than cation in affecting gas hydrate stability in electrolyte solution?- A recognition from experimental results. *Fluid Phase Equilibria*, **178**:225-232.

Marshall, J, Jones, H. and C. Hill. 1998. Efficient ocean modeling using non-hydrostatic algorithms. *Journal of Marine Systems*, **18**:115-134.

Michaelides, A. and Morgenstern, K., 2007. Ice nanoclusters at hydrophobic metal surfaces, *Nature Materials*, **6**, 597-601.

Nago, A. & Neito, A. 2011. Natural gas production from methane hydrate deposits using CO₂ clathrate sequestration: State-of-the-Art review and new technical approaches, *Journal of Geological Research*.

Nauhaus K., Treude T., Boetius A., Krüger M. 2005. Environmental regulation of the anaerobic oxidation of methane: a comparison of ANME-1 and ANME-2 communities. *Environ Microbiol.* **71**: 98–106

- Nercessian O., Noyes E., Kalyuzhnaya M. G., Lidstrom M. E., Chistoserdova L. 2005. Bacterial populations active in metabolism of C₁ compounds in the sediment of Lake Washington, a freshwater lake. *Appl. Environ. Microbiol.* **71**: 6885-6899.
- Niemann H., Losekann T., De Beer D. 2006. Novel microbial communities of the Haakon Mosby mud volcano and their role as a methane sink. *Nature* **443**: 854–858.
- Nihous, G.C. and S.M. Masutani. 2007. Notes on the modeling of methane in aging hydrothermal vents. *Journal of Marine Research*, **65**(6), 789-812.
- Nihous, G.C. and S.M. Masutani. 2006. A model of methane concentration profiles in the open ocean,” *Journal of Marine Research*, **64**(4), 629-650.
- Rajagopalan, K. and G.C. Nihous. 2013. An assessment of global Ocean Thermal Energy Conversion (OTEC) resources with a high-resolution Ocean General Circulation Model,” *Journal of Energy Resources Technology*, **135**, 041202, 9 p.
- Rajagopalan, K. and G.C. Nihous. 2013. Estimates of global Ocean Thermal Energy Conversion (OTEC) resources using an Ocean General Circulation Model. *Renewable Energy*, **50**, 532-540.
- Sabil, K.M., Roman, V.R., Witkamp, G-J., Peters, C.J., 2010. Experimental observations on the competing effect of tetrahydrofuran and an electrolyte and the strength of hydrate inhibition among metal halides in mixed CO₂ hydrate equilibria, *J. Chem. Thermodynamics*., **42**, 400-408.
- Sloan, E.D., Koh, C.A., 2008. Clathrate hydrates of natural gases, 3rd edition, Taylor & Francis, CRC Press, Boca Raton, Fl.
- Sloan, E.D., Lederhos, J.P., Long, J.P., Sum, A., Christiansen, R.L., 1996. Effective kinetic inhibitors for natural gas hydrate. *Chem. Eng. Sci*, **51**, 1221-1229.
- Takeya, S., Hori, A., Hondoh, T., & Uchida, T. 2000.. *Journal of Physics and Chemistry B*, **104**, 4164.
- Trofimuk, A.A., Cherskii, N.V., Tsarev, V.P., & Nikitin, S.P. 1982. *Geologiya i Geofizika*, 23, 3.
- Uchida, T., S. Takeya, Chuvilin, E.M., Ohmura, R., Nagao, J., Yakushev, V.S., Istomin, V.A., Minagawa, H., Ebinuma, T., & Narita, H. 2004. Decomposition of methane hydrates in sand, sandstone, clays, and glass beads, *J. Geophys. Res.*, **109**, B05206.
- Waite, W.F., Winters, W.J., Mason, D.H. 2004. Methane hydrate formation in partially water-saturated Ottawa sand, *American Mineralogist*, **89** (8-9), 1202-1207.
- Whittenbury, R., Phillips, K.C. and Wilkinson, J.F. 1970. Enrichment, isolation and some properties of methane-utilizing bacteria. *J. Gen. Microbiol.* **61**: 205-218

Yan T., Ye Q., Zhou J., Zhang C.L. 2006. Diversity of functional genes for methanotrophs in sediments associated with gas hydrates and hydrocarbon seeps in the Gulf of Mexico. *FEMS Microbiol Ecol.* **57**(2): 251-9.

Yoneda, J., Hyodo, M., Nakata, Y., Yoshimoto, N., & Orense, R. 2011. Deformation of seabed due to exploitation of methane hydrate reservoir, *Frontiers in Offshore Geotechnics II*, 245-250.

TASK 4. ALTERNATIVE ENERGY SYSTEMS

4.1 OTEC Heat Exchanger

Ocean Thermal Energy Conversion (OTEC) power plants have the potential to contribute to the energy needs of many Navy bases. However, no cost-effective commercial technologies are available today. The single most expensive and technically critical component in an OTEC plant is the heat exchanger, making its development crucial to the economic viability of OTEC. Small changes in heat exchanger performance are critical to the overall efficiency of the plant, and will have significant economic consequences. Previously, under separate funding from Naval Facilities Engineering Command, Makai developed the infrastructure for a heat exchanger test facility at the Natural Energy Laboratory of Hawaii Authority (NELHA) on the Island of Hawaii. Existing infrastructure at NELHA includes ready access to deep seawater (from 2,200' or 3,000' deep) and surface seawater flows in quantities exceeding 10,000 gallons per minute. Under HEET09, HNEI contracted Makai Ocean Engineering (Makai) to continue efforts initiated under HEET08 to validate the performance of heat exchanger designs, materials and fabrication methods for OTEC applications.

The goal of the heat exchanger development program is to optimize OTEC heat exchanger cost, lifetime, and performance. To meet this goal, the OTEC heat exchanger testing program is divided into three areas: performance testing, development, and corrosion testing. Key design, materials and fabrication features in HEET09 included:

- A brazed aluminum evaporator with brazed aluminum fins in the ammonia channels and square extruded passages for the seawater channels. The fins enhance heat transfer and the extruded channels eliminate exposing brazed joints to the corrosive seawater environment.
- A Lockheed Martin shell and tube condenser to showcase the use of tubular friction stir welding – a new manufacturing technique – to join aluminum alloys; 6063 tubes to 6061 tubesheet. This combines the desirable corrosion resistance of the Alloy 6063 and with the friction stir welding method, as well as lowering the cost of manufacturing.

Accomplishments under HEET09 include:

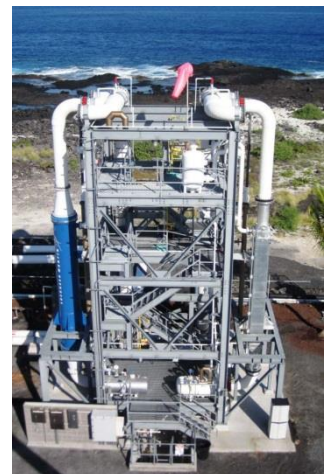


Figure 4.1.1 OTEC Test Facility at NELHA designed and operated by Makai Ocean Engineering

Design and Construction of a Heat Exchanger Performance Testing Facility

- Construction of the heat exchanger Testing Facility
- Installation of Chart Industries and Lockheed Martin heat exchangers
- Design, development, and validation of heat exchanger Facility Control System
- Completion of Shakedown Testing

Heat Exchanger Development

- Design, installation, and functional testing of Chart brazed aluminum evaporator and Lockheed shell and tube condenser

Corrosion Testing

- Evaluation of 6-month, 1-year, and 18-month hollow extrusion corrosion samples

Findings under HEET09 include:

Heat Exchanger Testing Facility Design and Operation

- Design phase was extended due to delays in heat exchanger delivery. The extended design phase allowed for better facility design.
- Construction was smooth overall. The two delays experienced prior to running the facility were caused by electrical inspection and leaking ammonia control valves.
- Manufacturer supplied calibration data was found to be questionable, so in future work Makai plans to independently validate each sensor reading with their own calibration since instrument calibration and reliability is vital to testing.
- As a result of the testing facility now being equipped with high accuracy instrumentation, lower uncertainties are expected compared to previous testing.
- A wide range of testing conditions has been confirmed. However, higher sensitivity can be attained when testing at higher duties than during testing at low duties.
- At maximum duty, the rate of condensate flow exiting the condenser may be limited due to pipe sizes.
- Heat transfer to/from the environment (e.g., condensation on the outside of the condenser) may introduce errors in heat exchanger testing. Further investigation will be required for highly reliable performance data.
- Ammonia vapor/liquid mixture at the evaporator outlet must travel up an additional 12 feet prior to reaching the separator. This may affect evaporator performance.
- Steady state can be attained in ~ 3 minutes when control system parameters are optimized, compared with previous testing that required approximately 1 hour to reach targeted steady state conditions.

Heat Exchanger Development

- The Lockheed shell and tube condenser were manufactured using a new Tubular Friction Stir Weld technique to join the tubes into the tube sheet. This technique minimizes both manufacturing costs and the affected weld zone to improve corrosion resistance.
- The condenser is constructed of Alloy 6063. The selection of Alloy 6063 for its manufacturability and corrosion resistance illustrates the synthesis of the program's multiple goals.
- Brazed joints in the Chart brazed aluminum evaporator were isolated from seawater exposure to protect against corrosion.

- The Chart brazed aluminum evaporator has extruded channels for seawater passages. This design is optimized for OTEC as extruded channels are unconventional in a brazed aluminum heat exchanger.

Corrosion Testing

- Uniform corrosion rates are low and comparable amongst the different alloys.
- Braze joints and electropolished surfaces are susceptible to severe pitting in cold seawater.
- Focus on quantifying and comparing susceptibility to localized corrosion will determine whether aluminum is a viable heat exchanger material.

More detailed results from this task can be found in Appendix 4.1 which contains Makai's annual report summarizing HEET09 activities in the OTEC heat exchanger testing program. The report can also be accessed on HNEI's website at: <http://www.hnei.hawaii.edu/publications/projects-other-reports#HEET09>.

4.2 Grid Storage

Under this subtask, HNEI conducted testing and evaluation of a grid-scale Battery Energy Storage System (BESS) on the Island of Hawaii and has completed facility acceptance testing for a BESS that is to be installed on the Island of Molokai. The BESS are intended to address issues associated with the very high penetration of intermittent renewable energy resources found on the two islands.

On the Island of Hawaii, the grid has a peak load of 180 MW with approximately 32 MW of installed nameplate wind capacity and 66 MW of photovoltaic (PV) capacity. The grid is owned and operated by the Hawaii Electric and Light Company (HELCO). A 1 MW, 250 kWh BESS on Hawaii was installed at the interconnection between the 10.6 MW Hawi wind farm and the grid. The BESS can be controlled by either of two real-time algorithms: a primary frequency response algorithm, and a wind power smoothing algorithm. This system has been running for 3 years and has cycled (alternately sourced or absorbed) over 3.1 GWh of energy (January, 2013 through November, 2015, equivalent to over 6000 round trip, charge-discharge cycles).

On the Island of Molokai, the 5.4 MW grid, owned and operated by the Maui Electric Company (MECO), has about 2 MW of distributed PV capacity and no significant wind generation. A 2 MW, 397 kWh BESS has been procured and factory-acceptance tested. It will be installed, commissioned, and tested on the Molokai grid under a subsequent ONR award. With that amount of PV and the small size of Molokai's power grid, the grid's inertia is extremely low. This requires very fast responses to disturbances to prevent load shed and even island wide outages. This is a challenge that HNEI and its development team have been working to resolve. It is anticipated that the system will be installed and commissioned in June, 2016.

In the sections below, the BESS for the Island of Hawaii will be discussed first. This will include an introduction to the development team, a description of the hardware, an overview of the two algorithms, a description of the experiments, a review of some key results, and a discussion

about lessons learned. The Molokai BESS discussion will follow and will introduce the development team, hardware and the control algorithm.

Island of Hawaii BESS

The initial investigation into a BESS system for the Island of Hawaii began in 2009 with a modeling effort performed by General Electric (GE) under contract with HNEI using funding from the US Department of Energy. The study included use of Positive Sequence Load Flow (PSLF) power system analysis software and historical data to model the dynamic response of the Hawaii Island grid during an under-frequency event on May 23rd, 2007, which was attributed to a sudden drop in wind power production. The model runs simulated the effect of adding fast-acting energy storage to an electric grid that was capable of providing 1 MW of power. Results showed that this relatively small battery system could significantly reduce the severity and duration of frequency events.

Collaboration and Site Preparation

These model results prompted HNEI to seek funding to allow installation and testing of a fast response battery on the HELCO grid. Funding for procurement, installation, and testing of an Altairnano Lithium-ion (Li-ion) titanate battery was included under the HEET 09 ONR award. Subsequent to receipt of funding, HNEI and HELCO developed and executed a Memorandum of Agreement (MOA). As stipulated in the MOA, the BESS was to be procured by HNEI. After commissioning, the ownership of the BESS was turned over to HELCO with HNEI retaining the right to operate the BESS (with prior notification to HELCO) and collect data for a three year period. Key participants in the public-private partnership are described in Table 4.2.1.

Table 4.2.1: Project team.

| | |
|---------------------------------|--|
| Hawaii Natural Energy Institute | Project Management Technical Oversight Algorithm Development Support |
| Office of Naval Research | Primary Funding Source |
| Department of Energy | Partial Funding for Algorithm Development |
| Hawaiian Electric Light Company | Infrastructure Development Interconnection Planning Grid Management |
| Hawi Renewable Development | Host Site |
| Altairnano | Battery Technology Developer Systems Integrator |
| Integrated Dynamics, Inc. | Frequency Algorithm Development Real-time Software Development |
| SCADA Solutions | Wind Algorithm Development |
| Parker-Hamilton | Power Conversion System Developer |

A Li-ion titanate battery chemistry was chosen due to the desire for an extended cycling lifetime and faster charge/discharge rates compared to the more common carbon anode electrochemistry. The BESS was designed for interconnection to electrical power systems (as defined by ANSI C84.12006), and to be compliant with applicable standards during discharge (IEEE 1547-2003) and standby/charging modes (IEEE 519).

Site construction started in April of 2012 (e.g., ground leveling and pouring of concrete pads). Between April and December, all of the construction, planning, electrical design, communications design, and algorithm development efforts were conducted. In tandem with site preparation work, the BESS and the control algorithms were put through a series of factory acceptance tests. A deliverable report (for each of the acceptance tests) was prepared by Altairnano for HNEI.

Hardware Description, Algorithm Development and Acceptance Testing

The Hawaii Island BESS is housed in two containers, one for the Power Module (PM, Figure 4.2.1) and a second for the Power Conversion System (PCS, Figure 4.2.2). The PM contains the battery modules, along with a ground fault detection system, a fire suppression system, HVAC system, the Battery Management System (BMS), and the Site Dispatch Controller (SDC). The BMS is responsible for monitoring, controlling, and protecting the battery cells, including monitoring state of charge, cell voltage balancing, and protecting against thermal damage. The SDC is a computer that communicates with both the PCS and the BMS, reads the grid-connected meters, and calculates power commands based on those measurements. The SDC also communicates with a secure cloud server to provide data logging, data access, and system control to Altairnano, HELCO, and HNEI. The PCS contains a four-quadrant inverter (+/- real and reactive power), coolant system, metering units, processing units, and associated protection.



Figure 4.2.1: Power Module (PM) houses batteries as well as other systems.



Figure 4.2.2: Power Conversion System (PCS) contains inverters and all necessary support systems.

The PM and PCS were assembled and interconnected at the Altairnano facility in Anderson, Indiana. After assembly, representatives from HNEI and HELCO attended a Facility Acceptance Test (FAT) to verify that the BESS operated to specification. The hardware was disassembled and shipped to the Island of Hawaii where the system was re-assembled and re-tested. This Site Acceptance Test (SAT) was designed to verify that the system operated as it did during the FAT, proving correct re-assembly.

The two algorithms (frequency response and wind smoothing) were developed in tandem with the hardware. Like the hardware, the algorithms went through a series of acceptance tests (Figure 4.2.3).

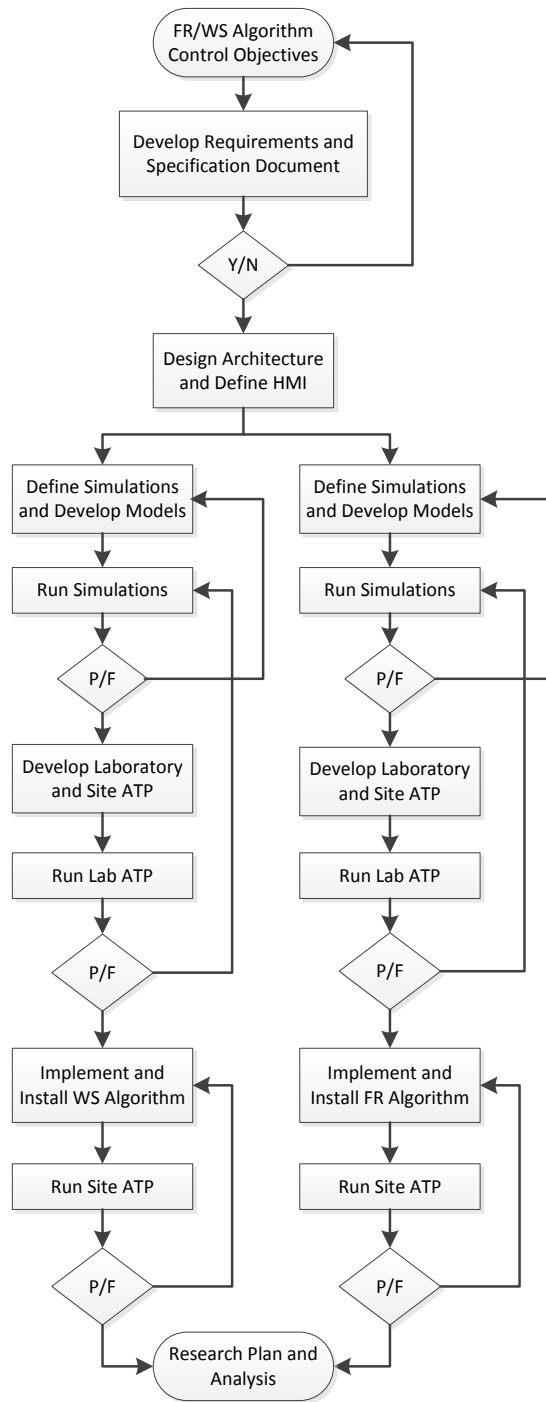


Figure 4.2.3: Algorithm development process. Abbreviations: FR/WS indicate Frequency Response or Wind Smoothing algorithm; ATP indicates Acceptance Test Plan.

The development process started with the development of requirements and functional specifications to define how the algorithms would respond to measurements, what data would be stored, and provide some performance objectives. Architecture and HMI design included block diagrams, mathematics, and the layout of the user interface. After the algorithms were designed, simulations were conducted to determine how well the specified algorithms were

expected to perform. In the case of the wind power smoothing algorithm, 10 days of archived wind power data was used. In the case of the frequency response algorithm, a simple grid model (Figure 4.2.4 and Table 4.2.2) was used along with a series of different assumptions about grid parameters (Table 4.2.3 shows the first 2 of 4 assumptions used). All sets of model parameters resulted in a good fit between simulated and real frequency data for several historical datasets. This showed that the BESS and algorithm were sufficient across a number of possible grid models to reduce grid frequency variability. The reason for using such a simple model (which assumes all generation can be approximated as a single generator) was to avoid repeating a complex grid model simply to get an estimate of performance. Plans were then developed and it was demonstrated that the algorithms were correctly coded into the target platform (embedded MOXA computer running Linux). Next, a site acceptance test plan was developed to describe how the algorithms would be tested in the real system at the actual installation site. This concluded the algorithm development efforts.

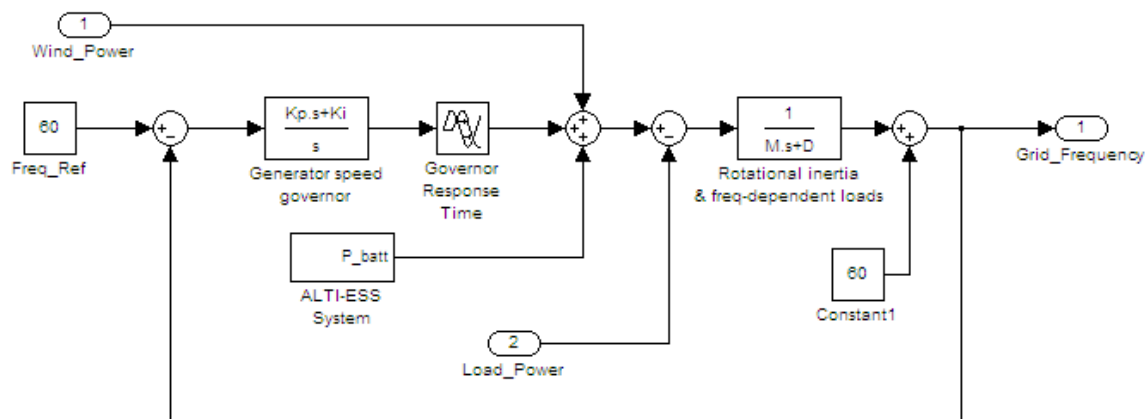


Figure 4.2.4: Simple grid model.

Table 4.2.2: Description of simple model parameters.

| Parameter | Units | Description |
|-------------------|---------------|--|
| M | MW per Hz/sec | Inertia constant |
| D | MW per Hz | Damping constant |
| Kp | MW per Hz | Governor proportional gain |
| Ki | MW/sec per Hz | Governor integral gain |
| Tgen | Sec | Generator response time – pure delay |
| Tau_gen | Sec | Generator response time – filter time constant |
| Gen_10pct_ramp_tm | Sec | Limit on integral term's ramp rate, measured as time to change by 10% of nominal generator output. |

Table 4.2.3: Some model parameter sets used. Two more were eventually used as well.

| Parameter | Grid Model #1 | Grid Model #2 | Units |
|-------------------|---------------|---------------|---------------|
| M | 1.5 | 1.6 | MW per Hz/sec |
| D | 26.7 | 10.0 | MW per Hz |
| Kp | 3.3 | 4.0 | MW per Hz |
| Ki | 0.72 | 0.5 | MW/sec per Hz |
| Tgen | 0.4 | 5.0 | Sec |
| Tau_gen | 0.4 | 5.0 | Sec |
| Gen_10pct_ramp_tm | 900 | 900 | Sec |

The following indicates the dates at which some key milestones were completed with respect to this development effort:

- Installed: 12/9/12
- Initiated Algorithm Testing: 01/30/13
- Completed Formal Training: 03/22/13
- Approved Results of the ATP: 04/12/13
- Product Transfer Agreement executed: 05/09/13
- Tri-annual inspections, testing, and monthly data reporting agreements in place: start 7/13

Experiments and Algorithm Parameter Tuning

After efforts to develop data access and basic analysis software, experiments and tuning efforts were started, less than 2 months after commissioning. The frequency response algorithm was the focus of the experimentation and tuning during the first few months after commissioning. A MATLAB/Simulink block diagram of the algorithm is shown in Figure 4.2.5. The “simulated inertia” and “disturbance feed-forward” chains were disabled to focus on fast frequency response. Also, a “Shark 100” meter used for frequency measurement was disabled because (1) there was an installation/noise issue, and (2) there was a significant delay in measurements coming from the meter because of the internal filtering performed to improve frequency precision. In Figure 4.2.5below, the τ_{Input} parameter representing a time constant associated with an input low-pass filter (to smooth frequency measurements) was varied. Also, the proportional gain labeled “Gain” was varied. This is the slope of the frequency-Watt (f-W) curve in MW/Hz.

Shark Meter:
Disabled

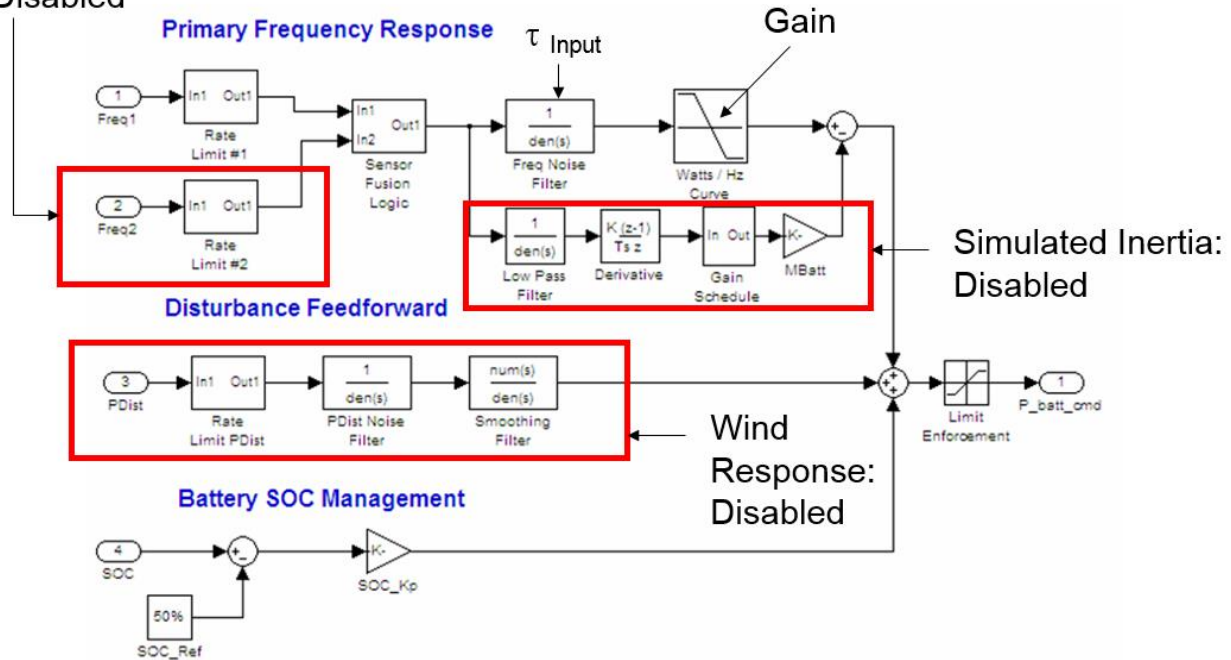


Figure 4.2.5: Frequency response algorithm block diagram.

The default value of τ_{Input} was 1 second. It was found that this value was too high. The left plot in Figure 4.2.6 shows the HELCO grid frequency for one experiment under ‘typical’ operating conditions with and without the BESS. In these experiments, the BESS was switched off (black trace) for 20 minutes, then turned on (red trace) for 20 minutes, then repeated. Each 40 minute period (containing one off sequence and one on sequence) is defined as a “group”. There are two groups shown in the left side of Figure 4.2.6. The plot on the right is a Power Spectral Density (PSD) plot of these frequency time series. Note that the PSD indicates a reduction in frequency variability when the BESS is on since the blue and red lines are generally lower than the green and cyan dots. There is an interesting spike at 0.2 Hz, which is the rate at which the data are sampled times $1/\tau_{\text{Input}}$. Further experiments also verified that this spike shifted right and diminished as the time constant was lowered. A time constant of 0.4 seconds was ultimately chosen as a new “default” parameter since there was no notable sign of a spike in grid frequency, yet the filter provided some level of smoothing against any erroneous measurements (that were too small to be removed by the rate limiter).

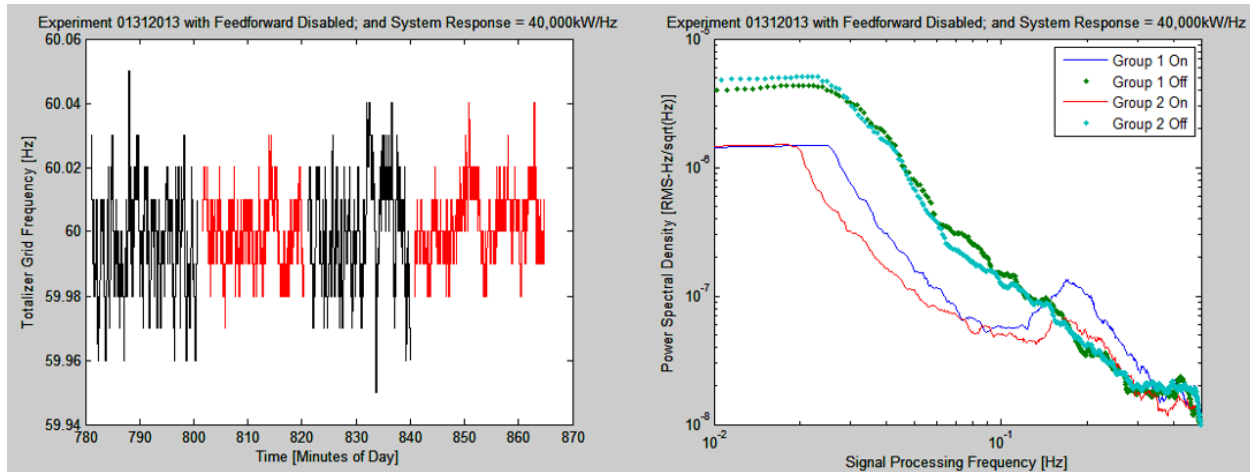


Figure 4.2.6: (Left): BESS was switched off (black) for 20 minutes, then turned on (red) for 20 minutes, then repeated. (Right): Power spectral density of the frequency shows a spike at the frequency associated with the τ_{Input} parameter.

After determination of the best τ_{Input} parameter, the experimental protocol in which the BESS is switched between off and on was adopted as a way to assess how well the BESS supported this grid. It was agreed that 20 minute off and on samples were about right since this limited the effects of changing grid conditions over time, but provided sufficient data for analysis. With a sampling frequency (for data storage) of 5 Hz, about 6000 samples were available for analysis for each off and on sequence.

Another parameter that was tuned was the gain in the f-W curve. During the site acceptance test, the gain was set at 10 kW/Hz. In subsequent on/off switching experiments, 20, 30, and 40 MW/Hz were attempted. When 40 MW/Hz was attempted the temperature of the battery cells increased significantly (Figure 4.2.7).

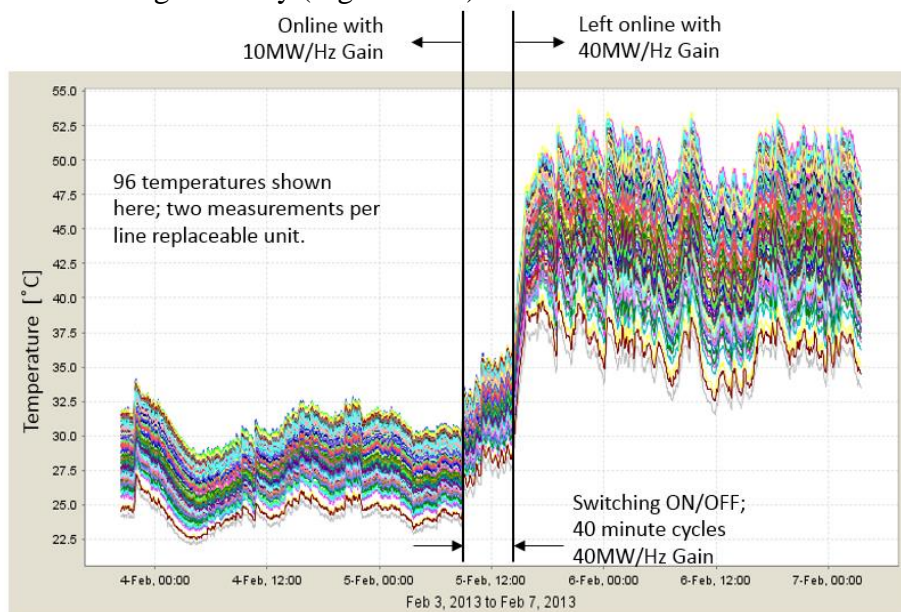


Figure 4.2.7: Temperature of individual battery modules.

The temperatures of the cells did not increase significantly when setting the gain at 20 or 30 MW/Hz but did increase significantly when the gain was set to 40 MW/Hz. Under this operation, the dispersion of the cell temperatures also increased.

On March 29th, 2013, it was found that the excessive module temperatures were partly due to poor balancing of HVAC vents. Major vents closer to the battery modules were closed while those closer to the SDC were open. Once the vents were adjusted, the 40 MW/Hz tests conducted on February 5th, 2013 were repeated. In this case, the battery modules showed a manageable temperature increase. These module temperatures are mapped by location in Figure 4.2.8. The depiction on the left side container drawing represents the temperatures before the adjustment. The depiction on the right side container represents the temperatures after the adjustment. In both, the large pixels represent battery modules. The extreme left and right edges of the pixel arrays represent modules near the top of the battery stack. The inner most pixels (appear adjacent to the walk way) represent modules near the floor. In the figure, the references to “vents open” and “vents closed” indicate the situation prior to the adjustments. In addition to modification of those major vents, smaller vents directly behind the battery modules were also adjusted.

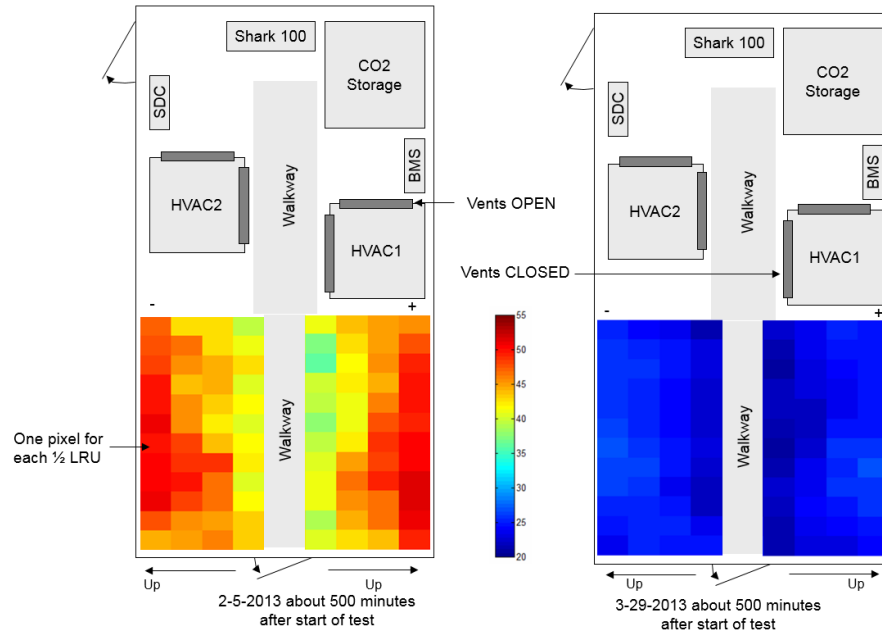


Figure 4.2.8: Temperature mapping. (Left) Temperatures (Degrees C as indicated in the color strip in the middle of the figure) before tuning HVAC vents and (Right) after tuning HVAC vents.

Results

At the time of this writing, over 100 switching experiments were conducted targeting a variety of grid conditions (day/night, windy/calm, etc.) and a variety of algorithm parameter settings (gain, limit on maximum power, and a “dead band” in which the algorithm does not respond to small fluctuations). One sample experiment is shown in Figure 4.2.9. The results show that the overall frequency variability is reduced by 30-50 % when the BESS is on compared to off. The term “overall frequency variability” is defined as the standard deviation of an entire 20 minute on or off sequence. The reduction in frequency variability is even more notable when looking at a 1-

minute time-scale. There are many ways workers have approached the problem of analyzing data in time-scales, such as PSD, or Allen Variances. Here, the frequency time series is simply divided into 1 minute samples. The standard deviation of each sample is computed. Those one minute samples are shown in the bottom plot of Figure 4.2.9. If the means of the 1-minute samples is taken, the reduction in frequency variability is about 50% under typical grid conditions.

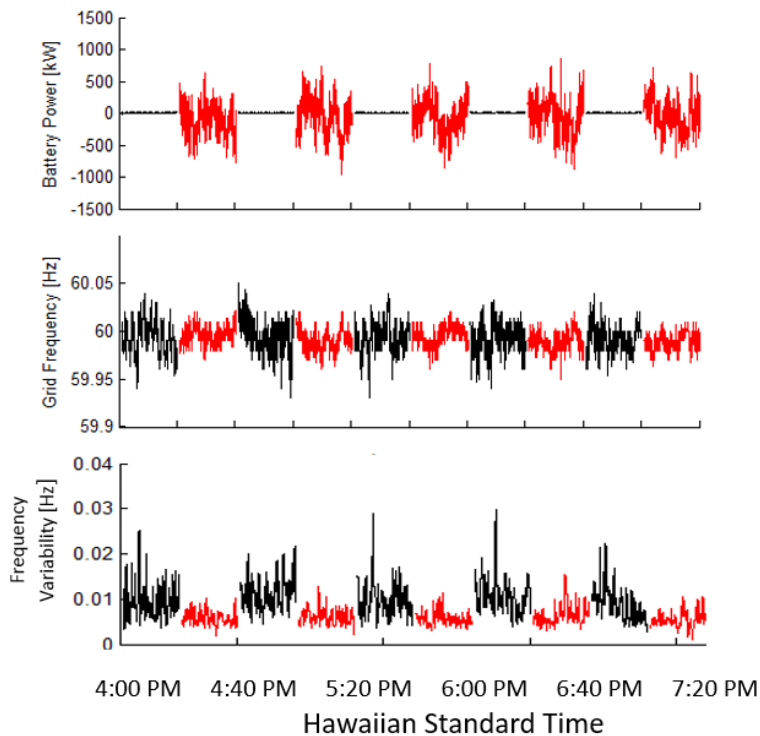


Figure 4.2.9: Time series of BESS real power output (top), HELCO grid frequency (middle), and one minute running standard deviation of grid frequency (bottom), for 20 minutes periods with the BESS alternating between active (red) and inactive (black) states. The data shown is from 3/15/2013.

Current Status and Lessons Learned

Under a future award (APRISES 10 and 11) HNEI is continuing the work described above, including a dead band in the frequency response algorithm so that the BESS does not respond to small variations in grid frequency. It was recently found that using a 20 MW/Hz gain with a 20 mHz dead band reduced cycling energy throughput 3-fold compared to running the system at 30 MW/Hz with no dead band, while still mitigating frequency events comparably outside of ± 10 mHz. Detailed results of the analysis under a variety of grid conditions and algorithm settings are being prepared for publication in archival journals.

Work was also performed to assess the functionality of the wind smoothing algorithm and the benefits of wind smoothing on the grid. In some cases, the wind smoothing algorithm acted to oppose the needs of the grid while improving the power quality of the HRD wind farm. This was attributed to the HRD wind farm being the smaller of two wind farms on the Island of Hawaii.

The BESS has exhibited an availability of approximately 90%. The primary reliability issues have been problems with the Uninterruptable Power Supply (UPS) and low voltage conditions. Both issues are currently being addressed. The UPS uses lead acid batteries to maintain operations in both the PM and PCS during power outages (which can be fairly common at the wind farm). There have been two incidents in which the UPS batteries failed. Those batteries are now tested every 18 months. To resolve the voltage problem, the BMS software is being modified so that the inverter's phase-locked loop will attempt to re-engage the grid after transient voltage drops (below 0.8 p.u.) rather than require an expert user to acknowledge the trip. Ongoing experimentation under a future ONR award will allow these solutions to be evaluated.

Molokai BESS

In recent years, the Molokai grid has experienced as many as 14 outages per year due mainly to its isolation and low inertia. In such a small grid, even damage to individual utility poles, whether due to car accidents or wind, can cause significant fluctuations to grid frequency. This, in turn, has the potential to trip significant portions of the 2 MW of residential PV systems. This instantaneous loss of generation then causes more PV inverters to trip (those with wider frequency ride through settings). In addition, since the diesel generators have to ensure that generation is equal to load at all times, the generators will be operating with a very low load (as a result of the very high penetration of PV on Molokai). In this case, the high penetration of PV effectively reduces the net load (real load-PV) to levels below the minimum generation required to have additional diesel generators on standby). Under this condition, the grid can become unstable. To address these problems, HNEI initiated a project to integrate a 2 MW, 397 kWh BESS into the grid for response to loss of generation or load

Collaboration and Site Preparation

The main partners of this collaborative project were HNEI, MECO, and Altairnano. The roles played by these and their subcontractors are shown in Table 4.2.5. As with the Island of Hawaii Project, the BESS will be signed over to MECO in accordance with the MOA after commissioning which is projected to occur in June of 2016.

Table 4.2.5: Project team.

| | |
|------------------------------------|--|
| Hawaii Natural Energy Institute | Project Management Technical Oversight |
| Office of Naval Research | Primary Funding Source |
| Maui Electric Company | Infrastructure Development Interconnection Planning Grid Management |
| Altairnano | Battery Technology Developer Systems Integrator |
| Integrated Dynamics, Inc. | Software Implementation Algorithm Evaluation and Redesign Design Modifications to Inverter (Speedup) |
| Northern Plains Power Technologies | Grid Modeling and Algorithm Development |
| Parker-Hamilton | Power Conversion System Developer Modifications to Inverter (Speedup) |

The Molokai BESS project was initiated with a site visit in April, 2013. A photograph from the site visit is shown in Figure 4.2.10, and the site layout is shown in Figure 4.2.11.



Figure 4.2.10: Initial site visit to main Molokai power station. Workers provide access to underground conduits.

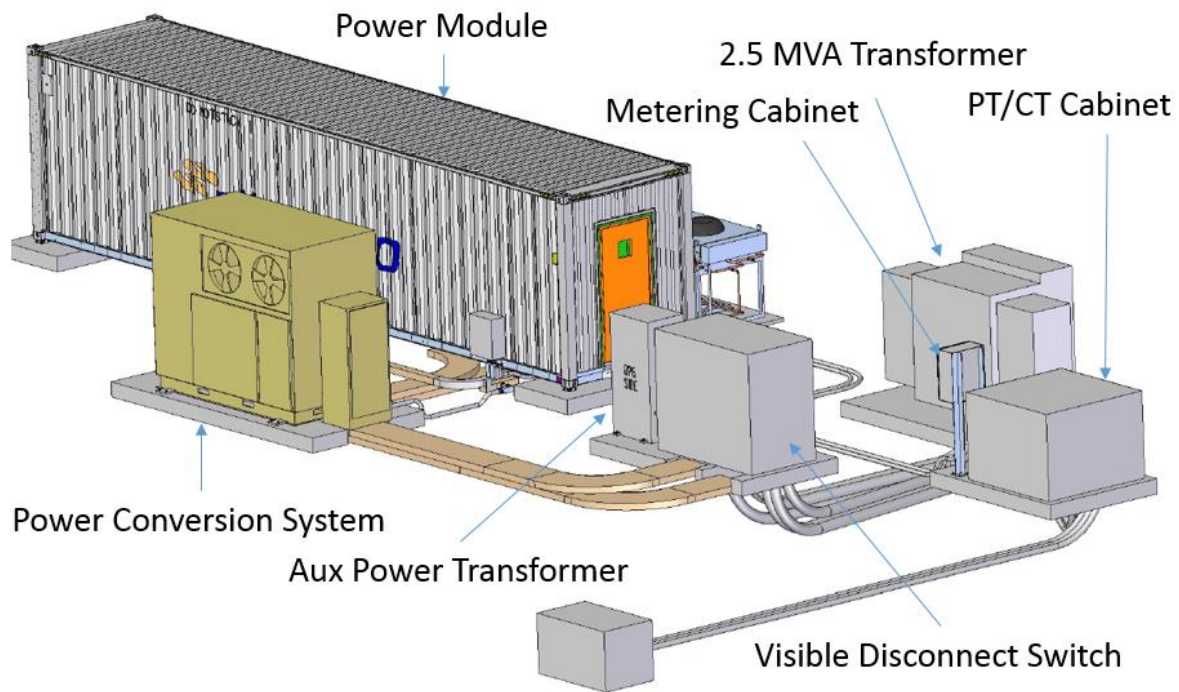


Figure 4.2.11: Site layout for Molokai BESS.

Hardware Description and Algorithm Development

The interior of the PM is shown in Figure 4.2.12. The system contains 104 Line Replaceable Units (LRU), each containing 4 modules. Each module contains 7 cells with each cell rated at 60 Ah (2.27 Vdc). The entire battery pack is capable of 397 kWh. The 2 MW PCS is capable of

four quadrant operation (+/- real and reactive power) and outputs three phase at 480 Vac. Other specifications include:

- IEEE 1547 compliance
- IEEE 519 power quality compliance
- Full power response time <100 ms
 - 96% efficiency at full power
- DC interface rating of 750 V to 1120 V
- DC breaker
- AC grid protection circuit breaker rated for system load
- Anti-islanding
- Direct transfer trip
- Pre-charge circuits
- Power filtering
- User interface for control and monitoring
- Dry-contact FM-200 fire suppression system with audible and visual alarms
- Schweitzer Engineering Laboratories SEL-700GT distributed generator interconnection relay



Figure 4.2.12: Interior of the power module (PM).

The grid interconnection study and algorithm development was funded by MECO. The interconnection study included the development and validation of a grid model. The algorithm was combined with a BESS/inverter model and run against the grid model to predict performance for several historical cases.

The objective was to operate the BESS to keep the grid frequency between 59.3 Hz and 60.5 Hz in order to avoid distributed PV inverters from tripping offline. To achieve this, the BESS was required to respond quickly during the onset of a frequency event. Once the frequency is stabilized, the algorithm is designed to slowly return the load back to the diesel generators. The algorithm was based on a finite-state machine shown in Figure 4.2.13.

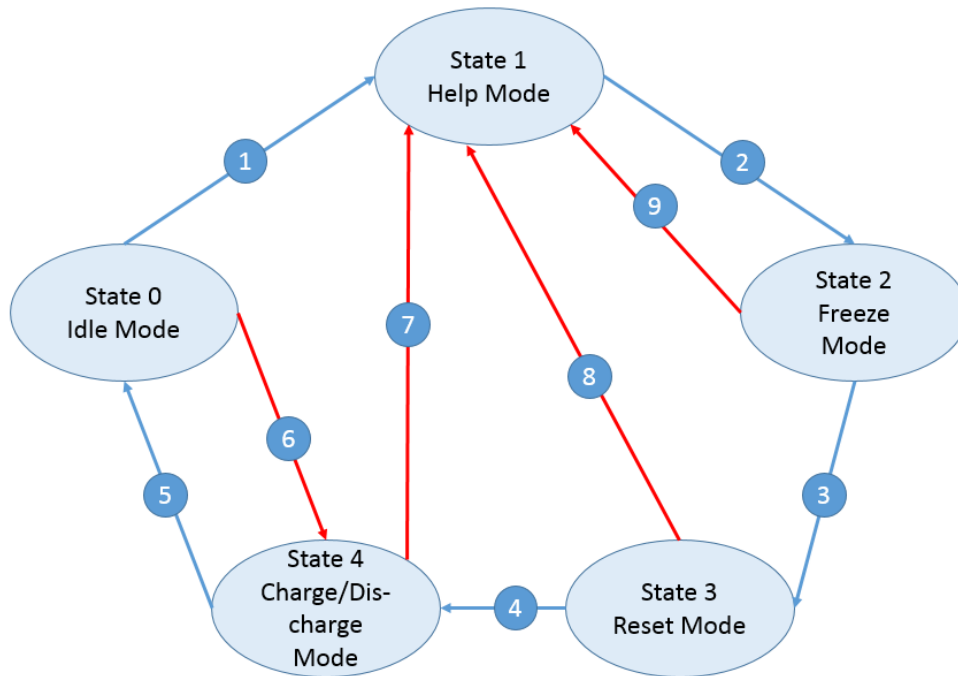


Figure 4.2.13: Finite-state machine algorithm.

When in State 1, the algorithm is simply attempting to detect the onset of a frequency event. However, if the State-of-Charge (SoC) diverges from a nominal value, the algorithm can go into State 4 until the SoC has returned to nominal (Path 6). If the grid frequency appears to be diverging, then Path 1 is taken and the BESS goes into State 1. Here, the real power command computed by the algorithm is essentially dictated by the f-W curve (similar, in some respects, to the HELCO project). The only path out of State 1 is Path 2 leading to State 2. The objective here is to maintain a fixed power output over a period of time long enough so that the generators can catch-up. State 3 is a transitional state in which the BESS does not supply quite enough power to maintain grid frequency. This prompts the generators to move in the right direction. Notice Paths 7-9 all allow the BESS to go into the f-W curve at any time to respond to frequency events.

Algorithm and Inverter Redesign

Leveraging experience other HNEI BESS projects, it was found that the computer architecture delays making it insufficient for supporting the Molokai grid (Figure 4.2.14). Modeling indicated that in order to stabilize the grid, a time delay between the measurement and the execution of a power command needed to be no longer than 50 ms.

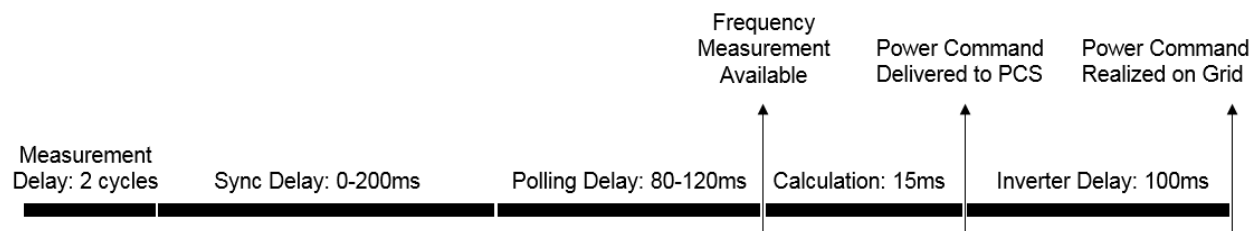


Figure 4.2.14: Time delays. Measurement Delay: Length of time required for meter to determine frequency. Sync Delay: Meters update every 200ms. When polled, the most recent measurement is delivered. However, the age of that measurement is unknown. Polling Delay: This is the amount of time required for the controller (algorithm) to acquire the newest measurement. Calculation Time: Given a frequency measurement, there is a small amount of time required to calculate a real power response. Inverter Delay: This is assumed to be a fixed 100ms delay.

The team has initiated a parallel research project to determine and verify methods to reduce the delay time to below 50 ms. The plan was to have the SDC pass solution “curves” to the PCS’s computer (the PLC) which then executes the power commands directly. A Shark 200 meter run in high speed mode was also added to minimize measurement delays. The performance of these solutions will be evaluated under a future ONR award.

Current Status

The FAT was performed between December 3rd and 4th, 2015. During the FAT, the operation of several subsystems were tested (HMI, internet connectivity, fire alarms, data access, power rating, energy rating, etc.). The results of the FAT showed that the system was functioning acceptably.

Conclusions

The HELCO BESS has been successfully used to provide ancillary services, in the form of frequency regulation for the Island of Hawaii, while providing HNEI with the data needed to conduct testing and evaluation. These studies are being used to develop a series of research papers to be submitted in the 2016 calendar year. . Topics of the papers range from grid performance to system health.

While still under development, the Molokai BESS has provided significant lessons about today’s technological barriers related to BESS and inverter response times as well as meter sensing delays. An improvement in this area can have applications in real-world micro-grids under heavy penetration from intermittent renewable energy resources.

Papers and Presentations Resulting from These Efforts

- R. Rocheleau. “Use of a Fast Response Battery System for Frequency Regulation.” Electrical Energy Storage Applications and Technologies Conference, San Diego Marriott Hotel and Marina, Oct 22-23, 2013
- R. Rocheleau, M. Matsuura, K. Stein, M. Tun. “Battery Energy Storage for Grid Support.” Energy Storage & Technology Conference, Karlsruhe Convention Centre, Germany, May 20-22, 2015

4.3 PV Deployment and Testing

Solar photovoltaic (PV) performance is dependent on the cell materials, module design, inverter technology and integration, and environment (solar radiation, temperature, cloud shadowing, etc.). The intent of this project is to characterize performance and durability of different PV and inverter technologies under differing environmental conditions. Data has been gathered on PV system performance and environmental factors at a variety of installations around Hawaii using several manufacturers' products and system architectures. The PV systems under test represent grid-tied, residential and small-scale commercial systems.

This project leverages work completed under US Department of Energy (US DOE) funding (DE-FC26-06NT42847 and DE-EE0003507) that included the installation of three PV test platforms located on Hawaii Island, Maui and Oahu, the development of a data acquisition system (DAS) and of the data management and analysis tools. Results of these efforts were reported in [1] for PV test platforms and test protocols and in [2] for the data management and analysis tools. Results provided a body of knowledge on PV test platform design, installation, instrumentation testing and analysis.

Under this HEET09 subtask, HNEI has performed the following:

- 1) Installed PV systems at three Hawaii Project Frog classrooms, located at two schools on Oahu and Kauai. PV systems were then instrumented, data collected and performance analyzed.
- 2) Designed larger test platforms for installation at the Maui Economic Development Board (MEDB) in Kihei, South Maui and at the Marine Corps Base Hawaii (MCBH) in Kaneohe, East Oahu.
- 3) Developed a new DAS for high resolution data collection from a wide variety of PV systems with different electrical characteristics and system architectures. Added capabilities include measurement of open-circuit voltage (Voc) and short-circuit current (Isc).

4.3.1 Data Collection and Analysis at Project Frog Classrooms

In August 2013, PV arrays were installed on the rooftops of three Project Frog classrooms. One classroom is at Ilima Intermediate School on Oahu and two classrooms are at Kawaikini Charter School in Lihue, Kauai. These are energy-neutral buildings studied as part of the energy efficiency task of this ONR award. Two PV systems were installed on the roof of each classroom. At the Ilima site, two PV material technologies, heterojunction with intrinsic thin layer (HIT) and thin film made of copper, indium, gallium and diselenide (CIGS) were compared side-by-side. At Kawaikini three PV technologies, HIT, CIGS, and monocrystalline were compared on two classrooms in close proximity, allowing essentially side-by-side comparison between the three technologies. In addition, two different system architectures, string versus

microinverter were compared. The rated power of each system is approximately 2.6kW. The rated power is the power the PV modules can produce as determined by the manufacturer's testing under standard test conditions (STC) and reported in a datasheet. At both sites, the PV modules are roof mounted, with orientation at 7 degrees tilt and 180 degrees azimuth. Data collection was initiated in November 2013, utilizing the DAS provided with the inverters. Five-minute average energy outputs and these datasets were recorded. Photographs of the test sites are shown in Figures 1 to 3.



Figure 1. Ilima classroom, South Oahu showing the two PV systems installed to compare heterojunction with intrinsic thin layer (HIT) to thin film made of copper, indium, Gallium and diselenide (CIGS), both in a string configuration. HIT is located on top and CIGS at the bottom.



Figure 2. Kawaikini West Building, East Kauai, with heterojunction with intrinsic thin layer (HIT) in a string configuration (top) and monocrystalline with microinverters (bottom).



Figure 3. Kawaikini East classroom, East Kauai, showing two PV systems both connected in string configuration, CIGS (top) and monocrystalline (bottom).

Data management tools were developed to transfer collected data from the test locations to a UH database on Oahu. Matlab analysis tools were adapted for the performance analysis of these PV systems. Performance data were collected for two years at both locations. The following analysis describes the performance of the two PV systems at the Ilima location on Oahu. Analysis of results collected at Kawaikini are being verified under funding from HEET10, with further data collection necessitated by the high solar variability at this site and complexity of the data acquisition. Kawakini analysis will be presented in the future HEET10 final report.

Datasets are analyzed using the following methodology:

1. Datasets are selected with angle-of-incidence (AOI) below 80 degrees due to measurement errors resulting from directional response of the solar sensors increasing at high AOI. AOI is the angle from the normal to the plane of the PV modules. The solar sensor is located in the same plane.
2. Datasets are averaged and the energy calculated to evaluate the solar energy (Wh/m²/day) and the energy production of the PV systems (Wh/day).
3. Results are normalized using the specifications of the PV modules provided in the datasheet. Normalization is useful for direct comparison between PV systems with different rated power and specifications.
4. The performance ratio (PR) of the PV systems is calculated using the normalized energies, i.e. solar yield (kWh/m²/day) and PV yield (kWh/kW/day). PR is defined as the operating efficiency divided by the efficiency at STC.

The daily solar yield (kWh/m²/day) and PV yield (kWh/kW/day) for alternating current (AC) and direct current (DC), from the Ilima PV systems, are presented in Figure 4 as monthly averages (extending from the middle of one month to the next). The solar and PV yields for both PV systems are highly correlated. Yearly average solar yield is calculated at 5.5kWh/m²/day at

this site. The PV yield in AC averages 4.36 and 4.47kWh/kW/day for HIT and CIGS, respectively.

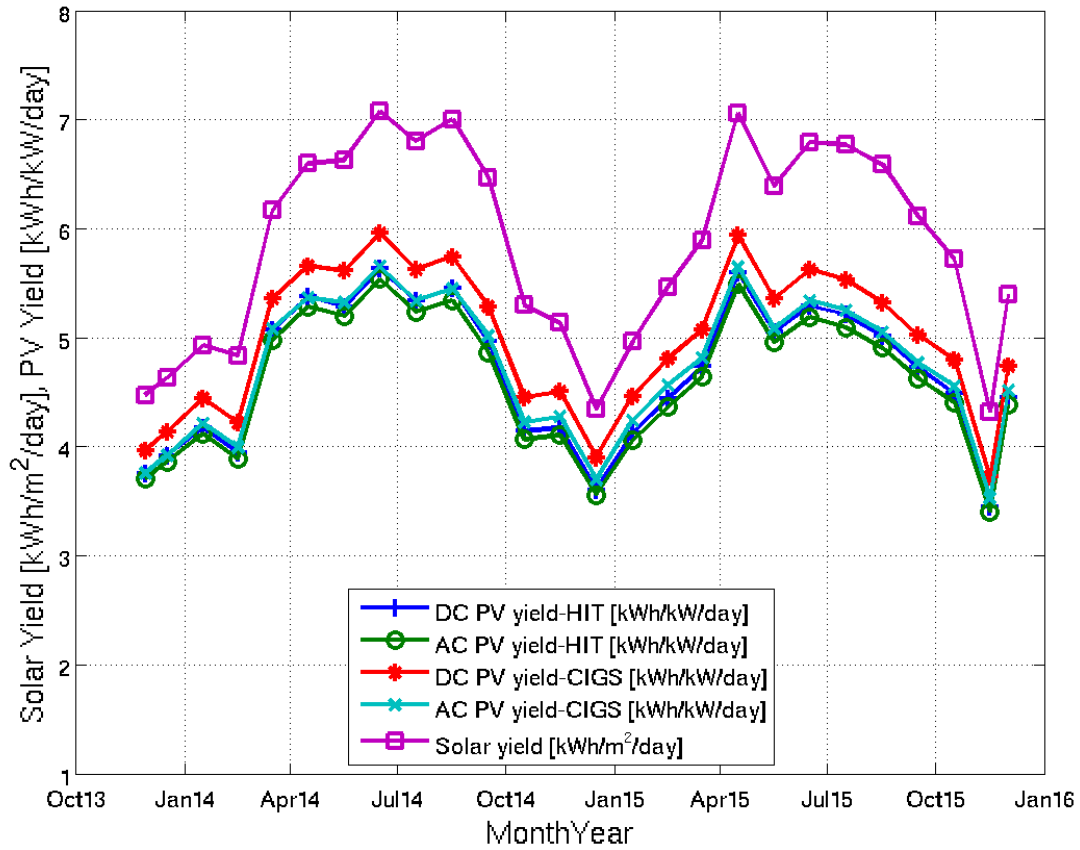


Figure 4. Monthly averages of the daily solar and PV yields over 2 years of operation at Ilima for the heterojunction with intrinsic thin layer (HIT) and thin film made of copper, indium, gallium and diselenide (CIGS). Solar yield is measured in kWh/m²/day and PV yield in kWh/kW/day, with the monthly average plotted at the mid-point of each month.

The monthly average PR of the two PV systems operating at Ilima is plotted in Figure 5. The two PV systems exhibit similar AC PR varying seasonally between 75% and 85%. Over the two years of operation, the PR averages 84% for the CIGS and 82% for the HIT. The DC and AC PR for both technologies have high values during winter months and low values in August-September. Seasonal PR variation appears related to the ambient temperature (AT) which varies between 28°C in winter and 35°C in late summer at this site.

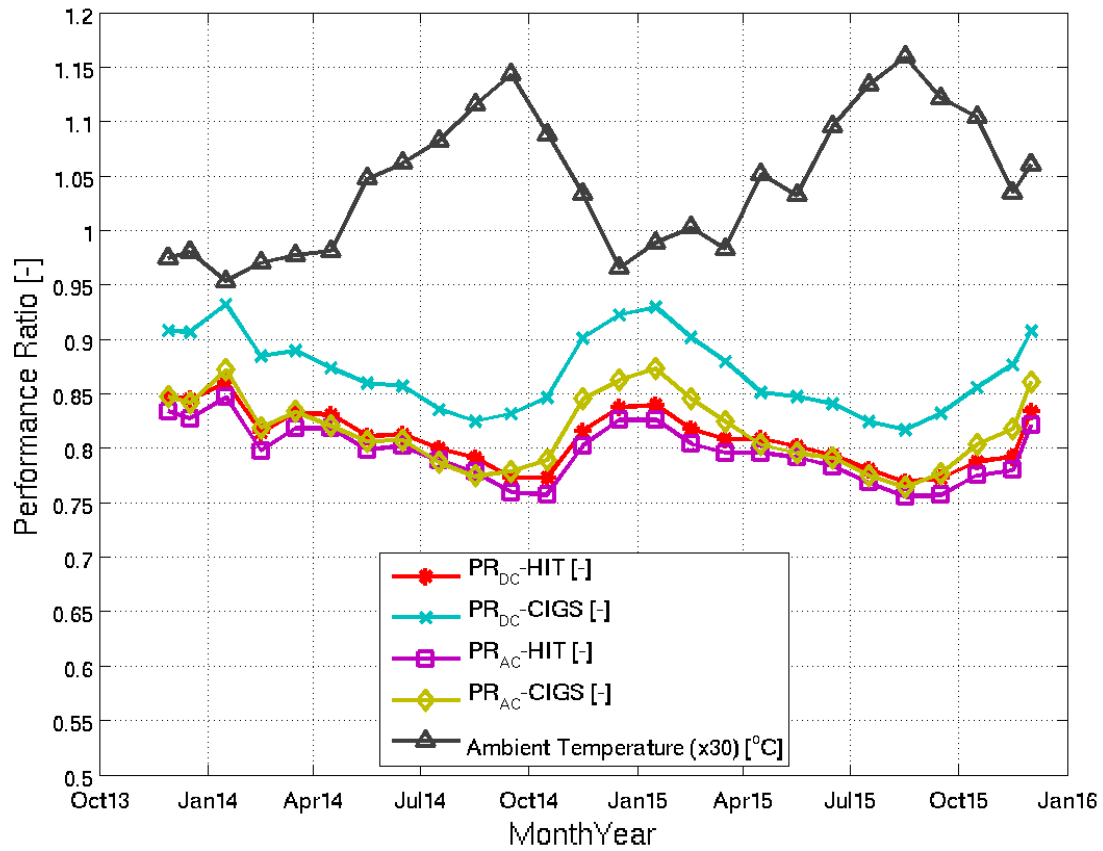


Figure 5. Monthly average Performance Ratio (PR) of the PV systems, HIT and CIGS operating over 2 years at Ilima. Ambient temperature (AT) is also plotted and varies between 28 and 35 °C.

The monthly average PR as a function of AT is shown in Figure 6. A linear relationship between monthly PR and AT, estimated (linear regression curves calculated by the least-squares method) between -1.4 and -1.2%/°C, is apparent. The CIGS is estimated to be slightly more sensitive to temperature variations, by 0.1%/°C as compared with the HIT.

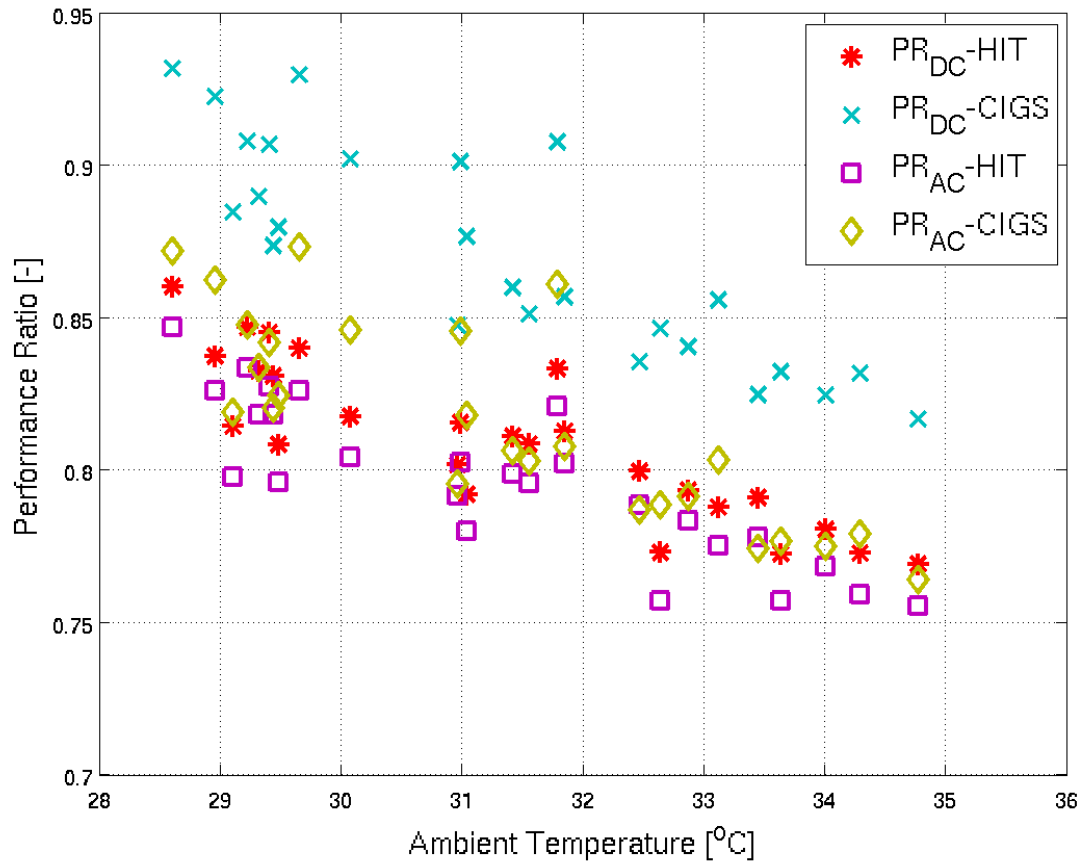


Figure 6. Monthly average PR of the PV systems, (HIT and CIGS) operating for the first 2 years at Ilima as a function of Ambient temperature (AT).

The operating voltage, inverter efficiency, and AT at Ilima are shown in Figure 7 for each month. The voltage is normalized by the STC specifications of the PV modules i.e., 1 on the y-axis of Figure 7 corresponds to 342V for CIGS and 512V for HIT. The voltages are fairly consistent throughout the two years, averaging 0.95 for HIT and 1.02 for CIGS. The HIT PV voltage is seen to deteriorate over time, however this needs to be investigated following collection of further data in the future to verify this trend. A high value for the normalized voltage for the CIGS system means the datasheet specifications do not accurately represent the actual electrical characteristics of the PV modules.

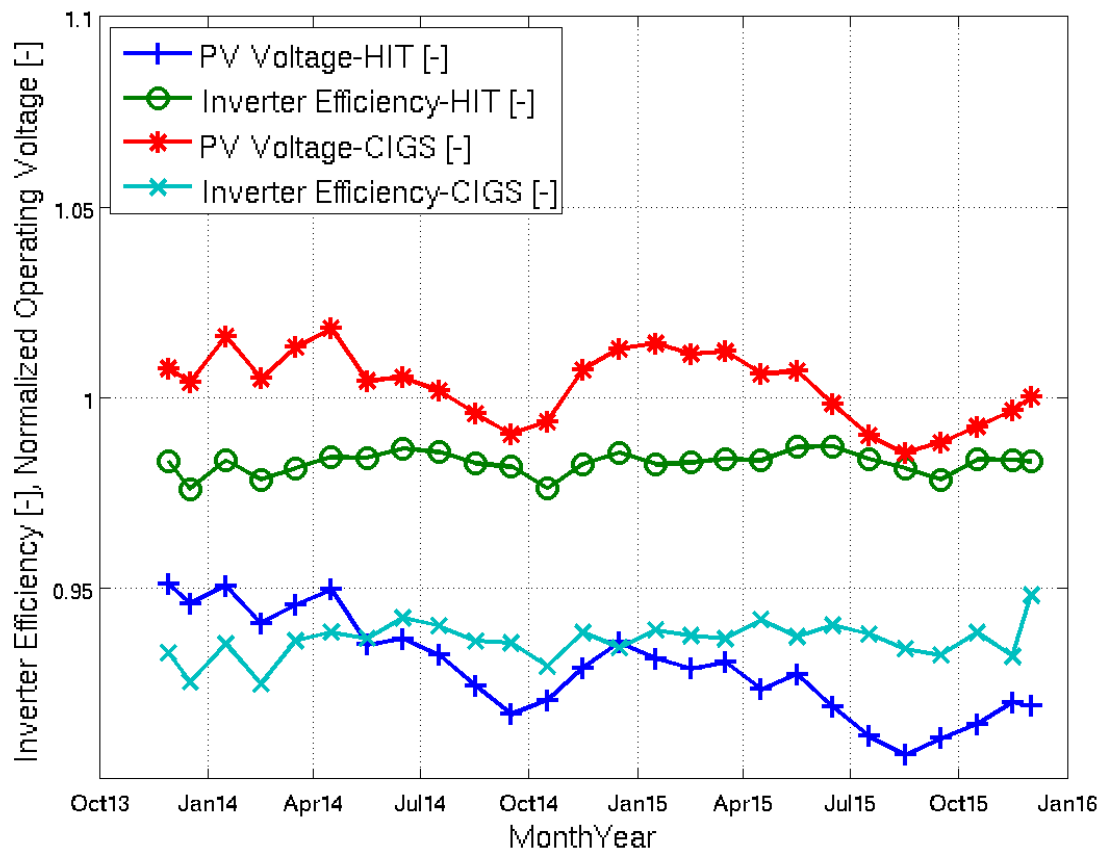


Figure 7. Monthly average variation of the inverter efficiency, and normalized operating voltage for 2 years of operation at Ilima.

The specifications for each individual PV module were supplied by the manufacturers with flash test results (FTRs). FTRs for all modules connected in each system were averaged and divided by the specifications of the entire PV system as indicated in the datasheets, (**Error! Reference source not found.**). Specifications include power (P), voltage (V) and current (I) at the maximum power point (mpp), as well as I_{sc} and V_{oc} . Both PV systems have on average 1.5% more power than indicated in the datasheets. The PR depends on the normalization, since PV energy is divided by datasheet rated power. PR results (Figure 6 above), indicate better performance from the CIS than the HIT, particularly with DC. To ensure that normalization did not lead to the PR difference between the 2 PV systems, FTR was used to give a better estimate of the actual rated power of the PV systems. As FTR for both PV systems shows the same extra power for both systems, it can be assumed the two PV systems have the same rated power, and the PR results calculated using datasheet information are correct. As the FTR power ratings of the two PV systems are similar, the results on the PR comparison are valid, not biased by the normalization. Small differences are observed in the other specifications (I_{sc} , V_{oc} , etc.) for the HIT modules. For the CIGS modules, FTR exhibit higher voltages (by 3-5%) and lower currents (by 2-4%), compared to the datasheet information. These results on FTR explain the high normalized operating voltage for the CIGS (shown in red in Figure 8).

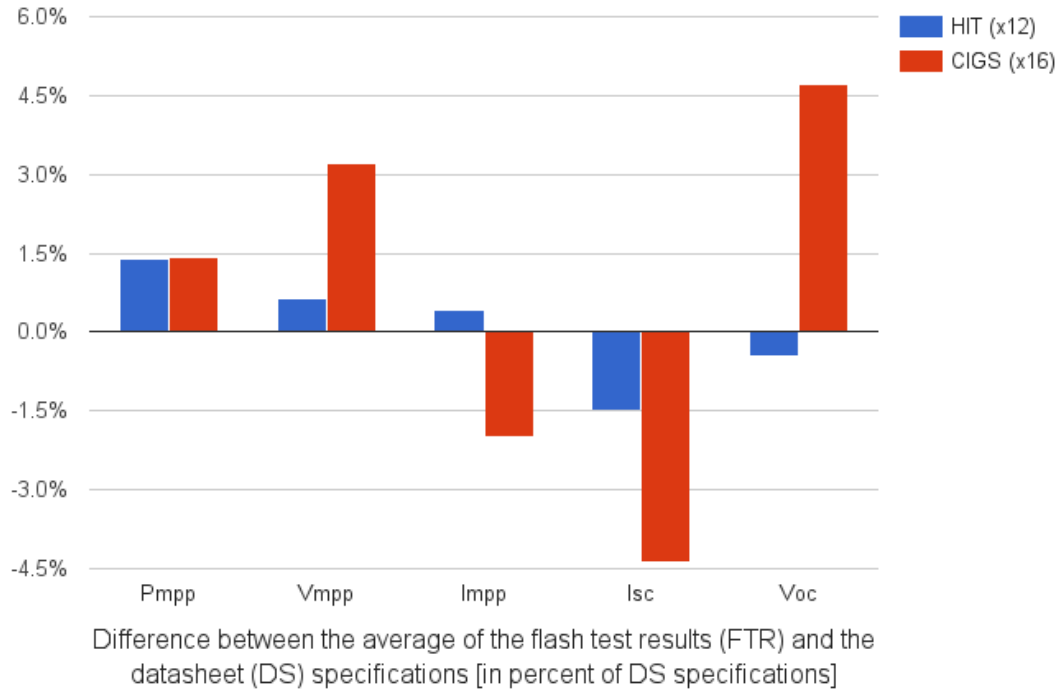


Figure 8. System specifications shown here include: power (P), voltage (V) and current (I) at the maximum power point (mpp); short-circuit current (I_{sc}), and; open-circuit voltage (V_{oc}). There were 12 modules in the HIT PV system and 16 in the CIGS PV system.

Both PV systems use the same inverter model, but the two tested inverters exhibit slightly different performance. The five-minute-averaged data of inverter efficiency is shown as a function of input DC power, normalized by the inverter power (2.5kW) (Figure 9). The monthly average efficiency of the inverters is fairly constant over the two years of operation, approximately 98% when connected to the HIT array operating at 450-490V and approximately 95% for CIS array with voltage ranging from 330-355V.

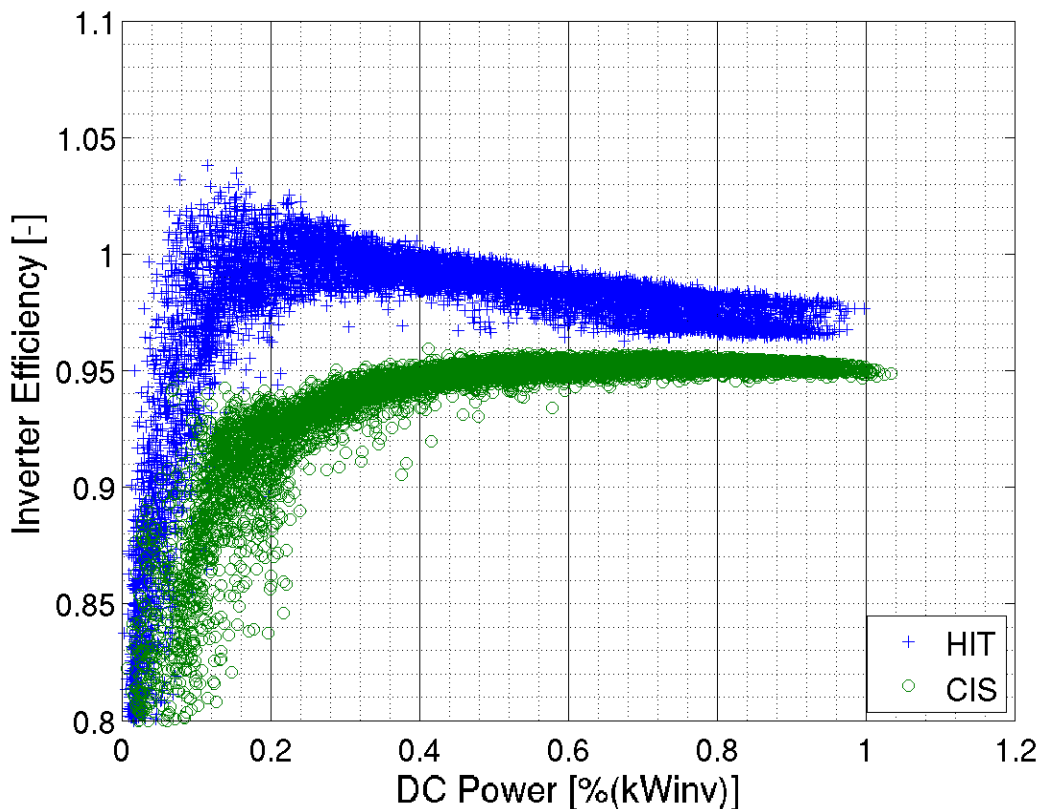


Figure 9. Inverter efficiency as a function of input DC power normalized to inverter power (2.5kW), five-minute averaged data set.

Based on this analysis, the two PV systems have similar AC performance (82-84%), despite different losses in the PV systems (see Figure 6 above). The CIGS PV system exhibits higher DC PR (by 6%), but higher loss in the inverter (by 4%) compared to the HIT PV systems.

4.3.2 Designs for Larger PV Test Platforms

In order to expand the variety of PV module and inverter technologies under test as well as the different environments, two additional test platforms were designed. Host sites were identified with differing environments; one leeward, very sunny and relatively dry on Maui, the other windward, cloudier, and corrosive on Oahu. These larger test platforms will allow the testing of multiple PV module technologies and various system architectures for direct side-by-side comparison in each environment. Similar configurations of PV modules/systems are planned at each location in order to evaluate the impact of the different environments on the system performance and degradation over time. Both test platforms will be installed on new carport structures.

The first of these larger test platforms with a total installed power ~25 kW, received grid connection approval and has been installed near the offices of the MEDB in Kihei, South Maui. Fifteen PV systems were selected including ten PV module manufacturers and seven PV technologies, including mono and polycrystalline, bifacial, HIT, and thin films comprised of Cadmium Telluride (CdTe) and CIGS. Some of the PV modules will operate in different system

architectures, allowing direct comparison of PV systems using microinverters, array inverters, or array inverters with optimizers.

A preliminary design has been completed for a second, larger, PV test platform to be located at MCBH in Kaneohe, on the windward/east side of Oahu. The design includes twenty PV modules in various system architectures for a total power of approximately 100 kW installed on two carport structures. MCBH personnel are currently seeking Secretary of the Navy approval to accept this system as a gift to the base. HNEI expects that this approval will be received and build-out may begin in the summer/fall of 2016. The PV carports will also provide a complement to the adjacent hydrogen filling station, another HNEI/ONR project, offsetting the electrical load of the electrolyzer at the station. The PV test platform design will need to be reviewed in order to adapt to the new grid connection guidelines adopted in Hawaii in October 2015, requiring advanced inverter capabilities. The draft concept is shown in Figure 10.

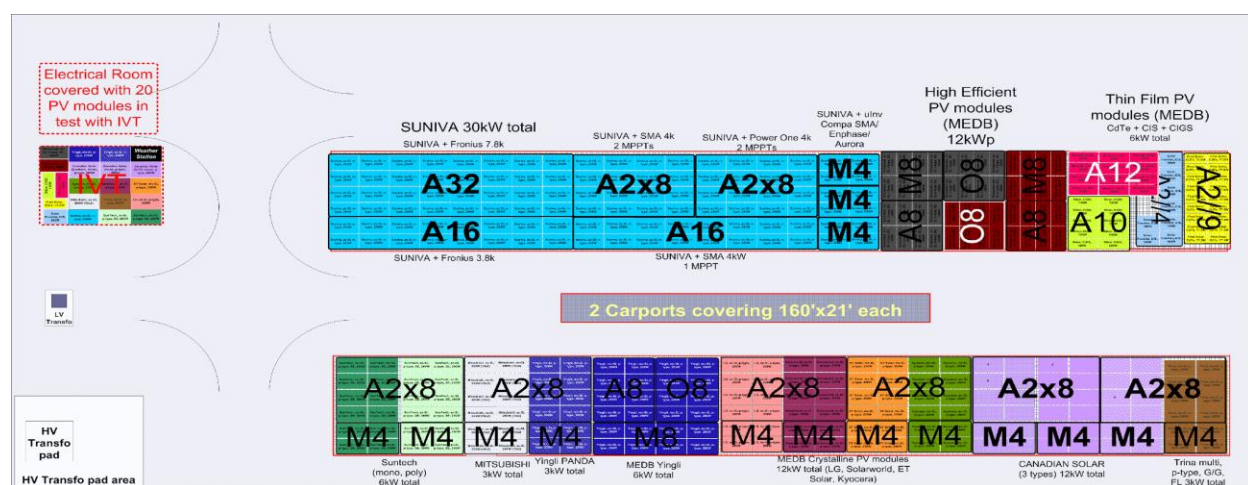


Figure 10. Draft design of the PV test platform to be located at Marine Corps Base Hawaii (MCBH), in Kaneohe, East Oahu.

4.3.3 Data Acquisition System (DAS) Development

To support high-resolution data acquisition at these larger test platforms, a new DAS was developed. The new design will enable collection of high resolution data from a wide variety of PV systems with different electrical characteristics and system architectures. The system includes sensors for weather conditions, PV panel performance (DC) and inverter performance (AC). Measurements of individual PV module outputs, string outputs, and optimizer inputs/outputs are made with custom-built measurement boxes. Once the demonstration is complete, these measurement boxes can be easily removed from the PV system without affecting system operations or performance. The DAS was designed with a recalibration unit in order to maintain high data quality over long recording periods. An additional feature of the new DAS is the ability to collect Voc and Isc of the PV modules in operation with microinverters. This feature will be tested to assure low impact on the PV system operation and performance. The test protocol also includes a current-voltage (IV) tracer to collect IV curves. This is used to measure and compare performance of individual PV modules isolated from the grid but operating in the same environmental conditions as the grid-connected PV systems under test.

An overview of the DAS and test protocol is shown in Figure 11. The system is comprised of six major groups of devices: the power/communication box, the controller box, the DC measurement boxes, the IV tracer, the weather station, and the calibration unit (not represented in the drawing).

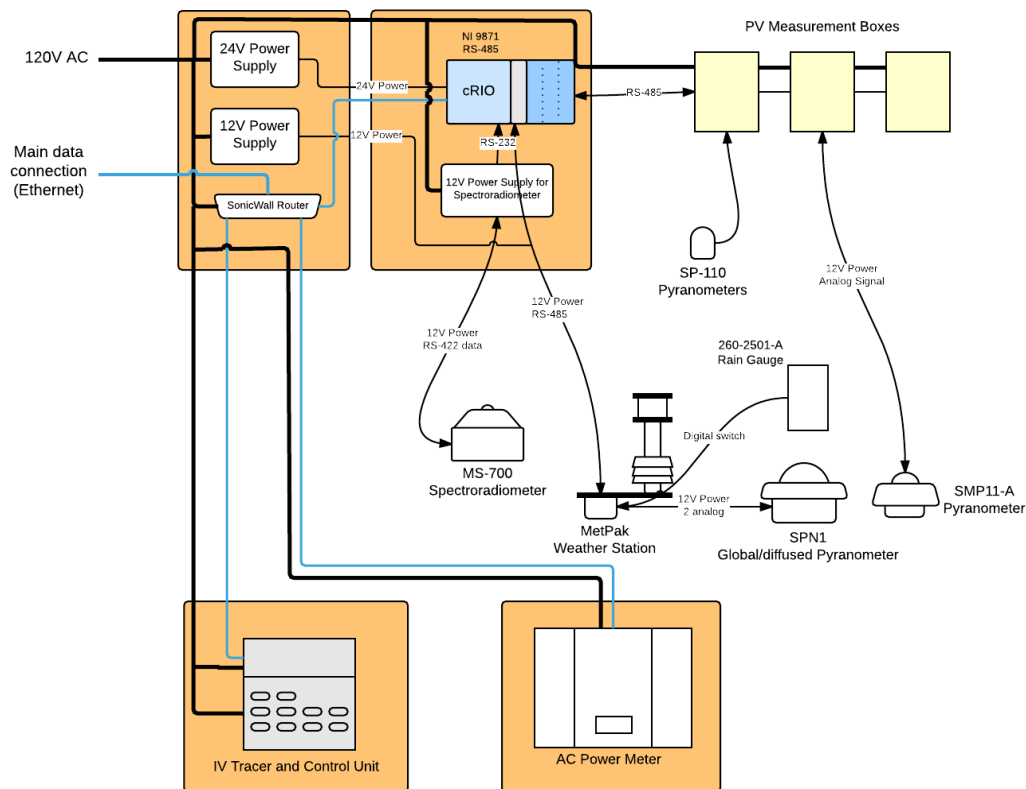


Figure 11. Schematic of the HNEI PV data acquisition system (DAS) and test protocol that will be implemented at the Maui Economic Development Board (MEDB) and MCBH PV test platforms.

The power/communication box provides power and communication distribution throughout the DAS. The controller box includes the DAS hardware (including a real-time embedded controller (cRIO), made by National Instruments) for data gathering, recording and storing. The DC measurement boxes measure the performance of the PV systems in normal operation (i.e. connected to the grid). These boxes are designed to collect one-second DC voltage, DC current, voltage-to-ground, back-of-the-module temperature, and an auxiliary DC voltage selected to allow connection of analog sensors such as pyranometers. The measurement boxes can be daisy-chained together to add more measurements to the DAS. Within each measurement box is one or more 32-bit Cortex-M0 microcontrollers, which handle one-second averaging of the analog-to-digital converters (ADC) used for DC measurements. The cRIO controller polls each microcontroller via the RS-485 bus to retrieve information or initiate commands (i.e., a synchronous reading command). Each microcontroller has a unique ID number from 0-254 that allows it to be identified by the cRIO controller. Although only one device is allowed to

communicate over the RS-485 bus at a given time, the multi-mode nature of RS-485 allows the system to scale up or down depending on how many measurement boxes are needed. The printed circuit boards (PCBs) within each measurement box are modular in design, which allows them to be combined in different ways to measure specific parameters. The PCBs were designed and tested at HNEI, and have undergone extensive iterations for improvement. The end result has been validated on operating PV systems on the Manoa campus test site. Recognizing a critical need for on-site calibration of these boxes, an easily portable calibration unit has been developed. This will allow periodic calibration of the DC measurement boxes on Maui and at MCBH in order to maintain high quality of the collected data.

The weather station is comprised of devices to measure multiple environmental parameters, such as wind velocity, temperature, humidity, and irradiance. The all-in-one MetPak weather station is a single unit that measures wind velocity, temperature, humidity, pressure, and dew point. A rain gauge is connected to the MetPak's digital input, and a Delta-T SPN1 global/diffuse pyranometer is connected to the MetPak's analog inputs to measure solar irradiance on the surface of the PV modules. Small silicon-based pyranometers (SP-110, Apogee) and the reference thermopile pyranometer (SMP11-A, Kipp and Zonen) are part of the weather station, but are connected to the auxiliary inputs of the DC measurement boxes to simplify wiring. A spectroradiometer (MS-700, Eko Instruments) is also used to provide fifteen-second spectral energy per wavelength between 350 nm and 1050 nm (10 nm spectral resolution).

In addition to monitoring DC performance and environmental conditions, the DAS collects information from an AC power meter (Shark MP200 from Electro Industries) to monitor one-second active and reactive power of the grid-connected PV systems. This data will provide information on the inverter performance and allow performance comparison of PV systems operating using various system architectures.

The final component of the new DAS is an IV tracer, which measures the performance of individual PV modules while isolated from the grid. The IV tracer selected for the MEDB test site is a multitracer (Daystar MT5) that connects to ten (10) individual PV modules and is able to take IV curve readings of each module once per minute. During normal operation, the IV tracer uses its internal 3.2kW resistive load bank to operate the PV modules at their maximum power point. The operation of the isolated PV modules will provide information on the electrical characteristics of the isolated PV modules to compare with operation of the grid-connected PV modules to help identify the different losses in the PV systems.

All components of this new DAS, including measurement boxes, weather sensors, and the IV tracer, have been installed at an existing HNEI PV test platform. Data collection and analysis has been initiated at this location to verify function prior to deployment at MEDB on Maui (under another project). Test protocols have been developed and will be further refined as data is collection on Maui, and subsequently at MCBH on Oahu. These protocols, along with more complete data analysis, will be presented in future reporting by HNEI.

References

- [1] PV Test Protocols and Data collection, Task 8 Subtask 11.1 Deliverables 2 & 4 for the United States Department of Energy Hawaii Distributed Energy Resource Technologies for Energy Security, DE-FC26-06NT42847, 2012.
<http://www.hnei.hawaii.edu/sites/dev.hnei.hawaii.edu/files/PV%20Test%20Sites%20and%20Test%20Protocols.pdf>
- [2] Solar Resource and PV Systems Performance at Selected Test Sites, Subtask 3.1 Photovoltaic Systems: Report 1 - Field Testing and Evaluation of Photovoltaic Technologies for the United States Department of Energy Hawaii Distributed Energy Resource Technologies for Energy Security, DE-EE0003507, 2014.
<http://www.hnei.hawaii.edu/sites/dev.hnei.hawaii.edu/files/Task%203.1%20Report%201%20with%20new%20cover.pdf>
- [3] Resource for inverter test protocol and results available online
<http://www.gosolarcalifornia.ca.gov/equipment/inverters.php>; Results on selected inverter:
http://www.gosolarcalifornia.ca.gov/equipment/inverter_tests/summaries/SMA%20SB2500HFUS-30-208.pdf

4.4 Power Park Support

The Hawaii Hydrogen Power Park Project was initiated with funding from the US Department of Energy's (US DOE's) Hydrogen Technology Validation Program, to conduct technical and economic validation of pre-commercial hydrogen technologies. A major challenge for hydrogen production and dispensing stations is the cost of hydrogen at the nozzle. In order to displace fossil fuels hydrogen must be economically competitive with other transportation options. Light duty vehicles have largely been designed to use high pressure (700 bar) hydrogen storage while most larger fleet vehicles use a lower pressure (350 bar) system. The primary objective of this US DOE project was to evaluate the technical performance of the system components including the electrolyzer, compressor, storage system, and the refrigeration and dispensing systems and to assess the economic performance of each in terms of the cost of hydrogen delivered at the fueling nozzle for both high and low pressure operation.

The original proposal to US DOE was based on supporting the deployment of hydrogen fuel cell buses at HAVO by installing a 350 bar hydrogen production and dispensing system inside the park at the Kilauea Military Camp (KMC), an Army recreational facility (Department of Defense, DoD) that already operates an existing fleet of shuttle buses for its military visitors. The electrolyzer system would have been powered by electricity (up to 50% renewable) supplied from the Hawaii Electric Light Company (HELCO).

Under the US DOE funding, a 350 bar hydrogen production and dispensing system was procured from Powertech Labs. Soon after fabrication of the 350 bar fueling station was completed, two significant events occurred:

1. HNEI secured funding from US DOE to fabricate and install a larger hydrogen production system at the Puna Geothermal Venture (PGV) geothermal plant about 40 miles by road from HAVO, the original site. A component of the new DOE agreement was for HNEI to deliver hydrogen using hydrogen transport trailers (HTT) to multiple sites on the Big Island including the HAVO site. This negated the need for the original, smaller electrolyzer/fueling system intended for HAVO.
- 2) The DoD initiated a program to evaluate 15 GM Equinox fuel cell electric vehicles (FCEV) on Oahu with 5 of the 15 vehicles being allocated to Navy. Marine Corps Base Hawaii (MCBH) was identified a suitable site for these vehicles. Operation at MCBH would allow a total system evaluation that included hydrogen production and dispensing.

In support of the ONR General Motors Equinox fuel cell electric vehicle project, the 350 bar hydrogen production and fueling station intended for installation at HAVO was modified and installed at Marine Corps Base Hawaii (MCBH). Funds from this ONR award were used to expand the capability at the fueling station by adding a 700 bar fast fill capability. The US DOE approved the changes to the Power Park scope. The combined 350/700 bar fast fill station became operational on 19 November 2014. As of August 2015, it successfully completed over 300 fills without any operational downtime.

Technical Accomplishments: Under This ONR grant the original 350 bar hydrogen station was upgraded by Powertech as a dual pressure 350/700 bar “fast fill” (under 5 minutes to fill a vehicle’s tank) hydrogen production and dispensing station. The system was highly automated to allow it to be used in unattended operation such that the vehicle operator could fill the vehicle to provide the same customer experience as a normal self-serve gasoline dispensing station. A site was secured at MCBH and site improvements were designed and installed (Figure 4.1). A site safety analysis was completed and the equipment and site designs were reviewed by the Pacific Northwest National Laboratory (PNNL) Hydrogen Safety Panel. The completed system was commissioned and commenced operations on 19 November 2014 (Figure 4.2). The station conducted over 300 filling events in unattended operation.

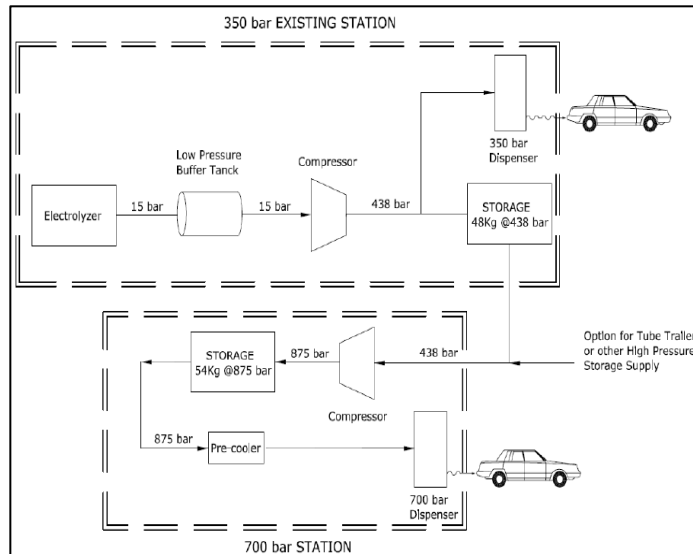


Figure 4.1: Hydrogen Fueling Station Design



Figure 4.2: MCBH Hydrogen Fueling Station

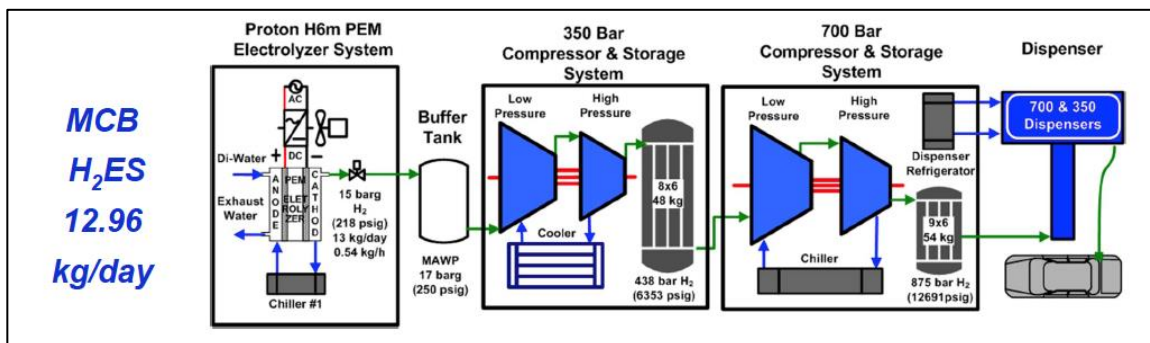


Figure 4.3: MCBH Hydrogen Fueling Station Systems Configuration

The system (Figure 4.3) is comprised of 350 bar and 700 bar dispensers integrated to take advantage of common production, storage, and compression. The 12 kg per day Proton HOGEN

Polymer Electrolyte Membrane (PEM) electrolyzer produces hydrogen at 15 bar. A HydroPac compressor increases the hydrogen pressure to 438 bar for storage in a bank of Luxfer composite tanks (48 kg capacity) feeding the 350 bar cascade fill dispenser. Hydrogen from the lower pressure system is further compressed to 875 bar at a maximum rate of 5.5 kg/hour to supply the high pressure dispenser. The second bank of Luxfer tanks has a capacity of 54 kg hydrogen. For high-pressure fast fill, the hydrogen is precooled to -20°C allowing 3 consecutive 700 bar fills.

Data Collection & Analysis

A data analysis framework (Figure 4.4) was defined for analyzing the performance of the hydrogen station. A data logging system that monitors and stores daily operating data was designed and installed to collect data to use in implementation of the data analysis framework (Figure 4.5).

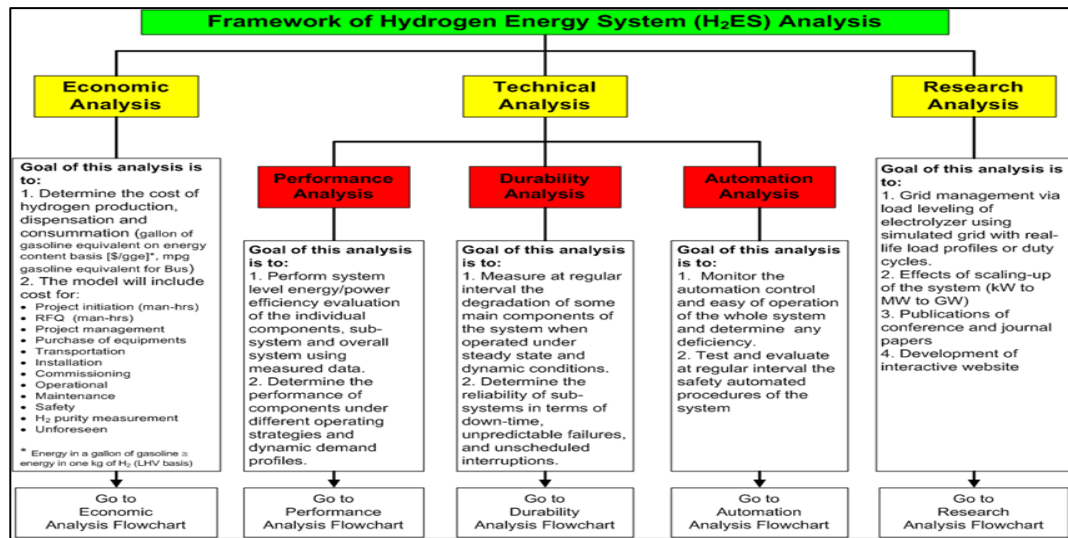


Figure 4.4: Data Analysis Framework

The main objective of the data analysis framework is to define methodologies for comprehensive performance and economic evaluations of the hydrogen system and to identify the measured data that will be required for this evaluation. The framework is divided into three main sections: Technical, Economic and Research analysis.

1. Technical analysis includes evaluating:
 - a. Performance of the overall system, sub-systems and components efficiency;
 - b. Durability of some main sub-system components;
 - c. Automation control of the system using Programmable Logic Controllers, (PLCs)
2. Economic analysis includes evaluating:
 - a. Benefits of hydrogen production using renewable energy
 - b. Operational benefits of the hydrogen fuelling system
 - c. Supplementary costs (H₂ purity, installation, maintenance, etc.)
3. Research analysis includes evaluating:
 - a. Effects of scaling-up the system

Performance Evaluation

The main objective of the performance evaluation of the hydrogen system was to determine the practical efficiencies of the sub-systems and the overall system using measured data. For this purpose, the hydrogen system was characterized into five main sub-systems of Hydrogen Production, Hydrogen Compression, Hydrogen Storage, Hydrogen Supply and Hydrogen Consumption. The system performance was estimated by implementing a “Water-to-Water” energy analysis, whereby the analysis would map all energy usage and losses from production of Hydrogen by a PEM water electrolyzer to consumption of Hydrogen by an FCEV to produce water as a by-product. Figure 4.6 shows the schematic representation of the Hydrogen energy flow in a Water-to-Water analysis.

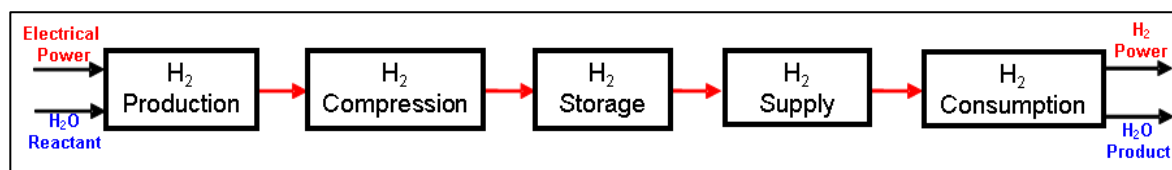


Figure 4.6: “Water-to-Water” Energy Flow Schematic

A data acquisition (DAQ) system was developed to collect seamless power and energy measurement data for in-depth realistic Water-to-Water energy analysis. Figure 4.7 shows the picture of the DAQ system implemented at MCBH fueling station. The DAQ system is mobile, self-contained, and weather proof. It has all pluggable connectors for the two power meters with three current transducers (CTs) each and eight current sensing switches (ON/OFF). The fully configurable National Instrument (NI) controller logs data at regular intervals and upon exceeding dead band. The data is transferred via Wi-Fi and is also backed up on the thumb drive. It has an internal buffer as well in case of Wi-Fi loss or the thumb drive is removed. The DAQ system has the potential of future upgrade to monitor electrolyzer water quality and main power sags/spikes i.e. power quality data.

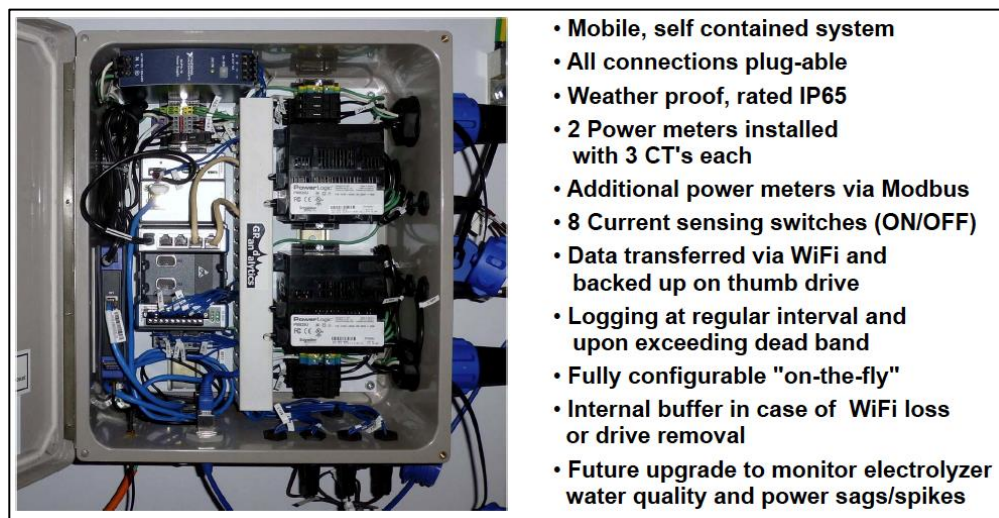


Figure 4.7: Data Acquisition (DAQ) System

Hydrogen Production - PEM Water Electrolyzer

A Proton H6M model electrolyzer is used at the MCBH fueling station. It has a maximum production capacity of 0.54 kg/hr. The electrolyzer has three DC power supplies for each of the three PEM stacks, a cooling system for cooling the stacks and power supplies, and a drying system to dry the water contained in the product hydrogen to less than 5ppm. The dry hydrogen is stored in a 250 psig buffer tank. Figure 4.8 shows the electrolyzer main components configuration.

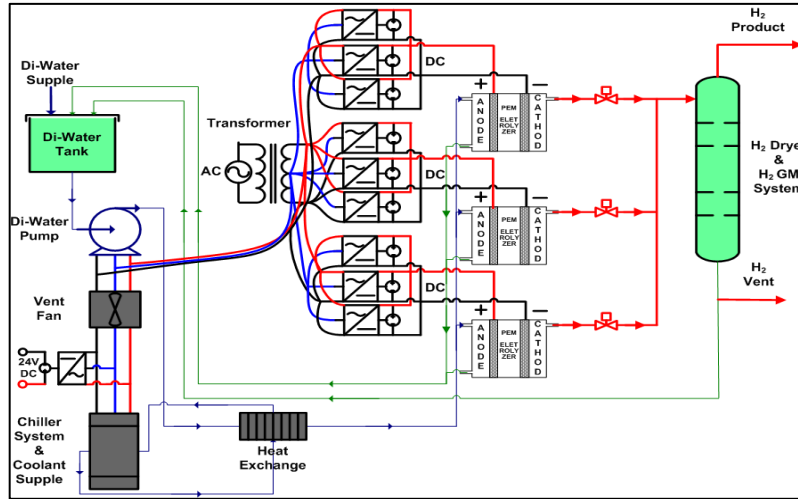


Figure 4.8: Proton H6M electrolyzer main components configuration

The hydrogen production performance was estimated from the 18 hours of electrolyzer operation using measured data from the Proton database during the commissioning phase of the hydrogen station system. The hydrogen production efficiency accounts for power used for electrolyzing water, parasitic load (pumps, fans, chiller etc.) and power losses of the electrolyzer system.

Table 4.1 shows the performance of the electrolyzer after 18 hours of operation that produced 8.5 kg of hydrogen. The table also shows the electrolyzer efficiency with and without the dryer and stack losses as well as the system efficiency with and without the chiller power. Approximately 10% of the hydrogen produced is lost within the electrolyzer in the drying process and through the stacks. The electrolyzer consumes about 72% of the supplied electrical power while 28% is consumed by the parasitic loads. The overall production efficiency of 43% was estimated based on higher heating value (HHV) of hydrogen (141.8 MJ/kg) which equates to about 91 kWh/kg of hydrogen. The electrolyzer efficiency was estimated to be 60%.

Table 4.1: Proton H6M Electrolyzer Performance

| MCBH H2 Energy System (H2ES) | | Oct 22 nd 2014 -18 hrs | |
|---|--------|-----------------------------------|--------|
| Hydrogen Production & Losses | Units | Proton H6 | % |
| PEM (3 Stacks) Electrolyzer H ₂ -Production (<i>Calculated</i>) | kg/hr | 0.60 | 100.0% |
| H ₂ Dryer Assembly & Stack losses (<i>Calculated</i>) | | 0.06 | 10.2% |
| Total H ₂ -Production (@STP) (<i>Measured</i>) | | 0.54 | 89.8% |
| Power Consumption of Electrolyzer System | Units | Proton H6 | % |
| DC Power Supply Losses (<i>assuming 95% efficiency</i>) | kWh | 1.86 | 3.8% |
| PEM (3 Stacks) Electrolyzer H ₂ -Production (<i>DC Power Measured</i>) | | 35.4 | 72.3% |
| Electrolyzer Water Pumps x 1 (<i>Max. 1.6 kW AC</i>) | | 1.36 | 2.8% |
| Vent Fans x1 (<i>Max. 1.28 kW AC</i>) | | 1.27 | 2.6% |
| Auxiliary [<i>PLC Rack/H2 Sensor/Valves...</i>] | | 0.11 | 0.2% |
| Total Power Consumption (<i>Without Chiller</i>) | | 40.00 | 81.6% |
| TCU Chiller (<i>PM2 Measured - Max. 15.40 kW AC</i>) | | 9.00 | 18.4% |
| Total Power Consumption (<i>With Chiller</i>) | | 49.00 | 100.0% |
| Overall Electrolyzer Efficiencies | Units | Proton H6 | % |
| PEM Electrolyzer (<i>Without Dryer/Stack Losses</i>) | kWh/kg | 58.9 | 66.9% |
| PEM Electrolyzer Stacks (<i>With Dryer/Stack Losses</i>) | | 65.6 | 60.1% |
| System (<i>Without Dryer/Stack Losses & Chiller Power</i>) | | 66.6 | 59.2% |
| System (<i>With Dryer/Stack Losses & Chiller Power</i>) | | 90.7 | 43.4% |

Hydrogen Compression and Storage

The MCBH fueling station has 438 and 875 bar compressors and storage systems. The 438 bar system has a 7.5 kW 2-stage Hydro-Pac Inc. linear compressor with a motor efficiency of 90% and requires 0.62 kW of cooling power. The compressor has the capacity of compressing 20 kg in a 24-hour period. The 438 bar storage has 8 Luxfer tanks with total storing capacity of 48 kg of hydrogen i.e. 6 kg per tank.

The 875 bar compressor is a 2-stage Hydro-Pac Inc. linear system with a nominal power of 30 kW with motor efficiency of 93% and cooling requirement of 12 kW. The compressor has the capacity of compressing 103 kg in a 24-hour period. The 875 bar storage has 9 Luxfer tanks with total hydrogen storage capacity of 54 kg i.e. 6 kg per tank.

Hydrogen Supply and Consumption

The MCBH fueling station has 350 bar “normal fill” and 700 bar “fast fill” dispensing capabilities for supplying hydrogen to FCEVs. The 350 bar dispenser has a WEH TK16 Hydrogen nozzle type and does not require cooling. The 700 bar dispenser has a type B -20°C (WEH TK17) nozzle with infra-red (IR) data interface. The 700 bar dispenser requires a pre-cooler to cool the gas down to -20°C.

FCEV specifications are also included in this report as a hydrogen consumer for the purpose of Water-to-Water analysis. The FCEV used in this study is the GM Chevrolet Equinox 2006 model that was used at MCBH and refuels at the MCBH fueling station. Table 4.2 shows the car specifications and Figure 4.2 shows a picture of the GM car.

Table 4.2: GM Chevrolet Equinox 2006 Specifications

| H₂ Storage System | |
|-------------------------------------|---|
| Type: | 3 carbon fiber fuel tanks |
| Service pressure (psi / bars): | 10,000 / 700 |
| Storage capacity (lb / kg): | 9.24 / 4.2 |
| Fuel Cell System | |
| Power (kW): | 93 |
| Efficiency: | 42-55 % |
| Performance | |
| Operating range (miles / km): | 200 / 320 [158 miles on EPA drive cycle] |

MCBH Hydrogen System Performance

Using the 18 hours of data from the power meters and current sensing switches during the commissioning phase, the performance of the MCBH hydrogen system was analyzed by carrying out an energy balance over this period to determine the efficiencies of main components and the overall system. Figure 4.9 shows the results of this energy balance analysis over the 18 hours period.

During the 18 hour period the hydrogen station consumed 1505 kWh of electricity that equates to about 104 kWh per kg of hydrogen produced (kWh/kg). The electrolyzer produced 14.5 kg of hydrogen at an efficiency of about 63% (66 kwh/kg). The compressors and cooling systems consumed about 6.3% and 25% of the total energy respectively. The total parasitic load from the electrolyzer chiller, 700 bar chiller, and 700 bar dispenser pre-cooler (refrigerator) was 5.7% of the total energy. The overall system efficiency was 38% based on the HHV of hydrogen (≈ 104 kWh/kgH₂).

The high energy consumption by the MCBH system during the commissioning phase is mainly due to the high parasitic loads of the electrolyzer chiller, 700 bar chiller, and 700 bar dispenser pre-cooler (refrigerator). The operational modes of these chillers and the pre-cooler need to be optimized by implementing hardware and algorithms to minimize their energy consumption and to maximize the overall efficiency of the MCBH hydrogen system.

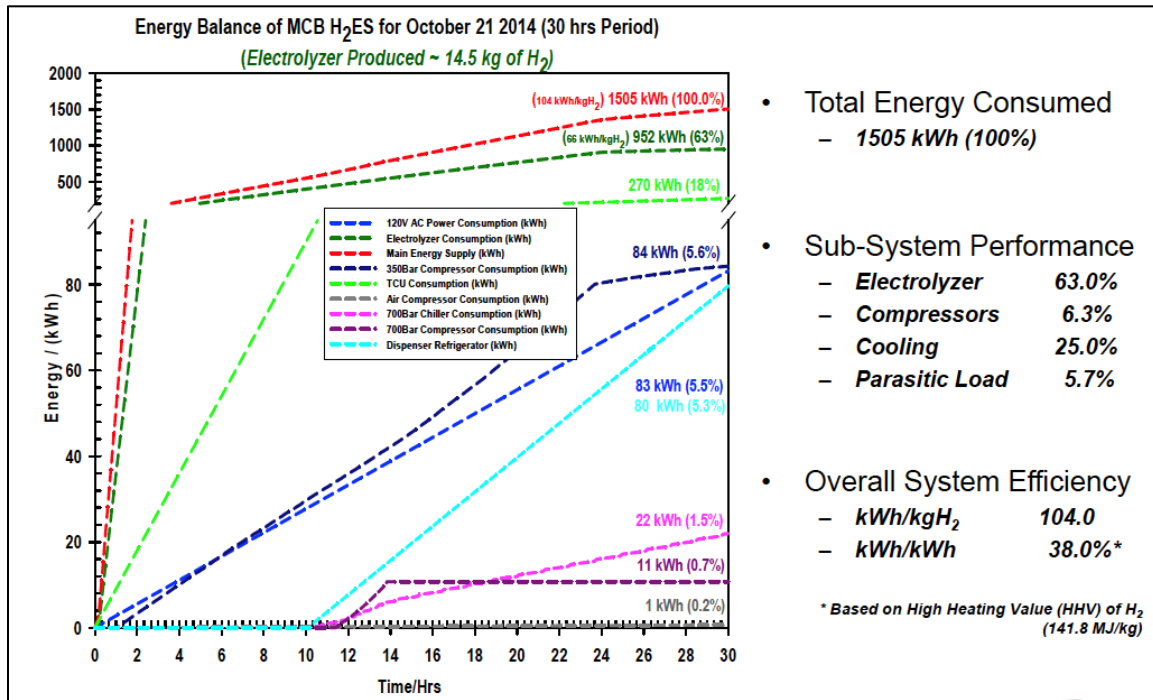


Figure 4.9: MCBH Performance

Water-to-Water Analysis

Based on the 18 hours of data from the DAQ system, a Water-to-Water analysis was carried out to determine overall system energy efficiency. This analysis includes the losses in the main transformer and the FCEV. The Water-to-Water efficiency accounts for the total energy required to electrolyze water for the production of hydrogen to the ultimate consumption of the compressed hydrogen by an FCEV to produce water as a by-product. Figure 4.10 shows the energy flow of the system. The Water-to-Water efficiency was estimated to be 22%.

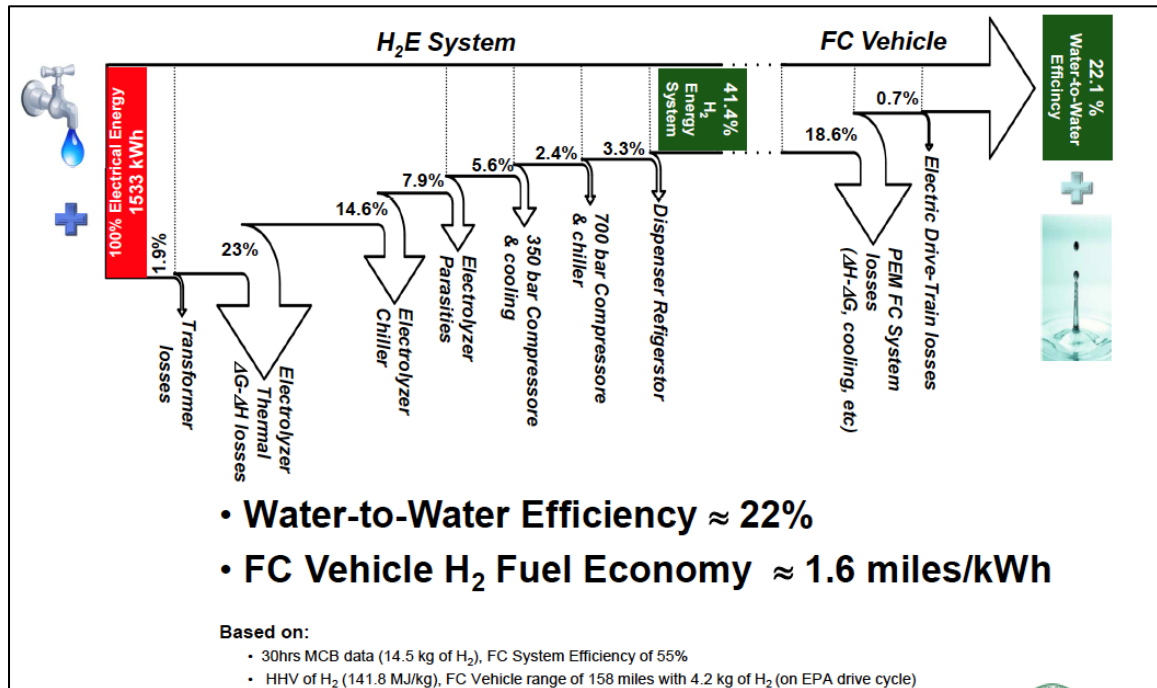


Figure 4.10: Efficiencies of the MCBH Hydrogen Station

The fuel economy of the FCEV was estimated to be 1.6 miles/kWh using the compressed hydrogen produced at the MCBH fueling station. This was based on the operating range of the GM FCEV on the US Environmental Protection Agency (EPA) drive cycle of 158 miles with 4.2 kg of hydrogen onboard, and the energy used to produce hydrogen at the MCBH production and fueling station during the 30-hour period. Furthermore, from the energy flow diagram in Figure 4.10, it can be observed that the PEM electrolyzer and fuel cell systems account for the majority of energy losses, i.e. 23.0% and 18.6% respectively.

Findings

Major challenges experienced in the project included:

- Legal agreements took over 2.5 years to resolve, highlighting one of the major barriers to implementation of hydrogen fueling stations shared by similar projects.
- Installing an upgraded power supply that involved replacing the existing 300 KVA transformer with a 500 KVA transformer extended the schedule and added a significant cost escalation.

Commissioning time was longer than expected due to technical issues with equipment and the need to eliminate trace contamination of the hydrogen supply to meet the Society of Automotive Engineers fueling standards.

Specific accomplishments included the following:

- Developed and executed legal agreements between University of Hawaii and MCBH;
- Procured a dual, 350/700 bar hydrogen production/dispensing system;

- Installed and commissioned the fueling station at MCBH meeting all base facility, security, and safety requirements;
- Conducted US DOE Hydrogen Safety Panel and independent third party safety reviews of the equipment and site;
- Commissioned and operated the first licensed hydrogen transport trailer in Hawaii to transport hydrogen between bases;
- Developed and installed a high-speed DAQ system to measure dynamic performance of the system;
- Demonstrated well-controlled, repeatable, 4 minute high-pressure fast fills (over 300 between Nov 2014 and August 2015).

This project also provided significant insight into the challenges required to deploy and operate hydrogen fueling infrastructure including:

- Hydrogen safety issues;
- Hydrogen station design;
- Hydrogen codes & standards;
- Working with the Authority Having Jurisdiction to obtain the necessary approvals to install and operate the systems;
- Developing a Project Hydrogen Safety Plan;
- Working with the PNNL Hydrogen Safety Panel;
- Developing operating and maintenance manuals;
- First Responder training and obtaining buy-in from the local fire departments;
- Equipment technical performance and reliability issues including providing feedback to equipment suppliers on the performance of their equipment;
- Equipment warranties, and after sales support issues;
- Costs involved in producing and dispensing hydrogen including operating and maintenance costs that are substantial;
- Training people to maintain and operate the systems;
- Developing legal agreements working with the legal profession who are unfamiliar with hydrogen;
- Addressing the concerns of host site owners;
- Addressing the concerns of the general public;
- Collecting data and analyzing technical and economic performance.

Future Work

The future work will involve the operation of three to five Toyota Mirai FCEVs, analysis of the durability of the electrolyzer using long term data, impact of the PLC on the operation of the system and the development of an economic model to estimate the benefits of hydrogen production via renewable energy including all the supplementary costs. The impact of optimizing the operation of both the electrolyzer and compressor chillers on the overall performance of the system, will also be investigated and will be compared to the performance of the system under commission phases reported in this report.

Publications and Presentations

- Rocheleau R., Ewan, M., “Hawaii’s Hydrogen Programs”, f-cell Hydrogen Conference, Stuttgart Germany, September 2011.
- Ewan, M., “Supporting a Hawaii Hydrogen Economy”, US DOE Webinar, 29 July 2014.
- Virji. M., Randolph, G., Polson, C., Ewan, M., “Water-to-Water Analysis of Hydrogen Energy System for Hydrogen Fueling Stations in Hawaii”, Fuel Cell Seminar & Energy Exposition 2014, Los Angeles, CA, 10-13 November, 2014.

Briefings

- Ewan M., “Hawaii Hydrogen Programs”, Briefing to Toyota Corporate, Honolulu, March 2012.

Acknowledgements

In addition to funding from ONR, additional funding for this project was provided by the US DOE and the State of Hawaii. MCBH provided electrical power, water, and the site at no cost to the project.

4.5 Energy Test Platforms

In the fall of 2008 Project Frog and the Office of Naval Research (ONR) began discussing a research program focused on energy efficient platforms tailored to the Pacific region with the potential for mass-deployment. The program spanned several years and was broken into multiple phases – Phase I: materials and technologies research; Phase II: technology integration and deployment feasibility studies; Phase III platform deployment and field testing to explore energy generation and performance monitoring. Phases I and II were previously funded by ONR directly with Project Frog. Phase III deployment was funded through HNEI and is the subject of this report.

Project Frog

In Phase I, Project Frog performed a comprehensive study of current and emerging materials and technologies as potential components of a systematized kit-of-parts for use in the Pacific islands.

The components were categorized into six general groups - structure, envelope, materials, energy generation and management, sensors and controls, and integrated building technologies, and were evaluated based on their performance as standalone parts, as well as sub-elements of an integrated building system. Through the use of computerized parametric modeling of design alternatives in different climates, Phase I of the program concluded in April, 2009 with the recommendation of a single type of pre-engineered Frog module appropriate for field-testing across the Pacific.

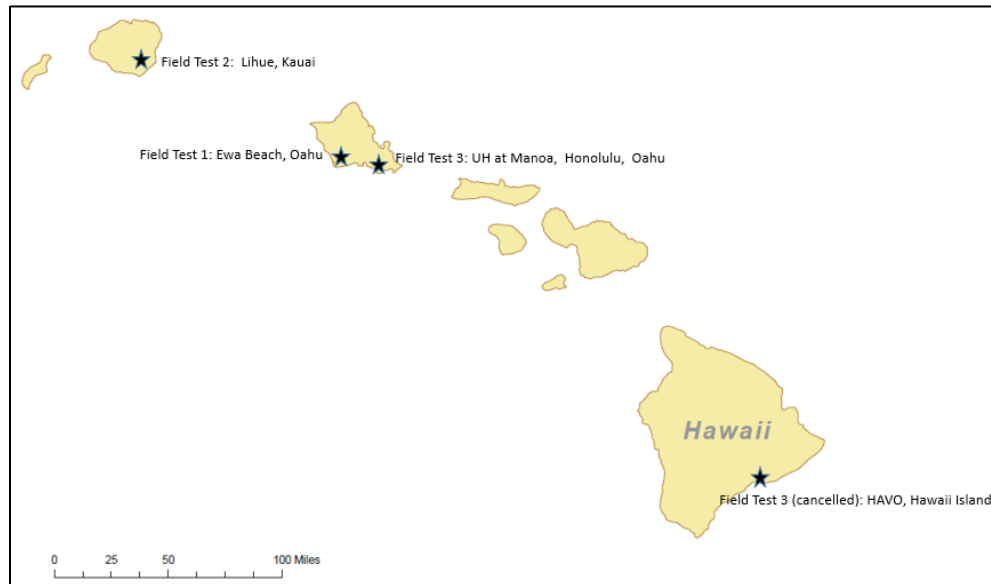


Figure 4.5.1 Field Test Locations

Building upon the findings of first stage, the second phase of the program focused on identifying several test locations across the Hawaiian Islands that are representative of the climate conditions of the Pacific Region. Within that context, the research further evaluated the integration of clean energy generation technology within the test platforms while taking into account the compatibility and structural requirements of the different systems. HNEI and Project Frog selected two sites – one platform at Ilima Intermediate School and two platforms at Kawaikini School New Century Public Charter School, based on their environmental diversity and availability for timely installation, see Figs. 4.5.1 and 4.5.2. A third location considered was Hawaii Volcanoes National Park (HAVO) on the island of Hawaii. Discussed later in the report, the HAVO site was determined to be unsuitable and an alternate location was selected at the University of Hawaii at Manoa (UH).

After the completion of phase Phase II and the issuance of a key report in January 2010, Project Frog and HNEI embarked on the third segment of the research program. This stage consisted of the deployment of the test platforms on two of the selected sites, and the assessment of the structures with regards to their manufacturing and installation cost effectiveness, and logistical efficiency.

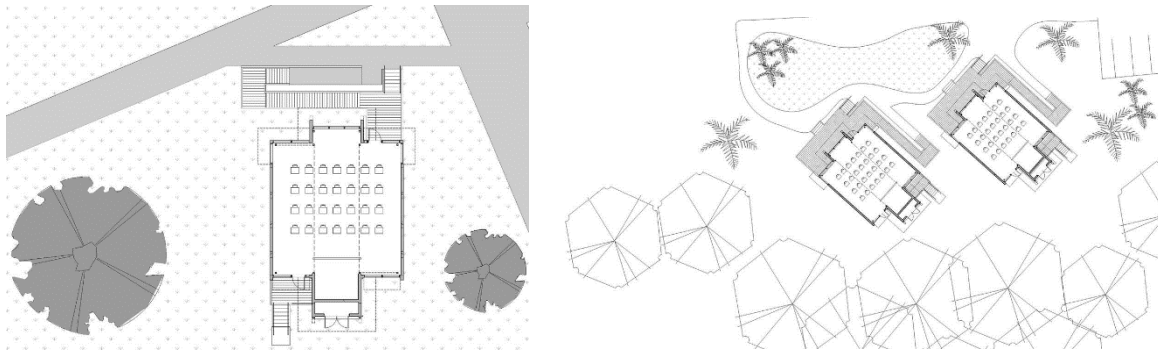


Figure 4.5.2 Site Layout: Ilima Intermediate School (l) and Kawaikini New Century Public Charter School (r)

The building prototypes analyzed in phase Phase III represented the latest version of the Frog structure – Frog platform v2.2, which achieves both performance enhancements and cost savings compared to the originally proposed Frog v2.0.

Project Frog identified four different building components and analyzed their design or material applicability in different tropical climates, in contrast to the v2.0 systemized kit. . These components included insulated wall panels, curtain wall system, integrated roof deck, and exterior cladding. Since the new generation Frog platform v2.2 implements a greater degree of integrated component prefabrication, the company also investigated the economic value of an increase in modularity with respect to mass-deployment in the Pacific region.

The purpose of the field tests was to establish experimental platforms in three climatically different environments with the intent to test how the platforms perform with respect to: daylighting, energy efficiency, thermal comfort, indoor air quality, material durability, and energy consumption. The research program aimed to also track the cost effectiveness of manufacturing and installing the platforms as well as the logistical efficiency of shipping the platforms. Finally, the platforms were tested for their ability to integrate energy generation and storage capabilities as net energy neutral platforms. Table 4.5.1 illustrates the basic parameters of the platform requirements and research intent of the various sites selected to field test the platform.

| Test Site Location | Climate | Platform Design | Cooling Approach | Unit Count | Automation | PV | Wind | Storage | Monitoring |
|----------------------|--|-------------------------------|---|------------|--|---------------------|------|---------|--|
| Ilima | Warm, dry, low cloud cover | Frog v2.2 | 1) Primary: Passive cooling & natural ventilation | 1 | No automated controls: manually operated louvers & windows | (1) 5 kW PV system | N/A | N/A | <ul style="list-style-type: none">• Exterior weather conditions• Interior environ. conditions (T, RH, CO2, light, air movement)• Energy consumption and renewable generation |
| Kawaikini | Warm, wet, moderate cloud cover | Frog v2.2 | 2) Fan assisted cooling/ ceiling fans | 2 | Some automated controls: manually operated louvers & windows | (2) 5 kW PV systems | N/A | N/A | |
| | | | 3) Split system underfloor mechanical cooling | | | | | | |
| UHManoa ¹ | Warm, moderately wet, high cloud cover | Frog "Library" modular design | Same as Frog v2.2 except mechanical: split system interior overhead ducting | 2 | No automated controls: manually operated windows | (2) est 6 kW | N/A | N/A | |

Note: ¹ University of Hawaii at Manoa location site was substituted for Volcano. UHM platforms under construction, to be completed spring 2016.

Table 4.5.1 Research Platform Parameters

The test platforms serve as the “control” in the field experiments, so the envelope, structure and mechanical specifications for the test platforms are identical across the Field Test sites. The envelope features highly reflective materials (cool roof and low-e glazing), high values of thermal insulation, large roof overhangs above the clerestories, sunshades over the lower windows, and a large open air vent for natural ventilation and cooling. The full specifications for the Frog v2.2 platform installed at Ilima and Kawaikini can be viewed in Table 4.5.2 below.

| Product Component | Sub-Component | Product Description / Spec | Notes |
|---------------------------|---------------------|--|--|
| Platform Structure | Floor Framing | Cold rolled steel perimeter chassis w/ light gauge steel purlins and structural steel V-deck. Lightweight Fortacrete subfloor surface. | |
| | Exterior Walls | 6" EPS foam panels with light gauge steel thermally broken frame. | Average R-Values = 23 |
| | Roof Decking | Epic integrated roof deck and acoustical ceiling | |
| | Foundation | Insulated cold-formed steel joist framing, concrete pier footings; refer to structural details. | |
| | Seismic | Steel moment frame construction with integrated cross bracing. | Low-VOC high performance coating |
| Platform Envelope | Roof Insulation | EPS foam board: 4 - 1 1/16" average wing roofs; 5 - 3/4" average infill roofs; 5" spine roofs | Average R-Values: R-21.1 at wings; R-25.8 at infill; R-22.5 at spine |
| | Roof System | Duro Last PVC single ply roof membrane | White. Cool Roof Certified; SRI of 100 |
| | Storefront System | YKK thermally enhanced aluminum curtainwall system with Solarban 70XL dual pane, low-E glass. Integrated sunshades at wing windows. | Anodized Aluminum Glass: U-value = 0.26; SHGC = 0.27; VT = 0.63 |
| | Louvers | Ruskin extruded aluminum moveable louvers | Manually operated for Ilima; integrated actuators for Kawaikini |
| Finishes | Exterior Cladding | Fraserview Products "Sylvaboard" FSC certified cedar siding. | Clear coat finish. |
| | Interior Walls | 5/8" Gypsum wallboard (Type-X where required) | Painted. |
| | Floors | Tate raised access floor. | |
| | Carpet | Interface carpet tile | Green Label Plus Certified; at least 60% recycled content |
| | Resilient Wall Base | Wall Base, Typ.: 4" applied rubber wall base. Wall Base, Wet Areas: 6" integral coved linoleum base | |
| | Ceilings | Epic integrated roof deck and acoustical ceiling | NRC = 0.95 |
| | Interior Paints | Low VOC interior paint by Pittsburg, Sherwin Williams, or equal | |
| Specialties | Signage | Interior ADA required signage | |
| | Appliances | NIC - By Owner | |
| | Furniture | NIC - By Owner | |
| Electrical | Exterior Lighting | NIC - By Owner | |
| | Interior Lighting | Peerless pendant mounted direct/indirect fluorescent fixtures with integrated Lutron Ecosystem ballast | |
| | Occupancy Sensors | Wattstopper or equal ceiling mounted occupancy sensors | |
| | Egress Lighting | Exit signs w/ emergency battery back-up and egress lighting by Lithonia or equal | |
| | Power | Sub-panel, equipment and interior convenience outlets & switches provided | Transformer and main switchgear NIC - By Owner |
| | Data/Telecom | NIC - By Owner | |
| | | | |
| Mechanical | HVAC | Carrier split system fan coil with condensing unit | Puron refrigerant (non-CFC) |
| | Exhaust Fans | Greenheck roof mounted exhaust fan | |
| | Ducting | Underfloor plenum with floor diffusers | |
| | Ceiling Fans | 9 Gossamer Industries ceiling fans | |

Table 4.5.2 Test Platform Frog v2.2 specifications

The test platform was designed to maximize daylight autonomy – or the amount of time when there is sufficient natural daylight in the space so that electric lighting is not required. The daylighting studies indicate that daylight autonomy is expected to occur over 95% of the time (for which the buildings are occupied) at each project location. To support natural daylight the other 5% of the time, high efficiency direct/indirect lighting is used. Each light fixture is outfitted with a Lutron Ecosystem ballast that works in conjunction with daylight and occupancy sensors to automatically adjust lighting levels.

The Test Platform uses both passive and active cooling and ventilation systems to ensure thermal comfort, while using energy efficiently. The main features include:

- Operable louvers at the base of the solid wall panels
- High and low operable windows in the glazed panels
- A roof mounted exhaust fan at the highest point of the roof
- Nine ceiling fans
- A split system fan coil and condensing unit

The Test Platform offers three options for cooling and ventilation with different levels of energy intensity.

- Least energy intense option: uses passive systems, which is achieved by opening the louvers and both the lower and upper windows, thus creating a stack effect of air movement through the space. This option can be slightly enhanced by using the roof mounted low-energy exhaust fan.
- Medium energy intense option: uses the ceiling fans in conjunction with the open louvers and windows. The ceiling fans selected for this project consume approximately half the energy when operating as compared with conventional ceiling fans. In addition, these fans produce greater airflow than other similarly sized fans and are significantly quieter, which improves acoustics.
- Most energy intense option: close all louvers and windows and use the mechanical fan coil and condensing unit. The early design simulation models predict that the mechanical system will only be required for a few hours per year at each site due to our careful passive design strategy.

Field Tests: Ilima Intermediate School and Kawaikini New Century Charter School

The assembly of the Test Platform at Ilima Intermediate School was completed and ownership transferred from UH to the Department of Education on September 30, 2011. The two test platforms at Kawaikini were completed and transferred March 15, 2013 (Figure 4.5.3).



Figure 4.5.3 Installed Ilima platform with deck and stairs

Table 4.5.3 highlights key logistical metrics, specifically an on-site completion time of 35 work days. The completed scorecard, Table 4.5.3 will serve as benchmarks to evaluate future installations. Similar metrics were not reported for Kawaikini, although Table 4.5.4 compares both fabrication and installation times between the two projects.

| Ilima Intermediate | Metric | Result | Unit |
|--------------------|------------------------------|--------------|----------------------------------|
| Logistics | Manufacturing time | 60 | in working days |
| | Transportation Time | 16 | in calendar days |
| | Ease of Transportation | 5 | # of flat racks |
| | | 5 | # of trucks to site |
| | Installation Time | | |
| | Platform (unload & pier set) | 4 | days |
| | Structure (incl subfloor) | 5 | days |
| | Enclosure (roof & Finish) | 17 | days |
| | Systems (MEP) | 9 | days |
| | Total Time | 35 work days | days |
| | Ease of Installation | 39 | Total # of workers |
| | | Approx 17-20 | Total “Requests for Information” |

Table 4.5.3 Measures of logistics for Ilima Intermediate platform

The few hurdles Frog did encounter at Ilima were primarily due to underestimating the complexity associated with managing the logistics of the multiple parties associated with the test site and the specific requirements associated with the end use of the platform. Specifically, the overall site requirements (especially regarding permitting) and utility connections were not sufficiently vetted which resulted in significant delays to the turnover of the platform.

During the process, Frog identified two ways to improve future deployments. Optimizing the packaging and shipping procedures would decrease the number of trucks and containers; and creating a certified installer network would allow us to use 100% locally sourced labor and management. For the installation of the Ilima test site, Frog hired local labor, supplementing the crew with mainland installers (Figures 4.5.4 and 4.5.5).



Figure 4.5.4 Platform components ready for shipment



Figure 4.5.5 Installation of steel frame

As reported in the Project Frog Phase III Update Report of March, 2011, few logistical hurdles were observed during the installation of the first test platform at Ilima Intermediate School. Similarly, the construction process at the second site, Kawaikini School, went unobstructed by

any major difficulties. A notable challenge during the construction process at the latter site was damage to a shear wall panel caused by the exposure of the panel to the elements during the prolonged period between material delivery and start of installation (due to permitting complications). Although the wall panel had to be rebuilt on-site, the work of the installation crew was minimally obstructed, and this did not result in any delays of the overall schedule. In regards to the wall, roof and curtain wall systems of the Frog v2.2 platform, Project Frog observed significant time savings during on-site installation when contrasted with an actual Frog v2.0 project of similar size (Table 4.5.4).

More specifically, the most considerable time reductions were observed in the roof-ceiling system, where the integration of the roof-ceiling assembly and the elimination of the drop ceiling system and roof deck panels, decreased on-site labor by approximately 17 days for the Ilima test platform compared to a Frog v2.0 building of similar size. In addition, the incorporation of the insulation and the steel stud panel frame reduced field installation time for the component by up to 6 days at Ilima.

Finally, the curtain wall system of the v2.0 platform was completed via traditional construction methods, where the glass procurement and sizing is carried out only after the framing installation is complete. For the two test sites, however, the curtain wall assembly arrived on-site correctly-sized and ready to be attached directly onto the structure, thus, cutting back up to 7 days from the installation schedule for that system at Ilima. Similar time reductions can be observed during the installation of Kawaikini Elementary School.

| Component | Task | Frog v2.0 Platform** (app. 1,200sf) | Test Platforms | |
|-----------------------|---------------|---|--------------------------------------|------------------------------------|
| | | | Kawaikini (2 str. x app. 1,200sf) | Ilima (app. 1,200sf) |
| Wall Panels | Fabrication | 60 days | 59 days | 45 days |
| | Installation* | 5 days Erection 16 days Finishes | 8 days Erection 6 days Finishes | 5 days Erection 3 days Finishes |
| Roof - Ceiling System | Fabrication | 60 days | 30 days | 25 days |
| | Installation | 5 days Roof Deck 15 days Ceiling | 4 days | 3 days |
| Curtain Wall System | Fabrication | 40 days Framing | 58 days | 52 days |
| | Installation | 2 days Framing 9 days Glass Installation | 5 days | 3.5 days |

Table 4.5.4 Comparison between the fabrication and installation schedules between Frog v2.0 and v2.2 for structures of comparable size. *Installation assumes a crew of 4

****Schedule presented as extrapolated from an actual Frog v2.0 project**

The platform costs were on-budget, and through the experience of developing the initial platform, Project Frog has identified ways to decrease the future manufacturing and shipping costs by 17%-26%. With respect to installation and site costs, Project Frog did not sufficiently anticipate the total requirements and did not allocate enough of the budget to address means of egress to and from the test platform. As a result, they encountered significant cost over-runs associated with designing and building decks and stairs.

One of the objectives of the platforms was to test the ability to self-generate enough energy to offset consumption. Five kilowatt PV systems were installed on each platform mid-2013 under project funding from another HEET09 project, that compares performance of three PV materials (thin film, amorphous silicon, and monocrystalline silicon) and two inverter types (string inverters and micro-inverters) in different combinations. Monitoring of these solar systems commenced in October of 2013. Preliminary data is reported in Tables 4.5.6- 4.5.8 of this report.

As discussed earlier, the objective of the field test was to evaluate the performance and applicability of the Frog platform in three different climates. The building model used in this study incorporates design changes that result in greater prefabrication scope, higher performance and quicker deployment, all at an economic advantage over the v2.0 structure (Figure 4.5.6). Among these improvements and the sustained components of the original platform, Project Frog recognized four major areas that provide valuable lessons for prospective building projects in the Pacific Region.

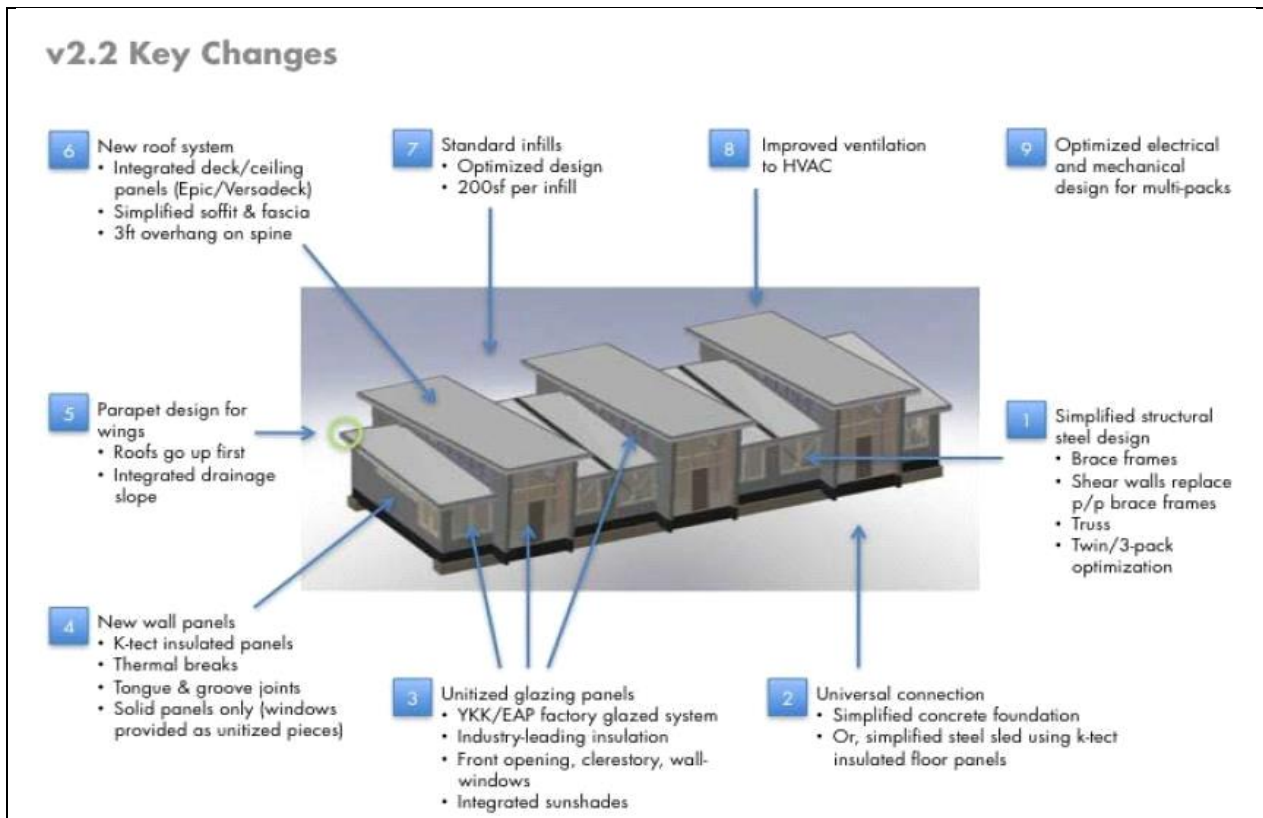


Figure 4.5.6 Frog v2.2 significant design changes in comparison with the Frog 2.0 platform

Due to the large impact of the building envelope on indoor quality and occupants' satisfaction and productivity, one of Frog's primary goals during the design optimization process was the performance enhancement of the platform's wall panels. A frequently encountered problem with the insulation qualities of steel stud wall panels is the thermal bridging effect, which occurs when a material with high thermal conductivity, such as steel, creates heat flow pathways that circumvent thermal insulation. Studies have shown that the thermal performance of steel stud walls can be reduced by up to 55% due to the steel elements that serve as thermal connections. Thermal bridging is primarily a concern in cold climates, however, it leads to design inefficiency due to the additional insulation thickness, and for energy-neutral design purposes it becomes an important factor in climates similar to the environmental conditions of the Pacific Region.

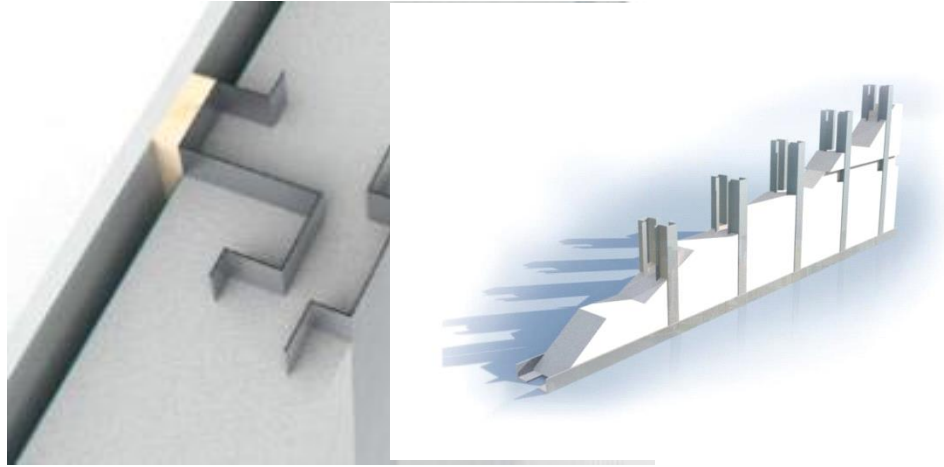


Figure 4.5.7 K-Tect wall systems; thermally broken wall panels with EPS core

Although the v2.0 wall panels provided a high overall thermal resistance value, the thermal bridging effect caused by the panel studs had to be compensated with a thick layer of insulation, which was applied on-site in the original kit version. In order to enhance the wall panel functionality, in the v2.2 platform Project Frog incorporated the thermally broken K-Tect Wall System. The stud pattern of the K-Tect panels is specifically designed to allow for a continuous cross-sectional layer of insulation in order to avoid thermal and sound pathways between the interior of the building and the outside environment (Figure 4.5.7). The pre-fabricated combination of light gauge structural steel and the expanded polystyrene (EPS) insulation foam provide the cost, time and quality benefits of factory-manufactured materials, while at the same time, the ductility of the metal allow for easy manipulation on-site.

As Phase II of the research program established, the climate zone of the Pacific is generally characterized as tropical, although some climate variations occur due to changes in landscape and trade winds. Such climate conditions dictate the need for high performance glazing, especially when energy neutrality is an objective. Since the Frog test buildings are designed for maximum daylight autonomy at each project location, glazing takes up a significant portion of the building envelope. The v2.2 platform re-evaluated the balance between the solid and glazing wall panels from the perspectives of occupants' satisfaction and energy consumption loss and gain due to the increased daylight amount and the heat conductivity of glass respectively.

By incorporating the v2.2 specified glazing type, the overall heat transfer though indirect radiation exposure was reduced by 27% across the window area. While higher heat transfer control is usually achieved at the cost of visible light transmittance (VLT), the current curtain wall system admits 17% more visible light, to a total of 63%, thus, increasing the daylighting potential of the structure without compromising energy efficiency. The resulting design specifies a better performing glazing system with assured quality since the entire glass-framing assembly is prefabricated in a factory. Furthermore, the new system also minimizes field labor, particularly at the clerestory and front spine all window sections which were provided and site-built by the General Contractor in the v2.0 version (Figure 4.5.8).



Figure 4.5.8 Crated curtain wall components at Ilima (l) and installed curtain wall at Kawaikini (r)

Another area of major design improvement between the two Frog generations is the roof deck of the structure. The ceiling roof system of the 2.0 platform consisted of a metal deck screwed to light gauge steel roof panels, single-ply roof membrane over rigid insulation, and an acoustical drop ceiling. Albeit the roof components had been performing effectively from a thermal and acoustical standpoint, their cost and required installation time and labor put the assembly at a disadvantage compared to integrated systems.



Figure 4.5.9 Acoustical and non-acoustical integrated roof deck

The v2.2 design comprises of an interior acoustical and exterior non-acoustical Epicore roof system with exposed bottom surface (Figure 4.5.9). The integrated assembly eliminates the roof panels and drop ceiling of the v2.0 platform, and results in material, installation and shipment cost and time savings. The light weight of the roof deck - 4.4psf, and the long clear span - up to 20ft for gauge 18, also provide design flexibility for projects of different purposes. An additional benefit is the perforation pattern of the flat ceiling surface which allows direct interaction between the sound waves and the sound absorption elements. This profile enhances the noise reduction coefficient to 95%, or 25% more than the v2.0 drop ceiling system (Figure 4.5.10).

The siding of a building plays a crucial role in the structure's cold shell protection against the elements, as well as its exterior appearance. Using a natural red cedar laminate has been one of two preferred siding materials for Frog's second-generation buildings, and

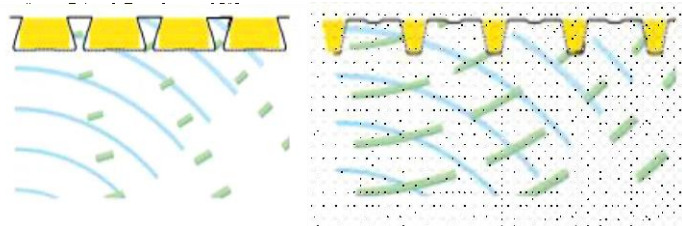


Figure 4.5.10 Sound reflectance comparison between the Epicore acoustical deck and standard ribbed deck profile

was held constant in the transition between v2.0 and v2.2. Apart from their appealing aesthetic exterior and environmental advantages of using natural wood, the treated laminate panels also exhibited durability, high quality and low need for maintenance when subjected to laboratory testing conducted by the manufacturer. Taking into consideration the theoretical performance, aesthetics and sustainability of the system, the cladding was found suitable for rain screen application across the Pacific (Figure 4.5.11).



Figure 4.5.11 Prefabricated wall panel with exterior natural wood siding, Ilima

The findings presented in this report are based on field observations during the construction process and site visits of the first two test platforms. The erection of the third test structure was scheduled for late 2010, however, due to material performance and durability concerns under the HAVO climate conditions, and more specifically, the high concentrations of sulphur dioxide in the Park, construction did not take place. Project Frog conducted material testing on a roof deck and two wall panel samples through directly exposing the samples to the local environmental conditions for approximately twelve months.

At the time of the current report, Phase IV of the research program focused on energy generation and performance monitoring has not been executed, and the theoretical performance of the two deployed test platforms has not been confirmed. It is Project Frog's understanding that HNEI will conduct this final stage of the research program under a separate contract.

Project Frog carried out a comparative cost analysis of the Frog platforms on a square foot basis, and determined cost reductions across every modified component of the v2.2 kit. The data presented in Table 4.5.5 has been averaged based on the installation and material cost for the first two test sites in order to minimize sampling error. Among the three assemblies studied in this section, the most significant cost savings are achieved in the roof-ceiling system where the integrated roof deck amounts to only 71% of the v2.0 assembly economically. Similarly, the v2.2 wall panels and curtain wall result in 10% and 29% cost reductions respectively.

It is important to note that given the original contract between the company and HNEI was signed close to two years before construction, Frog experienced a significant overrun of initial cost estimates for the company's scope at the time of the two installations. In addition, Project Frog had grossly underestimated the General Contractor's costs inflicted on the company, which in Kawaikini's case amounted to approximately 150% of initial estimates. As a result, the cost savings related to material optimization of the v2.2 platform helped compensate the company's aforementioned losses.

| Component | Frog v2.2 Cost Reduction Compared to Frog v2.0 |
|-----------------------|--|
| Wall Panels | 10% |
| Roof - Ceiling System | 29% |
| Curtain Wall System | 19% |

Table 4.5.5 Material and installation cost savings of the v2.2 Frog kit compared to Frog v2.0

Frog's project management team responsible for the construction of the two test structures visited site one in January, 2012, and site two in April, 2012 to assess material performance. During the site inspections, the wall, roof and curtain wall assemblies were found to be suitable for both the warm and dry climate of Ilima, as well as the warm and wet climate of Kawaikini. In the latter case, a number of concerns were raised to Project Frog about rusting of the roof deck, as well as of the curtain wall framing, after spots in red color were observed in some regions of both components. Upon investigation, it was confirmed by the company and HNEI that the spots on the roof deck were in fact stains of dirt mistaken for rusting due to the red pigment of the local soil. Similarly, Frog examined what was thought to be rusting on the mullion of the curtain wall system, and found that the rust specs were actually rusted steel shavings which had fallen down during the attachment of the roof deck to the structure. When these shavings were removed from the mullion with a sanding sponge, it was determined that there was no impact of corrosion on the surface of the aluminum.

The exterior wood siding, however, exhibited significant weathering in both climates. Under the low cloud-cover, dry weather conditions of the first test location, the primary problem observed with the wood material was its fast and uneven fading due to the different intensity and duration of sun exposure of the four sides of the building. On the other hand, the warm and wet climate of the second location could potentially cause excessive water absorption, which may lead to delamination in natural wood laminates.

The material performance study Project Frog conducted at HAVO shows satisfactory conditions of the pre-fabricated wall panel samples, although considerable weathering has been observed on components directly open to the elements. The highly acidic nature of sulphur dioxide has accelerated the corrosion of exposed galvanized steel. Similarly, the roof deck also demonstrated extensive deterioration. The two wall panel samples include different types of exterior siding - treated and untreated natural wood laminate, and bio-composite material. As expected, the untreated laminate showed the most severe weathering, while the bio composite, made of post-consumer recycled paper and bamboo fiber, was barely affected. It is important to note, however, that the superior performance of the bio-composite siding comes at a non-trivial cost premium. HNEI let sub-contracts to MKThink under N00014-11-1-0391 and N00014-12-1-0496 to monitor environmental and performance factors in the Kawaikini and Ilima platforms. While the details of the monitoring studies will not be discussed in this report, they are being referenced as relevant to the conclusions that may be drawn from the ongoing operation and observation of these experimental platforms.

After the first complete year of data collection in 2014, the three platforms performed as designed, achieving one of three bracketed estimates made in the Phase II report: “High Estimate”, “Anticipated Performance”, and “Optimal Performance”. The structure in the hotter Oahu microclimate performed exactly at the “High Estimate” which assumed significant dependence on air conditioning, resulting in an actual electric site EUI of 7.8 kWh/sf-yr. (excluding solar). The two predominantly naturally ventilated structures in the more temperate Kauai location produced twice as much energy than was used, realizing an average electric site EUI of about 4.7 kWh/sf-yr, achieving the “Optimal Performance” target. This difference in performance may be attributable to two factors: differences in micro-climates and difference in policies, awareness and user response to the internal environment.

In addition to evaluating annual energy flows, energy consumption was evaluated in different time frames, including school days only. Below are examples of preliminary tables of performance that will be presented in detail in future reports. Table 4.5.6 presents relative energy and environmental performance. Table 4.5.7 disaggregates energy consumption by end-use. Table 4.5.8 is a preliminary evaluation of energy consumption compared to generation for the most recent data set. The Kawaikini Frogs are net zero, they generate more than they consume. The Ilima platform, during this time frame was slightly net negative, consuming 6.5% more energy than it generated. These numbers will vary year to year depending on climatic conditions.

| | Classroom Type | Total Energy [kWh/ft ²] | Environmental Performance Criteria Score* |
|-----------------------|----------------------|-------------------------------------|---|
| Ilima | Project FROG Modular | 5.03 | 60.7% |
| Kawaikini West | Project FROG Modular | 2.19 | 65.0% |
| Kawaikini East | Project FROG Modular | 2.05 | 79.0% |

*Calculated by aggregating the following 3 percentages: (1) % of time PMV is inside the ASHRAE Comfort Zone, (2) % of time CO₂ concentration is below 1100 ppm, the ASHRAE threshold for ventilation, (3) % of time lights were off while the wall illuminance > 5 ft-cd and wall/ceiling illuminance ratio < 5

Table 4.5.6 Preliminary energy and environmental performance, school days only⁴

TOTAL NORMALIZED ENERGY USE (2013-2014 HIDOE school year, school days only)

| | Ilima | KW West | KW East |
|--------------------------------------|--------------|----------------|----------------|
| Total Energy [kWh/ft ²] | 5.03 | 2.19 | 2.05 |
| Mech. Cooling [kWh/ft ²] | 3.74 | 1.21 | 1.07 |
| Fans [kWh/ft ²] | 0.01 | 0.32 | 0.18 |
| Int. Lighting [kWh/ft ²] | 0.50 | 0.27 | 0.11 |
| Ext. Lighting [kWh/ft ²] | 0.32 | 0.49 | 0.44 |
| Plugs [kWh/ft ²] | 0.47 | 0.26 | 0.25 |

Table 4.5.7 Preliminary energy consumption during school days only⁵

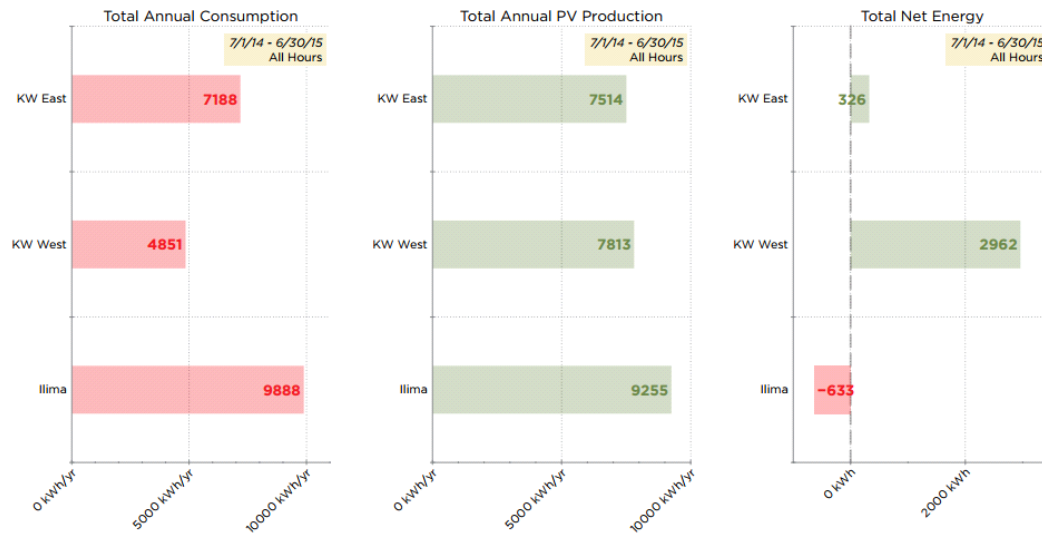


Table 4.5.8 Energy Consumption v Generation 7/14 to 6/15⁶

In its Phase II final report, Project Frog evaluated the time and cost effectiveness and the material performance of four building components as parts of a quickly-deployed, systemized kit tailored to the Pacific Region. The analysis demonstrates that an increase in the prefabricated scope of the wall panels, roof-ceiling assembly and curtain wall system results in material and installation cost reductions, and time savings during construction. These factors, as well as the implied greater ease of transportation and installation and decrease in shipping costs, give such modular assembly systems great advantage over traditional construction for the purposes of mass- deployment in various environments across the Pacific.

Project Frog also found that natural wood siding, in its role as the first line of defense against the elements, may be prone to severe visual deterioration when exposed to tropical climate conditions. Despite that weathering may not pose immediate threat to the performance of the building and the satisfaction of its occupants, such siding material requires frequent maintenance in order to sustain desirable building aesthetics.

Finally, as explained earlier, the purpose of the collaboration between Project Frog and HNEI was to develop and test a kit in various climate conditions representative for the Pacific. While the first and second test platforms performed as expected across two contrasting tropical climates, analysis of the HAVO location found the local environmental conditions to be prohibitive for the construction of a third test structure with similar characteristics. Although Project Frog does not advise against construction in areas with high concentration of volcanic air pollution altogether, it recommends extensive research of the building materials' susceptibility to deterioration and corrosion due to meteorological factors specific to that region.

The Ilima and Kawaikini structures as commissioned and accepted are shown in Figure 4.5.12.



Figure 4.5.12 Completed projects: Ilima site visit, January, 2012 (l); Kawaikini site visit, April, 2012 (r)

¹Project Frog, The Science and Technology of Advanced Structural, Material and Environmental Systems in Quick-to-Deploy, High-Performance Green Solutions, Phase II Draft, January 2010

² Project Frog, The Science and Technology of Advanced Structural, Material and Environmental Systems in Quick-to-Deploy, High-Performance Green Solutions, Status Report, May 2012

³ Project Frog, The Science and Technology of Advanced Structural, Material and Environmental Systems in Quick-to-Deploy, High-Performance Green Solutions, Phase III Update, March 2011

⁴ MKThink, Mid-Study Integrated Report: HNEI Test Platform Analysis Part Two, April 2015

⁵ MKThink, Mid-Study Integrated Report: HNEI Test Platform Analysis Part Two, April 2015

⁶ MKThink, custom graphic based on captured data. Email to Jim Maskrey, December 10, 2015

Crissy Field Center Wind Power Study

Under HEET 2009, HNEI was awarded funding to conduct research including the installation, testing, and evaluation of passive and active energy systems using modular test platforms fabricated by Project FROG, Inc. The test platforms incorporate advanced design elements to decrease user energy demand, thus increasing the effectiveness of integrated renewable energy generation systems. The research intent was to study the integrated performance and effectiveness of the test platforms and energy systems in relevant Pacific region environments for potential future Navy applications.

Under the same ONR award, the energy systems research, testing and evaluation were extended to take advantage of a Project Frog test platform site uniquely suited for wind energy technology research located in San Francisco, California. Under this subtask, HNEI contracted the Golden Gate National Parks Conservancy (Conservancy) to install 5 small (1 kW) wind turbines adjacent to, and connected with, Project FROG test platforms located at the Crissy Field Center (Center) in the Presidio of San Francisco, a proven wind resource for collection of comparative wind energy data.

The Conservancy, the lead organization for operation of the Center, planned, permitted, and installed five wind energy systems including connection with the test platforms. The wind turbines were located proximate to each other to ensure consistency of the wind resource and

comparability of data. HNEI served as the technical expert for the project including data collection and analyses.

The objective of this research was to evaluate and test selected wind turbine technologies to determine the relative effectiveness of differing designs, the impact of different climatic conditions, and integration with the test platform systems toward the achievement of energy neutrality and/or net positive energy within the test site.

Turbines manufactured by Venco Power, GMBH, Windspire Energy and Tangarie Alternative Energy Power, LLC were selected after a vetting process was conducted of small, vertical axis technology. The Conservancy, with support of Project Frog and HNEI, integrated the wind energy data into a dashboard based, public monitoring system, tracking overall building performance as well as its environmental sub-systems.

The Crissy Field project site is located in the Golden Gate National Recreation Area, federal land managed by the National Park Service. Figure 4.5.13. Vertical helical turbines were selected to meet the requirements of the Center and the National Park Service for bird safety and low visual, noise and vibration impact on staff and visitors. In anticipation of wind turbines, conduit from the proposed site to the Center's mechanical closet was installed during the Center's construction.

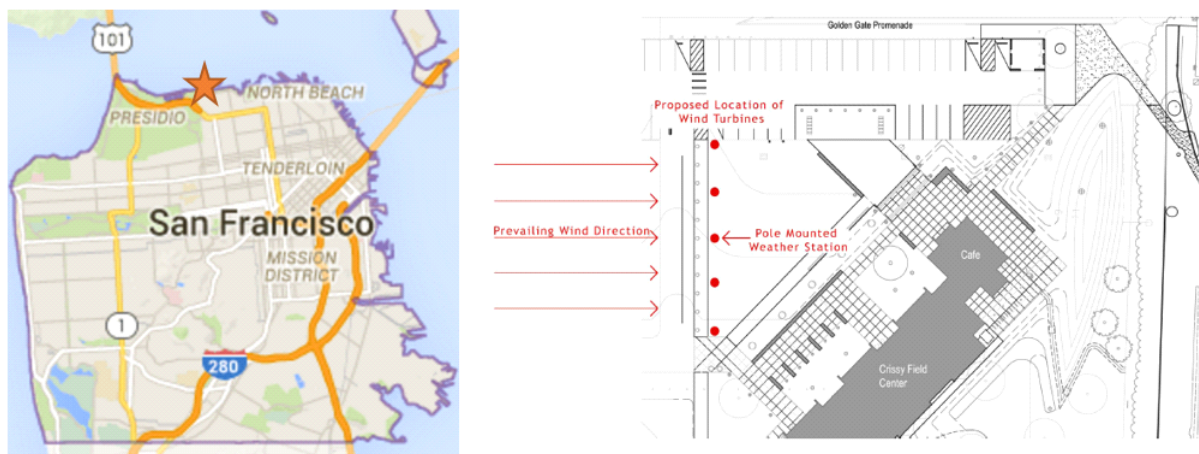
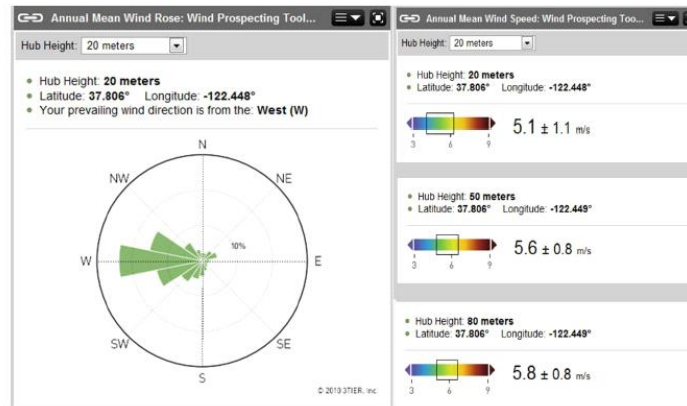


Figure. 4.5.13 Crissy Field Center site location

Under this project, the Conservancy commissioned a wind study specific to the location of the Center, as close to the estimated hub height of the turbines as possible. Results are represented in Figure 4.5.14. Average annual wind speeds at a height of 20 meters was calculated at 5.1 m/s \pm 1.1 m/s (10.5 miles per hour (mph)).



Prevailing Wind Direction is from the West. Site Average wind speed is 10.5 mph.

Figure 4.5.14 Third Party Wind Assessment

The Conservancy also acquired average wind speed data from project partners operating in the immediate vicinity of the project site. Four years of data (from 2007 to 2010) were provided from the Anita Rock site, a Coast Guard station located approximately 200 yards offshore near the Center. Data was provided in annual averages and in 5 minute intervals.

The wind turbine array was also subject to visual evaluation by the National Park Service in order to establish that the cultural and historical fabric of the site was not compromised by the project. For complete report detail, please see [“Golden Gate National Parks Conservancy Deliverable 1: Recommendations for Wind Turbine Systems and Data Acquisition Systems”](#)¹.

Design and engineering services were underway from November 2011 through January 2012. The Conservancy contracted with Luminalt Energy Corporation as the prime contractor for the design/build installation of the selected turbine array. The Conservancy provided the layout plan for the wind turbines. Tower Engineering Professionals (TEP) produced the structural analysis and foundation design for the wind turbines. Consolidated Engineering Labs (CEL) was contracted to perform compaction testing, reinforced steel inspection, anchor bolt testing and concrete testing. Amec Engineers provided geotechnical analysis and recommendations for the project footing design. Amec also reviewed the final footing design produced by TEP to ensure conformance with geotechnical requirements. Luminalt Energy Corporation provided electrical design and design-build plans for the project. For complete engineering reports, please see [“Golden Gate National Parks Conservancy Deliverable 2: Report on Final Design and Permitting”](#)^{2,3,4}.

Construction consisting of trenching, footing reinforcement, running of electrical conduit, concrete work, mast and installation of 2 turbines took place January and February of 2012, with a public opening ceremony on February 15, 2012. The remaining three turbines were installed in March and April, 2012 (Figure 4.5.15):

- (2) “Windspire” 1.2 kW, with integrated inverters (February 2012)
- (2) “Venco Twister” 1000 with Power One 3.0 kW Inverters (April 2012)
- (1) “Tangarie Gale” T2 with a Power One 3.6 kW Inverter (March 2012)



Figure 4.5.15 Vertical Axis Wind Turbines Windspire (l), Venco (m), Tangarie (r)

The turbines were all operating by April 2012, with each of the five units required varying amounts of diagnostics, field tuning and, in some cases, the replacement of specific components before they became operational. Details for each of the selected technologies follows:

WINDSPIRE: Over the first year the Windspire turbines had several issues regarding “wobbling” which began upon operation in February. After several adjustments to the shaft assemblies no pronounced improvement was evident. In March 2012 base and shaft assemblies were replaced, solving the wobble issues. In September 2012, a wobble was again noticed that was attributed to the anchor bolts loosening. Maintenance protocols were put in place to regularly inspect and tighten the anchor bolts with a torque wrench. In December of 2014, the North unit failed catastrophically in high wind and in order to ensure public safety, both units were taken off line. The Windspire turbines are equipped with a braking feature that is set to engage when a certain rpm limit is reached. During the first few months of operation, it was observed that the North and South units did not brake consistently in response to similar wind conditions. The Southern unit tended to brake much more frequently. Subsequently, it was determined that the “over speed” limit was set differently for the two units. The limit on the Southern unit was adjusted from 1,300 watts to 1,700 watts – thereby matching the 1,700 watt limit of the Northern unit.

VENCO: The Venco Twister 1000 TL units 1 and 2 were installed and began operating in April of 2012. The units were installed with Power One PVI-3.0 OUTD inverters per the recommendations of Castle Energy, the US distributor of Venco turbines. Although the Venco turbines are typically mated with SMA Windy Boy inverters, the Power One units were selected due to their potential ability to realize increased energy harvests.

With the installation complete, the Venco units appeared to be operating properly but the Power One inverters gave readings indicating a ground fault error. Consultation with Venco engineers suggested several possible reasons for the error, including incompatibility between the Vencos and Power One inverters.

The Venco engineers suspected a ground fault in the eddy current brake, and instructed the installer (Luminalt) to disconnect it and take insulation resistance readings. When the current

brake was disconnected the error readings disappeared and the units started functioning properly. The disconnection of the integrated Venco current brake was deemed acceptable because the Power One units had the capacity to perform the braking function through programming of the power curve. With the electrical error solved, the Venco units were fully operational by the end of May, 2012.

Between January and March of 2014, both Venco units stopped rotating. Luminalt was contracted for a maintenance visit at the site for all of the turbines, which was conducted on March 26, 2014. Lubricating grease was added to the Venco bearing assemblies and the units were cracked loose and rotated by hand. Although the units could be manually rotated, they would not rotate on their own in the wind.

Small stress cracks were observed in the blades at some locations where they attach to the struts.

TANGARIE: The Tangarie Gale T2 was installed in March of 2012. Despite what appeared to be a correct installation, the Tangarie turbine never turned freely in the wind and appeared to resist rotation. In higher winds, this resistance appeared to translate into the shaking of the entire turbine's tower. Per the manufacturer and distributor's directions, various inverter curves were programmed without significant effect.

After more than a month of operation, the Tangarie was incapable of consistently generating more than 50 Watts, even in 25 mph winds.

The performance described above persisted for the entire service life of the unit, despite repeated field adjustments made at the direction of the manufacturer.

In July, 2013, the Tangarie was inspected by Luminalt and "severe signs of failure and was removed from the tower" for service or replacement. It was determined that neither was an option, so the unit sat idle without producing energy.

For detailed reports and documentation for each of these units please refer to "[Golden Gate National Parks Conservancy Deliverable 5: Wind Turbine Commissioning and Interconnection](#)"⁵.

The Data Acquisition System (DAS) was installed to monitor wind turbine performance as well as building performance of the Center. The components specific to monitoring the wind turbine performance include two sets of wind speed and direction sensors. These were mounted at the center of the row of wind turbines as well as on the roof of the cafe, along with power monitoring sensors mounted on each wind turbine power circuit. Hardware components of the system are indicated in the as-built system diagrams, see reference 6.

For wind speed and direction at the center turbine, the sensors are connected to a microcontroller. This microcontroller was powered through low voltage power cables from the building and communicates via ZigBee radio transmission to a receiver located near the cafe weather station. The microcontroller located at the wind instrument holds 60 1-second interval measurements in memory. When prompted by a serial call, the microcontroller calculates minimum, maximum, mean, and standard deviation of the two datasets, and returns these summary statistics via serial connection. A vector average is used for the mean of the wind direction. Data are logged in flash memory at the controller.

For power, each wind turbine circuit is monitored using current transformers and reference voltage that are wired to an electrical monitoring device to calculate power use. The controller logs these readings in its flash memory.

Data accumulated in flash memory is retrieved approximately monthly via manual File Transfer Protocol (FTP) request. Both the original data file and the consolidated ("pivoted") data file are uploaded to a web server for distribution.

The DAS for the building operates on a 10-minute interval and also reports power data for each individual turbine. These data are collected and processed automatically and are ultimately visualized using a custom dashboard interface that shows data in real time (see Appendix B, Dashboard Screenshots). This visual representation of the data has been helpful for assessing whole building performance and to identify issues with wind turbine performance. Several times during the project, the dashboard helped alert the team to issues with wind turbines.

Several issues arose in the commissioning and ongoing operation of the DAS. These include the following issues:

- Wind speed readings tended to be less than expected. Replacement of an anemometer unit at the rooftop of the café helped identify a likely issue with anemometer calibration for each original anemometer. Using a statistical analysis of anemometer readings before and after the replacement of this anemometer, we identified a correction factor that could be applied to the anemometer at the wind turbines to correct the calibration (see Appendix C, Anemometer Correction Factor memo). Even after the correction, the wind speed readings still tended to be lower than what was expected from a previously completed site survey.
- Wind turbines and inverters were expected to be producers of electricity, not consumers. The Tangarie turbine unit appeared to be producing a constant output of 20W. However, an analysis of Tangarie output revealed that this 20W was most likely 20W of electrical use on the Tangarie circuit (see Appendix D, Power Production of North Windspire and Tangarie Turbines, November 1–17, 2012). It is unclear whether the source of this 20W load was the inverter or another load on the same circuit.

HNEI was able to receive the data collected from the DAQ system. An analysis was completed of this data, during which process they collected notes on lessons learned. In particular, issues were identified as attempts were made to extract performance curves from the wind and wind turbine data. The primary issue was that the power use and wind data didn't show a strong relationship at the level of the most detailed data collected due to the timing and nature of the readings. Instantaneous power readings and 1-minute averaged wind data demonstrated wind turbine performance over time, but the analysis team found they wanted more detailed data that showed performance at a 1-second sample interval. Other issues were identified as well, and include gaps in the data and a bug in data processing software that omits or duplicates a line of data at the edges of monthly datasets.

Recommendations for the next phase of the project to address issues identified in the first phase include:

- Data Acquisition (DAQ)
 - Record wind and energy data in synchronized 1 Hz intervals.
 - With 1 Hz data for wind and turbine output, we would not require additional pre-processing (min, max, ave, std dev)
 - Synchronize time stamps across all sensors in DAQ system.
 - Localize anemometers to each turbine, 1 anemometer per turbine
 - Identify sources of false signals (e.g., 10-20W signal from non-performing Tangarie)
- Data Processing
 - Troubleshoot sources of missing data
 - E.g., Network, internet, archiving, instrumentation, communication, inverter, connection, logging, etc.
 - Request direct access to raw data
 - Make data format consistent across sub reports (monthly)
 - Eliminate redundant reporting across sub reports (monthly); double reporting of same timestamps on different reports causes data reconciliation issues.

For detailed report and DAQ system drawings please see “[Golden Gate National Parks Conservancy, Deliverable 6: Installation and Commissioning of the Data Acquisition System](#)”⁶.

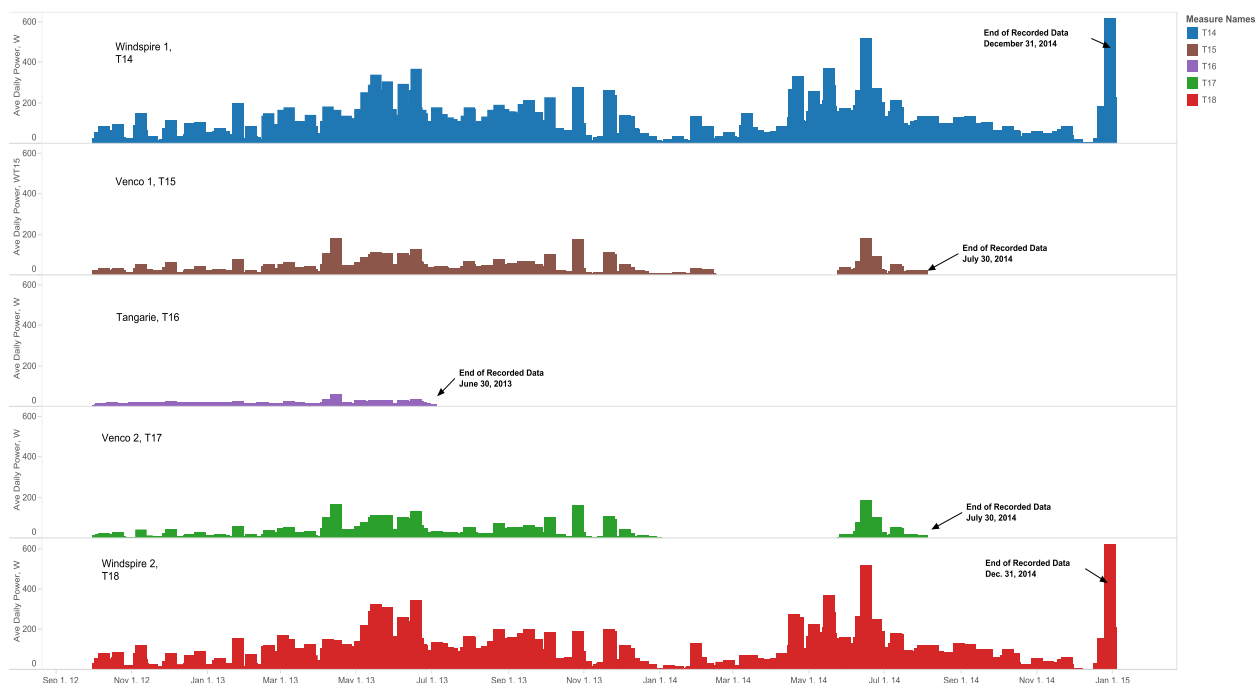


Figure 4.5.16 Daily average power output over turbine life (Watts)

The five turbines were installed and commissioned by July of 2012. Simultaneous wind speed and turbine output was recorded from October 5, 2012 forward. Figure 4.5.16 illustrates power generated over the project life of each turbine. The two Windspires (T14 and T18) generated energy continuously from project beginning through Dec 31, 2014. The Venco turbines operated up to July 31, 2014, when the turbines experienced a mechanical failure. Bearing seizures were responsible for lack of production for several months in 2014. They were repaired but failed and were taken offline July 30, 2014. The Tangarie turbine experienced blade failure late June 2013 and was decommissioned shortly thereafter.

With 816 days of minute-level data, actual performance was compared to expected performance for both wind resource and turbine generation. Table 4.5.9 presents key findings from the data.

| Annual Generation Summary (Period of Performance October 5, 2012 to December 31, 2014) | | | | | | | | Rated Capacity Factor | |
|---|---------------------------|----------|--|---------------------------------------|---|--|--|---------------------------|---------------------------|
| Manufacturer | Rated Power (kW) | Run Days | Observed Average Wind Speed (m/s) | 2012 to 2014 Total Output (kWh) | 2012-2014 Average Daily Output (kWh/day) | Projected Ave. Daily Output at Observed Wind Speeds per Manuf. Spec. ¹ (kWh/day) | Capacity Realization Rate at Observed Wind Speeds (%) | Rated Capacity (kW) | Capacity Factor (%) |
| Windspire 1 ² | 1.2 @ 10.7 m/s | 816 | 3.6 | 1,196 | 1.47 | 0.72 | 204% | 1.20 | 5.09% |
| Windspire 2 ² | 1.2 @ 10.7 m/s | 816 | 3.6 | 1,058 | 1.30 | 0.72 | 180% | 1.20 | 4.50% |
| Venco 1 ³ | 1.0 @ 12.0m/s | 556 | 3.6 | 280 | 0.50 | 0.72 | 70% | 1.00 | 1.43% |
| Venco 2 ³ | 1.0 @ 12.0 m/s | 514 | 3.6 | 194 | 0.38 | 0.72 | 52% | 1.00 | 0.99% |
| Tangarie ⁴ | 2.0 (speed not specified) | 268 | 3.6 | 107 | 0.40 | NA | NA | 2.00 | 0.27% |

¹ Estimate of manufacturer's output at observed average wind speed of 3.6 m/s.

² Windspire units taken offline December 31, 2014 due to materials failure

³ Venco units taken offline July 2014 due to materials failure

⁴ Tangarie unit taken offline July 1, 2013 due to materials failure

Table 4.5.9 Summary of key turbine performance findings

Finding 1: Both Windspire turbines operated from October 6, 2012 through December 31, 2014, or 816 days. The Venco 1 and 2 turbines had intermittent operating issues described in other sections of this report operating for a total of 556 and 514 days respectively. The Tangarie turbine operated for only 268 days, having failed by June 30, 2013.

Finding 2: The observed average wind speed was lower than predicted from the wind study commissioned by the Parks Conservancy. The predicted average wind speed was 5.1 m/s (11.4 mph) using the data from the Anita Rock wind site. The observed average wind speed was 3.6 m/s, 70% of the projected wind speed.

Finding 3: From an observed wind velocity profile created on a minute to minute basis, the projected turbine outputs were forecasted based on the manufacturers power curves. For the Windspire turbines, the total actual generated energy was nearly twice as high as would have been forecast at the observed wind regime. The Windspire 1 and 2 generated 204% and 180% respectively, of the energy expected at observed wind regime. The Venco 1 and 2 turbines generated 70% and 52% of the expected energy, respectively, during actual periods of operation. The energy expected from the Tangarie could not be determined since there was no manufacturer's power curve available.

Finding 4: While Finding 3 was a comparison of actual energy to the power curve, Finding 4 highlights the capacity factor at rated conditions. The Windspire rated capacity is 1200 Watts at a wind speed of 10.7 m/s. The Venco rated capacity is 1000 Watts at wind speed of 12.0 m/s. The Tangarie capacity is rated at 2000 W with no wind speed specification.

The Capacity Factor is the observed amount of energy produced relative to the amount that would have been generated if the turbine ran at rated capacity over the specified duration. For this analysis, the duration is the 816 days of measured data from October 5, 2012 through December 31, 2014.

The Windspire capacity factors were 5.09% and 4.50%. The Venco capacity factors were 1.43% and 0.99%. The Tangarie capacity factor could not be determined due to lack of manufacturer data.

There is no robust relationship between average wind speed and the power output of any of the Vertical Axis Wind Turbines (VAWT) at Crissy field on a minute-to-minute basis, as can be seen readily by examining the scatterplots in Figures 4.5.17 and 4.5.18 below.

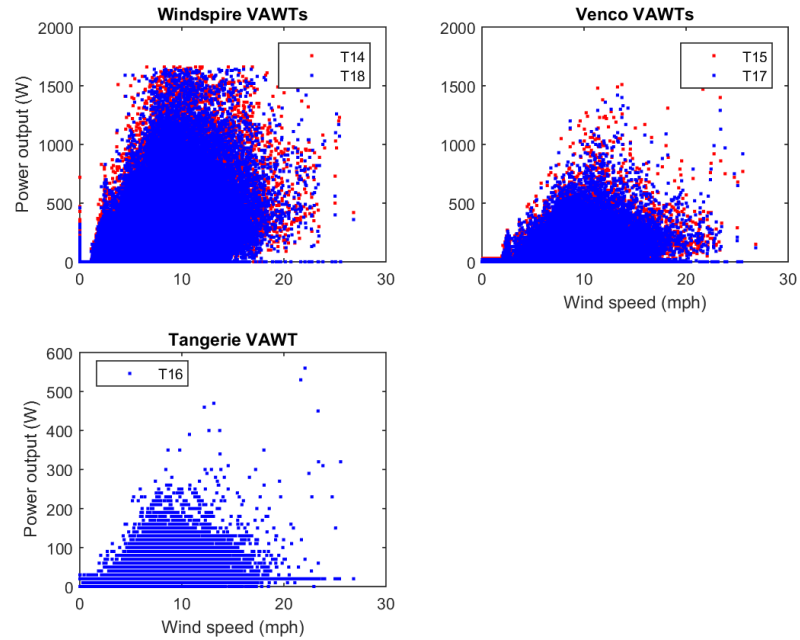


Figure 4.5.17 Power plotted against wind indicating weak relationship

The poor relationship in the data set between wind speed and power output seems to be due to the fact that the wind turbines are sampled instantaneously every 60 seconds, whereas the wind data is an average over 60 seconds. As the output from the VAWTs varies significantly within a one minute time period, the instantaneous “snapshots” recorded every 60 seconds are not representative of the power output over the rest of the period. This idea is supported by the fact that there is significantly less scatter in the relationship between wind speed and VAWT output if one only considers “steady wind”, defined as the average of wind speed per minute, at a standard deviation of wind speed over one minute of less than 1 mph, Figure 4.5.18 below.

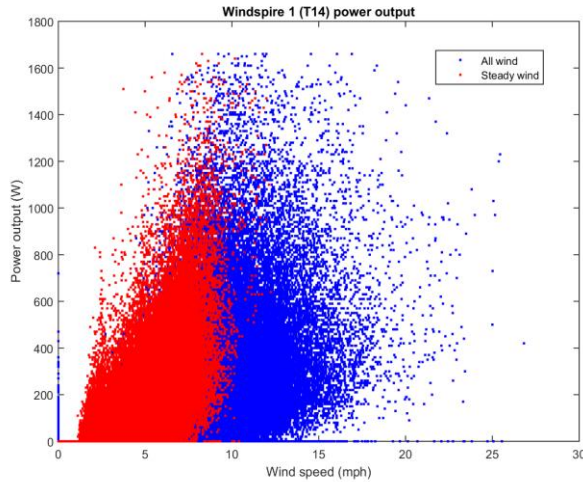


Figure 4.5.18 Scatterplot of power and wind, as well as steady wind (in red) for Windspire 1

Effectively, the 60 second snapshots are a random sampling of the underlying probability distribution of turbine power output. In order for these random samples to be representative of the real output from the turbines, they must be averaged over a long period of time. A straightforward way to accomplish this is to examine wind speed daily averages, as can be seen in the plots in Figure 4.5.19 below, the daily averages of wind speed and power output for the various VAWTs for the year 2013. Note that we have excluded the Tangarie VAWT from the remainder of the analysis due to the short period it was operational.

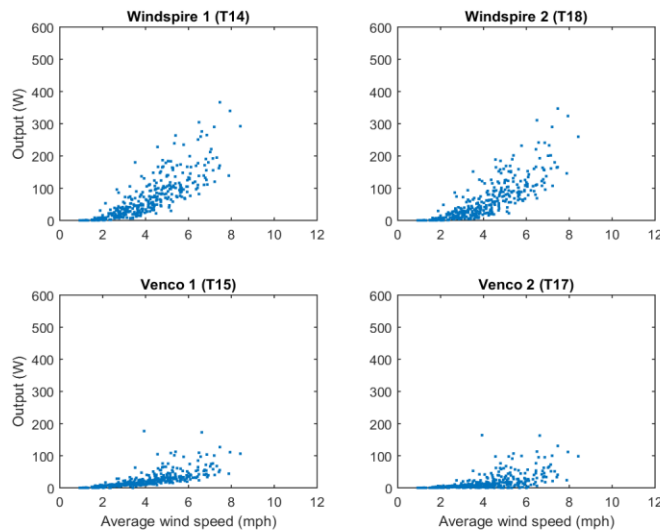
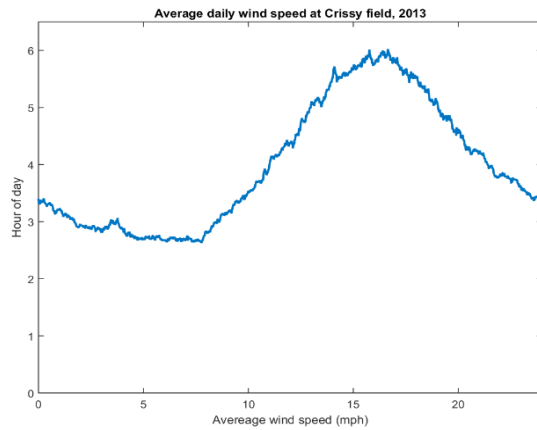
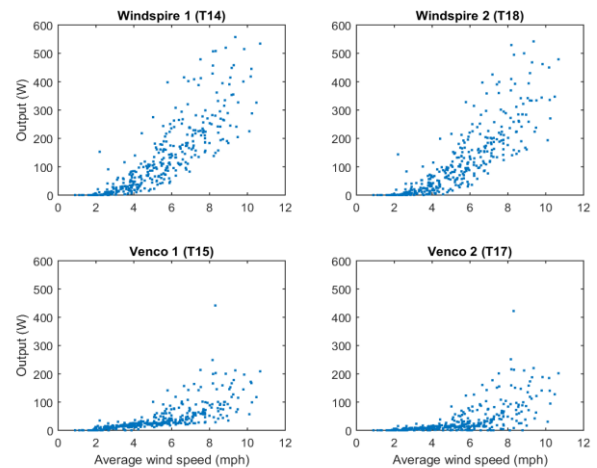


Figure 4.5.19 Power plotted against daily average wind speed

In Figure 4.5.19 the relationship between wind speed and VAWT power output are much more robust on a day to day basis. However, the daily average of the wind speed rarely exceeds 8 mph, which allows for examining only the lower end of the power curves. A daily average wind profile over a 12 month period (2013) shows in Figure 4.5.20 that at Crissy Field the wind peaks in the afternoon, so we repeat the analysis using only data from between 12 – 9 pm, as shown in Figure 4.5.21.



**Figure 4.5.20 Average daily wind profile
Crissy Field, 2013**



**Figure 4.5.21 Afternoon average power
output, 12-9 pm**

Better representing actual short term turbine performance, the resulting afternoon averages show a similar relationship between wind speed and power output for the Windspire and Venco VAWTs at lower wind speeds, while revealing more of the relationship at higher wind speeds. Overall, it is apparent that the Windspire turbines outperform Venco turbines by a large margin. This is true both for total power output and power output relative to the rated power. The plot below in Figure 4.5.22 shows the actual afternoon averages of VAWT power output versus what would be expected given the published power curves for the respective VAWTs. Simple linear estimates of the actual versus expected power output indicate that the Windspire turbines perform at approximately 45% of their rated value at Crissy field, while the Venco turbines perform and approximately 27%.

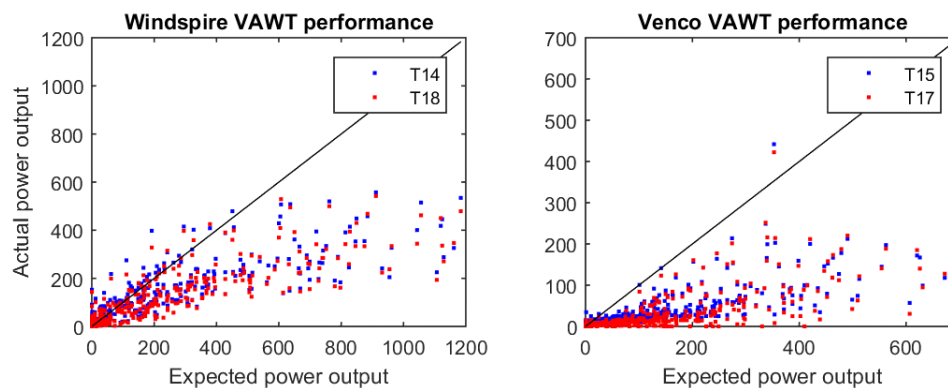


Figure 4.5.22 Actual power output compared to expected, rated power output (black line)

The annual average wind speed measured at the Center is shown in Figure 4.5.23, showing observed annual averages ranging from 3.73 to 3.98 m/s for the two years with complete data. Data for 2012 was only available from October 5-December 31. By comparison, the 4 year average at Anita Rock is 4.28 m/s, with gusts to 5.25 m/s.

The histogram in Figure 4.5.2.12 illustrates the counts of one minute periods of averaged measured wind speed, in binned increments of 0.5 m/s. Much of the observed wind is less than 8.0 m/s, with the velocity ranging from 1.0 to 5.0 m/s and a mean of 3.59 m/s.

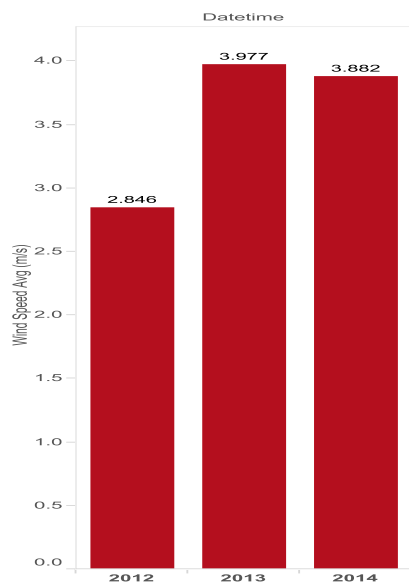


Figure 4.5.23 Average annual wind speed measured at Crissy Field. Data for 2012 was only available from October 5-December 31.

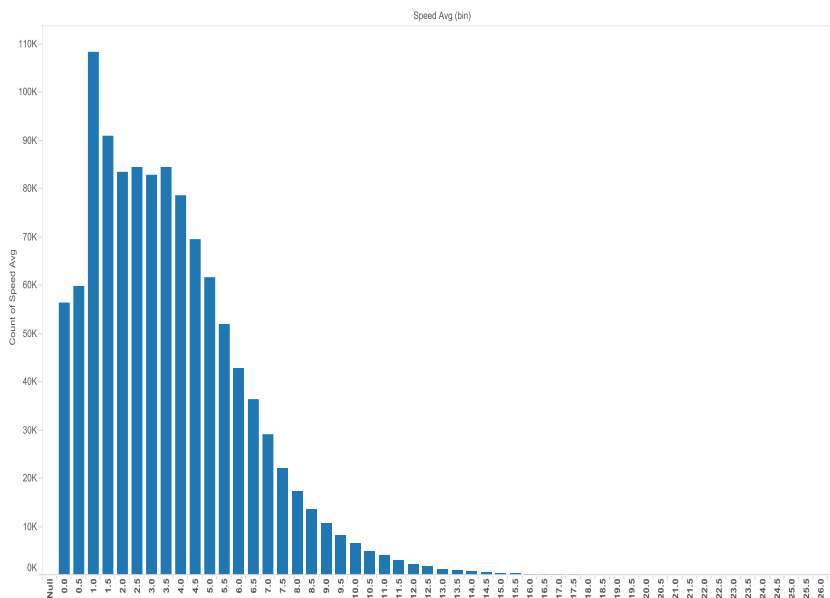


Figure 4.5.24 Histogram of Count of Average Wind Speed (one minute averages)

A pronounced seasonality exists with the Crissy Field wind regime, Figure 4.5.2.13, with the fall/winter average approximately 66% of the average spring/summer wind speed.

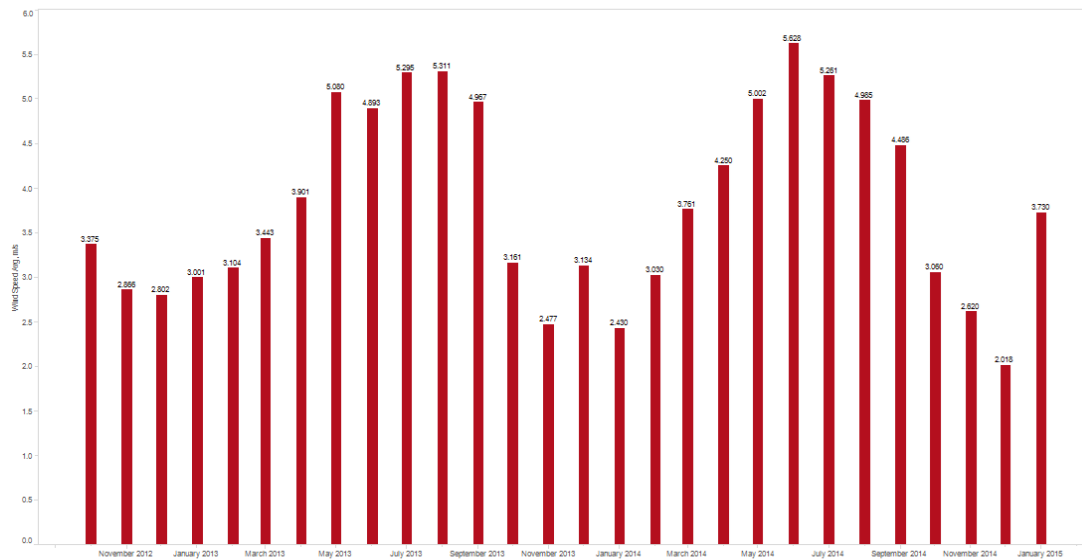


Figure 4.5.25 Monthly variation of wind speed (in average wind speed (m/s) from November 2012 to January 2015)

Wind is predominantly WSW, with a secondary north component as illustrated in the wind rose, Figure 4.5.26. Figure 4.5.27 adds a time dimension by indicating percent of total wind hours for each 45 degree segment.

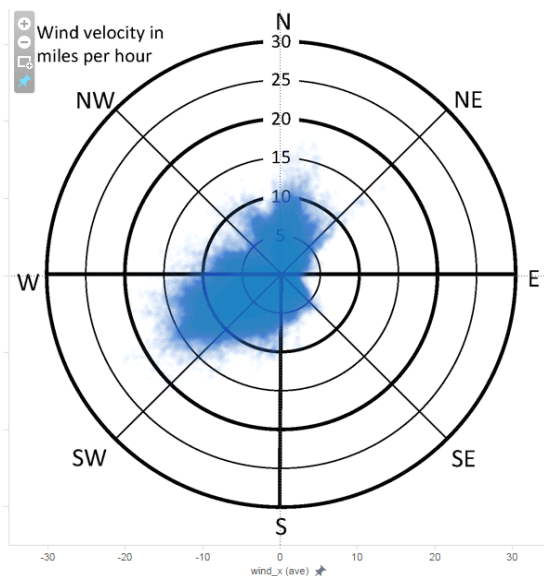


Figure 4.5.26 Wind rose for all observed data points

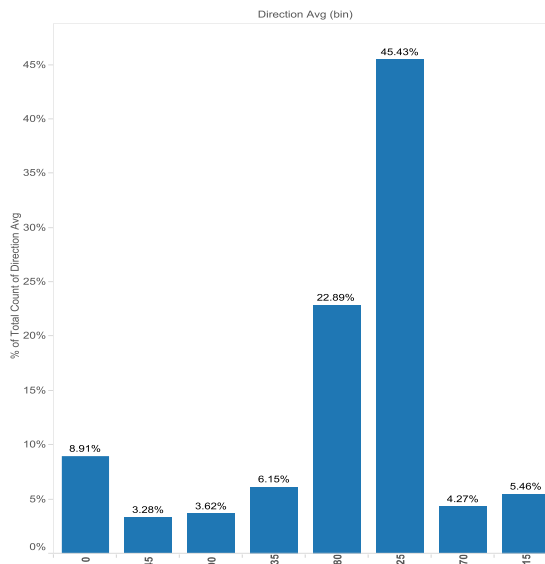


Figure 4.5.27 Wind direction in 45 degree bins. Percent of total measured wind hours

From a request by the Conservancy, the weather tracking firm, WeatherFlow, provided 2 years of 2012-2104 data collected from Anita Rock as indicated in Figure 4.5.28. Visual inspection shows prevailing direction of approx. 240 degrees.

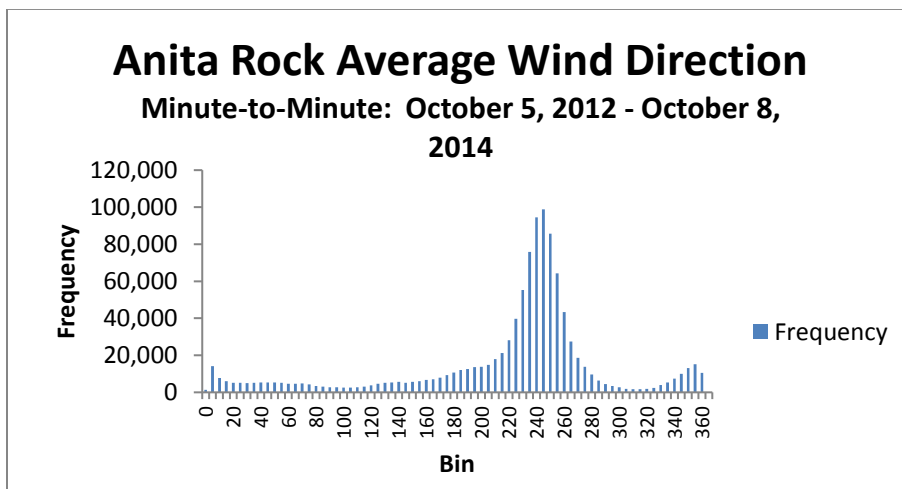
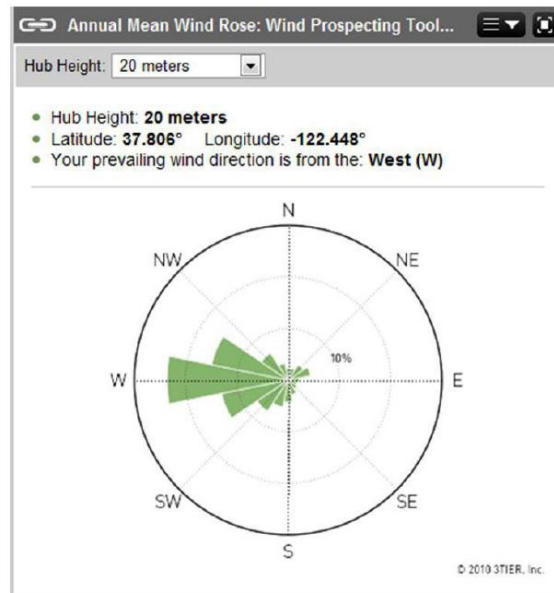


Figure 4.5.28 Anita Rock wind direction data sourced from Weatherflow.

The wind data collected on site, and at Anita Rock conflicts with the initial wind rose provided to the Conservancy in 2010, suggesting further investigation to determine which data source accounted properly for the magnetic declination for this region. A misapplication of the

magnetic declination correction factor can make from 15 to 30 degree difference in reported wind direction in 2011 third party wind prospecting study, Figure 4.5.29.



**Figure 4.5.29 Wind Rose From Crissy Field
Wind Prospecting Study, 2011**

References:

1. [Golden Gate National Park Conservancy, Deliverable 1: Recommendations for Wind Turbine Systems and Data Acquisition Systems](#). November 2012
2. [Golden Gate National Park Conservancy, Deliverable 2: Final Design and Permitting](#). December 2012
3. [Golden Gate National Park Conservancy, Deliverable 3: Site Preparation and Footings](#). March 2013
4. [Golden Gate National Park Conservancy, Deliverable 4: Turbine Installation, Installation Completion](#). April 2013
5. [Golden Gate National Park Conservancy, Deliverable 5: Wind Turbine Commissioning and Interconnection](#) September 2015
6. [Golden Gate National Park Conservancy, Deliverable 6: Installation and Commissioning of the Data Acquisition Systems](#) September 2015
7. [Golden Gate National Park Conservancy, Deliverable 7: Final Report](#) September 2015

4.6 Variable Power Icemaker

4.6.1 Background

The US military deploys to demanding environments such as Forward Operating Bases and Humanitarian and Disaster Relief operations that often lack basic infrastructure to provide necessities such as pure drinking water and refrigeration. The logistics of providing these capabilities to deployed units can be very expensive in terms of the need to use expensive lift equipment that could be better utilized in delivering other supplies such as food, ammunition, and fuel. A potential solution is to use in-theater solar, wind, and water resources (including seawater) to produce ice and potable drinking water on site.

The objective of this project was to demonstrate a ruggedized, variable powered ice machine (VPIM) designed to produce flake ice and desalinated water. Flake ice is preferable for food and medical supply storage because it provides more surface area coverage to cool supplies. The intent of demonstrating the VPIM was to determine its durability and several performance parameters, optimize its operation based on Lynntech Inc.'s rapid turn-down technology, and identify design improvements that would contribute to the development of a robust product for the Navy.

Current ice systems typically operate either “on” or “off” with no capability to follow a variable power supply. This project was intended to demonstrate high efficiency ice creation under variable power levels including high turndown ratio. This “load following” ice generation solution can use intermittent power, such as direct coupling to a PV array or wind turbine, to produce high quality fresh water ice from seawater or other non-potable water sources. The system tested is load-following from 3kW to 10kW and the available power defines the ice generation output.

4.6.2 General Description

The overall design of the system is illustrated in Figure 4.6.1 and consists of an ice maker module stacked on top of an ice chest module. The ice that is produced in the ice maker falls through a chute in the roof of the ice chest. Access to the ice chest is via a door in the side of the unit. The two modules are designed to fit inside a 20' ISO shipping container for rapid deployment as illustrated in Figure 4.6.2.

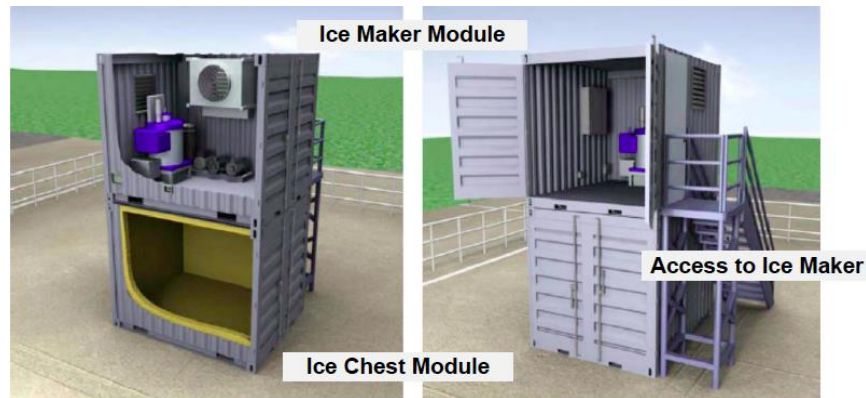


Figure 4.6.1: Variable Power Ice Machine



Figure 4.6.2: Loading Ice Storage Chest into 20' ISO shipping container

The VPIM utilizes commercial off-the-shelf refrigeration hardware and electronic equipment that is controlled and monitored via National Instruments LabVIEW Real-Time software to maintain maximum ice production for a given amount of power input to the system without sacrificing ice quality. The device was automated to minimize the need for operator intervention. An anti-microbial system was incorporated in the VPIM to produce drinking quality water from typical ocean water resources. The 2.5-ton per day unit produces up to 5,000 lbs. of ice per day with a sustained 10kW supply of power.

4.6.3 Specifications

Input Characteristics

| Parameter | Value | Unit |
|-------------------------------------|---------------------------|-----------|
| Voltage | 208/220-240, Single Phase | VAC |
| Operating Current | 0 – 50 | Amps |
| Frequency | 60 | Hz |
| Power Cable (2 conductor + ground) | 6 | AWG |
| External Control Signal | 4 – 20 | mA |
| Water Supply Inlet (free of debris) | 0.5 – 5 (20 – 80) | GPM (PSI) |
| Water Supply Inlet Connection | 3/4 | Inch FNPT |
| Ice House Drain Connection | 1-1/2 | Inch FNPT |
| Ice Storage Drain Connection | 1-1/2 | Slip |

Output Characteristics

| Parameter | Value | Unit |
|---|----------|------------|
| SPST Normally Open Dry contacts | 10 (240) | Amps (VAC) |
| Ice Production (based on power available) | 0 – 2.5 | Tons/day |

Environmental Conditions

| Parameter | Value | Unit |
|---------------------------------|-------------------|------|
| Operating (Storage) Temperature | 0 – 70 (-10 – 85) | °C |
| Operating (Storage) Humidity | 10 – 90 (5 – 95) | % RH |
| Maximum Altitude | 2000 | m |

Mechanical

| Parameter | Value | Unit |
|--|-----------------------|------|
| Weight | 17,000 | Lbs |
| Fully Assembled Dimensions (W x H x D) | 152.5 x 178.0 x 121.9 | Inch |

Tabl 4.6.1. Lynntech variable powered ice machine specifications.

4.6.4 Approach and Scope of Work

To demonstrate the VPIM's performance and durability, the approach was to install the machine at the Natural Energy Laboratory Hawaii Authority (NELHA) on the Island of Hawaii in order to use NELHA's seawater distribution system. HNEI retained an engineer who had experience with the NorthStar icemaker used in the VPIM to assist with experiments. Performance parameters to be evaluated included: ease of deployment, operator usability/user interface, operation at various power levels supplied by PV and by wind resources, operation at various seawater temperature inputs achieved by mixing deep seawater with surface seawater, operation at various incoming salinity mixing freshwater with seawater, dynamic load testing, desalination, ice dispensing rate, ice storage, ruggedness and corrosion resistance. Following demonstration of

performance, operation of the VPIM was to be optimized based on Lynntech Inc.'s rapid turn-down technology. Design improvements were to be identified that would contribute to the development of a robust product for the Navy. The following Scope of Work was developed comprised of the following tasks:

Task 1: Ease of Deployment

- 1) Identify the equipment required to transport the system to a specified site.
- 2) Identify the time required to setup the system at a specified site
- 3) Identify equipment and tools required to setup the system at a specified site
- 4) Recommend design alternatives to decrease/eliminate the need for specialty equipment such as forklifts required to set up the system and improve transportation of the system to remote sites

Task 2: Operator Usability, User Interface

- 1) Evaluate the LabView user interface control system for:
 - a) Ease of Use – can the user easily navigate the user interface?
 - b) Reliability – does the program run consistently while power is available?
 - c) Remote Access – how easy is it to access the system from a remote location?
 - d) Suggested Improvements – what are the program's weaknesses that need to be addressed before advancing to full commercial deployment?
- 2) Evaluate the system's manual on-site controls

Task 3: Operation at Various Power Levels

- 1) Conduct testing using fresh water and saltwater – start at 100% (10 kW) power level and decrease by 10% (1 kW) until reaching 30% (3 kW) power level. The lowest power setting at which the compressors will operate in order to make ice is 30% (3 kW). Lower power settings may be tested to determine operation of other components with lower set-points.
 - a) Measure ice quantity (by weight) at each power set-point
 - b) Measure incoming seawater salinity vs. product ice salinity (by conductivity)
- 2) Keeping the refrigerant temperature constant, evaluate the effect of seawater temperature on ice production – measure ice production and salinity at different incoming water temperatures. Test engineer working in consultation with HNEI to develop a matrix of temperatures that will be used in the test program prior to starting the test runs.
- 3) Evaluate the effect of salinity on ice production – measure ice production and salinity at different incoming water salinities. Working in consultation with HNEI, develop a matrix of salinity levels that will be used in the test program prior to starting the test runs.

Task 4: Dynamic Load Testing

- 1) Use simulation mode and the Wind Profile.txt file provided by HNEI to vary power available input in a controlled but dynamic manner.
- 2) Vary the ramp rates (i.e. power increase/minute and power increase/second). Working in consultation with HNEI, develop a detailed test procedure that will be used in the test program prior to starting the test runs.

Task 5: Desalination Testing

- 1) Evaluate the effect of refrigerant temperature on desalination –
Measure ice production and salinity at a fixed power level, at the lowest recirculation ratio for various refrigerant temperature set points, dependent on incoming sea water temperature and (assuming standard ocean incoming ocean salinity) at various refrigerant temperature set points. Incoming seawater temperature was adjusted by mixing deep seawater with surface seawater to adjust input temperature. Working in consultation with HNEI, develop a matrix of refrigerant temperatures that will be used in the test program prior to starting the test runs.
- 2) Evaluate the effect of incoming water temperature on desalination
Measure ice production and salinity at a fixed power level, at lowest recirculation ratio, standard ocean incoming salinity, and best, or select, (previous test) refrigerant temperature at various incoming water temperatures. Working in consultation with HNEI, develop a matrix of temperatures that will be used in the test program prior to starting the test runs.
- 3) Evaluate the effect of incoming salinity on desalination
Measure ice production and salinity with various incoming water salinities, holding all other variables constant (at values based on previous tests). Working in consultation with HNEI, develop a matrix of incoming salinity levels that will be used in the test program prior to starting the test runs.
- 4) Evaluate the effect of recycle rate on desalination
Measure ice production and salinity with various water recycle ratios, holding all other variables constant (at values based on previous tests). Working in consultation with HNEI, develop a matrix of water recycle rates that will be used in the test program prior to starting the test runs.

Task 6: Simulated Wind Turbine Testing

- 1) Measure ice production and salinity using optimum settings determined in previous tasks, while using the Wind Profile.txt file (provided by HNEI) to run a simulated test of the variable power supplied by a small wind turbine. Working in consultation with HNEI, develop a detailed test procedure that will be used in the test program prior to starting the test runs.
- 2) Test freshwater settings, “hard” salt-ice settings, and desalination settings. Working in consultation with HNEI, develop a detailed test procedure that will be used in the test program prior to starting the test runs.

Task 7: Ruggedness Testing

- 1) Inspect the unit for items shifted or damaged during shipping and setup.
- 2) Make recommendations for enhanced ruggedness (if additional design is needed).

Task 8: Ice Dispensing/Storage

- 1) Evaluate how long it takes to fill the storage volume under different operating conditions. Working in consultation with HNEI, develop a detailed test procedure that will be used in the test program prior to starting the test runs.
- 2) Evaluate any ice-handling issues (i.e. ice dispersion in container, clogging, etc.)

Task 9: Ice Storage Testing

- 1) Evaluate how long the ice will last before melting. Working in consultation with HNEI, develop a detailed test procedure that will be used in the test program prior to starting the test runs.
- 2) Evaluate the suitability of the ice for food storage.
- 3) Evaluate the ability of the melted ice to drain.
- 4) Evaluate ice management, (ice drops through the ice chute from the ice making module into the ice chest where it builds up into a pile. It is shoveled out by hand to bins or into bags for delivery to the end user).
- 5) Recommend design changes.

Task 10: Corrosion Resistance

- 1) Maintain a bi-weekly photographic journal of inspections.
- 2) Identify areas that need improvement (i.e. materials, protective coatings, etc.).

4.6.5 Findings

The VPIM system was installed and commissioned at NELHA as illustrated in Figure 4.6.3 and initially worked satisfactorily. We were able to complete tasks 1, 2, 7, 8, 9, and 10 while our system operation contractor familiarized himself with the operation of the system. However we encountered numerous challenges as time progressed including establishing a working internet connect to allow remote monitoring of the unit, the control system laptop computer which burned out in the hot ice maker compartment, loss of refrigerant from the ice maker, and then an ongoing series electronic equipment failures due to heating and design problems. A major design flaw was identified in the choice of using two vapor compressors rather than using a single compressor. While the system was able to provide the required variable performance under moderate variable input power conditions, the design choice of stopping one compressor when large variations in input power were experienced caused the compressor to vapor lock. This prevented the system from restarting until the vapor lock cleared itself which could take up to 45 minutes. Due to these ongoing challenges it was not possible to test the ability of the system to run the detailed system tests defined in tasks 3, 4, 5, and 6. The following findings were made from the operations we were able to perform.

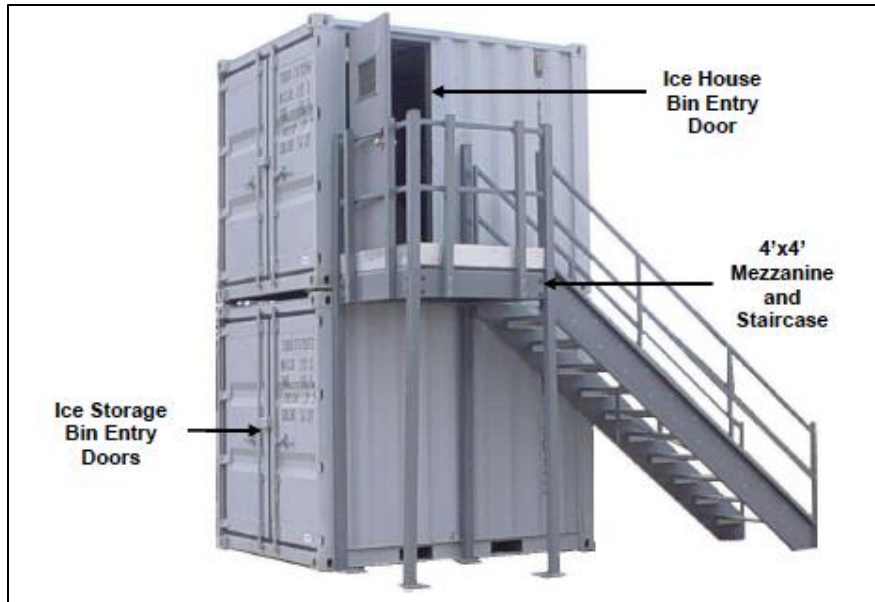


Figure 4.6.3: VPIM Assembled at NELHA

Task 1: Ease of Deployment

In order to be deployed to a Forward Operating Base or a Humanitarian and Disaster Relief operation one of the design criteria was that the unit be easily deployed and setup on the site. In general, the VPIM was simple to deliver and deploy. The VPIM was packaged in two steel container modules that were designed to fit inside a 20ft ISO shipping container. After the VPIM was transported on site by truck, two NELHA staff members were able to assemble it with the small crane shown in Figure 4.6.4.



Figure 4.6.4: NELHA Crane

The crane provided an easy way to move the containers into position vertically but the equipment available could not reach into the container and remove the cubes. Each cube was

dragged out with a truck and cribbing boards to act as a slide. A telescopic forklift would have eliminated dragging of the cubes and would have been the tool of choice for the job (see Figure 4.6.5). Such a machine would have minimized scratches and wear and tear on the container. The telescoping boom forklift would have cut out an hour or so of equipment time.



Figure 4.6.5: Gradall Telescopic Forklift

Container improvements could be made to ease deployment, decrease VPIM maintenance, and improve the functionality of the ice machine.

The operators had to install the electrical connection box outside of the top cube (Figure 4.6.6). This makes it more prone to damage by less professional installers. A recessed or internal connection would make installation simpler and more robust.

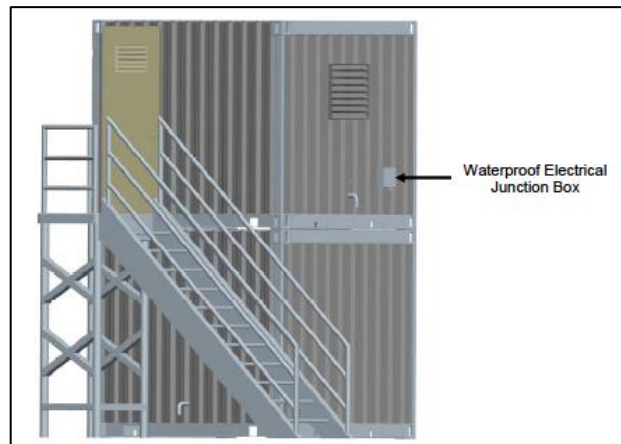


Figure 4.6.6: View of the waterproof electrical junction box on side of Ice Maker Module

Task 2: Operator Usability, User Interface

Labview Interface Evaluation

The VPIM is controlled via a system controller that hosts the main control and data acquisition algorithms embedded on its own processor. The User Interface allows for the user to manipulate the system set points and monitor system conditions. A screenshot of the user interface can be seen in Figure 4.6.7.



**Figure 4.6.7: Screenshot of VPIM User Interface
Graphical User Interface (GUI) Indicators**

Indicators are used to show the current system status. They are represented as both numeric indicators for displaying pressures, temperatures, motor speeds, and power consumed, and Boolean indicators for determining the on/off status of key system components and alarm conditions. Centered on the user interface is a power chart which displays the power available and power consumed values versus time. The chart displays data over a 10-minute window.

At the bottom of the user interface is a status bar that has multiple indicators informing the user of the program's connection status and operating mode. A Boolean indicator and shutdown time alert the user of power outage to the system and time to shutdown while on battery backup.

File Transfer

In the bottom-left corner of the GUI is a file transfer icon the user can select in order to go to the file transfer menu of the program. While on the file transfer menu, the user has the option to download the current data file by selecting the "Download VPIM Data File" icon, upload a new simulation wind profile by selecting the "Upload New Wind Profile" icon, or change the data acquisition settings. All files are maintained in the memory of the system controller. FTP is used to transfer files between the controller and the user's computer.

Mode Selection

A unique feature of the Variable Power Ice Machine is its versatility for testing. In the bottom-right corner of the GUI is a mode selection icon the user can click in order to go to the mode selection menu of the program.

While in the mode selection menu, the user has the option to choose which operating mode they would like to run. There are 4 different modes the user can select to operate the system. Below is a list of each mode and its function.

1. Manual Mode – The manual mode allows the user control over the system's "Power

Available” variable. Running in manual mode assumes sufficient power is available at all times. Within this mode, the user can adjust the power available set point between 0 and 10,000 watts. The user also has the ability to adjust the “Saturation Temperature Set Point” which is a measure of the refrigerant used to cool the ice maker chamber. By varying this point, the user can dictate the rate at which the water freezes on the walls of the ice maker unit. This is a critical set point that will be necessary in determining whether or not this system can properly desalinate incoming salt water.

2. Simulation Mode – While in simulation mode, the user will not have the ability to manually set the “Power Available” set point. Instead, the program is set to run a wind profile that can be changed to accommodate user specific profiles. The program will acquire a value from the wind profile once every 10 seconds and use it to update the power available which in turn determines the operation of the machine. The user will maintain the ability to adjust the “Saturation Temperature Set Point” in the same method as that of the manual mode above.

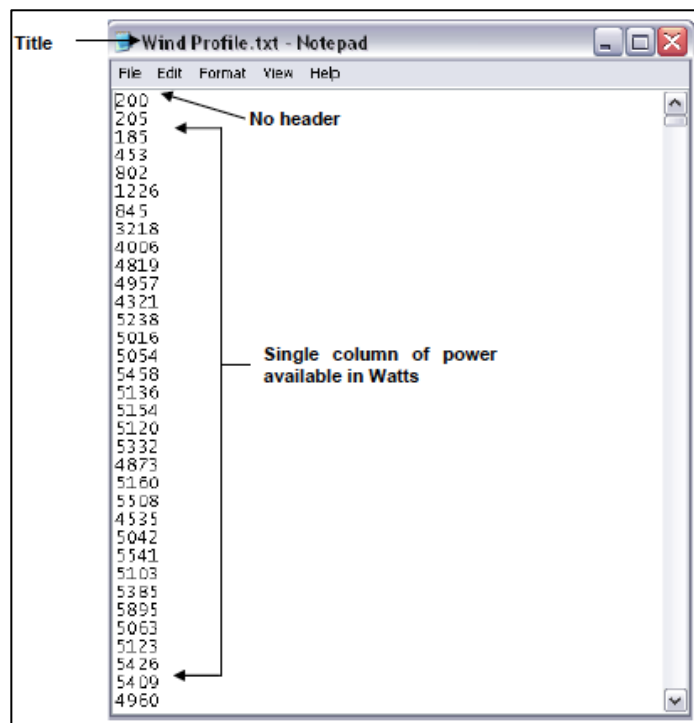


Figure 4.6.8: Example of Wind Profile text file for use in Simulated Mode

3. Real Mode – This mode uses the signal from actual power source such as a wind turbine or diesel generator to determine power available. The VPIM takes an external 4-20 mA signal from the power source and correlates that to 0-100% of the system’s power rating. For instance, if the VPIM is rated for 10 kW, then 4 mA would equal 0 W and 20 mA would equal 10 kW.
4. Administrator Mode – The administrator mode is for Lynntech purposes only.

After selecting the operating mode for the VPIM system, the user may click on the checkmark to confirm the selection and return to the power chart.

Ease of Use

The control system is very easy to navigate and use. The program runs consistently and the controls maintained a consistent set evaporator pressure and power usage. The software hunts a bit overshooting and undershooting its target parameters but this is not abnormal for a system with this many transients and control variables. Evaporator temperature was adjustable but suction pressure was fixed and not adjustable.

The evaporator settings could be manipulated to produce very high quality ice. When the evaporator temperature was dropped to the lower end of the setting the ice that came out of the machine was very high in salt content and perfect for packing fish. Fish packed in this ice did not need added salt to keep the eyes from hazing (a problem common with low salinity ice). It was observed that the ice drum scraper ran rougher as salinity was reduced.

Reliability

One of the Achilles heels of this machine is that it needs a laptop to make adjustments, see fault displays, etc. The laptop that was supplied with the unit failed due to overheating. A PLC is much more robust and reliable than a computer. Since they are sealed inside a control panel, they are better suited for the marine environment. Computers are much more likely to have hardware failures and they can get viruses. PLC's also do not need updates to the software like PC's do. Remote control access by computer could be interfaced remotely to the PLC using Modbus or other control system protocol. Although the National Instruments hardware coupled to LabView is nice for prototype testing, in a commercial model it would be cost prohibitive to use. The same functions could be carried out with a PLC / touchscreen at a fraction of the price.

The program remains stable as long as the user stays within certain operational parameters. However, the program is sensitive to changes in inputs. The more abrupt the change in conditions, the more time it takes to correct. The NorthStar flake ice machine is designed to run at fixed loads. Deviations in available power do not instantly affect all parts of the system. A total power down and restart can cause the system compressors to fail and not be able to restart for up to 45 minutes. Once compressor #1 faults, the program stopped running. If compressor #2 faults, this is not the case. The control system will try to restart compressor #2 once every two minutes after a failed start. As long as the system has over 3250 watts of power available, compressor #1 will keep running. With a variable power source that can dip below this threshold the machine will be very unreliable. On top of the minimum 3250 watts needed to keep compressor #1 on line, 500 watts or more surplus availability may be needed to keep the system from crashing during variable loading.

A battery backup could provide this level of power however this may be costly. A more economical solution would likely be to use a solenoid or control valve plumbed between the high pressure and low pressure side compressor manifolds to lower the differential pressure across the

compressor as needed. This bypass valve would give the ability to lower the torque load on the compressor enabling rapid restarts and quickly flatten out transient system pressures. Lower rotational speeds can even require more current on the compression stroke than full speed due to the lack of rotational inertia available to aid in compression. By using a bypass valve, the compressor load torque (ΔP) can be optimized for the compressor RPM. This may save power and extend the compressor life.

Remote Access

The machine worked very well in this regard as long as there was a reliable internet connection.

Suggested Improvements

If this VPIM were to be remotely operated, there must be a computer or PLC on site to see what is going on with the machine. It would be desirable for the control system to illuminate indicator lights and possibly an audible alarm on the control panel in the event of a fault condition. The audible alarm is helpful to someone shoveling ice to know there is a problem with the system and not just a dip in available power that is inhibiting ice production. Some type of permanently mounted control system is definitely a step forward to commercialization.

The VPIM fills a tank with water and water is pumped from this tank to the VPIM. Water is circulated but a portion of this total is drained to prevent salinity buildup.

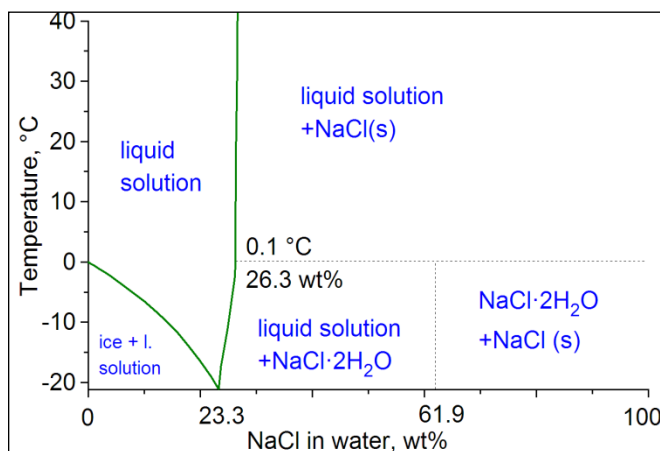


Figure 4.6.9: Salinity versus freezing temperature in water

Part of the water in the tank is cooled by the freezing drum and this energy is wasted as a portion of the chilled water is rejected to drain. A heat exchanger between the discharged water and the inlet water could help retain some of this lost cooling. Salinity management of the tank could also be of benefit to the efficiency as well as the consistency of the ice produced. The evaporator can be set to varying temperatures so the amount of water drained from the tank can vary to maintain the desired reservoir tank salinity.

The drum flake ice machine runs much smoother with saline water.

The program can easily control the ice machine at varying conditions but some conditions are not right for the machine. At the upper end of the power range, this machine makes very high quality ice in good quantities. At power levels below 6500 watts applied (likely dependent on inlet water temperature, salinity and ambient conditions), the ice shaved off the sides of the evaporator drum becomes more like shaved ice (or shave ice as we say in Hawaii) rather than flakes. The flaked ice falls out of the drum nicely but the shaved ice is like powder and can build up. When run at sustained lower power levels, this will prevent the machine from making ice and cause water to drain into the sump below – See photos (Figures 4.6.10 and 4.6.11).



Figure 4.6.10: Ice jammed up (top view)

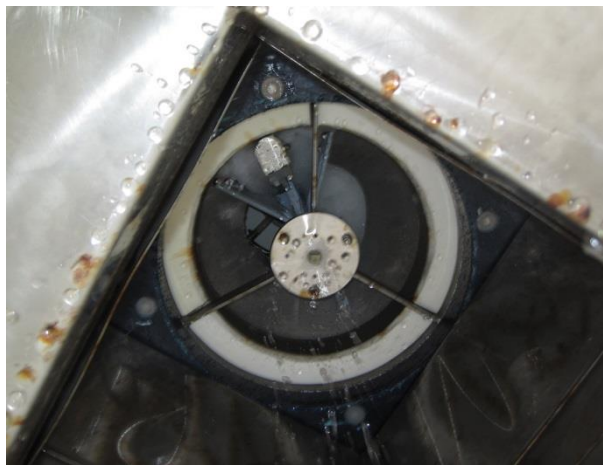


Figure 4.6.11: Water raining down (looking from bottom)

The condition shown in Figures 4.6.10 and 4.6.11 occurred after the machine ran for one hour at 6500 watts sustained using surface seawater. The shaved ice condition could possibly be prevented in different ways:

- 1) Slowing down the drum rotational speed at lower power levels. Lowering the rotational speed is not recommended with the motor powering the drum because it is TEFC (Totally Enclosed Fan Cooled) configuration. These motors have a cooling fan that is

attached to the drive shaft. The faster the motor turns, the more air the fan moves across the motor cooling fins. TEFC motors are designed to run between 50-60 Hz at its rated torque. The drum motor is currently attenuated from 30 Hz to 60 Hz that is slower than the recommended rotational speed. At slower speeds there is less cooling however the force needed to scrape the ice may not be lower. An inverter duty motor has an independent external blower to keep it cool and is industry standard for applications running at less than 50Hz rotational speed.

- 2) Maintaining less liquid refrigerant level in the drum at lower power levels. Lowering the liquid level would concentrate the liquid boiling to a smaller area by concentrating the cooling to the lower part of the drum. This would involve changing the control scheme and adding hardware to detect liquid level height.

Tasks 3 to 6: Operations could not be performed (as mentioned) so there were not test results for these tasks.

Task 7: Ruggedness Testing and Design Recommendations

Electrical System

Most of the major machine components are made for three-phase power. It would be desirable to incorporate a means of bypassing the phase converter on this system. In applications where three-phase power is present, it would boost the efficiency of the system by approximately 12%. It also would help balance the load on the legs of any three-phase generation equipment connection. Of all of the electrical components, the phase converter is also among the most likely to fail.

A number of improvements could be made in a commercial model of this ice machine to enhance its safety and functionality:

- Some of the power is not distributed in a manner that is appropriate for a commercially sold unit.
- The variable frequency drives are stacked too close together and do not meet the manufacturers ventilation requirements. The control panel is too small for all of the components installed in it. A fan was added to help mitigate the lack of heat removal from this panel. The heat generated is substantial and it will likely reduce the service life of the equipment inside the control panel.
- Connections between a power source and a drive should include a disconnect switch and a fuse. One disconnect switch for the entire panel does not suffice. A motor starter protector (MSP) should be used in place of a contactor for each variable frequency drive.
- The use of panel breakers that are branch circuit, UL 508 compliant such as the Siemens SJ series for any AC power leaving the panel are preferred.

- One of the junction boxes is made for home wiring. It cannot seal out moisture. NEMA 4X non-metallic junction boxes are recommended for a commercial version of this machine.
- Control systems should optimally have isolated power supplies. It is better to isolate Relay / Digital switching power with analog control power. This can cause noise and harm circuits. National Instruments chassis do not electrically isolate chassis power with card power.
- Tinned copper wire with silicone grease in the connection or hermetically sealed terminations, (using heat-shrink crimp terminals or adhesive-lined heat-shrink tubing on conventional crimp connectors) is preferred in a marine environment over plain copper wire.

Water System

Copper tubing was observed in the water system plumbing and performs poorly in sea water in terms of corrosion. Cuprous ions can also cause corrosion problems elsewhere in the system. Brass is preferable but only if it is Naval Brass (unlike the fittings on this machine). The bottom line is plastic is cheaper and better for this application and metal fittings should be eliminated wherever possible. The water strainer used in the system is a good idea but it is recommended to use a 100% plastic Y-strainer like IPS or Hayward makes (Figure 4.6.12).



Figure 4.6.12: Hayward Clear All PVC Plastic Strainer

The strainer should be the first line of filtration followed by the 5 micron filter and last, the UV light. The current layout puts the strainer after the UV system. It is recommended that all connections outside the machine be HDPE, Schedule 80 PVC or some other low light transmission product. Sunlight penetrating pipe such as schedule 40 PVC can instigate algae growth in the plumbing that increases maintenance.

Compressor System

Prevention of compressor faults is possible and would be necessary in a commercial model. The Variable Frequency Drive (VFD) settings could be altered and may provide more starting power. The compressor is given 40Hz at startup, ramping up in power level over a couple seconds. It may be beneficial to alter the ramp profile. There is also the possibility of adding a valve

between the high and low side of the compressor to equalize the system pressure at startup to unload the compressor as described above. This would help start the machine regardless of ramp profile on the VFD. If this machine must be operated with only wind or solar power, adding the bypass valve may be necessary.

Task 8: Ice Dispensing/Storage

The steel container holding the ice is not the preferred choice for corrosion and longevity reasons. Shoveling ice out of it eventually caused tears in the insulation. During the first test at startup the plastic paneling became unglued and started to sag away from the foam. The salt water will likely find a way to seep under the insulation and cause corrosion problems.

The use of a refrigerated container would be preferred. These containers are already insulated and very tough. The interior walls are extruded aluminum that is very impact resistant. If the cube containing the icemaker was placed on top of a refrigerated container, the ice storage capacity could be more than doubled and there would be one less cube to deal with. Having the cube holding the ice making equipment able to rise out of the ice storage cube on rails would be an attractive product from the standpoint that the same piece of equipment that offloads the unit from the tractor-trailer base it arrives on could raise the ice making equipment.

Task 9: Ice Storage Testing - Evaluate suitability of the ice for food storage

Initial testing using salt water input produced high quality sea water ice that was used by local NELHA aquaculture companies to freeze their fish. The evaporator settings could be manipulated to produce very high quality ice. When the evaporator temperature was dropped to the lower end of the setting the ice that came out of the machine was very high in salt content and perfect for packing fish.

The UV water purification system will reduce algae and pathogens but it will not sanitize water to make it potable in the configuration currently installed in the system. Additional, pre-filters will be needed to make the UV sanitizer work against viruses and bacteria. Viruses and bacteria can hide in the shadows of floating debris so it must be micron filtered before the UV.

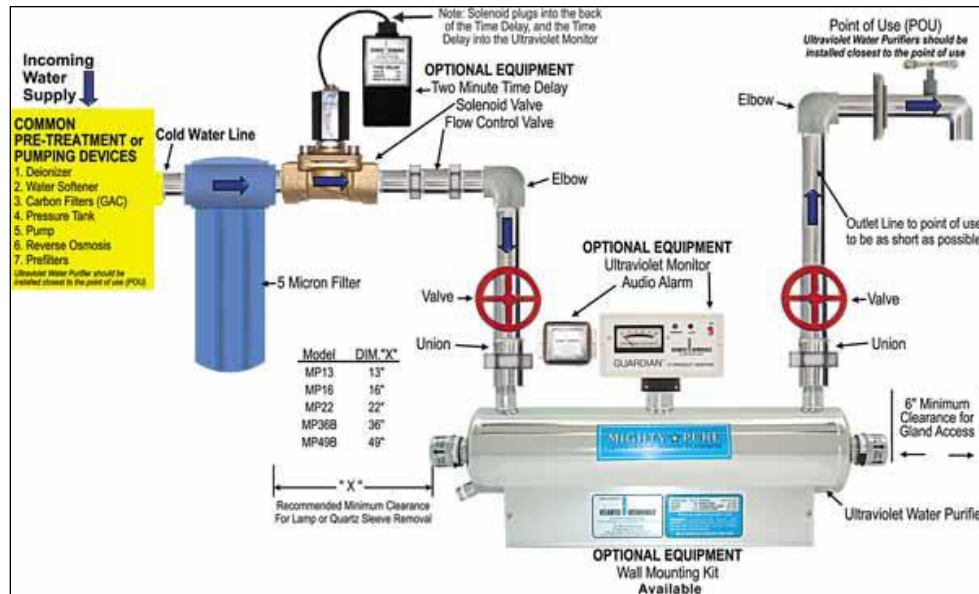


Figure 4.6.13: UV System Layout Recommendations

Note that the manufacturer uses a 5-micron filter in Figure 4.6.13. After water is shut off, either a solenoid valve (Plastomatic brand is recommended) should be used to drain the unit to the exit level when the light is off, or the light should be kept on at all times because micro-organisms can still drift around past the sterilizer after flow is stopped. Most UV lights require a warm up time of 2 minutes before they are effective (note 2-minute delay timer in Figure 4.6.13). Also the monitor is a good feature to include.

In addition to the setup issues, the unit that is installed is not suitable for seawater service. The shell is made from 316 SS that is not suitable for ocean water. Corrosion product from this shell can stain the quartz tube that the bulb sits in and weaken the UV sterilizer effectiveness. It is recommended that this unit be replaced with one featuring a plastic housing in future designs.

Task 10: Corrosion Resistance

As can be observed in Figure 4.6.14, the condition of the modules after five years exposed to a tropical salt air environment in a site located 100 feet from the shoreline at NELHA is considered to be excellent. Items that need some work are the door and hinges to the Ice Making Module, and to the stairs.



Figure 4.6.14: Condition of the modules after 5 years

4.6.6 Conclusions

An advanced prototype VPIM was tested at NELHA in challenging tropical marine environmental conditions. While the initial operations showed considerable promise, the electronics failed due to high heat loads and the moist salt air. A major design flaw was identified in the choice of using two vapor compressors rather than using a single compressor. While the system was able to provide the required variable power supply performance under moderate variable power conditions, the design choice of stopping one compressor when large variations in input power caused the compressor to vapor lock preventing it from restarting until the vapor lock cleared itself. Due to these challenges it was not possible to test the ability of the system to desalinate seawater. On the positive side, the control software worked well, the VPIM did ramp up and down in response to a variable power input, the VPIM was capable of being operated remotely, and high quality seawater flake ice was produced when the power supply was sustained at the high end of the range (over 6,500 watts). Overall the project identified many design improvements to be included in a new design going forward.

4.7 Alternative Biofuels Development

Green Era LLC (GEC) and its partners proposed to develop alternative fuels production facilities, within the State of Hawaii, capable of producing ethanol, renewable diesel and/or jet fuel for commercial and military use. The facilities would apply leading-edge bioconversion and biomass gasification technologies to convert biomass to renewable liquid fuels including ethanol, cellulosic Fischer-Tropsch diesel and renewable jet fuel

Under this agreement, GEC conducted a biofuels assessment using characteristics of agricultural lands in Hawaii as the basis for a case study. The purpose of the assessment is to identify specific biomass feedstock that will provide optimal yields for the selected site; identify “best practice” policies, procedures, and infrastructure for harvesting the feedstock and handling the associated trash. Due to the availability of existing biomass research, initial activities will focus on a detailed examination of existing data and studies to minimize duplication of past efforts. The biofuels assessment comprised four activities described below.

Site Survey: The survey focused on selected agricultural lands in Hawaii. The resulting report including the integrated graphical and tabular database of environmental and production information relevant to biofuels production is available at <http://www.hnei.hawaii.edu/>.

Crop Assessment: The crop assessment included plants suitable for high-yielding production throughout a broad spectrum of agricultural lands. The resulting report is available at <http://www.hnei.hawaii.edu/>.

Production, Harvesting, and Handling Assessment: Various production, harvesting, and handling methodologies for candidate plants included in the crop assessment were evaluated for their applicability on selected agricultural lands in Hawaii. Common harvesting concerns include access, slope and rockiness. The resulting report is available at <http://www.hnei.hawaii.edu/>.

Feedstock Assessment, Processing Assessment, and Waste Handling: The completed crop and production, harvesting, and handling assessments were used as the basis to identify feedstock, processing, and waste handling issues for a number of thermochemical, biochemical and hybrid conversion technologies that could be used to convert the selected feedstocks into usable, sustainable, high-value energy products. The resulting report is available at <http://www.hnei.hawaii.edu/>.

4.8 Algal Production Studies

In this task, Hawaii BioEnergy LLC (HBE) conducted research on the feasibility of growing microalgae as a biofuel. The project investigated the challenges of an open, mixotrophic algal system, i.e. one that is able to grow photosynthetically, utilizing light and inorganic carbon (CO₂), and heterotrophically, using organic carbon (OC). The report summarizing the results of this effort is available at <http://www.hnei.hawaii.edu/>.